Università degli Studi di Ferrara

Dottorato di ricerca in
FISICA
CICLO XXIII

Coodinatore Prof. Filippo Frontera

STUDY OF DOUBLE CHARMONIUM PRODUCTION IN THE *BABAR* EXPERIMENT

Settore Scientifico Disciplinare FIS/04

Dottorando
Dott. Elisa Fioravanti

Tutore
Dott. Diego Bettoni

Anni 2008/2010

... E ho guardato dentro un'emozione
e ci ho visto dentro tanto amore
che ho capito perchè non si comanda al cuore
... E va bene così
... senza parole ...
(Vasco Rossi)

A MATTEO

... Perchè tu sarai sempre il mio solo destino
posso soltanto amarti, senza mai nessun freno ...

Contents

Introduction

The goal of high energy physics is to identify the elementary constituents of matter and to understand their fundamental interactions. Over the last twenty years, this endeavor has been extraordinarily successful. A gauge theory called *Standard Model* provides a satistactory description of the strong, weak, and electromagnetic interactions of all the known elementary particles. There are very few discrepancies between theory and experiment, and most of them are at the level of a few standard deviations or less. However there are processes for which experimental results have differed from theoretical predictions by orders of magnitude: some of these studies are related to the production of charmonium. This dramatic conflict between experiment and theory presents a unique opportunity to make a significant step forward in our understanding of heavy quarkonium physics.

Quarkonia play an important role in several high energy experiments. The diversity, quantity and accuracy of the data still under analysis and currently being collected in many high energy experiments around the world is impressive.

These data come from experiments of quarkonium formation (BES at the Beijing Electron Positron Collider, E835 at Fermilab, and CLEO at the Cornell Electron Storage Ring), clean samples of charmonia produced in B-decays, in photon-photon fusion and in initial state radiation, at the B-meson factories (*BABAR* at PEP-II and Belle at KEKB), including the unexpected observation of large amounts of associated $(c\bar{c})(c\bar{c})$ production and the observation of new and possibly exotics quarkonia states. The CDF and D0 experiments at Fermilab measuring heavy quarkonia production from gluon-gluon fusion in $p\bar{p}$ annihilations at 2 TeV; ZEUS and H1, at DESY, studying charmonia production in photon-gluon fusion; PHENIX and STAR,

at RICH, and NA60, at CERN, studying charmonia production, and suppression, in heavy-ion collisions.
This has led to the discovery of new states, new production mechanisms, new decays and transitions, and in general to the collection of high statistics and precision data sample. In the near future, even larger data samples are expected from the BES-III upgraded experiment, while the B factories and the Fermilab Tevatron will continue to supply valuable data for few years. Later on, new experiments at new facilities will become operational (the LHC experiments at CERN, PANDA at GSI, Super-B factory etc.) offering fantastic challenges and opportunities in this field.
In this thesis the analysis on double charmonium production at the energy of the $\Upsilon(4S)$, with the *BABAR* data is documented. The aim of this analysis is to understand the mechanism of production of double charmonium states from e^+e^- annihilation, in particular after the discrepancies which appeared at the beginning of these studies. With successive studies, these discrepancies have been almost solved.
In particular, in this thesis we present the study of $e^+e^- \to J/\psi c\bar{c}$. This analysis was already performed by the *BABAR* collaboration [21], and in this thesis we want to update that work, with a luminosity nearly four times higher (476 fb^{-1}). In the mean time, also the Belle collaboration published on this analysis [35], obtaining results compatible with *BABAR* and discovering a new charmonium state, named X(3940). We aim here also to confirm this state.
In this thesis we also present the results of $e^+e^- \to \psi(2S)c\bar{c}$ with $\psi(2S) \to J/\psi\pi^+\pi^-$, this analysis was already performed by the Belle collaboration [38] but never by the *BABAR* collaboration.
Finally we also present the analysis $e^+e^- \to \psi(2S)c\bar{c}$ with $\psi(2S) \to \ell^+\ell^-$ for which there are no experimental references available.
The J/ψ or the $\psi(2S)$ is fully reconstructed and the other charmonium state is indirectly detected from the recoil mass. That analysis is performed blind, i.e. the event selection is optimized without looking at the data in the signal region (2-4.5 GeV/c^2 in the recoil mass).
This thesis consists of five chapters:

- Chapter 1: is an introduction to charmonium spectroscopy, with a description

of the NRQCD, which is the theorethical framework of this analysis, then the potential models that have been developed to describe the mass spectrum.

- Chapter 2: is a description of the theories related to the double charmonium production mechanisms, in particular the calculation of the cross section and the discrepancies between theory and experiment is presented.
- Chapter 3: is a description of the *BABAR* detector.
- Chapter 4: is a description of the analysis strategy, selection and cut optimization, efficiency and resolution studies, background evaluation.
- Chapter 5: is a description of the final results, after unblind.

Chapter 1

Charmonium physics

Until 1974 all the known hadrons were composed by three quark flavours: the *up (u)*, *down (d)* and *strange (s)*, with masses of a few MeV/c^2 for the first two and of $\sim$ 100-200 MeV/c^2 for the strange.
In november of 1974, a remarkably massive and narrow resonance, named "J" was discovered [1] with a mass of 3.1 GeV/c^2, decaying to e^+e^-, in the reaction $p+Be \rightarrow e^+e^- + X$ (Fig. 1.1). Simultaneously, the resonance was discovered [2] in the direct channel $e^+e^- \rightarrow hadrons$ (also to $e^+e^-, \mu^+\mu^-$) and was named the "ψ" (Fig. 1.2). The dual name J/ψ has afterwards persisted. This was followed shortly by the discovery of another narrow state at SLAC, which was called ψ' [3].
The unusual narrowness of these two resonances ($\Gamma_{J/\psi} = (93.2 \pm 2.1)$ KeV; $\Gamma_{\psi'} = (286 \pm 16)$ KeV) [4] suggested an interpretation as bound states of new quark, the charm quark (c) and its antiquark ($\bar{c}$), whose existence had been theorized in 1970 because of the absence of flavour changing neutral currents [5]; in fact a pure weak process would not suffice to give the observed width and, otherwise, the abundance of hadronic products denied a pure electromagnetic decay, pointing out as the most resonable explanation an extremely forbidden strong decay [6]. Charm is conserved in strong and electromagnetic processes, so a charmed particle can not decay strongly into a non-charmed particles. However, this decay mode is suppressed by the OZI rule (S. Okubo, G. Zweig, J. Iizuka), which states that disconnected quark-line diagrams are highly suppressed relative to connected ones (Fig. 1.3).

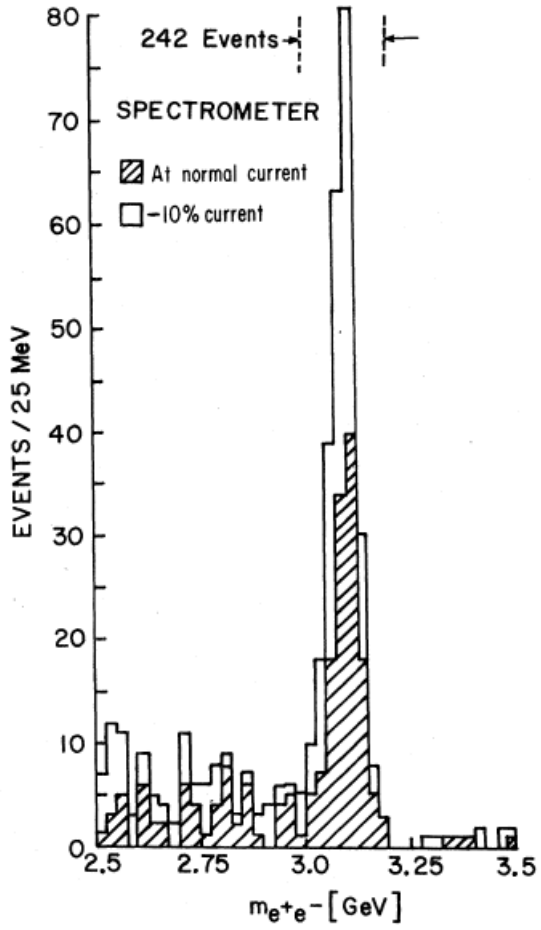

Figure 1.1: *Brookhaven: discovery of a massive and narrow resonance named "J" in the reaction* $p + Be \rightarrow e^+e^- + X$

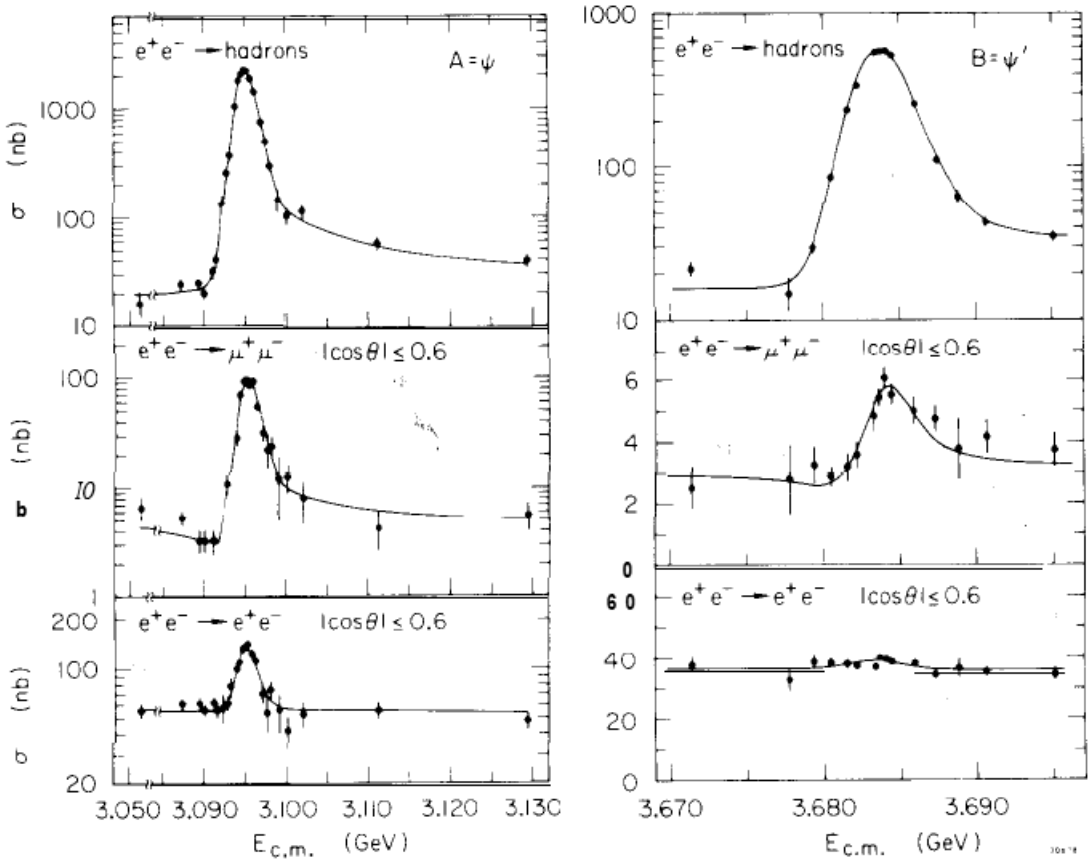

Figure 1.2: $\mu^+\mu^-$ *and* e^+e^- *pair production cross section in the region of the* ψ *(on the left) and* ψ' *(on the right)*

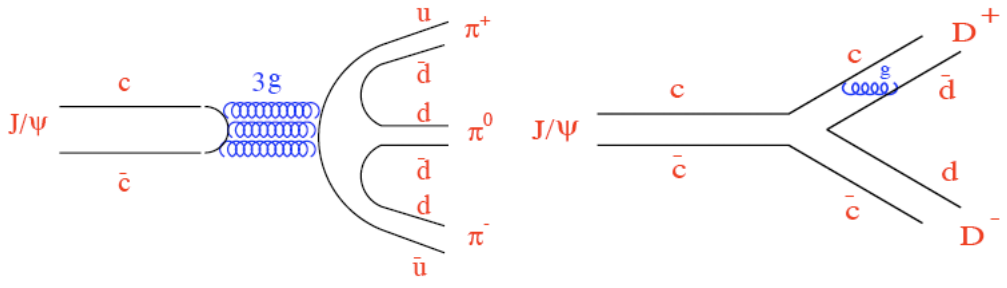

Figure 1.3: *On the left picture we have a disconnected quark-line diagram, while in the right picture we have a connected one which represents an OZI allowed transition, but forbidden by energy conservation.*

With the discovery of the J/ψ, the existence of a new quark flavour called *charm* (c), with a mass of the order of 1 GeV/c^2, as well as the existence of a family of states called *charmonia* was demonstrated.
The J/ψ is a member of this family, that is composed by the bound states of charm quark and antiquark ($c\bar{c}$). The charmonium is the most widely studied heavy quarkonium system, and the goal of this chapter is to give the theoretical tools necessary to face the quarkonium, and in particular charmonium, physics.
Since 1974, quarkonium production and decay is one of the most interesting field to test quantum chromodynamics (QCD), the field theory of the strong interaction, in particular perturbative QCD (PQCD) and effective theories.

1.1 Quantum Chromodynamics

Quantum Chromodynamics is a quantum field theory obtained from the full Standard Model (SM). What remains is a Yang-Mills (YM) theory with local gauge group SU(3) (colour) vectorially coupled to six Dirac fields (quarks) of different masses (flavours). The vector fields in the YM Lagrangian (gluons) live in the adjoint representation and transform like connections under the local gauge group whereas the quark fields live in the fundamental representation and transform covariantly. The QCD Lagrangian is:

$$L_{QCD} = -\frac{1}{4}F^a_{\mu\nu}F^{a\mu\nu} + \sum_{\{q\}} \bar{q}(i\gamma^\mu D_\mu - m_q)q \tag{1.1}$$

where

$$\{q\} = u, d, s, c, b, t$$
$$F^a_{\mu\nu} = \partial_\mu A^a_\nu - \partial_\nu A^a_\mu + g f^{abc} A^b_\mu A^c_\nu$$
$$D_\mu = \partial_\mu - iT^a A^a_\mu$$

and f_{abc} are the SU(3) structure constants and T^a form a basis of the fundamental representation of the SU(3) algebra. When coupled to electromagnetism, gluons behave as neutral particles whereas u, c and t quarks have charges +2/3 and d, s

and b quarks have charges -1/3.
The main properties of QCD are the following:

- It is Poincaré, parity, time reversal and hence charge conjugation invariant. It is in addition invariant under $U(1)^6$ which implies individual flavour conservation.

- Being a non-abelian gauge theory, the physical spectrum consists of colour singlet states only. The simplest of these states have the quantum numbers of quark-antiquark pairs (mesons) or of three quarks (baryons) although other possibilities are not excluded.

- The QCD effective coupling constant $\alpha_s(q)$ decreases as the momentum transfer scale q increases (asymptotic freedom) [10, 11], as also already explained before. This allows to make perturbative calculations in α_s at high energies.

- At low energies it develops an intrinsic scale (mass gap), usually referred as Λ_{QCD}, which provides the main contribution to the masses of most light hadrons. At scales $q \sim \Lambda_{QCD}$, $\alpha_s(q) \sim 1$ and perturbation theory cannot be used. Investigations must be carried out using nonperturbative techniques, the best established of which is lattice QCD. Quark are conventionally divided into light $m_q << \Lambda_{QCD}$ (q = u, d, s) and heavy $m_Q >> \Lambda_{QCD}$ (Q = c, b, t) [1]:

$$m_u\text{=1.7-3.3 MeV/c}^2\text{; } m_d\text{=4.1-5.8 MeV/c}^2\text{; } m_s\text{=}101^{+29}_{-21}\text{ MeV/c}^2\text{,}$$
$$m_c\text{=}1.27^{+0.07}_{-0.09}\text{ MeV/c}^2\text{; } m_b\text{=}4.19^{+0.18}_{-0.06}\text{ GeV/c}^2\text{; } m_t\text{=172.0}\pm\text{0.9}\pm\text{1.3 GeV/c}^2$$

- If light quark masses are neglected, the $U(1)^3$ flavour conservation symmetry of the QCD Lagrangian in this sector is enlarged to a $U(3) \otimes U(3)$ group. The axial U(1) subgroup is explicity broken by quantum effects (axial anomaly). The vector U(1) subgroup provides light flavour conservation. The remaining $SU(3) \otimes SU(3)$ subgroup, known as chiral symmetry group, turns out to be spontaneously broken down to the diagonal SU(3) (flavour simmetry). This produces eight Goldstone bosons, which, upon taking into account the explicit

[1] All these values are taken from [4]

breaking of the symmetry due to the non-zero quark masses, acquire masses that are much smaller than Λ_{QCD}.

- Hadrons containing heavy quarks have masses of the order of m_Q rather than of the order of Λ_{QCD}. They enjoy particular kinematical features that allow for specific theoretical treatments.

1.2 Potential models

Quarkonium is a good testing ground for QCD because the energy levels are due to the strong interaction. In particular, the heavy quarkonium system ($Q\bar{Q}$, where Q can be either c, the charm, or b the bottom flavour) can be treated with non-relativistic models for the two valence quarks, with a great semplification of the theoretical treatment.
When two particles form a bound state, the attractive potential can be studied measuring the energy spectrum of the system. In atomic physics, the binding energy of the electron-nucleus system depends on the orbital angular momentum (L), spin (S) and total angular momentum (J=L+S) state (neglecting the nucleus angular momentum I). To classify the energy levels of the system the spectroscopic notation $n^{2S+1}L_J$ is used. A similar pattern of energy levels is present in positronium (the e^+e^- bound state); this has been used to study the potential between the electron and the positron.
The same concept can be applied also to the mesons: the quark-antiquark ($q\bar{q}$) bound states. Also in this case the spectroscopic notation $n^{2S+1}L_J$ for the classification of the mesons is used.
The intrinsic parity P and charge conjugation C of a charmonium state are related to angular momentum and spin by the relations:

$$P = (-1)^{L+1}$$
$$C = (-1)^{L+S}$$

and so also the J^{PC} notation can be used to classify the $c\bar{c}$ states.

Quantum Chromodynamics (QCD) is the modern theory of the strong interactions. The non perturbative features of QCD prevent the possibility of describing it on the basis of the fundamental theory of the interaction. For this reason the natural approach to charmonium spectroscopy is to build an effective potential model describing the observed mass spectrum. This approximation allows to integrate out many fundamental effects like gluon emission or light quark pairs and to deal with an effective potential which is the result of the $q\bar{q}$ direct interaction as well as the energy of the gluon field. This potential should nevertheless reproduce the two main features of the bound quark states in the two limits of small and large distance: asymptotic freedom and confinement.

The $c\bar{c}$ system can be described with a Schroedinger equation:

$$H\Psi(x) = E\Psi(x), \tag{1.2}$$

where the hamiltonian for the $c\bar{c}$ system can be written as:

$$H = H_0 + H'. \tag{1.3}$$

H_0 can be expressed as a free particle hamiltonian plus a non-relativistic potential V(r):

$$H_0 = 2m_c + \frac{p^2}{m_c} + V(r), \tag{1.4}$$

where m_c is the charm quark mass and p its momentum.

V(r) can be built taking into account the properties of strong interaction in the limit of small and large distances. At small distances the potential between the quarks for a quark-antiquark pair bound in a color singlet, is coulomb-like:

$$V(r) \sim \frac{4}{3}\frac{\alpha_s(r)}{r}, \tag{1.5}$$

where r is the distance between the quarks, α_s is the strong coupling constant and the factor 4/3 comes from the group theory of SU(3), related to the colour.

The value of the running coupling constant α_s depends on the energy scale of the interaction in the way shown in Fig. 1.4, which shows the decrease of α_s with increasing μ.

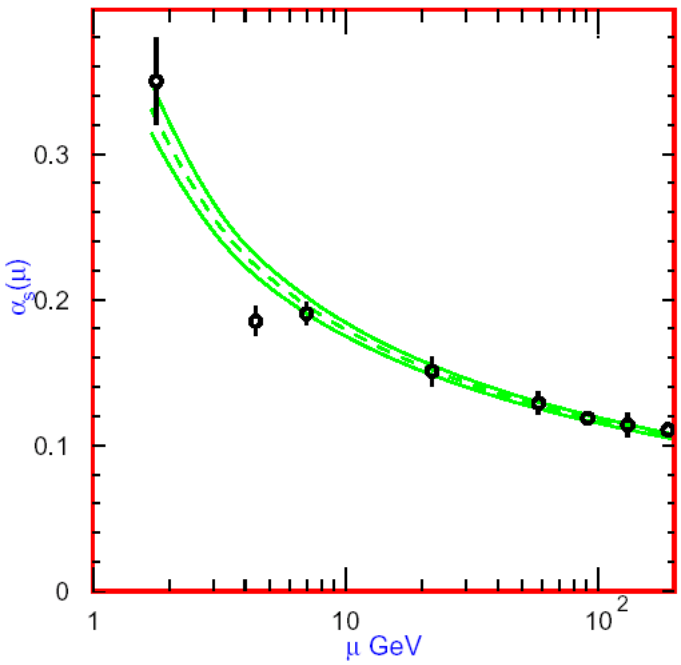

Figure 1.4: *Behaviour of α_s [4], which shows the decrease of α_s with increasing μ.*

At the leading order in the inverse power of $ln(\mu^2/\Lambda^2)$, α_s is described by:

$$\alpha_s(\mu) = \frac{4\pi}{\beta_0 ln(\mu^2/\Lambda^2)}, \tag{1.6}$$

$$\beta_0 = 11 - \frac{2}{3}n_f \tag{1.7}$$

where $\Lambda \sim 0.2$ GeV is the non-perturbative scale of QCD (the energy where Eq. 1.6 diverges) and n_f is the number of quarks lighter than the energy scale. It is clear from Eq. 1.6 that, as the energy scale of a strong process decreases and becomes closer to Λ, α_s increases and the QCD can not be treated as a perturbative theory. As a result of Eq. 1.6 the coupling $\alpha_s(\mu)$ varies logarithmically with μ, so that at very short distances, gluon exchange becomes weaker. This property, known as *asymptotic freedom*, is responsible for the quasi-free behaviour exhibited by quarks in hadrons probed at very short distances by deep inelastic scattering.
At large distance, that means at momentum scales smaller than $\Lambda \sim 200$ MeV the *confinement* term is dominating. It can be written in the form:

$$V(r) \sim kr,$$

where $k \sim 1$ GeV/fm is called string constant. The absence of free quarks in nature is explained exactly by the confinement term, because it implies that the energy of a $q\bar{q}$ system increases with the distance.
By putting together these two behaviours, one can write the Cornell potential, shown in Fig. 1.5 [7]:

$$V(r) \sim -\frac{4}{3}\frac{\alpha_s(r)}{r} + kr, \tag{1.8}$$

with this potential, the charmonium wave function can be expressed as:

$$\Phi(r, \theta, \phi) = R_{nl}(r)Y_l^m(\theta, \phi) \tag{1.9}$$

where we factorize the radial dependence of the wave function in $R_{nl}(r)$ and the angular dependence in the harmonic function $Y_l^m(\theta, \phi)$. This description, however, is not enough to reproduce the mass difference for charmonium states in the same orbital angular momentum or spin multiplets.

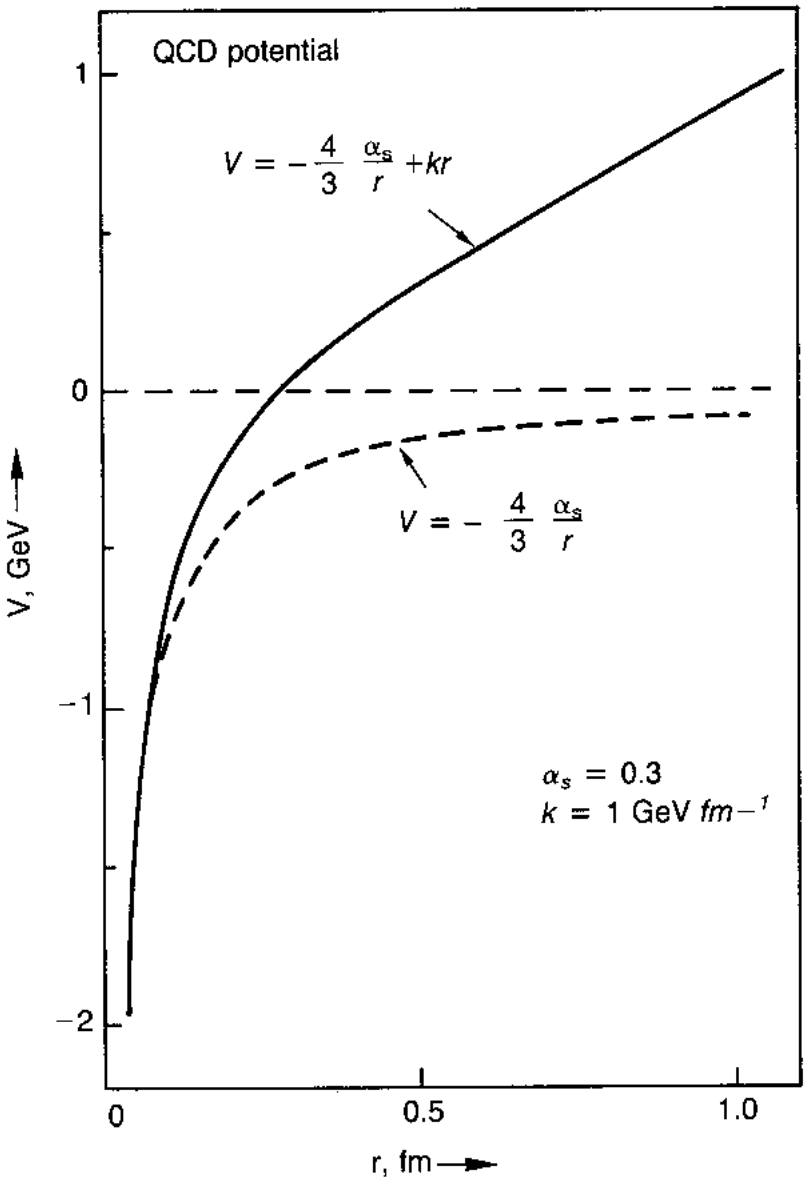

Figure 1.5: *Plot of the QCD potential , for quark-gluon coupling* α_s*=0.20 and* $k = 1$ *GeV/fm.*

H' in the equation 1.3 includes the spin (S) and orbital (L) dependent part of the strong interaction, explaining the charmonium fine and hyperfine structure [8]:

$$H' = V_{LS} + V_{SS} + V_{tens}. \tag{1.10}$$

The various terms of interaction are described in the following:

- **spin-orbit ($\mathbf{V_{LS}}$)**: spin-orbit forces between quarks are present for both vector and scalar interactions, but in different form. We find for quarks of equal mass m_c:

$$V_{LS} = \frac{(\mathbf{L}\cdot\mathbf{S})\left(3\frac{dV_V}{dr} - \frac{dV_S}{dr}\right)}{2m_c^2 r} \tag{1.11}$$

  where V_S and V_V are the scalar and vector components of the non-relativistic potential V(r). This term splits the states with the same orbital angular momentum depending on the ($\mathbf{L}\cdot\mathbf{S}$) expectation value (fine structure);

- **spin-spin ($\mathbf{V_{SS}}$)**: the hyperfine electromagnetic interaction between a proton and an electron leads to a 1420 MHz level splitting between singlet and triplet states of atomic hydrogen. In light-quark system, a similar spin-spin force due to single-gluon exchange between quarks generates the splittings between the masses of the pion and the ρ resonance, the nucleon and the Δ resonance, the Σ and the Λ hyperons, and so on. The spin-spin interaction is of the form:

$$V_{SS} = \frac{2(\mathbf{S_1}\cdot\mathbf{S_2})}{3m_c^2}\cdot\nabla^2 V_V(r) \tag{1.12}$$

  and the expectation value for $(\mathbf{S_1}\cdot\mathbf{S_2})$ is +1/4 for S=1 and -3/4 for S=0;

- **tensor ($\mathbf{V_{tens}}$)**: the tensor potential, in analogy with electrodynamics, contains the tensor effects of the vector potential:

$$V_{tens} = \frac{S_{12}}{12m_c^2}\left(\frac{1}{3}\frac{dV_V}{dr} - \frac{d^2V_V}{dr^2}\right), \tag{1.13}$$

$$S_{12} = 2\cdot\left[3\cdot(\mathbf{S}\cdot\hat{\mathbf{r}})(\mathbf{S}\cdot\hat{\mathbf{r}}) - S^2\right]. \tag{1.14}$$

  where S_{12} has nonzero matrix elements only for $L \neq 0$.

The Coulomb-like part of V(r) correspondes to one-gluon exchange and contributes only to vector term V_V of the potential, while the scalar term V_S is due to the linear confining potential which could in principle contribute to both V_S and V_V, but the fit of χ_{cJ} masses suggests that V_V is small [55]. It is significant to underline that the theory can not predict the coefficients weighting the different contributions from the various terms of hamiltonian Eq. 1.10; in addition, all the theoretical energy levels can be corrected to take into account relativistic effects. All those contributions need to be compared with experimental data of charmonium spectroscopy to evaluate the relative weight.

Another possibility to predict the charmonium mass spectrum is to compute it with lattice QCD (LQCD) [9], which is essentially QCD applied on a discrete Euclidean space-time grid. Indeed, QCD has been very successful in predicting phenomena involving large momentum transfer. In this regime the coupling constant is small and perturbation theory becomes a reliable tool.

On the other hand, at the scale of the hadronic world, $\mu \leq 1$ GeV, the coupling constant is of order unity and perturbative methods fail. In this domain lattice QCD provides a non-perturbative tool for calculating the hadronic spectrum and the matrix elements of any operator within these hadronic states from first principles. Since no new parameters or field variables are introduced in this discretization, LQCD retains the fundamental character of QCD.

The fundamental principles of field theory and the path integral can be used to calculate on a computer the properties of the strong interaction, with Monte Carlo integration of the Euclidean path integral. The value of the lattice spacing, usually denoted with a, can be decided depending on the specific problem that has to be solved; its typical value is $a \sim 0.1$ fm. The physical quantities can be obtained in the limit $a \to 0$.

The only tunable input parameters in these simulations are the strong coupling constant and the bare masses of the quarks. Our belief is that these parameters are prescribed by some yet more fundamental underlying theory, however within the context of the standard model they have to be fixed in terms of an equal number of experimental quantities.

1.3 Effective Field Theories

From the point of view of QCD the description of hadrons containing two heavy quarks is a rather challenging problem, which adds to the complications of the bound state in field theory those coming from a nonperturbative low-energy dynamics. A proper relativistic treatment of the bound state based on the Bethe-Salpeter equation [12] has proved difficult. Perturbative calculations have turned out unpractical at higher order and the method has been abandoned in recent QCD calculations. Moreover, the entanglement of all energy modes in a fully relativistic treatment is more an obstacle than an advantage for the factorization of physical quantities into high-energy perturbative and low energy nonperturbative contributions. Partial semirelativistic reductions and models have been often adopted to overcome these difficulties at the price to introduce uncontrolled approximations and lose contact with QCD. The fully relativistic dynamics can, in principle, be treated without approximations in lattice gauge theories. This is in perspective the best founded and most promising approach, as already said in section 1.2.

A nonrelativistic treatment of the heavy quarkonium dynamics, which is suggested by the large mass of the heavy quarks, has clear advantages. The velocity of the quarks in the bound state provides a small parameter in which the dynamical scales may be hierarchically ordered and the QCD amplitudes systematically expanded. Factorization formulas become easier to achieve. A priori we do not know if a nonrelativistic description will work well enough for all heavy quarkonium systems in nature: for instance, the charm quark may not be heavy enough. The fact that most theoretical predicitions are based on such a nonrelativistic assumption and the success of most of them may be seen as a support to the assumption.

We may, however, also take advantage of the existence of a hierarchy of scales by substituting QCD with simpler but equivalent *Effective Field Theory* (EFTs). EFTs have become increasingly popular in particle physics during the last decades.

They provide a realization of Wilson renormalization group ideas [13] and fully exploit the properties of local quantum field theories. An EFT is a quantum field theory with the following properties:

1. it contains the relevant degrees of freedom to describe phenomena that occur in certain limited range of energies and momenta;

2. it contains an instrinsic energy scale Λ that sets the limit of applicability of the EFT.

The Lagrangian of an EFT is organized in operators of increasing dimension, hence, an EFT is in general non-renormalizable in the usual sense. In spite of this, it can be made finite to any finite order in $1/\Lambda$ by renormalizing (matching) the constants (matching coefficients) in front of the operators in the Lagrangian until that order. This means that one needs more renormalization conditions when the order in Λ is increased. However, even if the only way of fixing the constants would be by means of experimental data, this would reduce but not spoil the predictive power of the EFT. If the data are abundant, the constants can be fit once for ever and used later on to make predictions on new experiments.
The prototype of EFT for heavy quarks is the *Heavy Quark Effective Theory* (HQET) which is the EFT of QCD suitable to describe systems with only one heavy quark [14, 15]. These systems are characterized by two energy scales: m and Λ_{QCD}. HQET is obtained by integrating out the scale m and built as a systematic expansion in powers of Λ_{QCD}/m.
As discussed above, bound states made of two heavy quarks are characterized by more scales. Integrating out only the scale m, which for heavy quarks can be done perturbatively, leads to an EFT, *Nonrelativistic QCD* (NRQCD) [16, 17], that still contains the lower scales and dynamical degrees of freedom. Disentangling the remaining scales is relevant both technically, since it enables perturbative calculations otherwise quite complicated, and more fundamentally, since it allows to factorize nonperturbative contributions into the expectation values or matrix elements of few operators. These may be eventually evaluated on the lattice, extracted from the data or calculated in QCD vacuum models.
In the next section we will give a brief general introduction to NRQCD, since this is the framework more relevant for the analysis presented in this thesis.

1.4 Nonrelativistic QCD

A particularly elegant approach for separating relativistic from nonrelativistic scales is to recast the analysis in terms of nonrelativistic quantum chromodynamics (NRQCD) [17], an effective field theory designed precisely to separate the relativistic physics of annihilation (which involves momenta $p \sim M$) from the nonrelativistic physics of quarkonium structure (which involves $p \sim Mv$).
NRQCD consists of a nonrelativistic Schroedinger field theory for the heavy quark and antiquark that is coupled to the usual relativistic field theory for light quarks and gluons. The theory is made precisely equivalent to full QCD through the addition of local interactions that systematically incorportate relativistic corrections through any given order in the heavy-quark velocity v. It is an effective field theory, with a finite ultraviolet cutoff of order M that excludes relativistic states (states that are poorly described by nonrelativistic dynamics). A heavy quark in the meson can fluctuate into a relativistic state, but these fluctuations are necessarily short-lived. This means that the effects of the excluded relativistic states can be mimicked by local interactions and can, therefore, be incorporated into NRQCD through renormalizations of its infinitely many coupling constants. Thus, nonrelativistic physics is correctly described by the nonperturbative dynamics of NRQCD, while all relativistic effects are absorbed into coupling constants that can be computed as pertubation series in $\alpha_s(M)$.
The main advantage offered by NRQCD in this context is that it is easier to separate contributions of different orders in v in NRQCD. Thus, we are able not only to organize calculations to all orders in α_s, but also to elaborate systematically the relativistic corrections to the conventional formulas.

1.4.1 The NRQCD Lagrangian

The most important energy scales for the structure and spectrum of a heavy quarkonium system are Mv and Mv^2, where M is the mass of the heavy quark Q and $v \ll 1$ is its average velocity in the meson rest frame. Momenta of order M play only a minor role in the complex binding dynamics of the system. We can take

advantage of this fact in our analysis of heavy quark mesons by modifying QCD in two steps.

We start with full QCD, in which the heavy quarks are described by 4-component Dirac spinor fields. In the first step, we introduce an ultraviolet momentum cutoff that is of order M. This cutoff explicitly excludes relativistic heavy quarks from the theory, as well as gluons and light quarks with momenta of order M. It is appropriate to an analysis of heavy quarkonium, since the important nonperturbative physics involves momenta of order Mv or less. Of course, the relativistic states we are discarding do have some effect on the low energy physics of the theory. However, any interaction involving relativistic intermediate states is approximately local since the intermediate states are necessarily highly virtual and so cannot propagate over long distances. Thus, generalizing standard renormalization procedures, we systematically compensate for the removal of relativistic states by adding new local interactions to the lagrangian. To leading order in $1/\Lambda$ or, equivalently, $1/M$, these new interactions are identical in form to interactions already present in the theory, and so the net effect is simply to shift bare masses and charges. Beyond leading order in $1/M$, one must extend the lagrangian to include nonrenormalizable interactions that correct the low energy dynamics order-by-order in $1/M$. In this cutoff formulation of QCD, all effects that arise from relativistic states, and only these effects, are incorporated into renormalizations of the coupling constants of the extended lagrangian. Thus, in the cutoff theory, relativistic and nonrelativistic contributions are automatically separated. This separation is the basis for an analysis of the annihilation decays of heavy quarkonia. The lagrangian for NRQCD is:

$$L_{NRQCD} = L_{light} + L_{heavy} + \delta L \tag{1.15}$$

The gluons and the n_f flavors of light quarks are described by the fully relativistic lagrangian:

$$L_{light} = -\frac{1}{2} tr G_{\mu\nu} G^{\mu\nu} + \sum \bar{q} i \not{D} q \tag{1.16}$$

where G_μ is the gluon field-strength tensor expressed in the form of an SU(3) matrix, and q is the Dirac spinor field for a light quark. The gauge-covariant derivative is $D^\mu + igA^\mu$, where $A^\mu = (\phi, \mathbf{A})$ is the SU(3) matrix-valued gauge field and g

is the QCD coupling constant ($\alpha_s(\mu) = g^2(\mu)/(4\pi)$). The sum in 1.16 is over the n_f flavours of light quarks.
The heavy quarks and antiquarks are described by the term:

$$L_{heavy} = \phi^\dagger \left(iD_t + \frac{\mathbf{D}^2}{2M} \right) \phi + \chi^\dagger \left(iD_t - \frac{\mathbf{D^2}}{2M} \right) \chi \tag{1.17}$$

where ϕ is the Pauli spinor field that annihilates a heavy quark, χ is the Pauli spinor field that creates a heavy antiquark, and D_t and $\mathbf{D}$ are the time and space components of the gauge-covariant derivative D^μ. Color and spin indices on the fields ϕ and χ have been suppressed. The lagrangian $L_{light} + L_{heavy}$ describes ordinary QCD coupled to a Schroedinger field theory for the heavy quarks and antiquarks.
The relativistic effects of full QCD are reproduced through the correction term δL in the lagrangian L_{NRQCD} [16].
In particular the correction terms most important for heavy quarkonium are bilinear in the quark field or antiquark field:

$$\begin{aligned} L_{bilinear} \;=\; & \frac{c_1}{8M^3}(\phi^\dagger(\mathbf{D^2})^2\phi - \chi^\dagger(\mathbf{D^2})^2\chi) \\ & + \frac{c_2}{8M^2}(\phi^\dagger(\mathbf{D}\cdot g\mathbf{E} - g\mathbf{E}\cdot\mathbf{D})\phi - \chi^\dagger(\mathbf{D}\cdot g\mathbf{E} - g\mathbf{E}\cdot\mathbf{D})\chi) \\ & + \frac{c_3}{8M^2}(\phi^\dagger(i\mathbf{D}\times g\mathbf{E} - g\mathbf{E}\times i\mathbf{D})\phi - \chi^\dagger(i\mathbf{D}\times g\mathbf{E} - g\mathbf{E}\times i\mathbf{D})\chi) \\ & + \frac{c_4}{2M}(\phi^\dagger(g\mathbf{B}\cdot\sigma)\phi - \chi^\dagger(g\mathbf{B}\cdot\sigma)\chi) \end{aligned} \tag{1.18}$$

where $E^i = G^{0i}$ and $B_i = \frac{1}{2}\epsilon^{ijk}G^{jk}$ are the chromo-electric and chromo-magnetic components of the gluon field strength tensor $G^{\mu\nu}$. By charge conjugation symmetry, for every term in Eq. 1.18 involving ϕ, there is a corresponding term involving the antiquark field χ, with the same coefficient c_i, up to a sign. The operators in Eq. 1.18 must be regularized, and they therefore depend on the ultraviolet cutoff or renormalization scale Λ of NRQCD. The coefficients $c_i(\Lambda)$ also depend on Λ in such a way as to cancel the Λ-dependence of the operators.
Notice that $L_{bilinear}$ does not contain mixed two-fermion operators involving $\chi^\dagger$ and ϕ (or $\phi^\dagger$ and χ), corresponding to the annihilation (or the creation) of a $Q\bar{Q}$ pair. Indeed such terms are excluded from the lagrangian as part of the definition of

NRQCD: if such an operator annihilates a $Q\bar{Q}$ pair, it would, by energy conservation, have to create gluons (or light quarks) with energies of order of M. The amplitude for annihilation of a $Q\bar{Q}$ pair into such high energy gluons cannot be described accurately in a nonrelativistic theory such as NRQCD.
The coefficients c_i must be tuned as functions of the coupling constant α_s, the heavy-quark mass parameter in full QCD, and the ultraviolet cutoff Λ of NRQCD, so that physical observables are the same as in full QCD.
In principle, infinitely many terms are required in the NRQCD lagrangian in order to reproduce full QCD, but in practice only a finite number of these is needed for precision to any given order in the typical heavy-quark velocity v.

1.5 Experimental methods for charmonium production

Charmonium can be produced in several ways, which reach different states in the mass spectrum; we are going to take into account the two main families of production methods: e^+e^- collisions and $p\bar{p}$ annihilations.

1.5.1 e^+e^- collisions

Studies of charmonium spectroscopy were initially performed almost solely at e^+e^- colliders. In these experiments we have to consider the reaction $e^+e^- \to \gamma^* \to c\bar{c}$, in which e^+e^- annihilation creates a $c\bar{c}$ bound state through an intermediate virtual photon (Fig. 1.6).

Additional production mechanisms include photon-photon fusion, initial state radiation (ISR) and B-meson decay.
Experiments that have studied charmonium physics in this channel are numerous: the first SLAC experiments Mark I, II and III, TPC and Crystal Ball; the DASP and PLUTO experiments at DESY; CLEO and CLEO-c at the Cornell Storage Ring; the LEP experiments; the BES experiment at the BEPC Collider in Beijing; *BABAR* and

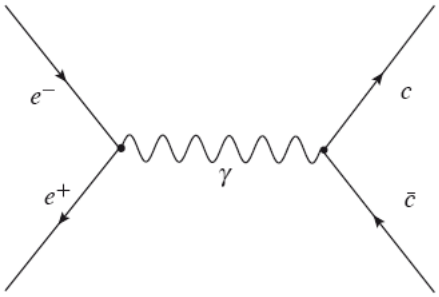

Figure 1.6: *The Feynman diagram for charmonium production in e^+e^- annihilations.*

Belle at the SLAC and KEK-B factories, respectively.

Direct Formation In e^+e^- annihilations direct charmonium formation is only permitted for states with the quantum numbers of the photon ($J^{PC} = 1^{--}$), namely the J/ψ, ψ' and $\psi(3770)$ resonances. All the other states are produced in the radiative decays of these $J^{PC} = 1^{--}$ particles, as we can see by observing the photon spectrum from the Crystal Ball experiment (Fig. 1.7) for the process $e^+e^- \to \psi' \to \gamma + X$. The peaks marked with the numbers 1, 2, 3 and 7 identify the $c\bar{c}$ states which can be reached from the ψ' with a radiative transition, namely the $\chi_{cJ}(1^3P_J)$ and the $\eta_c(1^1S_0)$; 4,5 and 6 correspond to the radiative decays from the χ_{cJ} states to the J/ψ. The parameters of these resonances are determined by measuring the recoil photon energy; for this reason, the accurancy in the measurement of the masses and widths of these states is limited by the detector resolutions, which is worse than the precision with which the beam energies are known. Morever, radiative cascades involving small branching ratios or multiple steps are difficult to observe.

Two-Photon production Electron-positron annihilation at high energies can produce the J-even charmonium states through two virtual photons interaction via the process $e^+e^- \to e^+e^- + c\bar{c}$, illustrated in Fig. 1.8. The production rate in this case decreases by a factor of α^2 compared to the rate for a single photon, where α is the fine structure constant. The $c\bar{c}$ state is identified by observing its hadronic

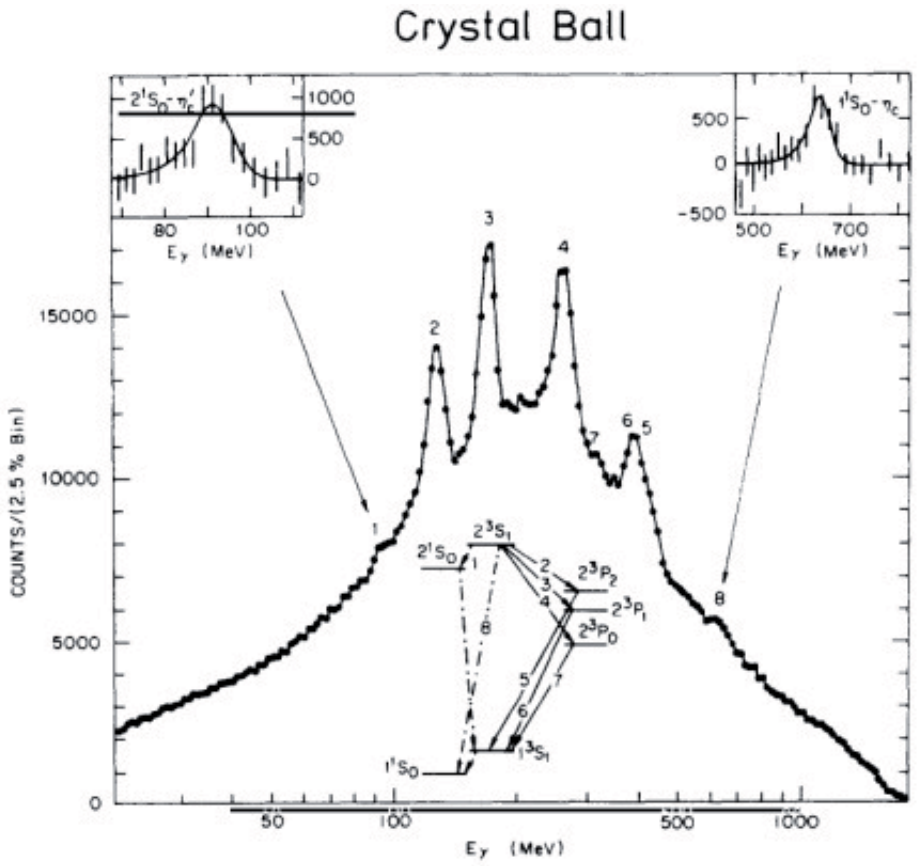

Figure 1.7: *The inclusive photon spectrum from the Crystal Ball experiment [20]*

decays.

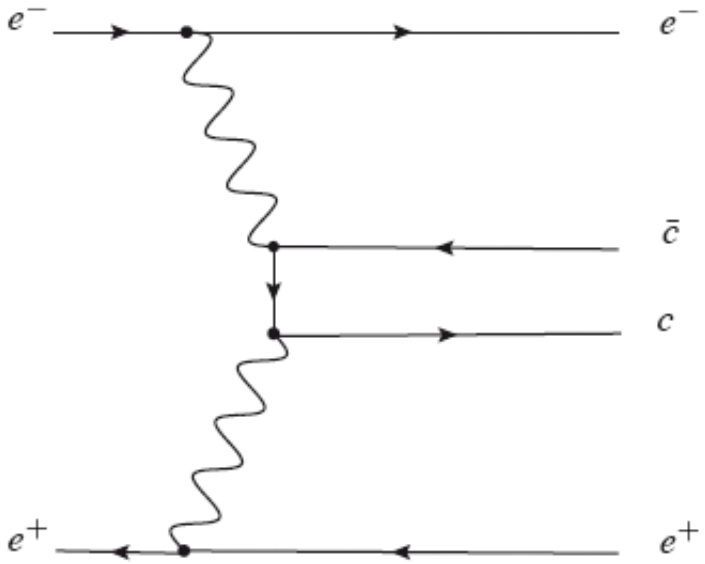

Figure 1.8: *The Feynman diagram for the two-photon fusion process*

Initial state radiation (ISR) Another interesting process for the charmonium production in e^+e^- collisions is Initial State Radiation (ISR) in which either the electron or the positron, as illustrated in Fig. 1.9, radiates a photon before the annihilation, therefore lowering the effective center-of-mass energy. Like in direct formation only $J^{PC} = 1^{--}$ states can be produced. This mechanism allows a large mass range to be explored and is very useful for the measurement of R, the ratio of the total $e^+e^- \to hadrons$ cross section to the $e^+e^- \to \mu^+\mu^-$ cross section, and for searching new vector states.

B meson decays Charmonium states can be produced in the decays of B mesons (Fig. 1.10), even if these kinds of process are colour suppressed. In this way we can produce states of any quantum number. The large samples available at the B factories make this approach very powerful to study known particles and to discover new resonances; the decays of the B mesons provide a clean production en-

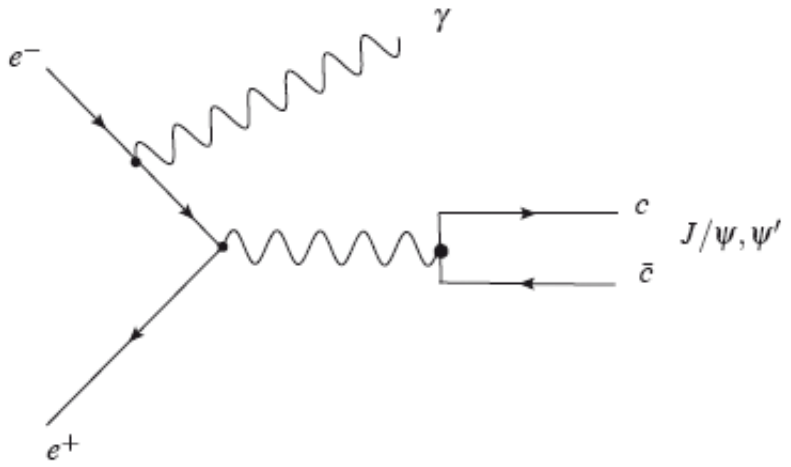

Figure 1.9: *Initial state radiation production of charmonium*

viroment for charmonium. The discovery in 2002 of $\eta_c(2S)$ [23] in the exclusive decays $B \to K\eta_c(2S) \to KK_sK^-\pi^+$ and in 2003 of X(3872) in the exclusive decay $B^\pm \to K^\pm X(3872) \to K^\pm\pi^+\pi^- J/\psi$ are examples of the discovery potential of the B factories.

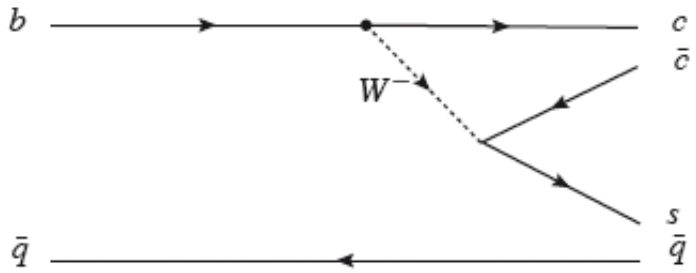

Figure 1.10: *Feynman diagram of a B meson decay to charmonium*

Double charmonium The production of double charmonium in e^+e^- annihilations (Fig. 1.11) was discovered by the Belle collaboration from data collected at the $\Upsilon(4S)$ resonance at a center-of-mass energy $\sqrt{s} = 10.6$ GeV by studying the recoil mass spectrum of the J/ψ in the process $e^+e^- \to J/\psi + X$. [19]

The collaboration measured the production cross section for $e^+e^- \to J/\psi\eta_c$ and found also evidence for $e^+e^- \to J/\psi\chi_{c0}$ and $e^+e^- \to J/\psi\eta_c'$ production. These measurements were improved by the *BABAR* collaboration [21], that also calculated the cross section for the last two mentioned processes. The measured cross section for double charmonium production was about one order of magnitude larger than the theoretical prediction of NRQCD. This discrepancy remains still unexplained, even if the experimental and the theoretical values are now closer [21, 38, 39, 43, 50]. This mechanism of charmonium production will be studied in detail in the analysis that will be presented in the chapter 4 of this thesis.

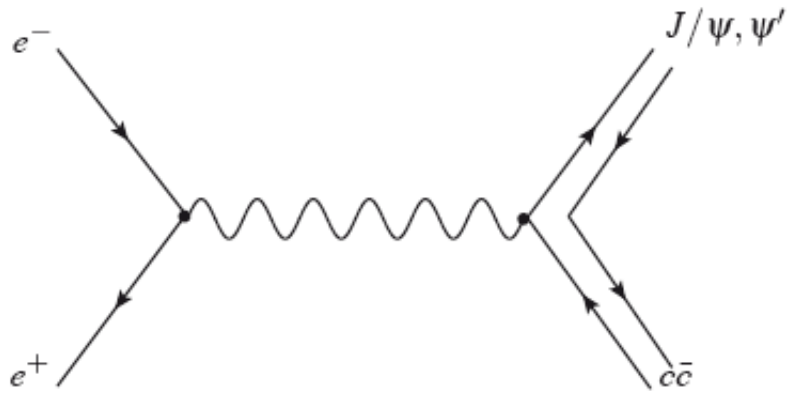

Figure 1.11: *Double charmonium production in e^+e^- annihilation*

1.5.2 $p\bar{p}$ annihilation

The instrinsic limitation of e^+e^- experiments, where direct formation is only possible for $J^{PC} = 1^{--}$ states, can be overcome by studying $p\bar{p}$ annihilation. In this process the coherent annihilation of the three quarks in the proton with the three antiquarks in the antiproton makes it possible to form directly states with all non exotic quantum numbers, via intermediate state with the appropriate number of gluons and/or virtual $q\bar{q}$ pairs.
In Fig. 1.12 we show the $p\bar{p}$ annihilation via two and three gluons intermediate states

for, respectively, J-even and J-odd charmonium states production. This technique, originally proposed in 1979 [22], became successfully employable some years later thanks to the development of stochastic cooling.
The resonant formation of charmonium states in $p\bar{p}$ annihilation has been studied at the CERN Intersecting Storange Rings by the R704 experiment (1983-1984), and at the Fermilab antiproton accumulator by E760 (1990-1992) and E835 (1996-2000) experiments.

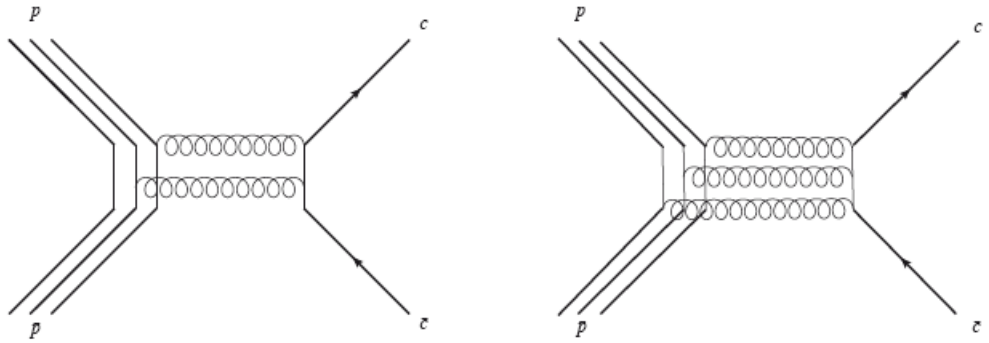

Figure 1.12: *Feynman diagrams for charmonium production in $p\bar{p}$ annihilation via two and three gluons intermediate states.*

1.6 Charmonium spectrum

The charmonium spectrum (Fig. 1.13) consists of eight narrow states below the threshold for open charm (the $D\bar{D}$ threshold at 3.73 GeV) and several tens of states above this threshold. The potential model, described in the previous section, can explain with the spin-spin interaction term V_{SS} the splitting between spin singlet and triplet states like η_c and J/ψ, and with the spin-orbit interaction term V_{LS} the splitting between states with different J like $\chi_{c0,1,2}$. The states below threshold are very narrow because they cannot decay in charmed hadrons for energy conservation reasons. Consequently the hadrons decays with the annihilation of the quark c and the antiquark $\bar{c}$ which is suppressed by the OZI rule.

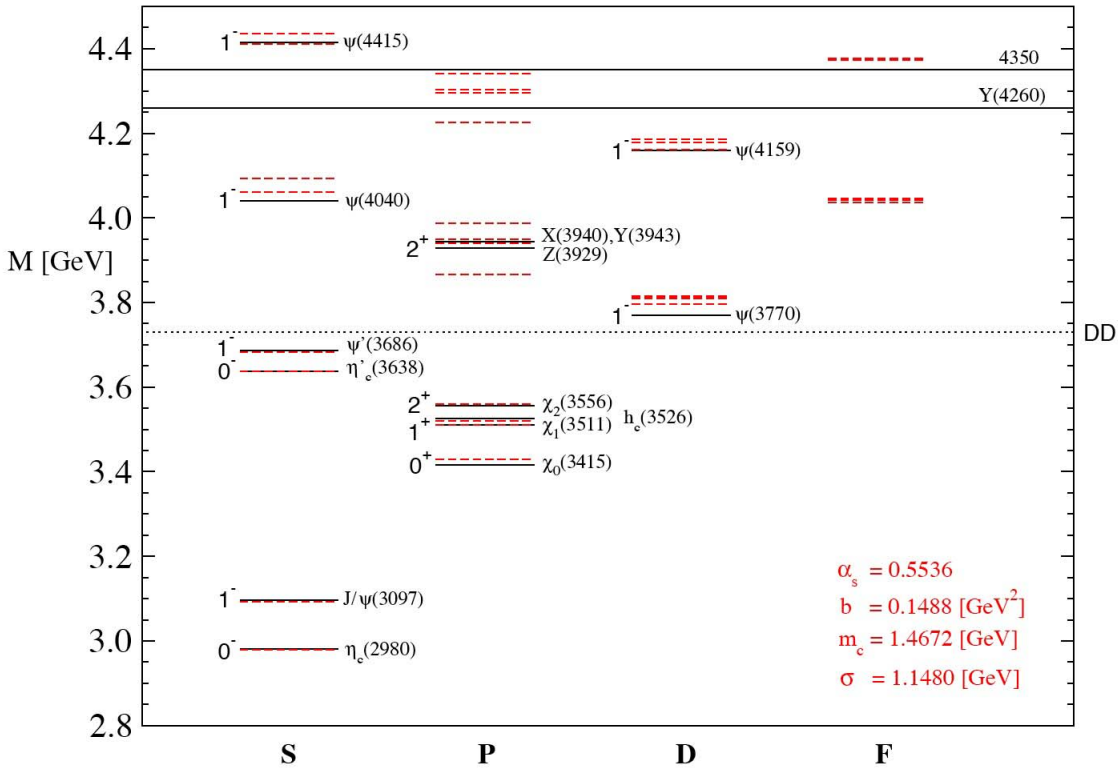

Figure 1.13: *The charmonium spectrum.*

1.6.1 States below $D\bar{D}$ threshold

Below the $D\bar{D}$ threshold almost all states are well established but for some it is necessary to improve the width and the mass measurements. Each state is described in the following:

- $J/\psi(1^3S_1)$ - $\psi'(2^3S_1)$. These two states have $J^{PC} = 1^{--}$. The J/ψ was observed for the first time in 1974 by SLAC in annihilation e^+e^- and by Brookhaven in the process $p + Be \rightarrow e^+e^- + X$ (see Fig. 1.1). This was followed by the discovery by SLAC of the $\psi(2S)$ (see Fig. 1.2). They were observed also in $p\bar{p}$ annihilation at Fermilab by the E760 experiment [26]. The width and the mass of these states are reported in Tab 1.1.

	$J/\psi(1^{--})$	$\psi'(1^{--})$
Mass	(3097 ± 0.011) MeV/c^2	(3686 ± 0.04) MeV/c^2
Width	(92.9 ± 2.8) KeV	(304 ± 9) KeV

Table 1.1: *Mass and width of J/ψ and ψ' [4].*

- $\eta_c(1^1S_0)$. This state has quantum number $J^{PC} = 0^{-+}$. η_c can be formed directly in $p\bar{p}$ annihilation [24] while in e^+e^- annihilation it can be produced only in the radiative decay of the J/ψ, in the two photon production or in the B meson decays [25]. Different measurements of η_c mass and width are available but the errors are too relevant.

- $\eta_c'(2^1S_0)$. This state has quantum numbers $J^{PC} = 0^{-+}$. The mass difference $\Delta' = M_{\eta_c'} - M_{\psi'}$ is related to $\Delta = M_{\eta_c} - M_{J/\psi}$ by the following equation:

$$\Delta' = \frac{\alpha_s(M_{\psi'})}{\alpha_s(M_{J/\psi})} \cdot \frac{M_{\psi'}^2}{M_{J/\psi}^2} \cdot \frac{\Gamma(\psi' \rightarrow e^+e^-)}{\Gamma(J/\psi \rightarrow e^+e^-)} \cdot \Delta \sim 67 \text{ MeV} \tag{1.19}$$

  using the theoretical hyperfine splitting, but the experimental one is smaller.

  This state was discovered in 2002 by the Belle collaboration [23] (Fig. 1.14), it was observed in $B \rightarrow K\eta_c'$ with $\eta_c' \rightarrow K_sK^+\pi^-$. Later it was confirmed by

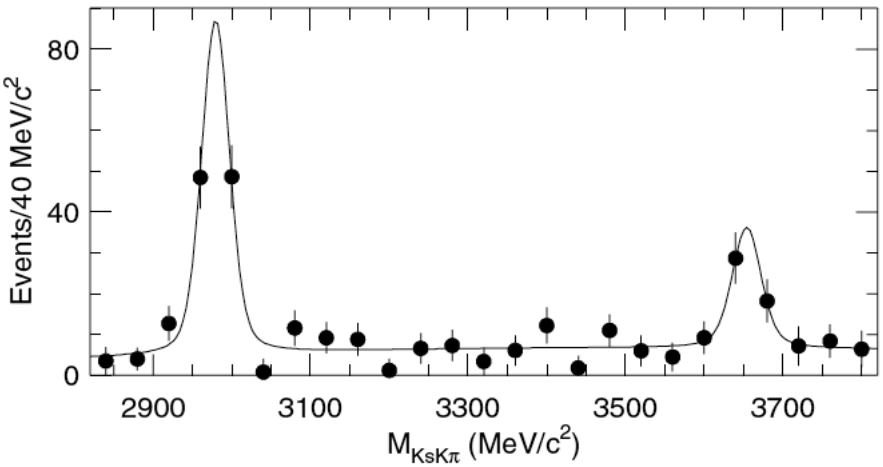

Figure 1.14: *η_c and η_c' confirmed by Belle.*

BABAR and CLEO. The experimental mass value is higher than the theoretical one and the width is given with an error of 50% (Tab. 1.2).

	$\eta_c(0^{-+})$	$\eta_c'(0^{-+})$
Mass	(2980 ± 1.2) MeV/c^2	(3637 ± 4) MeV/c^2
Width	(28.6 ± 2.2) MeV	(14 ± 7) KeV

Table 1.2: *Mass and width of η_c and η_c' [4].*

- $\chi_{c0} - \chi_{c1} - \chi_{c2}(^3P_J)$ These states have quantum numbers $J^{PC} = 0^{++}, 1^{++}, 2^{++}$ respectively. They were observed for the first time in e^+e^- colliders and then in $p\bar{p}$ annihilation (Fig. 1.15) [27, 28]. $\chi_{cJ} \to p\bar{p}$ was observed both in e^+e^- collider and $p\bar{p}$ annihilation. It is not known yet why the decay $\chi_{c0} \to p\bar{p}$ is four times higher than the decay of χ_{c1} and χ_{c2}. The width and the mass of these states are reported in Tab. 1.3.

- $h_c(1^1P_1)$ This state has quantum number $J^{PC} = 1^{+-}$. It was observed for the first time by E760 in the process $p\bar{p} \to h_c \to J/\psi\pi^0$ [29], but E835 doesn't confirm it. It was later confermed by CLEO [30] (Fig. 1.16) and the mass and width value are [4]:

$$M_{h_c} = (3525.42 \pm 0.29)\ \mathrm{MeV/c^2}$$
$$\Gamma_{h_c} < 1\ \mathrm{MeV}$$

State	Mass (MeV/c^2)	Width (MeV)
$\chi_{c0}(0^{++})$	(3414.75 ± 0.31) MeV/c^2	(10.3 ± 0.6) MeV
$\chi_{c1}(1^{++})$	(3510.66 ± 0.07) MeV/c^2	(0.86 ± 0.05) MeV
$\chi_{c2}(2^{++})$	(3556.20 ± 0.09) MeV/c^2	(1.97 ± 0.11) MeV

Table 1.3: *Mass and width of* $\chi_{c0,1,2}$ *[4].*

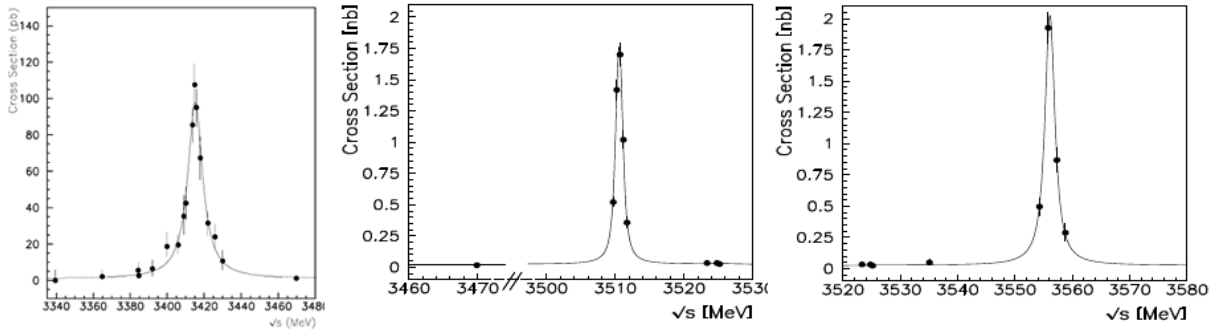

Figure 1.15: χ_{c0}, χ_{c1}, χ_{c2} *observed by the E835 Collaboration.*

1.6.2 States above $D\bar{D}$ threshold

The region above $D\bar{D}$ threshold is rich in interesting new physics but, on the other hand, very little is known about it. Only one state has been positively detected as a charmonium D state, the 1^3D_1 identified with the $\psi(3770)$ resonance and discovered by the Mark I collaboration [31]. It is a wide resonance ($\Gamma_{\psi(3770)} = (27.3 \pm 1.0)$ MeV/c^2 [4]) which decays predominantly to $D\bar{D}$; the D states with J=2 (1^1D_2 and 1^3D_2) are instead predicted to be narrow because parity conservation forbids their decay to $D\bar{D}$. Above the open charm thereshold, in addition to the D states, the radial excitations of the S and P states are predicted to occur, but none of them

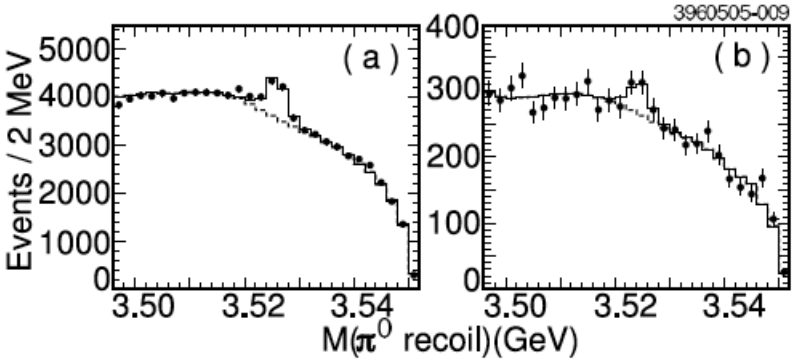

Figure 1.16: *h_c confirmed by CLEO Collaboration. On the left MonteCarlo signal, on the right Data.*

have been positively identified yet. Furthermore, there are serveral new states above the threshold, like the X(3872) observed in B mesons decays, that are very difficult to accomodate in the charmonium spectrum and whose nature is still not known. In the following we will discuss some of these new particles.

1.7 New charmonia

A lot of new states have recently been discovered (X, Y, Z mesons), mainly in the hadronic decays of the B meson: these new states are associated with charmonium because they decay predominantly into charmonium states such as the J/ψ or the ψ', but their interpretation is far from obious. In this section we are going to present some of these new resonances, including the X(3940), whose observation in double charmonium channel $e^+e^- \to c\bar{c}$ is one of the aims of this work.
The X(3872) was the first state that was not easy to fit in the charmonium spectroscopy; it was discovered by Belle [32] in decays $B^+ \to K^+X(3872) \to K^+(J/\psi\pi^+\pi^-)$, as we can see in Fig. 1.17. It is important to note that the mass of this resonance, $m_{X(3872)} = (3871.56 \pm 0.22)$ MeV/c^2 [4], is very close to the $D^0\bar{D}^{0*}$ threshold that is $m_{D^0} + m_{\bar{D}^{0*}} = (3871.8 \pm 0.4)$ MeV/c^2. This state is very narrow and the present 2.3 MeV/c^2 limit [4] on its width is compatible with a possible interpretation as

$^1D_2$ or $^3D_2$ charmonium state. In this case, the non-observation of the expected radiative transitions is a potential problem, but the present experimental limits are still compatible with these hypotheses.

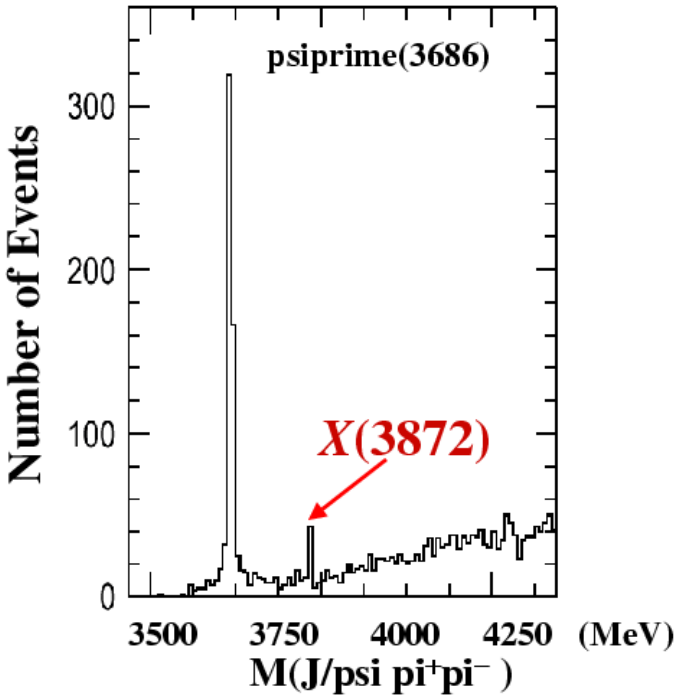

Figure 1.17: *The X(3872) observed by Belle in the channel $J/\psi\pi^+\pi^-$. The first high peak at 3686 MeV is due to the $\psi(2S)$.*

Nevertheless, numerous theoretical explanations of the X(3872) have been proposed. Close and Godfrey proposed the charmonium hybrid ($c\bar{c}g$) interpretation [33], even if present calculations indicate a higher value (around 4100 MeV/c^2) for the ground state; other possibilities include a $D^0\bar{D}^{0*}$ molecule [34] because of the X(3872) closeness to the $D^0\bar{D}^{0*}$ thereshold, a tetraquark and a glueball.
The charmonium like state X(3940) has been observed by Belle (Fig. 1.18) in the double charmonium production around the energy of the $\Upsilon(4S)$ in the process $e^+e^- \rightarrow J/\psi D\bar{D}^*$ in the mass spectrum recoiling against the J/ψ [35], to be

confirmed by this analysis for the *BABAR* collaboration. No peak has been seen by reconstructing the invariant mass $D\bar{D}$.
X(3940) is tentatively identified with $\eta_c(3S)$; its mass by PDG is $m_{X(3940)} = (3942 \pm 9)$ MeV/c^2, and its total width $\Gamma_{X(3940)} = (37^{+27}_{-17})$ MeV/c^2. We report the X(3940) branching ratios in Tab 1.4.

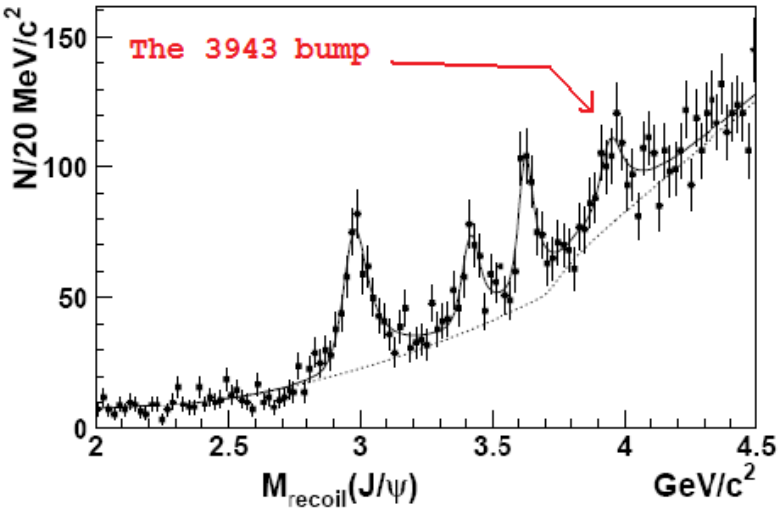

Figure 1.18: *The X(3940) observed by Belle.*

$B(X(3940) \to D\bar{D}^*)$	$> 45\%(90\% C.L.)$
$B(X(3940) \to D\bar{D})$	$> 41\%(90\% C.L.)$
$B(X(3940) \to J/\psi\omega)$	$< 26\%(90\% C.L.)$

Table 1.4: *Branching ratios of the X(3940).*

The last resonance we want to take into consideration is the Y(4260) (Fig. 1.19), discovered by *BABAR* [36] in the ISR reaction $e^+e^- \to \gamma_{ISR}Y(4260) \to \gamma_{ISR}J/\psi\pi^+\pi^-$. This production process tell us that its quantum numbers are $J^{PC} = 1^{--}$, thus the same of the photon. The possible interpretation is an conventional $c\bar{c}$ state, a molecule or an hybrid charmonium.

There are other resonances observed above the open charm threshold, like X(3930) or Y(3940), and for all these new states the interpretation is not clear, with speculations ranging from the numerous missing $c\bar{c}$ states to molecules, tetraquark and hybrids.

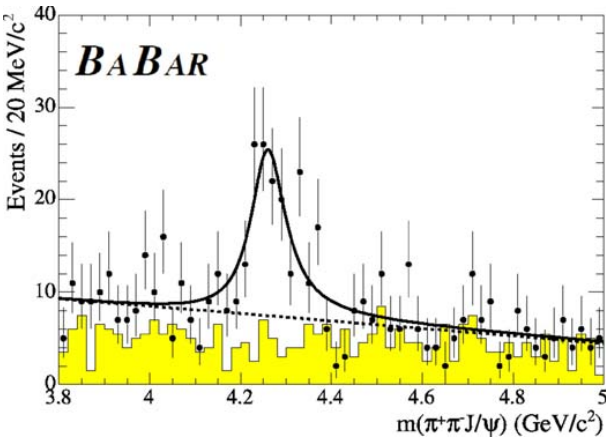

Figure 1.19: *The Y(4260) resonance observed by* BABAR .

Chapter 2

Double charmonium production

2.1 Introduction

The exclusive production of a pair of double heavy mesons with c-quarks in e^+e^- annihilation has attracted considerable attention in the last years. In fact, at the beginning of these studies, the cross section of the process $e^+e^- \to J/\psi\eta_c$, which was measured in the experiments on *BABAR* and Belle detectors at the energy $\sqrt{s} = 10.6$ GeV, turned out to be

$$\sigma(e^+e^- \to J/\psi\eta_c) \times B(\eta_c \to \geq 2charged) = \begin{cases} 25.6 \pm 2.8 \pm 3.4[38] \\ 17.6 \pm 2.8^{+1.5}_{-2.1}[21] \end{cases}$$

and led to discrepancy with the theoretical calculation in the framework of non-relativistic QCD (NRQCD) by an order of magnitude. This conclusion is based on calculations in which the relative momenta of heavy quarks and bound state effects in the production amplitude were not taken into account. A set of calculations was performed to improve the non-relativistic approximation for the process.
In particular, relativistic corrections to the cross section $\sigma(e^+e^- \to J/\psi\eta_c)$ were considered in a *color singlet model* in reference [39] using the methods of NRQCD [16]. A synthesis of this method will be given later.
Another attempt to take into account the relativistic corrections was done in the framework of the *light-cone formalism* [40, 41]. With this formalism the discrepancy

between experiment and theory can be eliminated completely by considering the intrinsic motion of heavy quarks forming the doubly heavy mesons.
In addition, *perturbative corrections* of order α_s to the production amplitude were calculated in reference [42], where Zhang, Gao and Chao could increase the cross section by a factor 1.8.
On account of different values of relativistic corrections obtained in references [39, 40, 41] and the importance of a relativistic consideration of the process $e^+e^- \to J/\psi\eta_c$ in solving the doubly heavy meson production problem, Ebert and Martynenko [43] have performed a new investigation of relativistic and bound state effects. This investigation is based on the relativistic quark model which provides the solution in many tasks of heavy quark physics. In [44, 45] they have demonstrated how the original amplitude, describing the physical process, must be transformed in order to preserve the relativistic plus bound state corrections connected with the one-particle wave functions and the wave function of a two-particle bound state.
In particular, in paper [43] they extend the method to the case of the production of a pair (P+V) of double heavy mesons containing quarks of different flavour b and c. They consider the internal motion of heavy quarks in both produced pseudoscalar P and vector V mesons, and the results of the cross-section will be presented later in this chapter.
In this chapter we will present an overview of the recent results on the analysis $e^+e^- \to \gamma^* \to \psi + X$ and of the possible interpretation of the state X(3940), which is expected to be seen in the double charmonium production process via one virtual photon. Also we will describe the theory concerning the double charmonium production with two virtual photons involved in the process ($e^+e^- \to \gamma^*\gamma^* \to c\bar{c}c\bar{c}$).

2.2 Cross section

If charmonium is the only hadron in the initial or final state, the color-singlet model should be accurate up to corrections that are higher order in v. The simplest examples of such processes are electromagnetic annihilation decays, such as $J/\psi \to e^+e^-$ and $\eta_c \to \gamma\gamma$, and exclusive electromagnetic production processes,

such as $\gamma\gamma \to \eta_c$.

Another process for which the color-singlet model should be accurate is e^+e^- annihilation into exactly two charmonia. There are no hadrons in the initial state, and the absence of additional hadrons in the final state can be guaranteed experimentally by the monoenergetic nature of a 2-body final state. For many charmonia, the NRQCD matrix element can be determined from the electromagnetic annihilation decay rate of either the charmonium state itself or of another state related to it by spin symmetry. Cross section for double-charmonium can therefore be predicted up to corrections suppressed by powers of v^2 without any unknown phenomenological factors.

One problem with e^+e^- annihilation into exclusive double charmonium is that the cross sections are very small at energies large enough to trust the predictions of perturbative QCD. A naive estimate of the cross section for $J/\psi + \eta_c$ in units of the cross section for $\mu^+\mu^-$ is [39]:

$$R[J/\psi + \eta_c] \sim \alpha_s^2 \left(\frac{m_c v}{E_{beam}}\right)^6 \tag{2.1}$$

The 2 powers of α_s are fewest required to produce a $c\bar{c} + c\bar{c}$ final state. There is a factor of $(m_c v)^3$ associated with the wavefunction at the origin for each charmonium. These factors in the numerator are compensated by the factors of the beam energy E_{beam} in the denominator to get a dimensionless ratio.

As an example, consider e^+e^- annihilation with center-of-mass energy $2E_{beam} = 10.6$ GeV. If we set $v^2 \sim 0.3$, $\alpha_s \sim 0.2$ and $m_c \sim 1.4$ GeV we get the naive estimate $R[J/\psi+\eta_c] \sim 4\times10^{-7}$. This should be compared to the total ratio $R[hadrons] \sim 3.6$ for all hadronic final states [46]. The decay of the J/ψ into the easily detectable e^+e^- or $\mu^+\mu^-$ modes suppresses the observable cross section by another order of magnitude.

Fortunately, the era of high-luminosity B factories has made the measurement of such small cross sections feasible. Braaten and Lee [39] calculated the cross sections for exclusive double-charmonium production via e^+e^- annihilation into a virtual photon. This process produces only charmonium states with opposite charge conjugation. The cross sections for charmonium states with the same charge conjugation, which proceed through e^+e^- annihilation into two virtual photons [47, 48] will be

illustrated later.

2.2.1 Color-singlet model calculation

In this section, the cross section for e^+e^- annihilation through a virtual photon into a double-charmonium final state $H_1 + H_2$ are calculated by using the color-singlet model. The color-singlet model (CSM) can be obtained from the NRQCD factorization formula by dropping all of the colour-octet terms and all but one of the colour-singlet terms. The term that is retained is the one in which the quantum numbers of the $Q\bar{Q}$ pair are the same as those of the quarkonium.
Charge conjugation symmetry requires one of the charmonia to be a C = - state and the other ot be a C = + state. The C = - states with narrow widths are the $J^{PC} = 1^{--}$ states J/ψ and $\psi(2S)$, the 1^{+-} state h_c, and the yet-to-be discovered 2^{--} state $\psi_2(1D)$.
The C = + states with narrow widths are the 0^{-+} states η_c and $\eta_c(2S)$, the J^{++} states $\chi_{cJ}(1P)$, J=0, 1, 2 and the yet-to-be-discovered 2^{-+} state $\eta_{c2}(1D)$. The results will be express in terms of the ratio $R[H_1 + H_2]$ defined by:

$$R[H_1 + H_2] = \frac{\sigma[e^+e^- \to H_1 + H_2]}{\sigma[e^+e^- \to \mu^+\mu^-]} \tag{2.2}$$

In the text, only the results for R summed over helicity states will be given. These results may facilitate the use of partial wave analysis to resolve the experimental double-charmonium signal into contributions from the various charmonium states.
When the e^+e^- beam energy E_{beam} is much larger than the charm quark mass m_c, the relative sizes of the various double-charmonium cross sections are governed largely by the number of kinematic suppression factors r^2, where the variable r is defined by:

$$r^2 = \frac{4m_c^2}{E_{beam}^2} \tag{2.3}$$

If we set $m_c = 1.4$ GeV and $E_{beam} = 5.3$ GeV, the value of this small parameter is $r^2 = 0.28$. The asymptotic behaviour of the ratio $R[H1 + H_2]$ as $r \to 0$ can be determined from the helicity selection rules for exclusive processes in perturbative QCD. For each of the $c\bar{c}$ pairs in the final state, there is a suppression factor of r^2

due to the large momentum transfer required for the c and $\bar{c}$ to emerge with small relative momentum. Thus, at any order in α_s, the ratio $R[H_1 + H_2]$ must decrease at least as fast as r^4 as $r \to 0$. However it may decrease more rapidly depending on the helicity states of the two hadrons. There is of course a constraint on the possible helicities from angular momentum conservation: $|\lambda_1 - \lambda_2| = 0$ or 1.
The asymptotic behaviour of the ratio $R[H_1 + H_2]$ depends on the helicities λ_1 and λ_2. The helicity selection rules imply that the slowest aymptotic decrease $R \sim r^4$ can occur only if the sum of the helicities of the hadrons is conserved. Since there are no hadrons in the initial state, hadron helicity conservation requires $\lambda_1 + \lambda_2 = 0$. The only helicity state that satisfies both this constraint and the constraint of angular momentum conservation is $(\lambda_1, \lambda_2)=(0,0)$. For every unit of helicity by which this rule is violated, there is a further suppression factor of r^2.
So, the resulting estimate for the ratio R at leading order in α_s is:

$$R_{QCD}[H_1(\lambda_1) + H_2(\lambda_2)] \sim \alpha_s^2 (v^2)^{3+L_1+L_2} (r^2)^{2+|\lambda_1+\lambda_2|} \tag{2.4}$$

The factor of v^{3+2L} for a charmonium state with orbital angular momentum L comes from the NRQCD factors. At leading order of α_s, there may of course be further suppression factors of r^2 that arise from the simple structure of the leading-order diagrams for $e^+e^- \to c\bar{c} + c\bar{c}$ in Fig. 2.1 but these suppression factors are unlikely to persist to higher orders in α_s.
The QED diagrams for $e^+e^- \to c\bar{c}(^3S_1) + c\bar{c}$ in Fig. 2.2 give contributions to $R[J/\psi + H_2]$ that scale in a different way with r. This case is actually interesting for the analysis documented in this thesis. As $r \to 0$ there is a contribution to the cross section from these diagrams into the cross section for $\gamma + H_2$ and the fragmentation function for $\gamma \to J/\psi$. This fragmentation process produces J/ψ in a $\lambda_{J/\psi} = \pm 1$ helicity state. The hard-scattering part of the process produces only one $c\bar{c}$ pair with small relative momentum, so there is one fewer factor of r^2 relative to equation 2.4. The cross section for $\gamma + H_1$ is still subject to the helicity selection rules of perturbative QCD, so the pure QED contribution to the ratio R has the behaviour:

$$R_{QED}[J/\psi(\pm 1) + H_2(\lambda_2)] \sim \alpha^2 (v^2)^{3+L_2} (r^2)^{1+|\lambda_2|} \tag{2.5}$$

There may also be interference terms between the QCD and QED contributions

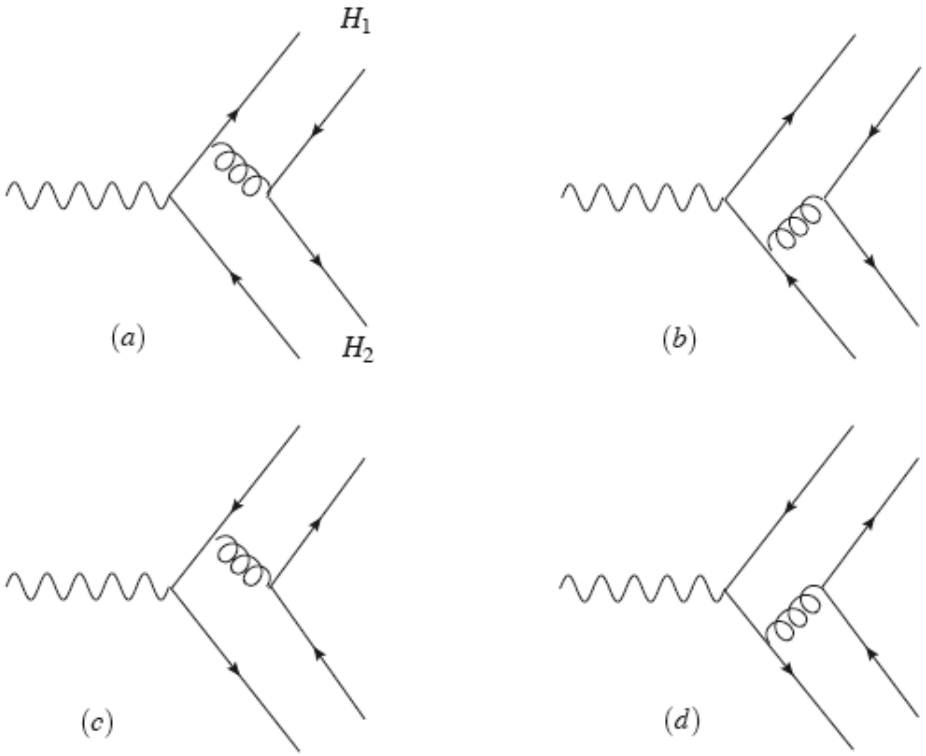

Figure 2.1: *QCD diagrams that can contribute to the color-singlet process* $\gamma^* \to c\bar{c} + c\bar{c}$

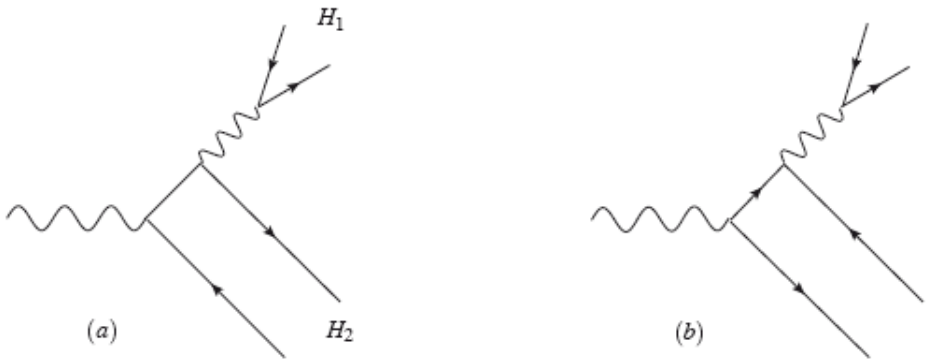

Figure 2.2: *QED diagrams that can contribute to the color-singlet process* $\gamma^* \to c\bar{c}(^3S_1 + c\bar{c})$

whose scaling behaviour is intermediate between equations 2.4 and 2.5.

2.2.2 Calculation of the cross sections

In this section, the cross sections for exclusive double-charmonium production in e^+e^- annihilation at the B factories are presented and partially calculated.
The results in section 2.2.1 were expressed in terms of the ratio R defined in equation 2.2. The corresponding cross sections are:

$$\sigma[H_1 + H_2] = \frac{4\pi\alpha^2}{3s} R[H_1 + H_2] \tag{2.6}$$

The ratios R depend on a number of inputs: the coupling constants α_s and α, the charm quark mass m_c, and the NRQCD matrix elements $\langle O_1 \rangle$.
The value of the QCD coupling constant α_s depends on the choice of the scale μ. In the QCD diagrams of Fig. 2.1, the invariant mass of the gluon is $\sqrt{s/2}$. We therefore choose the scale to be $\mu = 5.3$ GeV. The resulting value of the QCD coupling constant is $\alpha_s(\mu) = 0.21$.
The numerical value for the pole mass m_c of the charm quark is unstable under perturbative corrections, so it must be treated with care. Since the expressions for the electromagnetic annihilation decay rates include the perturbative correction of order α_s the appropriate choice for the charm quark mass m_c in these expressions is the pole mass with corrections of order α_s included. It can be expressed as:

$$m_c = \bar{m}_c(\bar{m}_c) \left(1 + \frac{4}{3}\frac{\alpha_s}{\pi}\right) \tag{2.7}$$

Taking the running mass of the charm quark to be $\bar{m}_c(\bar{m}_c) = 1.2 \pm 0.2$ GeV, the NLO pole mass in $m_c = 1.4 \pm 0.2$ GeV.
The Braaten-Lee predictions for the double charmonium cross sections without relativistic corrections are given in table 2.1[1].

The Braaten-Lee predictions for the double charmonium cross sections for the S-wave states $(\eta_c, \eta_c(2S), J/\psi, \psi(2S))$ including the leading relativistic correction are

[1] Only values interesting for this analysis have been reported. For all calculations see [39]

H_2/H_1	J/ψ	$\psi(2S)$
η_c	3.78 ± 1.26	1.57 ± 0.52
$\eta_c(2S)$	1.57 ± 0.52	0.65 ± 0.22
χ_{c0}	2.40 ± 1.02	1.00 ± 0.42
χ_{c1}	0.38 ± 0.12	0.16 ± 0.05
χ_{c2}	0.69 ± 0.13	0.29 ± 0.06

Table 2.1: *Cross sections in fb for e^+e^- annihilation into double charmonium states $H_1 + H_2$ without relativistic corrections. The errors are only those from variations in the NLO pole mass $m_c = 1.4 \pm 0.2$ GeV.*

obtained by multiplying the values in table 2.1 by the factor:

$$\left(1 + \frac{8Y + 3(Y+4)r^2 - 5r^4}{12(r^2 - Y)}\langle v^2\rangle_{J/\psi} + \frac{2Y + (Y+14)r^2 - 5r^4}{12(r^2 - Y)}\langle v^2\rangle_{\eta_c}\right)^2 \times \left(1 - \frac{1}{6}\langle v^2\rangle_{J/\psi}\right)^{-2} \times \left(1 - \frac{1}{6}\langle v^2\rangle_{J/\psi}\right)^{-2} \times \frac{M_{J/\psi}M_{\eta_c}}{4m_c^2} \times \left(\frac{P_{CM}/E_{beam}}{(1-r^2)^{1/2}}\right)^3 \tag{2.8}$$

where

$$Y = -\frac{\alpha}{\alpha_s}\left(1 + \frac{\alpha}{3\alpha_s}\right)^{-1};\ \langle v^2\rangle_H \sim \frac{M_H^2 - 4m_c^2}{4m_c^2}$$

and m_c is the pole mass of the charm quark. The first factor in 2.8, which appears squared, comes from the expansion of the amplitude in powers of the relative velocity of the $c\bar{c}$ pair. The values of $\langle v^2\rangle_H$ follow from the Gremm-Kapustin relation [49]. The resulting cross sections are given in table 2.2. The error bars are those associated with the uncertainty in the NLO pole mass m_c only.

The correction factors indicate that the relativistic corrections to the cross sections involving 2S states are too large to be calculated reliably using the chosen method. Indeed these factors are $(1.80)^2$, $(1.64)^2$, $(2.16)^2$, respectively for $J/\psi + \eta_c(2S)$, $\psi(2S) + \eta_c$, $\psi(2S) + \eta_c(2S)$.
Note that the method for calculating the relativistic correction significantly increases the sensitivity to the charm quark mass. The errors from varying m_c in table 2.1 are

H_2/H_1	J/ψ	$\psi(2S)$
η_c	$7.4^{+10.9}_{-4.1}$	$6.1^{+9.5}_{-3.4}$
$\eta_c(2S)$	$7.6^{+11.8}_{-4.1}$	$5.3^{+9.1}_{-2.9}$

Table 2.2: *Cross sections in fb for e^+e^- annihilation into S-wave double charmonium states $H_1 + H_2$ including relativistic corrections. The errors are only those from variations in the NLO pole mass $m_c = 1.4 \pm 0.2$ GeV.*

about 50% for the S-wave states, while the errors in table 2.2 correspond to increasing or decreasing the cross section by about a factor of 3. The strong sensitivity to m_c is another indication that this method for calculating the relativistic corrections is unreliable. So we can therefore take the values in table 2.1 to be correct predictions for the cross sections and use table 2.2 as an indication of the possible size of the relativistic corrections.

2.2.3 Cross section for the production of pseudoscalar and vector double heavy mesons

Another approach to calculate the cross section for the double charmonium production from e^+e^- annihilation is that proposed by Ebert and Martynenko in [43]. In their calculations, they take into account the internal motion of heavy quarks in both produced pseudoscalar P and vector V mesons. They obtain the cross sections for the production of a pair of S-wave double heavy mesons with opposite charge parity, in general, containing b and c quarks from e^+e^- annihilation. This work was done for generic pseudoscalar and vector heavy mesons. Then they have taken into account all possible sources of relativistic corrections including the transformation factors for the two quark bound state wave function, and they have investigated the role of relativistic and bound state effects in the total production cross sections using predictions of the relativistic quark model for a number of parameters entering in the obtained analytical expressions.

The total cross section for the exclusive production of P and V doubly heavy mesons

in e^+e^- annihilation is then given by the following expression:

$$\begin{aligned}\sigma(s) &= \frac{32\pi^3\alpha^2 M_0^2|\Psi_0^V|^2|\Psi_0^P|^2}{2187 M_V M_P s^8 k^{10}(1-k)^{10}}\left[k^3 Q_1\alpha_{s2}T_1 + (1-k)^3 Q_2\alpha_{s1}T_2\right]^2 \times \\ &\times\left\{\left[1-\frac{(M_V+M_P)^2}{s^2}\right]\left[1-\frac{(M_V-M_P)^2}{s^2}\right]\right\}^{3/2}\end{aligned} \tag{2.9}$$

In this formula, if m_1 and m_2 are the quark masses, M_0, M_V, M_P are the masses of vector and pseudoscalar mesons consisting of heavy quarks, expressed respectively as:

$$\begin{aligned}M_0 &= m_1 + m_2 \\ M_V &= m_1 + m_2 + W_V \\ M_P &= m_1 + m_2 + W_P\end{aligned}$$

where W_P and W_V are the binding energies between the two quarks, the constants $\alpha_{s1} = \alpha_s(4m_1^2)$, $\alpha_{s2} = \alpha_s(4m_2^2)$, Q_1 and Q_2 are the electric charges of heavy quarks, $\Psi_0^{V,P}$ are the wave function for the relative motion of heavy quarks in the vector and pseudoscalar meson at the origin in the rest frame, T_1 and T_2 are factors depending on quantities determining the numerical values of relativistic effects connected with the internal motion of the heavy quarks in vector and pseudoscalar double heavy mesons [2].

The results of this calculation of the cross section, expressed in 2.9 and presented in Fig. 2.3 in the case of double charmonium , evidently show that only the relativistic analysis of the production processes can give reliable theoretical predictions for the comparison with the experimental data. It follows from Fig. 2.3 that with the growth of the quantum number n the non relativistic approximation doesn't work near the production because the omitted terms in this case have the same order of the magnitude as the basic terms.

[2] For the total espression of T_1 and T_2 see the reference [43]

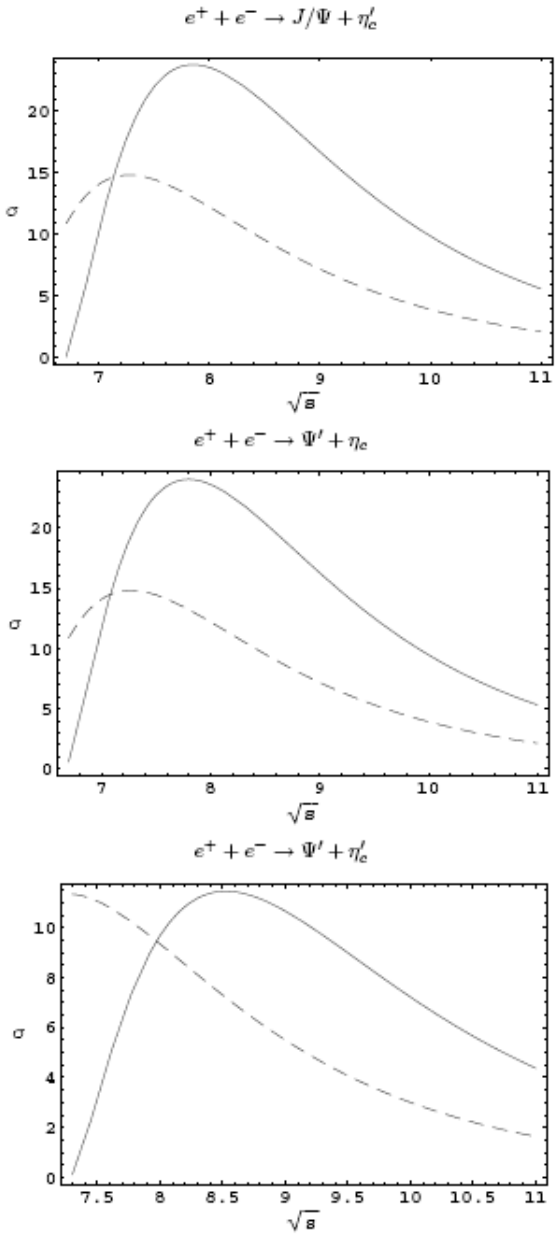

Figure 2.3: *The cross section in fb of e^+e^- annihilation into a pair of S-wave double charm heavy mesons with opposite charge parity as a function of the center-of-mass energy s (solide line). The dashed line shows the nonrelativistic result without bound state and relativistic corrections.*

2.2.4 Light cone formalism

Another systematic approach to the study of hard exclusive processes is light cone formalism (LC). Within this approach the amplitude of hard exclusive processes can be separated into two parts. The first part is *partons production at very small distances*, which can be treated within perturbative QCD. The second part is the hadronization of the *parton at larger distances*. This part contains information about non-perturbative dynamics of the strong interactions. For hard exclusive processes it can be parameterized by process independent distribution amplitudes (DA), which can be considered as 'hadrons' wave functions at light-like separation between the partons in the hadron. It should be noted that within LC one does not assume that the mesons are nonrelativistic. This approach can equally well be applied to the production of light and heavy mesons, if the DAs of the produced meson are known. For this reason, one can hope that within this approach one can study the production of excited charmonia states.

The first attemps to describe the experimental results obtained at Belle and *BABAR* collaborations within LC were done in papers [40, 50]. If the center-mass energy $\sqrt{s}$ is very large, i.e., $\sqrt{s} >> m_c$, one can take c-quark as a light quark. Then one can use light-cone wave-functions to describe non-perturbative effects of charmonia and a factorized form of the production amplitude in terms of these wave-functions and a perturbative part can be obtained. Such an approach for exclusive processes was proposed a long time ago [51].

In comparison with the approach based on NRQCD for the process $e^+e^- \to J/\psi\eta_c$, where the expansion parameter is the velocity, the approach with light-cone wave-function is with the expansion parameters $\lambda/\sqrt{s}$, where λ is a soft scale and can be λ_{QCD}, m_c and masses of charmonia. In references [40, 41] the authors studied processes of double charmonium production from e^+e^- annihilation with this approach. Within the error of the calculation the results of this study are in agreement with Belle and *BABAR* experiments. In addition, in order to answer the question - why LC predictions are much grater than the leading order NRQCD predictions - numerical results of the calculation show that large disagreement between LC and the leading NRQCD predictions can be attributed to large contribution of relativistic

and radiative corrections. From these results one can draw the conclusion that in hard exclusive processes relativistic and radiative corrections play a very important role and the consideration of such processes at the leading NRQCD approximation is unreliable.

The results of that paper are in agreement with recent NRQCD study of the process $e^+e^- \to J/\psi\eta_c$ [53, 54] where the authors took into account relativistic and one loopradiative corrections. However, Braguta in [33] showed also that the results of [53, 54] are overestimated by a factor 1.5.

On the other hand, Ma and Si in [40], have studied the exclusive production of $e^+e^- \to J/\psi\eta_c$, in which they have taken charm quarks as light quarks and used light-cone wave-functions to parametrize non-perturbative effects related to charmonia. In comparison with NRQCD factorization, the factorization of their approach may be achieved in a cleaner way and the perturbative coefficients will not have corrections with large logarithms like $ln(\sqrt{s}/m_c)$ from higher orders, while in the approach of NRQCD factorization, these large logarithms exist and call for resummation. The forms of these light-cone wave-functions are known if the energy scale is close to m_c or is very large. Unfortunately, these wave-functions at the considered energy scale, which is not close to m_c and far from being very large, are unknown. So, with a simple model of light-cone wave-functions, their are able to predict the cross-section which is at the same order of that measured by Belle. But this model may not represent completely the physics of charmonia.

2.3 Discrepancy between theory and experiment

As already mentioned above, the experimental results for the production of $J/\psi + \eta_c$ mesons measured at the Belle and *BABAR* experiments differ from theoretical calculations in the framework of NRQCD.

The experimental data on the production cross sections of a pair of S-wave charm mesons are presented in table 2.3. The numerical value for the cross section of $J/\psi + \eta_c$ production at $\sqrt{s} = 10.6$ GeV, obtained on the basis of equation 2.9 amounts to the value 7.8 fb without the inclusion of QED effects. In this case rel-

ativistic and bound state corrections increase our non-relativistic result by a factor 2.2 (see dashed lines in Fig. 2.3).
Accounting slightly different values of several parameters used in the Ebert-Martynenko model in the comparison with the Braaten-Lee model, that is the mass of c quark, the binding energy $W_{P,V}$, one can find a good agreement between the two results for the production of the charmonium states, if relativistic corrections are taken into account (see the sixth column of table 2.3).
Keeping in mind also the calculation of Zhang-Gao-Chao, which includes additional perturbative corrections of order α_s, one can observe the convergence between the experimental data and theoretical results obtained on the basis of approaches combining nonrelativistic QCD and the relativistic quark model [3].

State H_2/H_1	$\sigma_{BABAR} \times B(\eta_c \to \geq 2ch)$ (fb) [21]	$\sigma_{Belle} \times B(\eta_c \to \geq 2ch)$ (fb) [38]	σ_{LC} (fb) [50]	σ_{BL} Non Rel (fb) [39]	σ_{BL} Rel (fb) [39]	σ_{EM} (fb) [43]
$\Psi(1S)\eta_c$	$17.6 \pm 2.8^{+1.5}_{-2.1}$	$25.6 \pm 2.8 \pm 3.4$	26.7	3.78	7.4	7.8
$\Psi(1S)\eta_c(2S)$	$16.4 \pm 3.7^{+2.4}_{-3.0}$	$16.5 \pm 3.0 \pm 2.4$	26.6	1.57	7.6	7.0

Table 2.3: *Comparison of theoretical predictions (light-cone predictions [50], Braaten-Lee calculations with and without relativistic corrections [39] and Ebert-Martynenko predictions [43]) with experimental data (BABAR [21] and Belle [38]).*

2.4 Previous results on $e^+e^- \to \psi + X$

For the analysis $e^+e^- \to J/\psi + X$ the two main experimental results come from the *BABAR* [21] and Belle [38] experiments. In Fig. 2.4 are shown the mass distribution of the system recoiling against a reconstructed J/ψ in e^+e^- annihilation: *BABAR* made the analysis in the range 2.0 to 3.8 GeV/c^2, while Belle's authors saw the distribution up to 4.5 GeV/c^2. In Tab. 2.4 we report the cross section measured for $e^+e^- \to J/\psi c\bar{c}$ by Belle and *BABAR* .

[3] This model is not documented here. For any detail see [42]

$c\bar{c}$	$\sigma_{Belle} \times B_{>2}[fb]$	$\sigma_{BABAR} \times B_{>2}[fb]$
η_c	$25.6 \pm 2.8 \pm 3.4$	$17.6 \pm 2.8^{+1.5}_{-2.1}$
χ_{c0}	$6.4 \pm 1.7 \pm 1.0$	$10.3 \pm 2.5^{+1.4}_{-1.8}$
$\eta_c(2S)$	$16.5 \pm 3.0 \pm 2.4$	$16.4 \pm 3.7^{+2.4}_{-3.0}$

Table 2.4: *Cross section for $e^+e^- \to J/\psi(c\bar{c})$ measured by Belle [38] and BABAR [21].*

It is possible to note that Belle's analysys reported also an evidence of a state around 3.943 GeV/c^2, named X(3940), candidate to be the $\eta_c(3S)$. The cross section measured by Belle [35] for $e^+e^- \to J/\psi + X$ is:

$$\sigma_{Born} \times B_{>2} = (10.6 \pm 2.5 \pm 2.4) \text{ fb}$$

In the next section we will present a discussion about the interpretation of this state.

While for the analysis $e^+e^- \to \psi(2S)$ with $\psi(2S) \to \ell^+\ell^-$ there are no experimental reference available, for $e^+e^- \to \psi(2S)$ with $\psi(2S) \to J/\psi\pi^+\pi^-$ we have the results published by Belle [38] (see Fig. 2.5). This analysis was done in the range 2.2 to 3.8 GeV/c^2. In Tab. 2.5 we report the cross section measured by Belle.

$c\bar{c}$	$\sigma_{Born} \times B_{>0}[fb]$
η_c	$16.3 \pm 4.6 \pm 3.9$
χ_{c0}	$12.5 \pm 3.8 \pm 3.1$
$\eta_c(2S)$	$16.0 \pm 5.1 \pm 3.8$

Table 2.5: *Cross section for $e^+e^- \to \psi(2S)(c\bar{c})$ measured by Belle [38].*

2.4.1 The X(3940) interpretation

The state X(3940) has been seen only by Belle experiment recoiling against J/ψ. One of the aims of the analysis described in this thesis is also to confirm this state with *BABAR* data. The state has a Breit-Wigner mass of $(3943 \pm 6 \pm 6)$ MeV/c^2 and a width of less than 52 MeV at 90% C.L [35]. The X is seen to decay to $D\bar{D}^*$ and

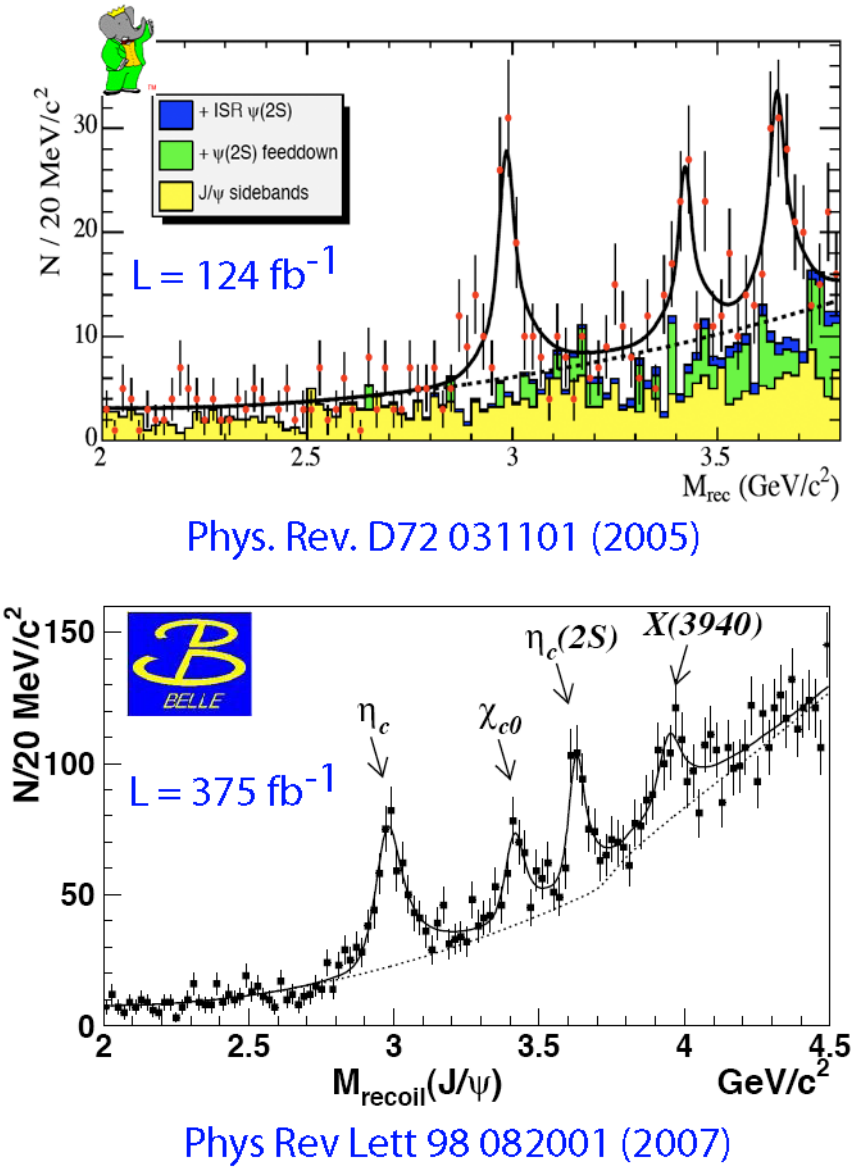

Figure 2.4: *The distributions of the mass recoiling against the reconstructed J/ψ in inclusive $e^+e^- \to J/\psi X$ for BABAR on the top and Belle on the bottom.*

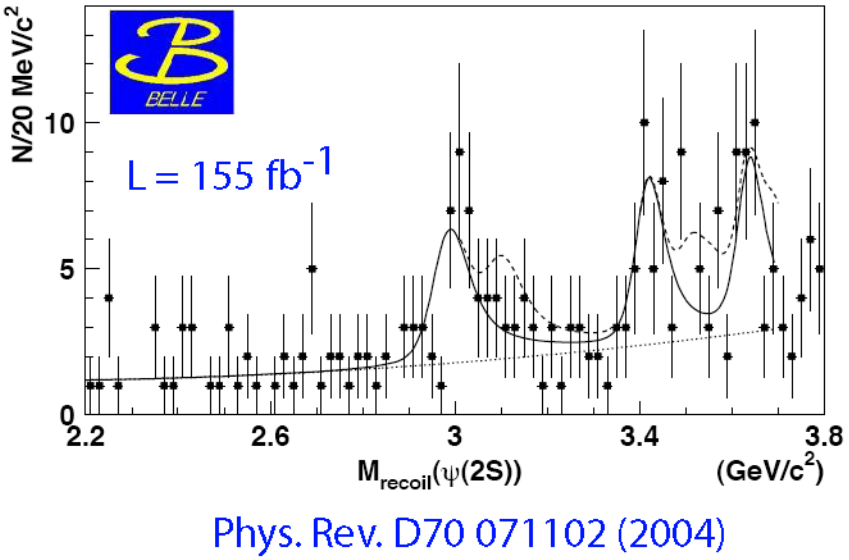

Figure 2.5: *The distributions of the mass recoiling against the reconstructed* $\psi(2S)$ *in inclusive* $e^+e^- \to \psi(2S)X$ *for Belle. The* $\psi(2S)$ *is reconstructed into* $J/\psi\pi^+\pi^-$.

not to $\omega J/\psi$ or $D\bar{D}$.

It is natural to attempt a $2P$ $(c\bar{c})$ assignment for this state since the expected mass of the 2^3P_J multiplet is 3840-3980 MeV/c^2 and the expected widths are 20-130 MeV [63]; then if the $D\bar{D}^*$ mode is dominant it suggestes that the X(3940) is the $\chi_{c1}(2P)$. There are however two problems with this assignment: the first is that there is no evidence for the 1^3P_1 $(c\bar{c})$ state in the data, and the second is that the predicted width of the 2^3P_1 $(c\bar{c})$ is 140 MeV (assuming $M_{2^3P_1(c\bar{c})}$=3943 MeV)) [64] and there is another candidate for the 1^3P_1 $(c\bar{c})$ state, the Y(3940).

The most likely interpretation of X(3940) is 3^1S_0 $(c\bar{c})$ $\eta_c(3S)$ state [65]. Tests of this assignment are to study the angular distribution of the $D\bar{D}^*$ final state and to observe it in $\gamma\gamma \to D\bar{D}^*$.

2.5 Double $c\bar{c}$ production via $\gamma^*\gamma^*$

The predictions and calculations until now were performed for final double charmoniums states with even charge-conjugation parity (C-parity), where the e^+e^- pair decays in the final state via one virtual photon ($J^{PC} = 1^{--}$).
But one can calculate the cross sections for e^+e^- annihilation into two charmonium states that have the same C-parity, such as $J/\psi + J/\psi$. These processes proceed, at leading order in the QCD coupling α_s, through QED diagrams that contain two virtual photons (see Fig. 2.6).

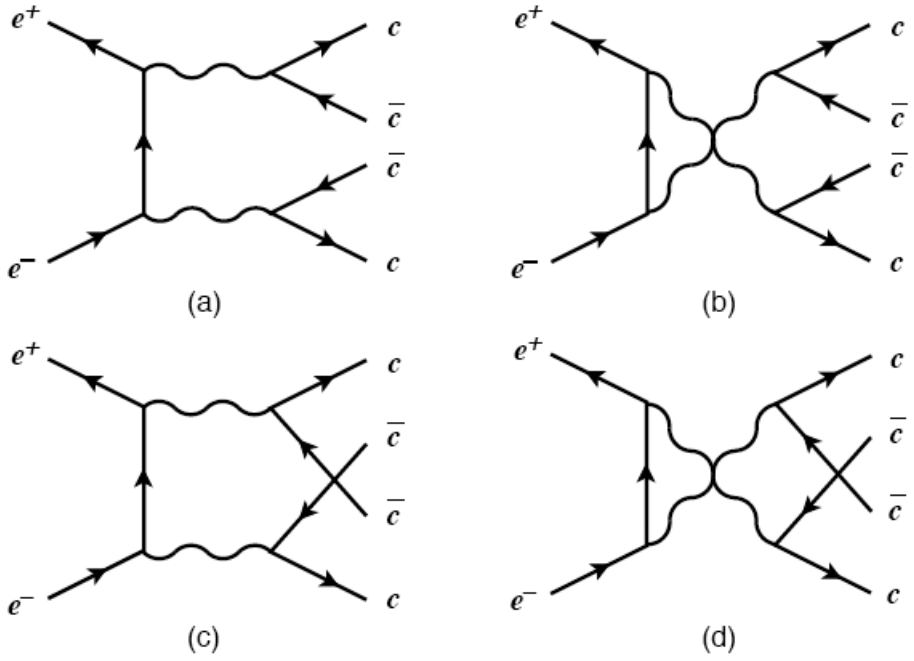

Figure 2.6: *QED diagrams for the process* $e^+e^- \to \gamma^*\gamma^* \to c\bar{c}c\bar{c}$.

One might expect these cross sections to be much smaller than those for charmonia with opposite C-parity because they are suppressed by a factor of α^2/α_s^2. However, if both charmonia have quantum numbers $J^{PC} = 1^{--}$, then there is a contribution to the cross section in which each photon fragments into a charmonium [47]. The fragmentation contribution is enhanced by powers of E_{beam}/m_c, where E_{beam} is the beam energy and m_c is the charm-quark mass [47]. This enhancement

can compensate for the suppression factor that is associated with the coupling constants. In particular, the predicted cross section for $J/\psi + J/\psi$ at the B factories is larger than that for $J/\psi + \eta_c$.

Bodwin, Braaten and Lee in [48] have calculated the cross sections for e^+e^- annihilation through two virtual photons into exclusive double charmonium states. The cross sections turn out to be particularly large if the two charmonia are both 1^{--} states. In the absence of radiative and relativistic corrections, the predicted cross section for the production of $J/\psi + J/\psi$ at the B factories is larger than that for $J/\psi + \eta_c$ by a factor of about 3.7. The perturbative and relativistic corrections for these two processes may be rather different and could significantly change the prediction for the ratio of the cross sections. Nevertheless the inclusion of contributions from processes involving two virtual photons in the theoretical prediction for the cross section for $J/\psi + \eta_c$ production is likely to decrease the large discrepancy between that prediction and the Belle measurement.

However, as was pointed out in [47, 48], the two-photon process contains photons-fragmentation contributions that are enhanced by factors $(E_{beam}/2m_c)^4$ from photon propagators and $log[8(E_{beam}/2m_c)^4]$ from a would-be collinear divergence. As a result, the predicted cross-section $\sigma(e^+e^- \to J/\psi J/\psi) = 8.70 \pm 2.94$ fb is larger than the predicted cross section $\sigma(e^+e^- \to J/\psi\eta_c) = 2.31 \pm 1.09$ fb. Corrections of higher order in α_s and v are likely to reduce the prediction for the $J/\psi J/\psi$ cross section by about a factor of three. Anyway, as visible in Fig. 2.4, no significant $J/\psi J/\psi$ signal was observed in the invariant mass distribution.

Chapter 3

The *BABAR* experiment

The B factory, PEP-II, located at the Stanford Linear Accelerator Center in Menlo Park, CA, and the *BABAR* detector, along with their perfomance for the years relevant for this thesis, will be described in this chapter.
The primary goal of the *BABAR* experiment is the systematic study of CP asymmetries in the decays of neutral B mesons. In addition to this, a sensitive measurement of the CKM matrix elements can be made, and a number of rare B meson decays may be measured, together enabling good contraints to be put on fundamental parameters of the Standard Model. A range of other physics may also be studied at *BABAR* , including other B physics, the physics of charm and tau leptons, and two-photon physics.
The cross section of $e^+e^- \rightarrow c\bar{c}$ events is of the same order of magnitude as the one of $e^+e^- \rightarrow b\bar{b}$ events. Therefore, high statistics charmed mesons and baryons are expected. In order to produce the hundreds of millions of B mesons necessary to study CP-sensitive rare decays, the B mesons must be produced at high luminosity in a relatively clean environment. To this end, the SLAC B factory studies electron-positron collisions at a center-of-mass (CM) energy of 10.50 GeV. This energy corresponds to the mass of the $\Upsilon(4S)$ resonance, which is a spin-1 bound state of a b quark and a $\bar{b}$ antiquark (a member of the "bottomonium" family of mesons). The $\Upsilon(4S)$ mass is just above the $B\bar{B}$ production threshold, and this resonance decays almost exclusively through the strong interaction to approximately equal

nunbers of $B^0\bar{B}^0$ and B^+B^- pairs, for which the two branching fractions are measured to be equal to high precision [56].
The *BABAR* experiment was designed and optimized to achieve the goals specified above. The PEP-II B factory was designed to deliver the B mesons to the experiment.
Tab 3.1 summarizes the cross sections for the various processes accesible by colliding two e^+e^- beams at the energy corresponding to the mass of $\Upsilon(4S)$ in the center of mass reference frame [57].

$e^+e^- \rightarrow$	Cross-section (nb)
$b\bar{b}$	1.10
$c\bar{c}$	1.30
$s\bar{s}$	0.35
$u\bar{u}$	1.39
$d\bar{d}$	0.35
$\tau^+\tau^-$	0.94
$\mu^+\mu^-$	1.16
e^+e^-	~ 40

Table 3.1: *Production cross-sections at* $\sqrt{s}$*=10.58 GeV.*

3.1 The Stanford Linear Accelerator Center (SLAC)

The Stanford Linear Accelerator Center (SLAC, Fig. 3.1) located in Menlo Park, CA, on the Stanford Campus, started in 1962; by 1966 its construction was completed and research commenced, achieving the design energy of 20 GeV the following year.

Many important discoveries in particles physics were made with this powerful LINAC. In 1968 there was the discovery of the point structure within a proton, with which came the realization that quarks, up until then a purely theoretical concept, were actually real.

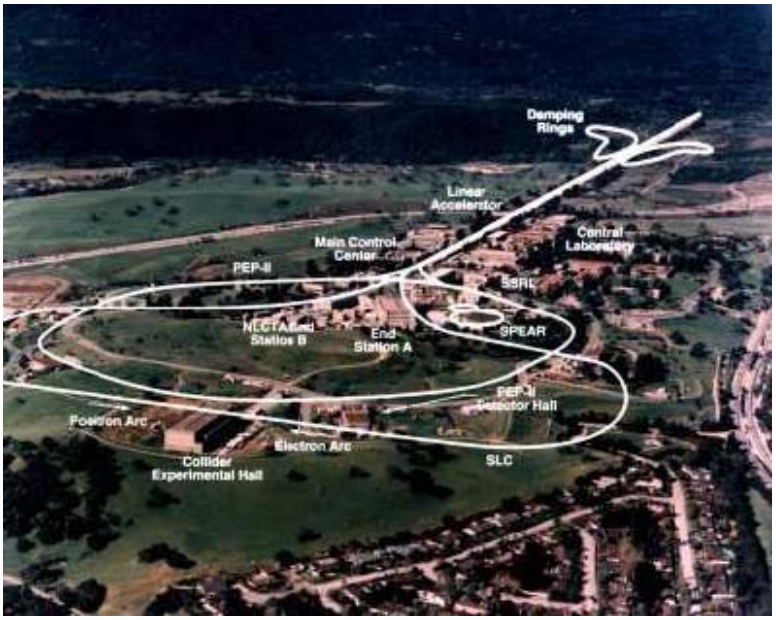

Figure 3.1: *An aerial view of SLAC.*

Next came SPEAR, the electron storage ring, it was completed in 1972. SPEAR is the acronym for Stanford-Positron-Electron-Asymmetric-Ring, but the asymmetry was too expensive and the ring had to be build in a symmetric configuration. In 1974 this ring was the site of the "November revolution" in which the ψ particle was discovered. On SPEAR, in 1976, the new τ meson was discovered.

In the 70s another electron storage ring, called PEP, was constructed in collaboration with the Lawrence Berkeley Laboratory and completed in 1980. PEP stands for Proton-Electron-Positron, even if the ring was only funded for electrons and positrons. In 1994, again with Berkeley as participant, was initiated the construction of an asymmetric electron-positron storage ring, using much of PEP and called PEP-II, which will be described here. The asymmetry allows study of the B meson, that has a particularly large amount of CP symmetry non-invariance, which is today an especially important subject of study in high-energy physics. Experimental study using PEP-II started in 1999 and stopped in 2008. A similar B factory has also been built in Japan.

In the 80s, SLAC built two arcs at the end of the two-mile accelerator and was able

to study the interaction between the two beams. This device, the Stanford Linear Collider (SLC), was the first linear collider. It came into operation in 1989 with 50 GeV electrons on 50 GeV positrons (a significantly higher energy than the original 20 GeV of the SLAC accelerator), but was almost immediately in competition with the much more intense LEP ring at CERN.
All the developments described above are in high energy physics, the primary purpose of SLAC. At the same time the use of SPEAR as a synchrotron radiation source of x-rays was being developed. Most recently, in 2002, SLAC has initiated work on a linear accelerator free-electron laser, called the Linac Coherent Light Source (LCLS). This device promises coherent x-rays at 0.15 mm and with a very short pulse [58].

3.2 The PEP-II asymmetric collider

The PEP-II B factory [59] is part of the accelerator complex at SLAC, shown in Fig. 3.2.

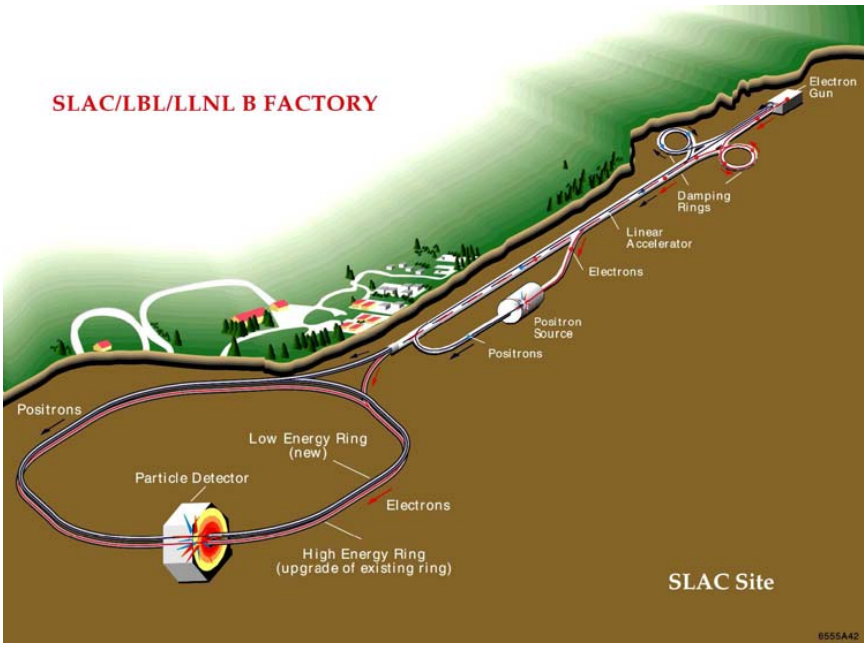

Figure 3.2: *A schematic description of the B factory accelerator complex at SLAC.*

The electron beam is produced by the electron gun near the beginning of the two-mile long linear accelerator (the "LINAC"). The gun consists of a thermally heated cathode filament held under high voltage. Large numbers of electrons are "boiled off" the cathode, accelerated by the electric field, collected into bunches, and ejected out of the gun into the LINAC. The electron bunches are accelerated in the LINAC with synchronized radio-frequency (RF) electromagnetic pulses generated in RF cavities through which the beam passes by a series of 50 Megawatt klystron tubes [1]. The steering, bending, and focusing of the beam is carried out with magnets throughout the acceleration cycle.

After acceleration to an energy of approximately 1 GeV, the electron beam is directed to a damping ring, where the beam is stored for some time. As it circulates in the ring, it loses energy through synchrotron radiation and is continuously re-accelerated by RF cavities. The radiation and careful re-acceleration has the effect of reducing the emittance, or spatial and momentum spread of the beam, a necessary step in high-luminosity collisions. The "dumped" beam is then re-directed to the LINAC and accelerated to 8.9 GeV. Half of the generated electron bunches are used for the generation of the positron beam. They are accelerated to approximately 30 GeV, extracted from the LINAC, and directed onto a tungsten target, producing electromagnetic showers that contain a large number of electron-positron pairs. The positrons are separated electromagnetically from the electrons, collected into bunches, accelerated, and sent through the return line to the source end of the LINAC. The positron beam is then accelerated and shaped like the electron beam through the LINAC and its own damping ring, culminating in an energy of 3.1 GeV. After reaching their respective collision energies, the electron and positron beams are extracted from the LINAC and directed to the PEP-II storage rings, the High Energy Ring (HER) for electrons and the Low Energy Ring (LER) for the positrons, both housed in the same tunnel of 2.2 Km circumference. As they circulate, they are focused further by a complex of magnets and accelerated by RF cavities to compensate the synchrotron-radiation losses. In the interaction region IR-2 (one of twelve such regions), where the *BABAR* detector is located, they are brought to a collision

[1] Klystrons generates the pulses with their lower energy electron beams passing through resonant cavities

after a final-focus system squeeze the beams to the smallest possible emittance. During data taking, each ring contains about 1600 circulating bunches colliding every 5 ns.

The collisions are then analyzed by the *BABAR* detector. About 10% of the time the beams are collided at an energy 40 MeV below the $\Upsilon(4S)$ resonance for calibration of the backgrounds, as no B mesons are produced then since this energy is below $B\bar{B}$ threshold. As data is collected, the collisions and other losses reduce the currents in the rings, necessitating re-injection of electron and positron bunches. Initially in the life of the B factory from 1999-2002, data was taken for about an hour or two while the currents diminished, and the additional current was injected into the rings for a few minutes. Data could not be taken during the injection due to the large backgrounds in the detector and the resulting danger to instrumentation. Notice that the detector would have to be put into a "safe" but non-operational state during injection, with, for instance, all high-voltage components ramped down to a lower, safer potential. Starting in 2003 a new scheme for injection, called *trickle* injection [60], was developed, where new bunches are continuously injected at a rate large enough to replenish beam losses but low enough to not damage the detector. This has allowed more efficient operation of the B-factory with 30% more integrated luminosity for a given highest instantaneous luminosity.

3.2.1 Luminosity

The luminosity L of the machine depends on the careful tuning of several parameters. This dependence is expressed as:

$$L = \frac{nfN_1N_2}{A} \tag{3.1}$$

where n is the number of bunches in a ring, f is the bunch crossing frequency, N_1 and N_2 are the number of particles in each bunch, and A is their overlap section.

The PEP-II collider was designed for an instantaneous luminosity of 3×10^{33} cm^{-2} s^{-1}, but has reached values of 1.2×10^{34} cm^{-2} s^{-1} due to improvements in the RF cavities, beam-shaping cavities and magnet systems. The increased luminosity

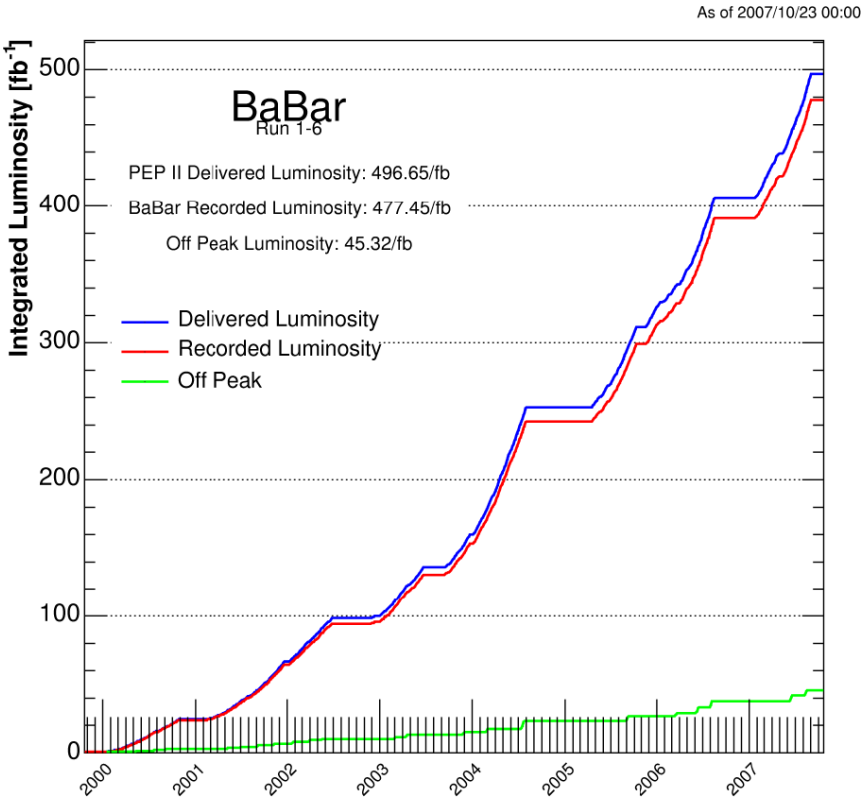

Figure 3.3: *Total integrated luminosity delivered by PEP-II and recorded by the* BABAR *detector.*

comes from large beam currents (up to 3A in the LER and 2A in the HER) and a reduced emittance. With these specifications and trickle injection, the machine generated hundreds of pb^{-1} of integrated luminosity daily during normal operations, and has integrated hundreds of fb^{-1} throughout its operation lifetime. Fig. 3.3 shows the integrated luminosity provided by PEP-II collider in the period October 1999-April 2008, along with the integrated luminosity recorder by the *BABAR* detector, that is 432.89 fb^{-1} collected at $\Upsilon(4S)$ resonance, plus 53.85 fb^{-1} off-peak. This analysis uses both $\Upsilon(4S)$ data sample and the off-resonance data sample. In addition, in 2008 *BABAR* undertook a data taking at different excited state energy, nominally 30.23 fb^{-1} at the $\Upsilon(3S)$ resonance and 14.45 fb^{-1} at the $\Upsilon(2S)$ resonance and an energy scan between $\Upsilon(4S)$ and the $\Upsilon(6S)$ mass, but these datasets are not considered in the present analysis.

3.2.2 Machine Background

Beam-generated background causes high single-counting rates, data acquisition dead times, high currents and radiation damage of both detector components and electronics. This resulted in lower data quality and may have limited the lifetime of the apparatus. For this reason the background generated by PEP-II was studied in detail and the interaction region was carefully designed. Furthermore, background rates were continuously monitored during data acquisition to prevent critical operation conditions for the detector.
The primary sources of machine-generated background are:

- **synchrotron radiation** in the proximity of the interaction region. A strong source of background (many kW of power) is due to beam deflections in the interaction region. This components is limited by channeling the radiation out of *BABAR* acceptance with a proper design of the interaction region and the beam orbits, and placing absorbing masks before the detector components.
- **interaction between beam particles and residual gas** in either ring. This can have two different origins: beam as bremsstrahlung and Coulomb scattering. Both types of interaction cause an escape of beam particles from their

orbit. This background represents the primary source of radiation damage of the inner vertex detector and the principal background for the other detector components.

- **electromagnetic showers generated by beam-beam collisions.** These showers are due to energy degraded e^+e^- produced by radiative BhaBha scattering and hitting the beam pipe within a few meters of the IP. This background is proportional to the luminosity of the machine and whereas it is under control it is expected to increase in case of higher operation values of luminosity.

3.3 Detector overview

In accordance with B-factory-enrivonment and program, the detector (Fig. 3.4, 3.5) must satisfy the following requirements:

- Excellent vertex reconstruction in the tracker, in both the parallel and transverse directions to the beam boost;
- Large acceptance, including at small polar angles relative to the boost direction in the lab frame;
- Excellent reconstruction efficiency and good momentum resolution for charged particles and photons from below 100 MeV to 5 GeV;
- Good charged-particle identification to separate lepton, pions and kaon candidates;
- Radiation hardness, particularly for the inner tracking sub-detectors

The detector coordinate system is defined with $+z$ in the boost (high-energy beam) direction and $+y$ in the vertical direction. The high-energy beam travels clockwise around PEP-II, so the $+x$ direction is away from the ring center. The

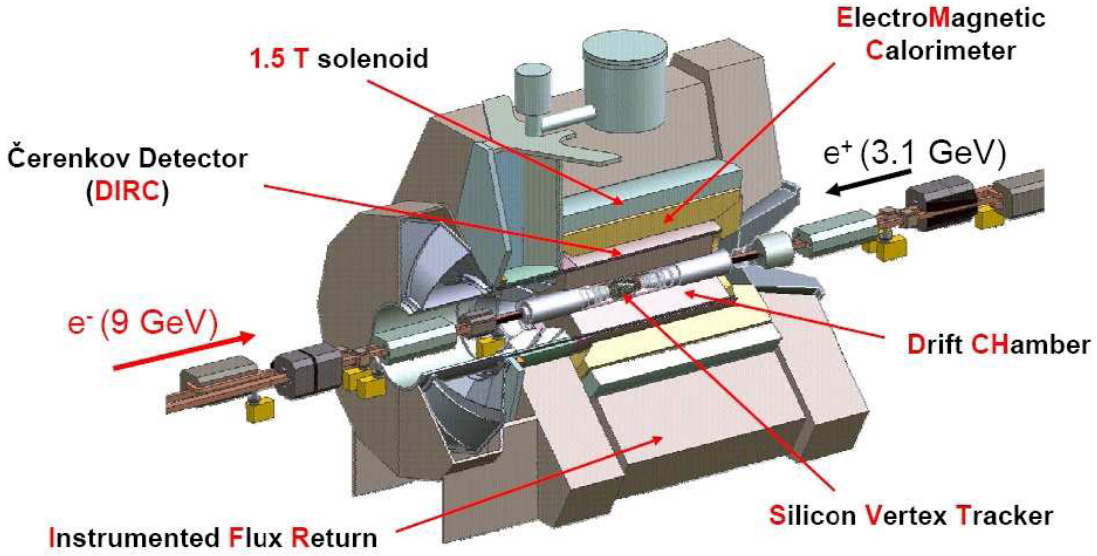

Figure 3.4: *Three-dimensional section of the BABAR detector where we can observe its different components.*

coordinate system origin is the nominal collision point, which is offset in the -z direction from the geometrical center of the detector magnet. Although the beams collide with each other head-on, they are separated while still inside the detector magnet field. The detector is rotated 20 mr relative to the beam direction (around the y axis) to minimize the resulting orbit distortions. The z direction thus corresponds to the magnetic field direction, and deviates slightly from the boost direction. The main subsystems are:

- The *Silicon Vertex Tracker (SVT)*, which provides precise position information on charged tracks, and also is the only tracking device for very low-energy charged particles;

- the *Drift Chamber (DCH)*, surrounding the vertex detector, filled with a helium-based gas, in order to try to minimize multiple scattering. In addition, it provides the main momentum measurement for charged particles and helps in particle identification through energy loss measurements;

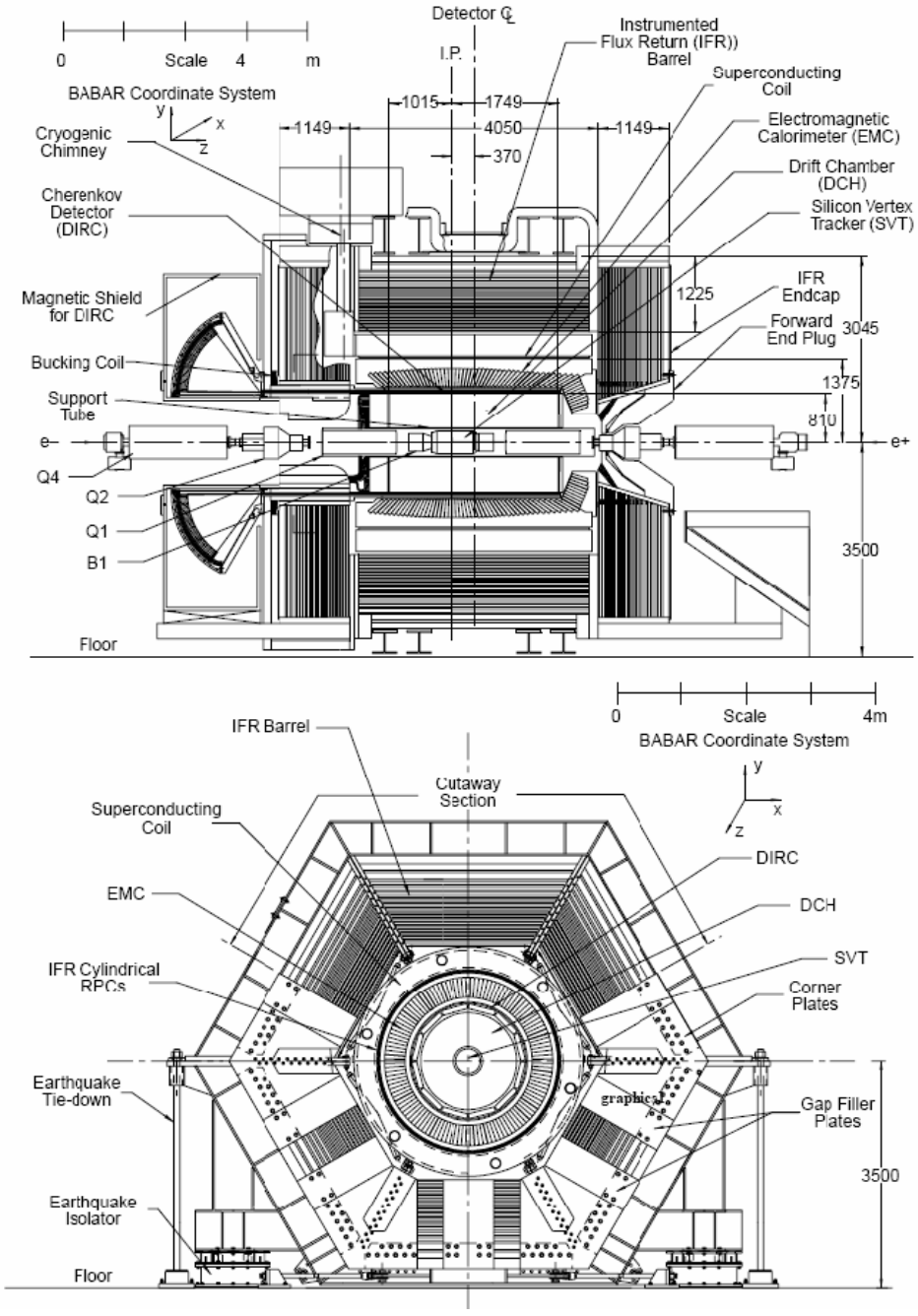

Figure 3.5: *Longitudinal (top) and front (bottom) view of the BABAR detector. All dimensions are given in millimeters.*

- the *Detector of Internally Reflected Cherenkov light (DIRC)*, which is designed and optimized for charge hadron particle identification;
- the *Electromagnetic Calorimeter (EMC)*, composed by Cesium Iodide crystals: it is designed to detect electromagnetic showers from photons and electrons with excellent energy and angular resolution. The calorimeter provides good electron identification down to about 0.5 GeV, and information for neutral hadron identification;
- a *superconducting solenoid*, surrounding the detector and producing a 1.5 T axial magnetic field;
- the *Instrumented Flux Return (IFR)* which provides muon and neutral hadron identification.

The next few sections will describe the individual detector components.

3.4 Tracking System

3.4.1 Silicon Vertex Detector

The SVT (Fig. 3.6) consists of five layers of double-sided silicon sensors segmented in both the x and ϕ directions (see Fig. 3.7), designed to measure accurately the positions and decay vertices of B mesons and other particle.

This measurement is most accurate at small distances from the interaction, as the trajectory of the particles farther away is affected by multiple scattering within the detector. Thus, the first three layers are located as close to the beam pipe as possible. The outer two layers are closer to the drift chamber to facilitate matching SVT tracks with DCH tracks. They also provide pattern recognition in track reconstruction, and the only tracking information for charged particles with transverse momenta below 120 MeV/c, as these may not reach the drift chamber. The SVT covers 90% of the solid angle in the CM frame, as visible in Fig. 3.8.

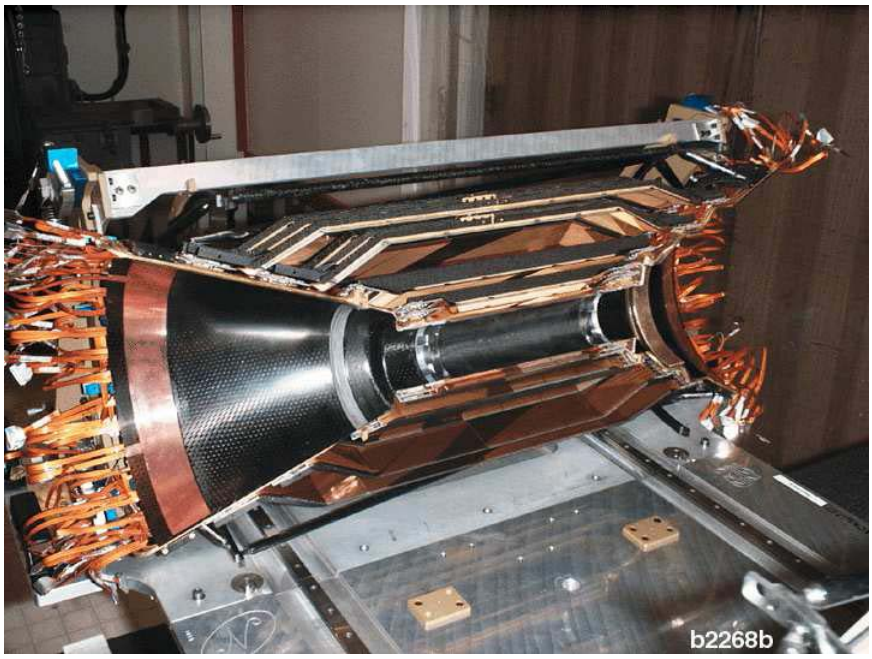

Figure 3.6: *Half cross section of the BABAR SVT.*

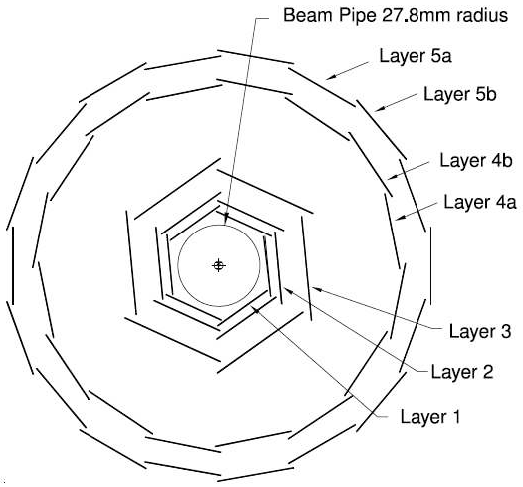

Figure 3.7: *Transverse cross section of the SVT.*

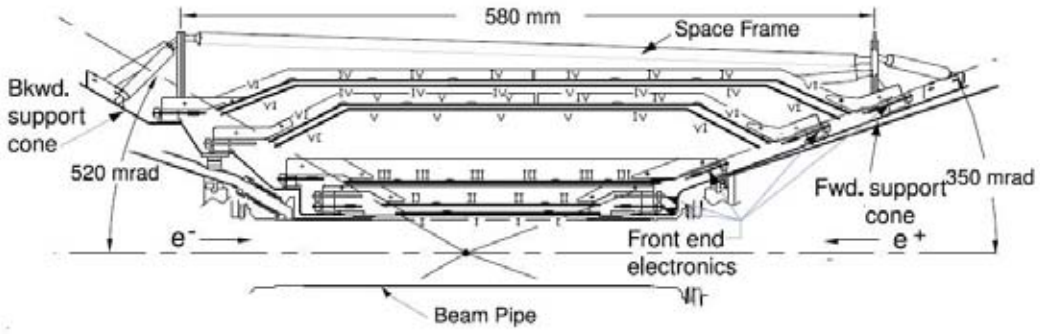

Figure 3.8: *Side view of the SVT.*

The silicon sensors are 300 μm thick-high-resistivity n-type silicon wafers, with n^+ and p^+ strips running orthogonally on opposite sides. As high-energy particles pass through the sensors they displace orbital electrons, producing conducting electrons and positive holes that then migrate under the influence of an applied depletion voltage. The resulting electrical signal is read-off from the strips, amplified, and discriminated with respect to a signal threshold by front-end electronics. The time over threshold of the signal is related to the charge of the signal and is read out by the data acquisition system for triggered events. The position resolution is in the 10 μm - 50 μm range, depending on the orientation of the strip (ϕ or z) and the layer number.

The SVT is water-cooled and monitored for temperature, humidity, and position variations. Local and global position alignment is performed frequently in the online reconstruction software. As the SVT has to withstand a lifetime integrated radiation dose of 2 Mrad, the sensors have a high threshold for radiation damage. Nevertheless, they are easily damaged by high instantaneous or integrated doses, and an extensive system of radiation monitoring with PIN and diamond diodes can abort the beam if dangerous background levels develop. Up to 2007 the monitoring system have prevented any significant damage from occurring and the SVT has performed extremely well, with an average track reconstruction efficiency of 97%, as shown in Fig. 3.9.

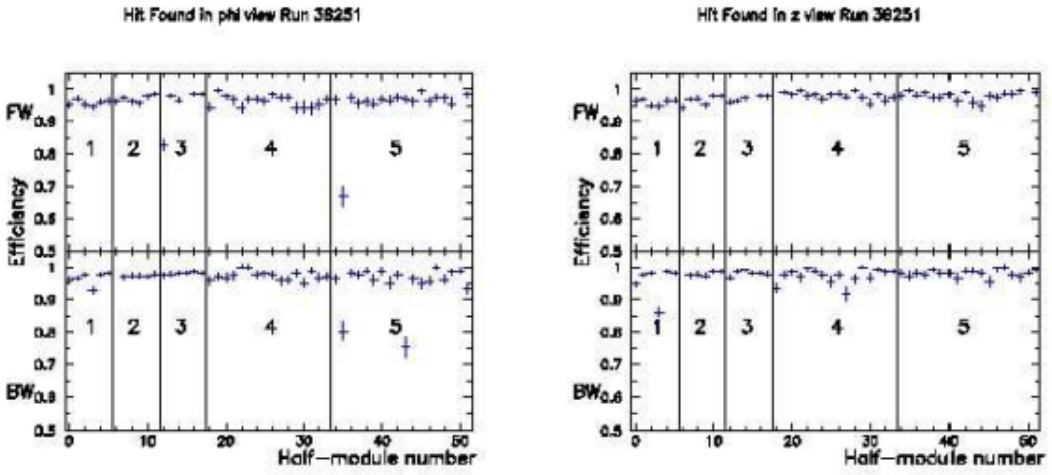

Figure 3.9: *SVT reconstruction efficiency in the ϕ view (left) and the z view (right) as measured in $e^+e^- \to \mu^+\mu^-$.*

3.4.2 Drift chamber

The Drift Chamber (Fig. 3.10) (DCH), a gaseous wire detector, is the main tracking device of *BABAR* . It is used for the measurement of the momenta of charged particles, and it is the only tracker for the subset of long-lived particles such as K^0, that decay outside of the SVT. In addition, the DCH provides particle-identification capability by measuring track ionization losses as a function of position (dE/dx), particularly for tracks with momenta less than 700 MeV/c. The inner wall of the drift chamber is placed close to the SVT outer wall to facilitate track-matching between the two devices.

The specific requirements for the drift chamber, which operates in a 1.5 T magnetic field, are to provide a spatial resolution better than 140 μm averaged over the cell and to supply identification for low momentum tracks through dE/dx with a resolution of 7% (40 measurements). In addition the drift chamber provides one the principal triggers for the experiment. These requirements are met through the use of a small-cell design, low density gas and light materials. The choice of the gas mixture (mixture of 80% helium and 20% isobutane) is motivated by considerations

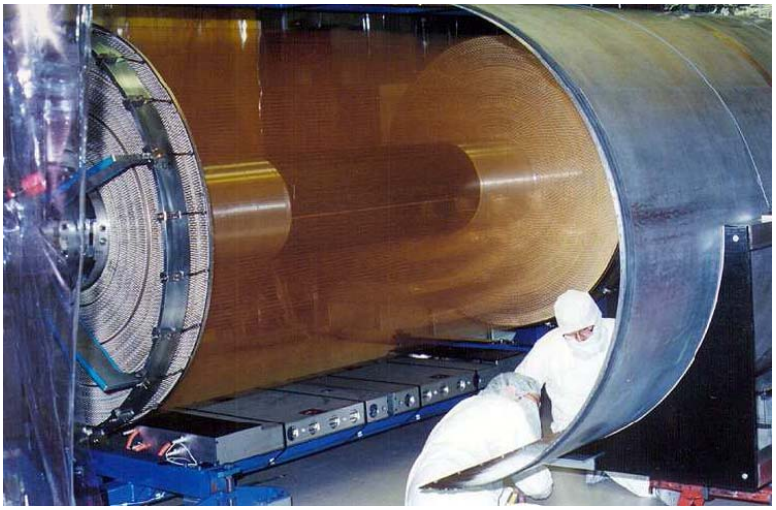

Figure 3.10: *A side view of the BABAR DCH.*

of aging and avalanche size as well as minimizing multiple scattering in the chamber, which is accomplished well by the lightweigth material for the multiple field wires. A schematic side view of the *BABAR* drift chamber is shown in Fig. 3.11.

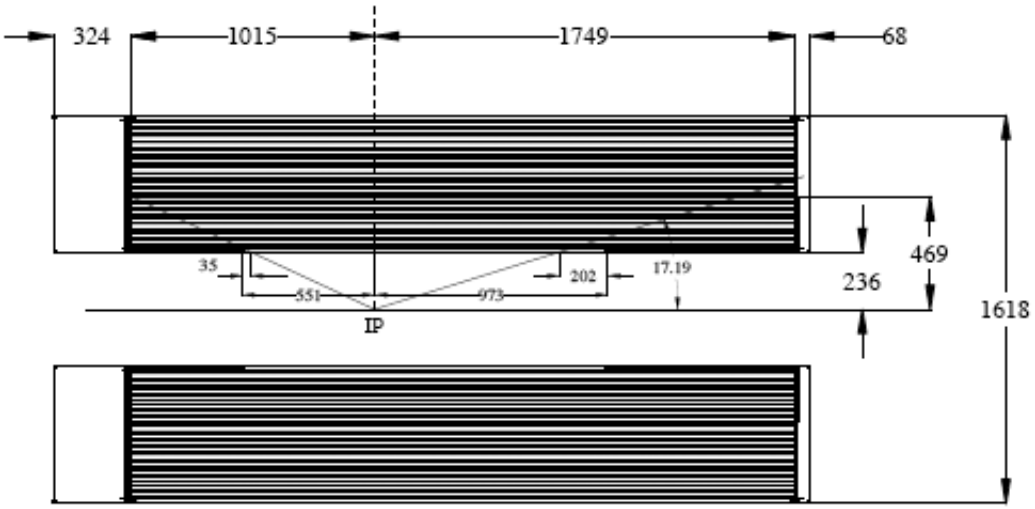

Figure 3.11: *Side view of the BABAR DCH. The dimensions are expressed in mm.*

The *BABAR* drift chamber is a 280 cm long cylinder, with an inner radius of 23.6

cm and an outer radius of 81 cm. Since the *BABAR* events will be boosted in the forward direction, the design of the detector is optimized to reduce the material in the forward end. The forward endplate is therefore made thinner in the acceptance region of the detector (12 mm thick) compared to rear end-plate (24 mm thick), and all the electronics is mounted on the rear end-plate.

The cells are arranged in 10 super-layers of 4 layers each, for a total of 40 layers. Axial (A) and stereo (U, V) super-layers are alternated following the pattern AUVAUVAUVA as shown in Fig. 3.12(a). The stereo angle varies from a minimum of 40 mrad in the innermost stereo super-layer, to a maximum of 70 mrad in the outermost stereo super-layer. The 7104 cells are hexagonal with typical dimension 1.2×1.8 cm^2. Fig. 3.12(b) shows the 50 ns isochrones in a typical cell in a 1.5T magnetic field.

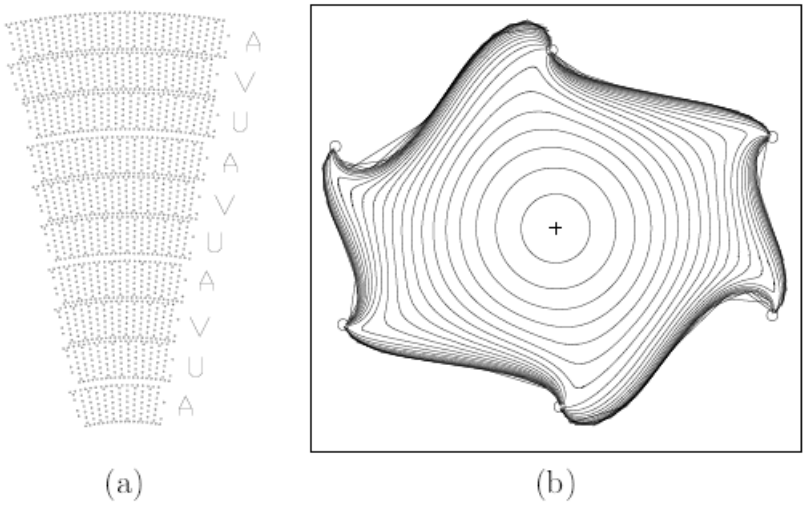

Figure 3.12: *a) Cell layout in the BABAR Drift Chamber. b) 50 ns isochrones in a typical BABAR drift chamber cell.*

The field wires are grounded, while the sense wire is held at high voltage, typically around 1900 V. The space around the wires is filled with the gas mixture. High-energy particles ionize the gas as they traverse it, and the liberated electrons are then accelerated toward the sense wires, ionizing additional electrons, which are

in turn accelerated themselves and result in the formation of a gas avalanche of electric charge. The avalanche collects on the sense wire with drift times of 10-500 ns and the charge and timing information of the signal is read-off through electronic circuits AC-coupled to the wire. The gain relative to the charge of the primary ionization is about 5×10^4. The grounded field wires produce a uniform electric field in the cell with evenly distributed isochrones, or contours of equal drift times. The DCH has demonstrated excellent performance throughout the life of *BABAR* with track-reconstruction efficiencies at the 95% level. This includes the effect of disconnecting a fraction of the wires in superlayers 5 and 6 that were damaged during the commissioning phase. The dE/dx response, with a resolution of about 7%, is shown in Fig. 3.13, and a new calibration in 2006 has improved the PID potential of this capability for high-energy tracks. The achieved resolution on transerve momentum is $\sigma_{p_t}/p_t = (0.13 \pm 0.01)\% \dot{p}_t (0:45 \pm 0:03)\%$, where p_t is given in units of GeV/c.

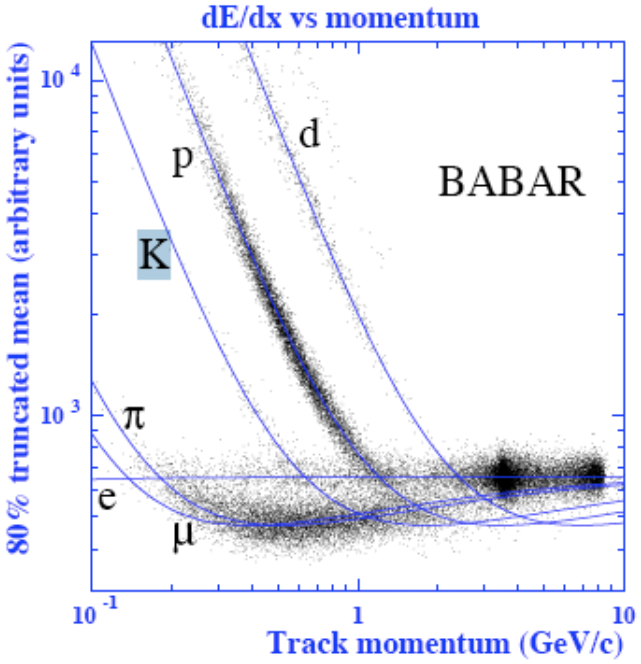

Figure 3.13: *DCH dE/dx as a function of track momentum.*

3.5 Cherenkov detector

Since the inner drift chamber tracker can provide sufficient $\pi - K$ separation up to only about 700 MeV/c, the dedicated Particle Identification (PID) system must perform well over a range from about 0.7 to 4.2 GeV/c, where the challenging upper end of this range must be achieved in the forward region of *BABAR* . *BABAR* has therefore a dedicated PID subdetector: the DIRC (Detector of Internally Reflection Cherenkov light), shown in Fig. 3.14 [61].

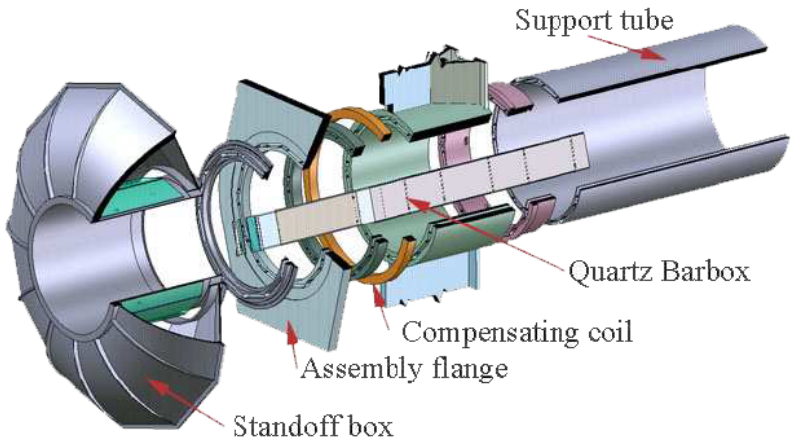

Figure 3.14: *A picture of the DIRC components.*

The pheonomenon of the Cherenkov light emission is widely used in particle detectors technology. A charged particle traversing a medium with a velocity of β greater than the speed of light in that medium - that is $\beta > 1/n$, where n is the medium refraction index - emits directional electromagnetic radiation, called *Cherenkov light*. The angle of emission θ_c of the photons with respect to the track direction is called *Cherenkov angle* and is determined by the velocity of the particle with the relation:

$$cos\theta_c = \frac{1}{n\beta} \tag{3.2}$$

where $\beta = \frac{v}{c}$ is the particle velocity, and c is the light velocity.
Thus, the measurement of θ_c determines β and, given the momentum of the particle, already measured in the DCH, the mass of the particle can be obtained. In fact, the

DIRC is placed between the charged particle tracking detectors (Drift Chamber) and the electromagnetic calorimeter. In order to minimize the worsening of the energy resolution and volume, and hence cost, of the electromagnetic calorimeter, the DIRC has been designed to be thin and uniform in terms of radiation lengths. Moreover, for operation at high luminosity, it needs fast signal response, and should be able to tolerate high background.
In Fig. 3.15 a schematic view of DIRC geometry and basic principles of Cherenkov light production, transport and image reconstruction are shown.

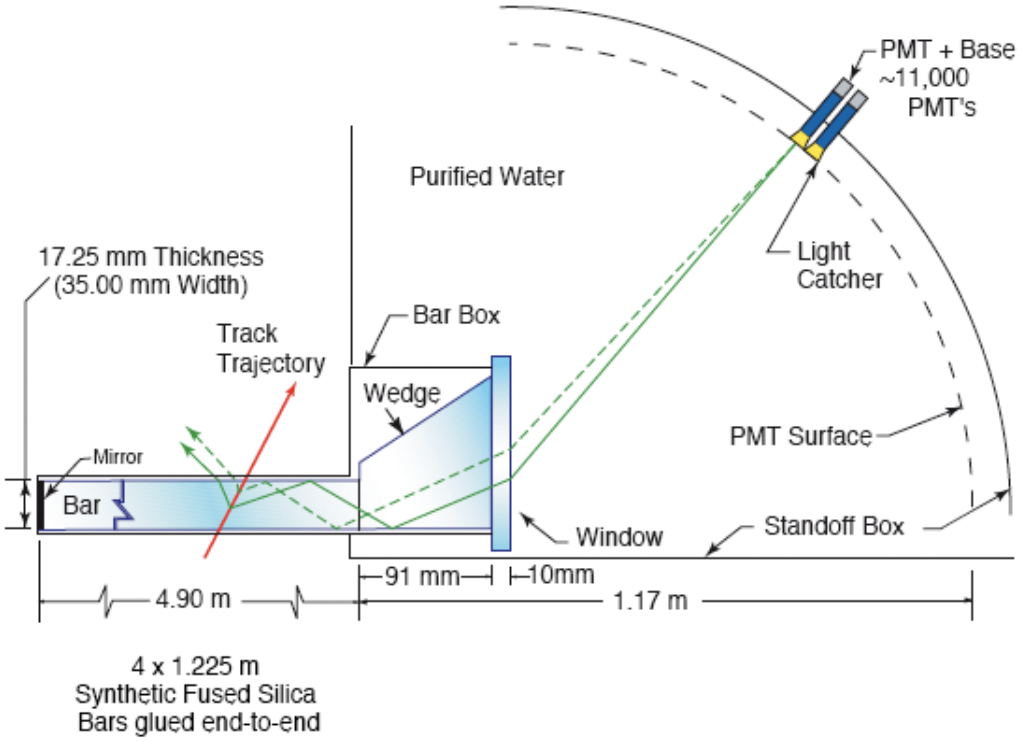

Figure 3.15: *Scheme of the DIRC working principle.*

The DIRC inverts the traditional concept of ring-imaging Cherenkov counters (RICH) in that it relies in the detection of Cherenkov photons trapped in the radiatior due to total internal reflection. The DIRC radiator consists of 144 long, straight bars of synthetic quartz with rectangular section, arranged in a 12-sided polygonal

barrel. The bars have transverse dimensions of 1.7 cm thickness by 3.5 cm width, and are 4.9 m long (see Fig. 3.16).

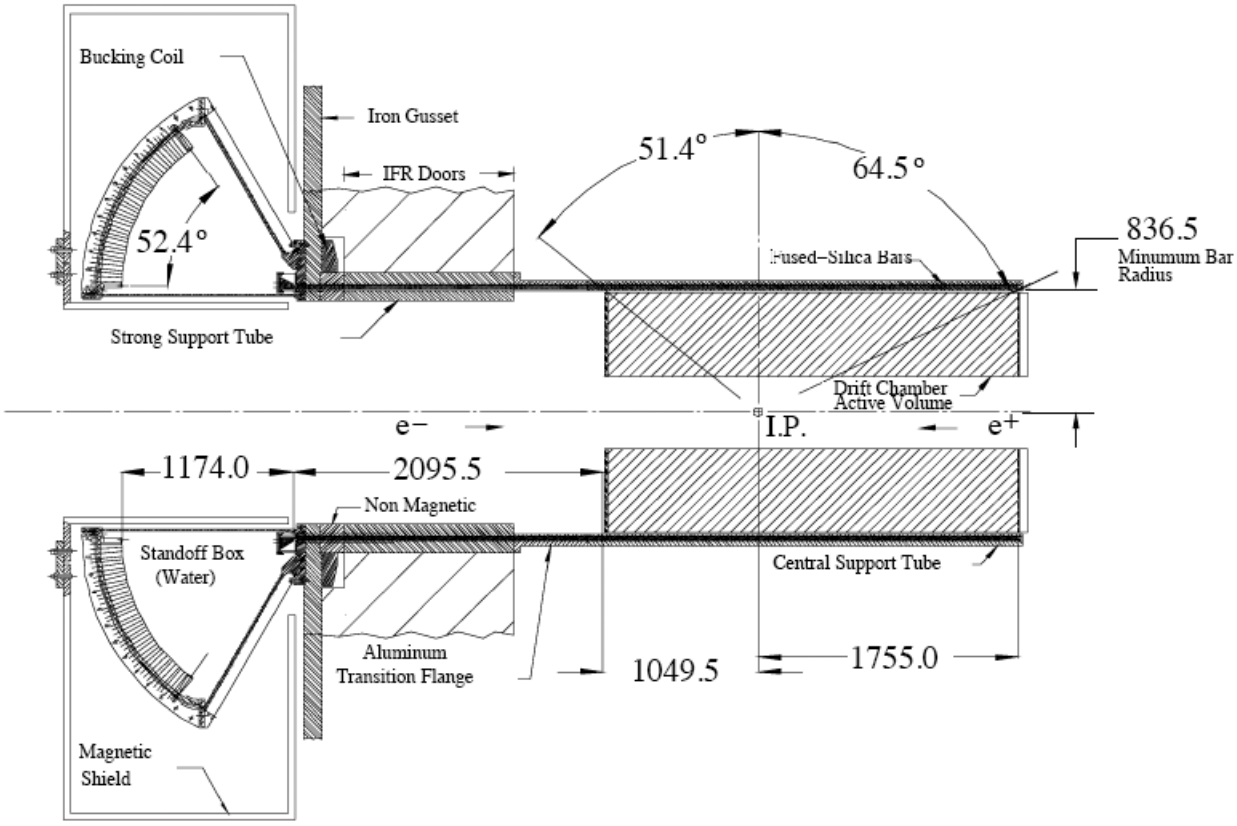

Figure 3.16: *Elevation view of the nominal DIRC system-geometry. All dimensions are given in millimeters.*

The DIRC radiator extends through the steel of the solenoid flux return in the backward direction, to bring the Cherenkov light, through successive total internal reflections, outside the tracking and magnetic volumes. Only this end of the bars is instrumented. A mirror placed at the other end of each bar reflects forward-going photons to the instrumented end. The Cherenkov angle at which a photon was produced is preserved in the propagation, modulo a certain number of discrete ambiguities, some of which can be resolved by the photon arrival-time measurement. Remaining ambiguities are dealt with by the pattern recognition during Cherenkov

angle reconstruction.
The radiatior material used for the bars is synthetic fused silica (n=1.474): the bars serve both as radiators and as light pipes for the portion of the light trapped in the radiator by total internal reflection. Synthetic silica has been choosen because of its resistance to ionizing radiation, its long attenuation lenght, its large index of refraction, its low chromatic dispersion within its wavelength acceptance.
At the instrumented end, the Cherenkov image is allowed to expand. The expansion medium is purified water, whose refractive index matches reasonably well that of the bars, thus minimizing the total internal reflection at the quartz-water interface. The region containing water is called the Stand-Off Box. Cherenkov photons are detected in the visible and near-UV range by a close-packed array of linear focused 2.82 cm diameter photomultiplier tubes (PMTs), lying on an approximately toroidal surface. A small piece of quartz with a trapezoidal profile glued at the back end of each bar allows for significant reduction in the area requiring instrumentation because it folds one half of the image onto the other half, while also reflecting photons with large angles in the radial direction back into the detection array. The dimensions of the Stand-Off Box are such that geometrical errors on angle measurements due to the finite size of bars and PMTs are of the order of the irreducible error due to quartz achromaticity. Six cubic meters of water are needed to fill the Stand-Off Box, and about 11000 PMTs to cover the detection area. The PMTs are operated directly in water, and are equipped with light concentrators. The PMTs are about 1.2 m away from the end of the quartz bar. Magnetic shielding around the Stand-Off Box is further needed to maintain the magnetic fringe field at an acceptable level for PMT operation.
The DIRC is intrinsically a three-dimensional imaging device, giving the position and arrival time of PMT signals. The three-dimensional vector pointing from the center of the bar end to the center of the PMT is computed, and then is extrapolated (using Snell's law) into the radiator bar in order to extract, given the direction of the charged particle, the Cherenkov angle. Timing information is used to suppress background hits and to correctly identify the track emitting the photons.
The discrimination between π and K due to the separation between the corresponding Cherenkov angles is greater than 3 standard deviations at about 3 GeV, as

shown in Fig. 3.17, and higher for lower momenta. Due to the fact that the photons inside the quartz are totally reflected, the association between phototube hits and single track can have more than one solution. These possible ambiguities are solved by measuring the time difference between the hits in phototubes and the expected arrival time of each track with a precision of 1-7 ns, which allows to estimate the propagation time for a given Cherenkov angle, and therefore to reduce the background from uncorrelated photons.

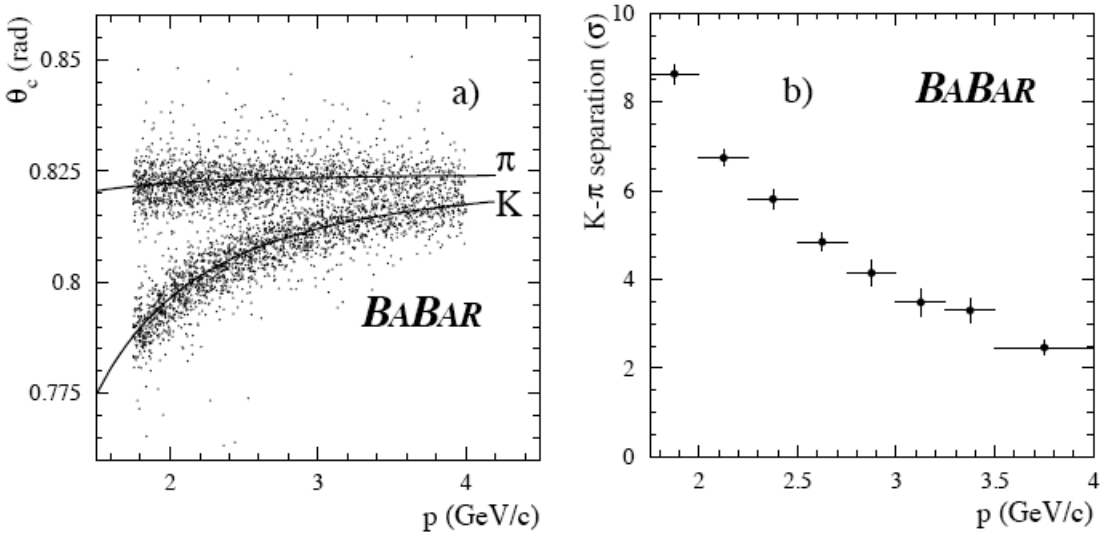

Figure 3.17: *a) Cherenkov angle and b) K-π discrimination power as a function of the momentum for single tracks. Discrimination quoted is computed performing the mean over all the polar angles.*

3.6 Electromagnetic calorimeter

The electromagnetic calorimeter (EMC) [62] is designed to measure electromagnetic showers with excellent efficiency, energy and angular resolution over the energy range from 20 MeV to 9 GeV.

This functionality is necessary to reconstruct π^0 and η mesons that decay to two

photons, as well as for identification of high-energy photons from rare radiative B decays. The electron ID is necessary for J/ψ reconstruction, for tagging the flavour of the non-signal B in the event through semileptonic decays, as well as for reconstruction of semileptonic and rare B decays. The detector must be hermetic and operate within the 1.5 T magnetic field. The amount of material in front of the EMC has been kept to a minimum in the design of the *BABAR* detector in order to allow for the detection of photons and electrons down to energies of 20 MeV.
The EMC is composed of 6580 Thallium-doped Cesium iodide (CsI(Tl)) scintillating crystals (Fig. 3.18), separated into a cylindrical barrel of 48 rings and a forward endcap of eight rings (Fig. 3.19). The EMC covers 90% of the CM acceptance and does not contain a backward endcap as the CM acceptance is low at backward polar angles. CsI(Tl) was chosen for its high light yield of 50,000 γ/MeV, allowing for excellent energy resolution, and its small Molière radius of 3.8 cm, which allows for excellent angular resolution. The transverse segmentation is at the scale of the Molière radius in order to optimize the angular resolution while limiting the number of crystals and readout channels.

The crystals serve as radiators for the traversing electrons and photons, with a short radiation length of 1.85 cm. The crystals scintillate under the influence of the showers, and the light is then passed through total internal reflection to the outer face of the crystal, where it is read out by silicon PIN diodes. As these diodes are well suited for operation in the high magnetic fields in the EMC, part of the motivation for the crystal choice was that the frequency spectrum of CsI(Tl) is detected by silicon PIN sensors with the high quantum efficiency of 85%. The EMC is cooled by water and Fluorinert coolant and monitored for changes in the environmental and radiation conditions and for changes in the light response of individual crystals.
The energy response of the EMC is calibrated using low-energy photons from a radioactive source and high-energy photons from radiative e^+e^- Bhabha events. As electromagnetic showers spread throughtout several crystals, a reconstruction algorithm is used to associate activated crystals into clusters and either to identify them as photon candidates or to match individual maxima of deposited energy to extrapolated tracks from the DCH-SVT tracker. Additional PID is obtained from

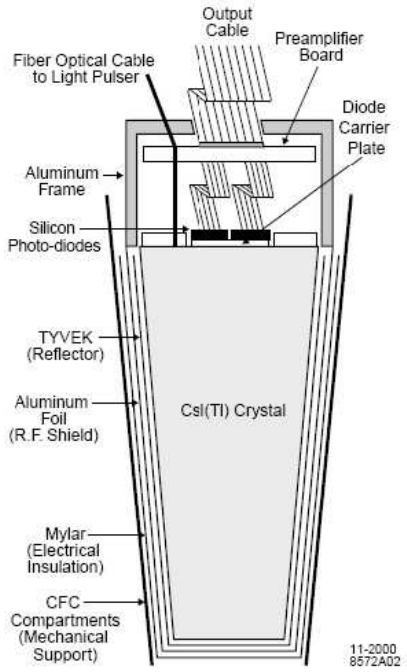

Figure 3.18: *Schematic view of the CsI(Tl) crystal with the front-end readout package mounted on the rear face.*

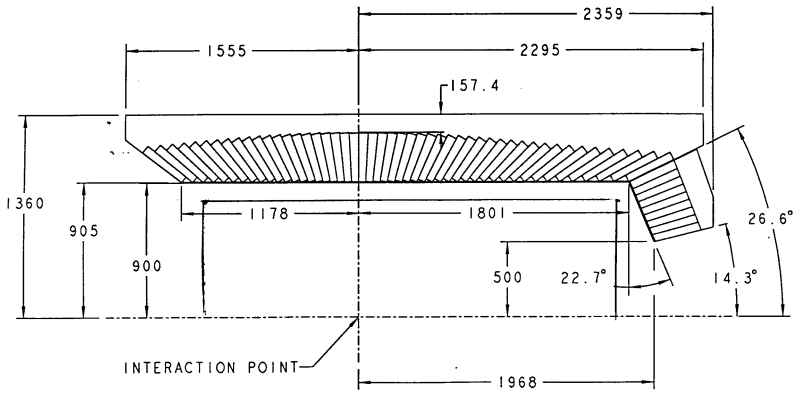

Figure 3.19: *Side view showing dimensions (in mm) of the calorimeter barrel and forward endcap.*

the spatial shape of the shower.
The target energy resolution for photons at a polar angle of 90° is:

$$\frac{\sigma(E)}{E(GeV)} = \frac{\sigma_1}{(E(GeV))^{1/4}} + \sigma_2 \tag{3.3}$$

where the expected $\sigma_1 \sim 1\%$ and $\sigma_2 \sim 1.2\%$ turn out to be higher when fitting the results from different methods of calibration, in fact they turn out to be $\sigma_1 = (2.32 \pm 0.03)\%$ and $\sigma_2 = (1.85 \pm 0.07)\%$. These differences come from cross-talk effects on the electronic readout. As it is possibile to see from the Fig. 3.20(a), the energy resolution ranges between 2% and 6%. The designed angular resolution is:

$$\frac{\sigma_{\theta,\phi}}{E(GeV)} = \frac{\sigma_1}{\sqrt{E(GeV)}} + \sigma_2 \tag{3.4}$$

ranging between 3 and 10 mrad (Fig. 3.20 (b)).

3.7 Instrumented flux return

The IFR is the primary muon detector at *BABAR* and is also used for the identification of long-lived neutral hadrons (primarily K_L^0's). The IFR is divided into a hexagonal barrel, which covers 50% of the solid-angle in the CM frame, and two endcaps (Fig. 3.21). Originally, it consisted of layers of steel of varying thickness interspersed with Resistive Plate Chamber (RPCs), 19 layers in the barrel and 18 in each endcap. The steel serves as a flux return for the solenoidal magnet as well as an hadron absorber, limiting pion contamination in muon ID. RPC's were chosen as they were believed to be a reliable, inexpensive option to cover the 2000 m^2 of instrumented area in this outermost region of *BABAR* with the desired acceptance, efficiency, and background rejection for muons down to momenta of 1 GeV/c.

The RPC's detect high-energy particles through gas-avalanche formation in a high electric field. The chambers consist of 2 mm-thin bakelite sheet kept 2 mm apart by an array of spacers located every 10 cm (Fig. 3.22). The space in between is filled with a non-flammable gas mixture of 56.7% argon, 38.8% freon 134a, and 4.5% isobutane, while the sheets are held at a potential of 8000 V. The inside surface of the

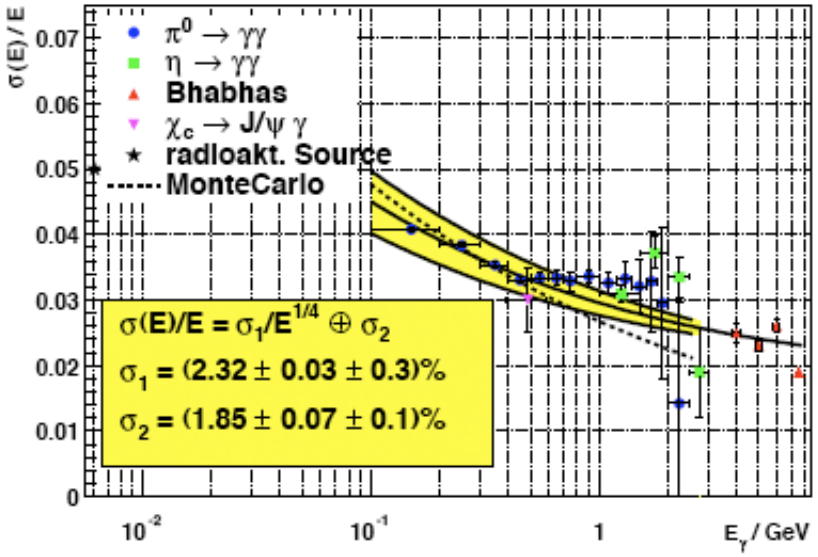

(a)

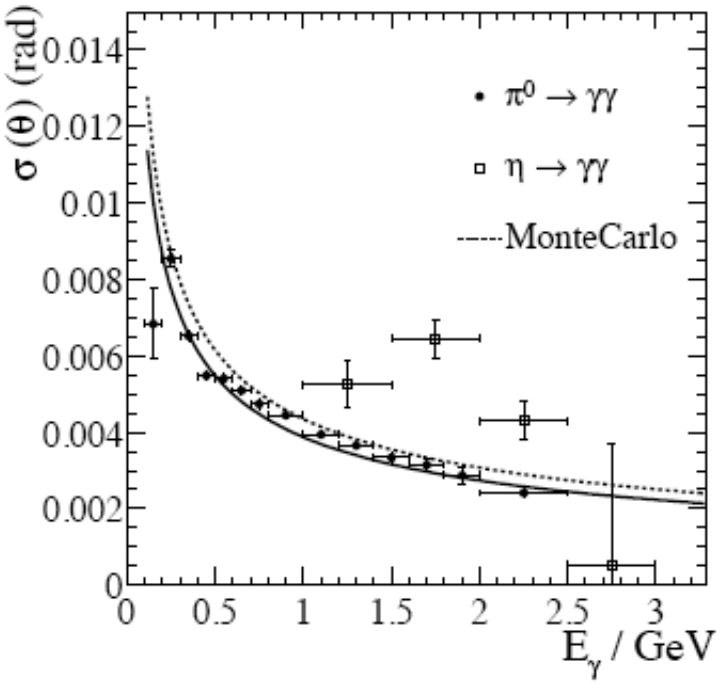

(b)

Figure 3.20: *a) Energy resolution versus photon energy for different calibrations. b) Angular resolution versus photon energy.*

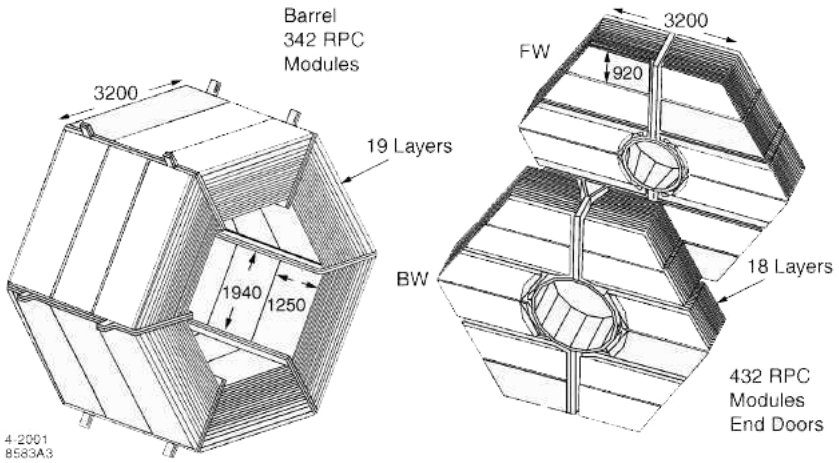

Figure 3.21: *Drawing of the IFR barrel and endcaps.*

bakelite is smoothed with a linseed-oil coating so that the electric field is uniform, thus preventing discharges in the gas and large dark currents. The RPC's operate in streamer mode, wherein the avalanche grows into a streamer, a mild, controlled form of electrical discharge in the gas. The streamer change is read out in both the ϕ and z directions by aluminum strips located outside and capacitively coupled to the chamber. The streamer is kept from producing electrical breakdown of the gas by the quenching action of the freon and isobutane molecules. Isobutane has large molecules with rotational degrees of freedom that can absorb electrical energy.

In streamer mode, the gas gain is at the 10^8 level. The factor of 10-1000 increase in gain over avalanche mode greatly simplifies the readout electronics. Moreover, the charge of the streamer is indipendent of the primary-ionization charge, resulting in an effectively digital signal with high efficiency. Initially, the RPC's performed at over 90% efficiency as expected geometrically from inactive space in the detector, resulting in a muon detection efficiency of 90% for a pion misidentification rate of 6-8% in the momentum range of $1.5 < p < 3.0$ GeV/c.
Shortly after the start of data-taking with *BABAR* in 1999, the performance of the RPCs started to deteriorate rapidly. Numerous chambers began drawing dark cur-

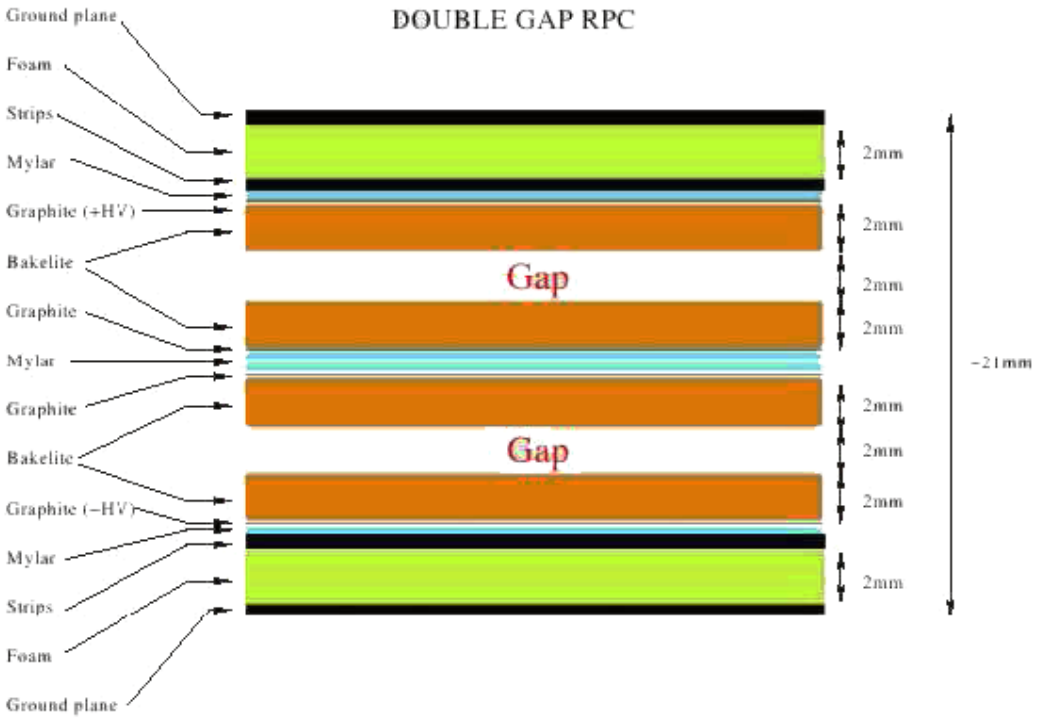

Figure 3.22: *Schematic structure of a Resistive Plate Chamber.*

rents and develop large areas of low efficiency. The overall efficiency of the RPC's started to drop and the number of non-functional chambers (with efficiency less than 10%) rose dramatically (Fig. 3.23), deteriorating muon ID. The problem was traced to insufficient curing on R&D of the linseed-oil-coating and to the high temperature at which the RPC's were operated initially. Uncured oil droplets would form columns under the action of the strong electric field and the high temperature (up to 37°C), bridging the bakelite gap and resulting in large currents and dead space (Fig. 3.24).

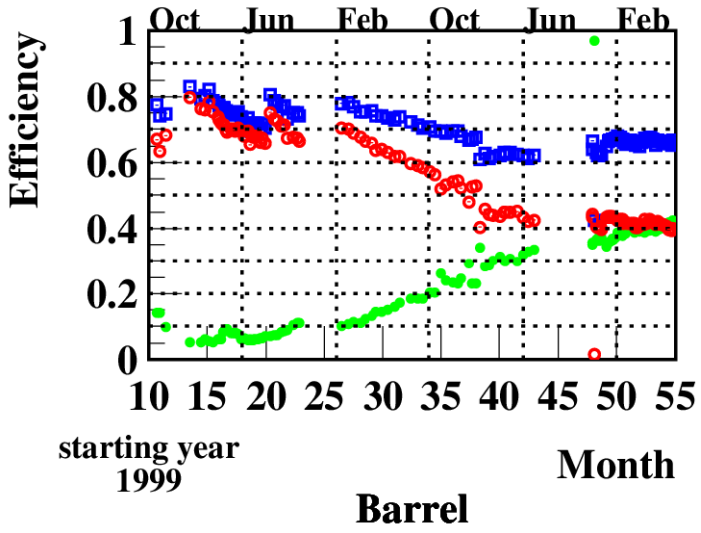

Figure 3.23: *Deterioration with time of the average RPC efficiency (red). The green dots show the fraction of RPC's with efficiency lower than 10%, and the blue dots show the fraction of RPC's with efficiency greater than 10%.*

Various remediation measures were attempted, including flowing oxygen through the chambers to cure the oil and introducing water cooling on IFR, but they did not solve the problem. Extrapolating the efficiency trend showed a clear path towards muon ID capability at *BABAR* within a couple of years of operations, so an upgrade of the IFR detectors was deemed necessary by the collaboration.
The forward endcap was retrofitted with new improved RPCs in 2002. The new chambers were screened much more stringently with QC test and had a much thinner

Figure 3.24: *Photographs of defects on the linseed oil coating of a malfunctioning RPC.*

linseed-oil coating that was properly cured and tested. They have performed well since then. The backward endcap wasn't retrofitted, as its acceptance in the CM frame is small. In the barrel, the collaboration decided to upgrade the detector with *Limited Streamer Tube (LST)* technology. The RPCs were removed and replaced by 12 layers of LSTs and 6 layers of brass to improve hadron absorption.
The LST consists of a PVC comb of eight 15 mm by 17 mm cells about 3.5 m in length, encased in a PVC sleeve, with a 100 μm gold-plated beryllium-copper wire running down the center of each cell (Fig. 3.25). The cells in the comb are covered with graphite, which is grounded, while the wires are held at 5500 V and held in place by wire holders located every 50 cm. The gas mixture consists of 3.5% argon, 8% isobutane and 88.5% carbon dioxide. Like RPCs and as their name implies, the LSTs are operated in streamer mode. The signal is read off directly from the wires through AC-coupled electronics and from strips running perpendicular to the tubes and capacitively coupled to the wires.

The project involved the manufacture of 1550 LSTs including contingency, with more than 1200 installed in the detector. It also necessitated the design and fabrication of custom read-out electronics, HV power supplies and gas system. The project was completed successfully and safely; after installation the tubes have performed extremely well since 2005, with failures rates below 0.5% for both the tubes and z-strip. The efficiencies of all layers were at the geometrically expected level of 90%.

Figure 3.25: *The mechanical structure of BABAR LST.*

3.8 Trigger, Data Acquisition and Reconstruction

Data relevant for B physics is selected for storage from the flow of collision information collected by the detector by a two-level trigger system. The Level 1 (L1) trigger is hardware-based, consisting of several dedicated microprocessor systems, that analyze data from the front-end electronics (FEEs) of the DCH, EMC, and IFR to form primitive physics objects used to make the trigger decision. These include tracks of minimum transverse momentum that penetrate to a particular depth into the DCH and energy clusters in the EMC above the thresholds. The selections are optimized to maintain nearly $B\bar{B}$ efficiency while removing most of the beam-induced backgrounds in the process of reducing the data collection rate from about 20kHz to a few kHz, which can be processed by the next trigger level. Some "prescaled" events of random beam-beam crossing and special event types are also collected for efficiency, diagnostic, and background studies. The trigger decision is made and communicated within the 12.8 μs buffer limit of the FEEs. The L1 trigger has greater than 99.5% efficiency for $B\bar{B}$ processes.

After an L1 accept decision, the L1 output is passed on to the Level 3 (L3) trigger,

which consists of software-based algorithms run on a farm of commercial PCs [2]. The L3 trigger also has access to the complete event data and refines the L1 decision with more sophisticated selections, such as requirements on a track's distance of closest approach to the interaction point or the total invariant mass of an event. It maintains the $B\bar{B}$ selection efficiency at more than 99% while reducing the data rate to about 200 Hz. Each event corresponds to about 30kB of detector information.
An event that results in an L3 accept decision is processed by the data-acquistion electronics and event-building software. In this process, charged tracks are reconstructed from DCH and SVT information and extrapolated to the outer part of the detector incorporating knowledge of the distribution of material in the detector and magnetic field. The momenta of tracks is measured from the sagitta in the curves of the tracks [3]. PID is refined with DIRC, EMC and IFR information as well as with attempts to match objects in those subdetectors with tracks in the DCH. Fundamental physical objects reconstructed in the detectors are also used to assemble candidates for composite particles, such as π^0's from two photon candidates and K^0_S's from two charged tracks candidates (from the $K^0_S \to \pi^+\pi^-$ process). Lists of particle candidates as well as the original digitized data are stored on tape in collections that are retrieved later for high-level analysis by individual groups of users. Throughout event reconstruction various calibrations such as alignment constants and energy-scale adjustments in the EMC are applied to detector information to refine reconstruction performance. Calibration information were updated frequently during data taking to keep it consistent with running conditions. Data-quality scripts monitor detector behaviour and various physics processes to verify that the collected data was not compromised by deviations from expected behaviour of the detector or accelerator. A parallel system based on the EPICS slow-control environment was used to monitor and control the detector elements for all subsystems.

[2] The numbering scheme is historical and based on trigger systems with two hardware based levels and a third, software-based level, as commonly implemented in hadron colliders. *BABAR* requires only one hardware-based level, but the first software-based level maintains the tertiary designation.

[3] Charged particles are deflected by the magnetic field of the solenoidal and propagate in helices around the magnetic field lines with the radius of curvature $R \sim p/B$, where p is the momentum of the particle and B is the magnetic field. The orientation of bending depends on the charge of the particle.

Detector, accelerator, and environmental conditions were recorded in another ambient database. The entire data-taking process was supervised at all times by at least two *BABAR* shifters on the detector side and several accelerator operators on the PEP-II side.

Chapter 4

Analysis

4.1 Analysis strategy

In the search for $e^+e^- \to c\bar{c}c\bar{c}$ events, a J/ψ or $\psi(2S)$ is fully reconstructed. The charmonium formed by the other $c\bar{c}$ pair in the event is indirectly detected looking at the recoil mass against the fully reconstructed J/ψ or $\psi(2S)$. Explicitly, the recoil mass, M_{rec}, is determined via:

$$M_{rec} = \sqrt{(\sqrt{s} - E^*_\psi)^2 - p^*_\psi} \tag{4.1}$$

where $\sqrt{s}$ is the center of mass (CM) energy of the e^+e^-, and E^*_ψ and p^*_ψ are the energy and momentum of the J/ψ or $\psi(2S)$ in the CM system, respectively.
In order to improve the resolution of the recoil mass, a kinematic fit with a "geometric" constraint and a mass constraint to the mass of J/ψ and $\psi(2S)$ is applied. After performing the selection and obtaining the M_{rec} distribution, enhancements in this distribution are studied.
The analysis is performed blind, i.e. the event selection is optimized without looking at the data in the signal region (2 - 4.5 GeV/c^2 in the recoil mass).

4.2 Data samples and preselection

4.2.1 Data processing in *BABAR*

The quality of data collected by the *BABAR* detector is checked online by the shifter on duty who discards the samples affected by sub-detector bad performance or unacceptably high backgrounds.
The raw data undergo then the *prompt calibration* and *event reconstruction* stages. At the beginning all calibration parameters and alignments, which can vary over the time, are update; this phase is done by SLAC's computing resources within a few hours from the data taking. Charged tracks and neutral particles are reconstructed from the single hits and energy deposits in each subdetector: this is performed at the dedicated processing farm in Padova (Italy), within the following 48 hours.
After the final validation, the data are subdivided into smaller samples (skims) which satisfy the needs of the main branches of physical analysis and are distributed over the computing facilities dedicated to data analysis.

4.2.2 Monte Carlo samples

This analysis has been set up using Monte Carlo samples of the signal:

- $e^+e^- \to J/\psi c\bar{c}$: $e^+e^- \to J/\psi\eta_c$, $J/\psi\chi_{c0}$, $J/\psi\eta_c(2S)$ and $J/\psi X(3940)$, $J/\psi \to e^+e^-(\mu^+\mu^-)$;

- $e^+e^- \to \psi(2S)c\bar{c}$: $e^+e^- \to \psi(2S)\eta_c$, $\psi(2S)\chi_{c0}$, $\psi(2S)\eta_c(2S)$ and $\psi(2S)X(3940)$, $\psi(2S) \to e^+e^-$ and $\psi(2S) \to \mu^+\mu^-$;

- $e^+e^- \to \psi(2S)c\bar{c}$: $e^+e^- \to \psi(2S)\eta_c$, $\psi(2S)\chi_{c0}$, $\psi(2S)\eta_c(2S)$ and $\psi(2S)X(3940)$, $\psi(2S) \to J/\psi\pi^+\pi^-$ and $J/\psi \to e^+e^-(\mu^+\mu^-)$.

For each decay mode, 216000 events are generated.

4.2.3 Data sample

The current analysis is based on 476 fb^{-1} *BABAR* data, collected from February 2000 to August 2007, during the data-taking periods Run1-Run6. This sample includes about 431 fb^{-1} taken at the $\Upsilon(4S)$ resonance (on-peak) and 45 fb^{-1} taken off-peak, 40 MeV below.
The data used in this analysis come from a skim *Jpsitoll*, where the events contain a J/ψ or a $\psi(2S)$ reconstructed by its decay in e^+e^- or $\mu^+\mu^-$, as discussed in the following.
In the case of e^+e^- pair, the requests are:

- The two electrons are selected by two different PID selectors: the first, which is a merged Bremsstrahlung-recovery list containing combination of a Bremsstrahlung-recovered electron for eLoose and noCal selectors, is named eBremRecELNC[1]. The noCal selector is for the electron identification outside of the acceptance region of the EMC. The second, named eBremRecoCT, is a merged Bremsstrahlung-recovery list containing combination of a Bremsstrrahlung-recovered electron for charged tracks.

- for J/ψ: the e^+e^- invariant mass must be 2.5 GeV/c^2 $< m(e^+e^-) <$ 3.3 GeV/c^2

- for $\psi(2S)$: the e^+e^- invariant mass must be 3.3 GeV/c^2 $< m(e^+e^-) <$ 4.0 GeV/c^2

For $\mu^+\mu^-$ the requests are:

- One muon comes from the PID list muNNVeryLoose, which is based on the use of a Neural Network (NN) algorithm; the other muon comes from the list ChargedTracks[2].

- for J/ψ: the $\mu^+\mu^-$ invariant mass must be 2.8 GeV/c^2 $< m(\mu^+\mu^-) <$ 3.3 GeV/c^2

[1] All the *BABAR* Particle Identification selectors are described in Appendix A
[2] All the *BABAR* Tracks lists are described in Appendix A

- for $\psi(2S)$: the $\mu^+\mu^-$ invariant mass must be 3.3 GeV/c^2 $< m(\mu^+\mu^-) <$ 4.0 GeV/c^2

The invariant mass ranges are different between electron and muon to take into account the Bremsstrahlung effect in the electron case.
Details on data samples are summarized in table 4.1

	On Peak Data		Off Peak Data	
Dataset	L(fb^-1)	Numer of events	L(fb^-1)	Number of events
Run1	20.8	19885315	2.6	2385889
Run2	61.6	63526552	6.9	6808557
Run3	32.5	34212178	2.5	2476919
Run4	101.6	110059396	10.3	10530272
Run5	134.9	146063697	14.6	15076407
Run6	79.6	80972090	7.9	7579105
Total	431	454719228	45.0	44857149

Table 4.1: *On-Peak and Off-Peak data collection used in the analysis: total luminosity 476 fb^{-1}*

4.2.4 Reconstruction of the J/ψ

During the n-tuple production phase, further requirements are imposed for the reconstruction of the J/ψ. In the case of $J/\psi \to e^+e^-$ the two electrons are selected by a PID selector, named eLHBremLH. In the case of $J/\psi \to \mu^+\mu^-$ the two muons are selected by the PID selector named muBDTVeryLoose (See Appendix A).
A geometric fitter fits both position and momentum information, whereas a kinematic fitter extracts only momenta: in particular, in this analysis the so-called Cascade geometric fitter has been used, which implements a χ^2-minimization process to perform vertex-position and momentum fits; it is a leaf-by-leaf fitter that uses the Newton-Raphson method.

4.2.5 Reconstruction of $\psi(2S) \to J/\psi\pi^+\pi^-$

After the reconstruction of the J/ψ, two pions from the PID selector named PiLHVeryLoose are requested, in order to reconstruct a $\psi(2S)$.
The Cascade geometric fitter is used to reconstruct the J/ψ whereas for the reconstruction of the $\psi(2S)$, the so-called TreeFitter fitter is used, where the global decay chain fit is based on Kalman filter that is not a leaf-by-leaf fitter.
In order to improve the resolution of the recoil mass, a kinematic fit with a mass constraint to the mass of J/ψ is applied.

4.2.6 Reconstruction of the $\psi(2S) \to \ell^+\ell^-$

During the n-tuple production phase, further requeriments are imposed for the reconstruction of the $\psi(2S)$. For $\psi(2S) \to e^+e^-$ the two electrons are selected by a PID selector, named eLHBremLH. For $\psi(2S) \to \mu^+\mu^-$ the two muons are selected by the PID selector named muBDTVeryLoose.
A geometric fitter fits both position and momentum information, whereas a kinematic fitter extracts only momenta: in particular, in this analysis the so-called Cascade geometric fitter has been used.

4.2.7 Candidate Selection

For the final candidate selection tighter cuts are imposed on the $\ell^+\ell^-$ invariant mass. The signal windows for each analysis are:

For $\mathbf{e^+e^- \to J/\psi c\bar{c} \to \ell^+\ell^- c\bar{c}}$:

- -0.050 GeV/c^2 $< m(e^+e^-) - M_{J/\psi} < 0.030$ GeV/c^2
- -0.030 GeV/c^2 $< m(\mu^+\mu^-) - M_{J/\psi} < 0.030$ GeV/c^2

For $\mathbf{e^+e^- \to \psi(2S) c\bar{c} \to \ell^+\ell^- c\bar{c}}$:

- -0.050 GeV/c^2 $< m(e^+e^-) - M_{J/\psi} < 0.030$ GeV/c^2

- $-0.030\ \mathrm{GeV/c^2} < m(\mu^+\mu^-) - M_{J/\psi} < 0.030\ \mathrm{GeV/c^2}$

For $\mathbf{e^+e^- \to \psi(2S)c\bar{c} \to J/\psi\pi^+\pi^-c\bar{c}}$:

- $-0.010\ \mathrm{GeV/c^2} < m(\ell^+\ell^-\pi^+\pi^-) - M_{\psi(2S)} < 0.010\ \mathrm{GeV/c^2}$

4.2.8 Background estimation

Since the aim of this analysis is to study the spectrum recoiling against a reconstructed J/ψ ($\psi(2S)$), the background is composed mainly by fake J/ψ ($\psi(2S)$). To study the background in the recoil system, we use the J/ψ ($\psi(2S)$) sidebands, i.e. data events which are defined in the following ranges.

For $\mathbf{e^+e^- \to J/\psi c\bar{c} \to \ell^+\ell^- c\bar{c}}$:

- For electrons:

$$\begin{aligned} 0.080\ \mathrm{GeV/c^2} < m(e^+e^-) - M_{J/\psi} < 0.120\ \mathrm{GeV/c^2} \\ -0.140\ \mathrm{GeV/c^2} < m(e^+e^-) - M_{J/\psi} < -0.100\ \mathrm{GeV/c^2} \end{aligned} \tag{4.2}$$

- For muons:

$$\begin{aligned} 0.080\ \mathrm{GeV/c^2} < m(\mu^+\mu^-) - M_{J/\psi} < 0.110\ \mathrm{GeV/c^2} \\ -0.110\ \mathrm{GeV/c^2} < m(\mu^+\mu^-) - M_{J/\psi} < -0.080\ \mathrm{GeV/c^2} \end{aligned} \tag{4.3}$$

For $\mathbf{e^+e^- \to \psi(2S)c\bar{c} \to \ell^+\ell^- c\bar{c}}$:

- For electrons:

$$\begin{aligned} 0.080\ \mathrm{GeV/c^2} < m(e^+e^-) - M_{\psi(2S)} < 0.120\ \mathrm{GeV/c^2} \\ -0.140\ \mathrm{GeV/c^2} < m(e^+e^-) - M_{\psi(2S)} < -0.100\ \mathrm{GeV/c^2} \end{aligned} \tag{4.4}$$

- For muons:

$$\begin{aligned} 0.080\ \mathrm{GeV/c^2} < m(\mu^+\mu^-) - M_{\psi(2S)} < 0.110\ \mathrm{GeV/c^2} \\ -0.110\ \mathrm{GeV/c^2} < m(\mu^+\mu^-) - M_{\psi(2S)} < -0.080\ \mathrm{GeV/c^2} \end{aligned} \tag{4.5}$$

For $\mathbf{e^+e^- \to \psi(2S)c\bar{c} \to J/\psi\pi^+\pi^- c\bar{c}}$:

- For $J/\psi \to \ell^+\ell^-$:

$$0.060 \text{ GeV/c}^2 < m(\ell^+\ell^-\pi^+\pi^-) - M_{\psi(2S)} < 0.070 \text{ GeV/c}^2$$
$$-0.060 \text{ GeV/c}^2 < m(\ell^+\ell^-\pi^+\pi^-) - M_{\psi(2S)} < -0.070 \text{ GeV/c}^2 \quad (4.6)$$

The choice of these sidebands is due to the asymmetric distribution of the mass produced by the Bremsstrahlung radiation, for the J/ψ ($\psi(2S)$) in the signal MC (see Fig. 4.1, 4.2, 4.3). Even if the Bremsstrahlung effect recovery required for the two electrons, the distribution of the J/ψ ($\psi(2S)$) mass in the electronic case has a tail for low values.

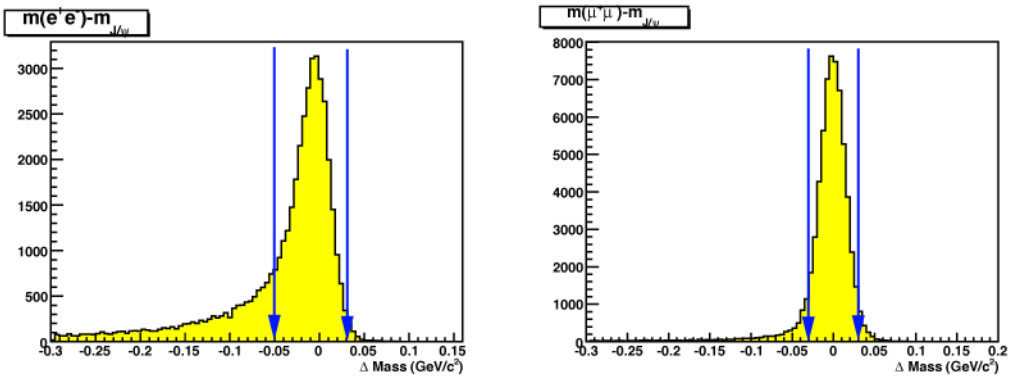

Figure 4.1: *$e^+e^- \to J/\psi c\bar{c} \to \ell^+\ell^- c\bar{c}$: Distribution of the $J/\psi \to \ell^+\ell^-$ mass in the signal MC, for $J/\psi \to e^+e^-$ and $J/\psi \to \mu^+\mu^-$ respectively. The signal windows is indicated.*

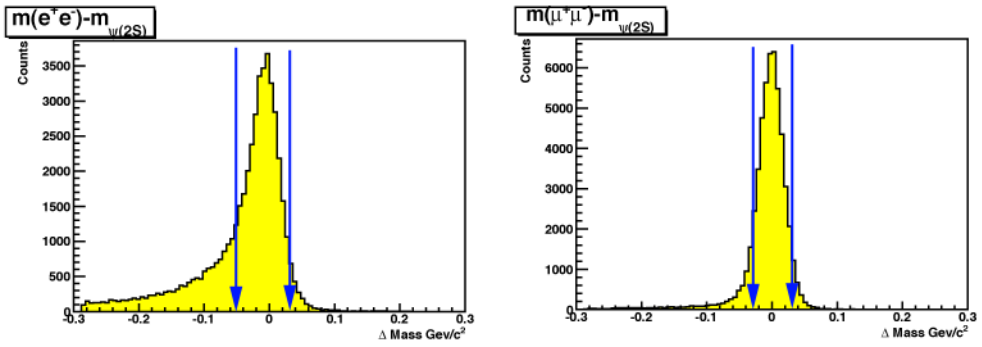

Figure 4.2: $e^+e^- \to \psi(2S)c\bar{c} \to \ell^+\ell^- c\bar{c}$: *Distribution of the* $\psi(2S) \to \ell^+\ell^-$ *mass in the signal MC, for* $\psi(2S) \to e^+e^-$ *and* $\psi(2S) \to \mu^+\mu^-$ *respectively. The signal windows is indicated.*

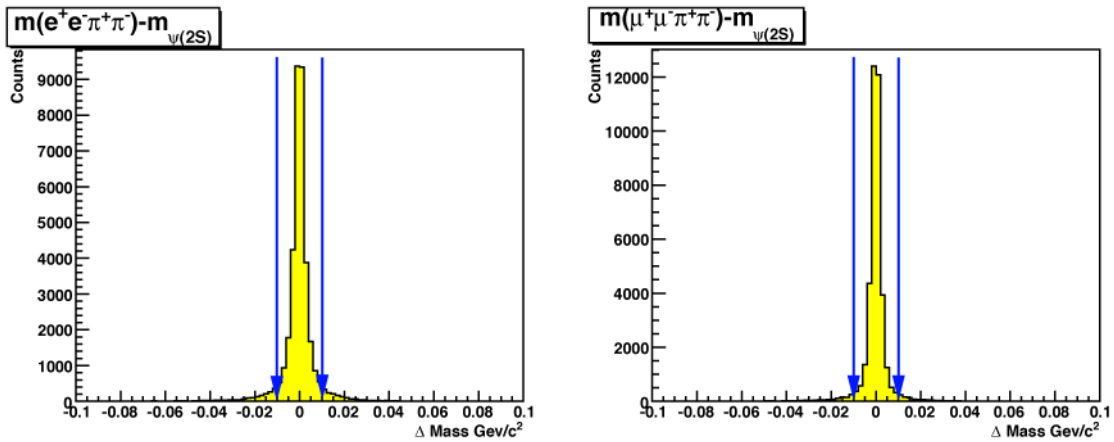

Figure 4.3: $e^+e^- \to \psi(2S)c\bar{c} \to J/\psi\pi^+\pi^- c\bar{c}$: *Distribution of the* $\psi(2S) \to J/\psi\pi^+\pi^-$ *mass in the signal MC, for* $J/\psi \to e^+e^-$ *and* $J/\psi \to \mu^+\mu^-$ *respectively. The signal windows is indicated.*

4.2.9 Selection strategy

The general procedure of selection consists of two main steps: preselection and selection.
In the preselection phase, cuts are based on physics remarks on the involved process. So this first step is simply cut-based (see next section).
In the second part, in addition to rectangular cuts (on the momentum and the number of charged tracks) we take into account also the helicity, the ψ $cos\theta_{CM}$ (defined in section 4.3.7) and the maximum photon energy.
This approach is aimed to maximize the figure of merit $N_S/\sqrt{N_S + N_B}$ where N_S and N_B are the signal and background samples, respectively.

4.2.10 Preselection

During the production of the n-tuples a primary selection has been carried out, doing the following requests:

- post fit selection for the J/ψ Mass (2.8 GeV/c^2 $< mass_{J/\psi} <$ 3.3 GeV/c^2);
- post fit selection for χ^2 probability ($0.001 < prob_{\chi^2} < 1.000$) for the J/ψ vertex reconstruction;
- post fit selection for the $\psi(2S)$ Mass (3.4 GeV/c^2 $< mass_{\psi(2S)} <$ 3.9 GeV/c^2);
- post fit selection for χ^2 probability ($0.001 < prob_{\chi^2} < 1.000$) for the $\psi(2S)$ vertex reconstruction;

In table 4.2, 4.3 and 4.4 one can see the effect of the preselection procedure: for each run the number of events before and after the preselection and the survival rate are reported.

Run	Events before	Events after	Survival rate ϵ
Run1 Off-Peak	2385889	229098	9.60%
Run2 Off-Peak	6808557	635155	9.33%
Run3 Off-Peak	2476919	226387	9.14%
Run4 Off-Peak	10530272	1027441	9.76%
Run5 Off-Peak	15076407	1422003	9.43%
Run6 Off-Peak	7579105	736241	9.71%
Total Off-Peak	44857149	4276325	9.53%
Run1 On-Peak	19885315	1852237	9.31%
Run2 On-Peak	63526552	5826765	9.17%
Run3 On-Peak	34212178	3052213	8.92%
Run4 On-Peak	110059396	10734916	9.75%
Run5 On-Peak	146063697	13914309	9.53%
Run6 On-Peak	80972090	7882512	9.73%
Total On-Peak	60691216	43262952	9.51%

Table 4.2: *$e^+e^- \to J/\psi c\bar{c} \to \ell^+\ell^- c\bar{c}$: Surviving events number in the preselection for $J/\psi \to \ell^+\ell^-$. "Before" means the number of events from the skim JpsiToll collections so before the ntuple production. "After" means the number of events after the preselection cuts.*

Run	Events before	Events after	Survival rate ϵ
Run1 Off-Peak	2385889	423895	17.77%
Run2 Off-Peak	6808557	1173851	17.24%
Run3 Off-Peak	2476919	420024	16.96%
Run4 Off-Peak	10530272	1932117	18.35%
Run5 Off-Peak	15076407	2672323	17.73%
Run6 Off-Peak	7579105	1381767	18.23%
Total Off-Peak	44857149	8003977	17.84%
Run1 On-Peak	19885315	3367703	16.94%
Run2 On-Peak	63526552	10598100	16.68%
Run3 On-Peak	34212178	5565828	16.27%
Run4 On-Peak	110059396	19903400	18.08%
Run5 On-Peak	146063697	25832520	17.69%
Run6 On-Peak	80972090	14604940	18.04%
Total On-Peak	454719228	79872491	17.57%

Table 4.3: $e^+e^- \to \psi(2S)c\bar{c} \to \ell^+\ell^- c\bar{c}$: *Surviving events number in the preselection for* $\psi(2S) \to \ell^+\ell^-$. *"Before" means the number of events from the skim JpsiToll collections so before the ntuple production. "After" means the number of events after the preselection cuts.*

Run	Events before	Events after	Survival rate ϵ
Run1 Off-Peak	2385889	1819	0.08%
Run2 Off-Peak	6808557	5743	0.08%
Run3 Off-Peak	2476919	2087	0.08%
Run4 Off-Peak	10530272	7874	0.07%
Run5 Off-Peak	15076407	10640	0.07%
Run6 Off-Peak	7579105	4116	0.05%
Total Off-Peak	44857149	32279	0.07%
Run1 On-Peak	19885315	52211	0.26%
Run2 On-Peak	63526552	164814	0.26%
Run3 On-Peak	34212178	87533	0.26%
Run4 On-Peak	110059396	258538	0.23%
Run5 On-Peak	146063697	329300	0.23%
Run6 On-Peak	80972090	166771	0.21%
Total On-Peak	454719228	1059167	0.23%

Table 4.4: $e^+e^- \to \psi(2S)c\bar{c} \to J/\psi\pi^+\pi^-c\bar{c}$: *Surviving events number in the preselection for* $\psi(2S) \to J/\psi\pi^+\pi^-$. *"Before" means the number of events from the skim JpsiToll collections so before the ntuple production. "After" means the number of events after the preselection cuts.*

4.3 Event selection for $e^+e^- \to J/\psi c\bar{c} \to \ell^+\ell^- c\bar{c}$

4.3.1 Calculation of $N_{S_{exp}}$ and $N_{B_{exp}}$

The selection strategy is aimed to maximized the figure of merit $N_S/\sqrt{N_S + N_B}$ where N_S and N_B are the number of signal and background events, respectively. In the next paragraph we will explain how $N_{S_{exp}}$ and $N_{B_{exp}}$ are computed.
$N_{S_{exp}}$ is the number of events that contain a true J/ψ: events where a J/ψ is actually well reconstructed and corresponding to the system against which another charmonium state recoils. $N_{B_{exp}}$ is the number of events with a fake J/ψ (i.e QED events).
The optimization process is performed evaluating the number of signal events in the mass distribution of the state recoiling against J/ψ. We perform this calculation for $J/\psi \to e^+e^-$ and for $J/\psi \to \mu^+\mu^-$ and for each recoil charmonium resonances (η_c, $\eta_c(2S)$, χ_{c0} and $X(3940)$).

$\mathbf{N}_{S_{exp}}$:

The expected number of signal events includes those events that are below the peak of the $c\bar{c}$ state recoiling against J/ψ, in the range of the the signal window, that identifies a J/ψ candidate:

- -0.050 GeV/c^2 $< m(e^+e^-) - M_{J/\psi} < 0.030$ GeV/c^2
- -0.030 GeV/c^2 $< m(\mu^+\mu^-) - M_{J/\psi} < 0.030$ GeV/c^2

It is calculated using the following formula:

$$N_{S_{exp}} = \sigma(e^+e^- \to J/\psi c\bar{c}) \cdot B(c\bar{c} \to > 2charged) \cdot L \cdot \epsilon_{sel} \cdot B(J/\psi \to \ell^+\ell^-)$$

where

- $\sigma(e^+e^- \to J/\psi c\bar{c}) \cdot B(c\bar{c} \to > 2charged)$ is the product of the *BABAR* double

charmonium production cross section (the Belle one for the X(3940) [35]) times the branching fraction for final states with more than two charged tracks [21];

- L=476 fb^{-1} is the integrated luminosity;
- ϵ_{sel} is the selection efficiency calculated on the signal MC in the previous *BABAR* analysis [21];
- $B(J/\psi \to \ell^+\ell^-)$ is the branching ratio for the J/ψ to e^+e^- or $\mu^+\mu^-$ from PDG [4], whose value is:

$$B(J/\psi \to \ell^+\ell^-) = \begin{cases} (5.94 \pm 0.06)\% & for \quad J/\psi \to e^+e^- \\ (5.93 \pm 0.06)\% & for \quad J/\psi \to \mu^+\mu^- \end{cases}$$

In Tab. 4.5 are reported all the values of the above parameters for each resonance in the recoil system.
It is necessary to specify that, for the X(3940) selection efficiency, no previous references are available, neither from *BABAR* nor from Belle. For this reason, when we evaluate $N_{S_{exp}}$ for the recoil state X(3940) we use a reconstructed efficiency estimated in this analysis.

$\mathbf{N}_{B_{exp}}$:

The number of expected background events is the number of events in the J/ψ sidebands mass distribution, defined in Eq. 4.2, Eq. 4.3.

4.3.2 $\psi(2S)$ veto

Lepton pairs with masses within ranges -0.050 GeV/c^2 $< M_{e^+e^-} - M_{J/\psi} <$ 0.030 GeV/c^2 for e^+e^- and -0.030 GeV/c^2 $< M_{\mu^+\mu^-} - M_{J/\psi} <$ 0.030 GeV/c^2 for $\mu^+\mu^-$ are referred to as J/ψ candidates on the signal MC in the following sections.
Since we obtain very similar values for η_c, χ_{c0}, $\eta_c(2S)$ and X(3940), we decide to choose one single cut for electrons and muons for all the recoil resonances.

$J/\psi \to e^+e^-$			
Recoil system	$\sigma \cdot B(c\bar{c} \to 2ch)(fb)$	$\epsilon_{sel}(e^+e^-)$	$N_{S_{exp}}(e^+e^-)$
$\eta(1S)$	$17.6 \pm 2.8^{+2.5}_{-2.1}$	$(30.8 \pm 1.0)\%$	153 ± 31
χ_{c0}	$10.3 \pm 2.5^{+1.4}_{-1.8}$	$(33.9 \pm 1.1)\%$	99 ± 28
$\eta_c(2S)$	$16.4 \pm 3.7^{+2.4}_{-3.0}$	$(32.5 \pm 1.2)\%$	151 ± 41
X(3940)	$10.6 \pm 2.5 \pm 2.4$	$(24.2 \pm 0.2)\%$	73 ± 18
$J/\psi \to \mu^+\mu^-$			
Recoil system	$\sigma \cdot B(c\bar{c} \to 2ch)(fb)$	$\epsilon_{sel}(\mu^+\mu^-)$	$N_{S_{exp}}(\mu^+\mu^-)$
$\eta(1S)$	$17.6 \pm 2.8^{+2.5}_{-2.1}$	$(28.2 \pm 0.9)\%$	140 ± 28
χ_{c0}	$10.3 \pm 2.5^{+1.4}_{-1.8}$	$(30.4 \pm 0.9)\%$	88 ± 25
$\eta_c(2S)$	$16.4 \pm 3.7^{+2.4}_{-3.0}$	$(27.9 \pm 1.0)\%$	129 ± 35
X(3940)	$10.6 \pm 2.5 \pm 2.4$	$(34.4 \pm 0.2)\%$	103 ± 26

Table 4.5: *$e^+e^- \to J/\psi c\bar{c} \to \ell^+\ell^- c\bar{c}$: Summary of the double charmonium production cross section, the selection efficiency and the expected signal events for each recoil resonance, both in electronic and muonic channel. Note that, for X(3940), the cross section value is from Belle because BABAR has never confirmed this state.*

In order to suppress the QED background due to the initial state radiation process of the $\psi(2S)$, we require no J/ψ candidate satisfing:

$$|m(\ell^+\ell^-\pi^+\pi^-) - M_{\psi(2S)}| < 15 \text{ MeV/c}^2$$

4.3.3 Number of charged tracks

The plot in Fig. 4.4 shows the distribution of the number of charged tracks (NTRK) in the signal MC and in the J/ψ sidebands, for both electronic and muonic decays of the J/ψ.
To remove background events, in the electronic and muonic decay channels, we select events with at least 5 charged tracks. Some signal events have NTRK=3 and NTRK=4, but the J/ψ mass peak for NTRK=3 and NTRK=4 have a signal-background ratio too poor to be included in the final signal sample, so the final decision is $NTRK > 4$.

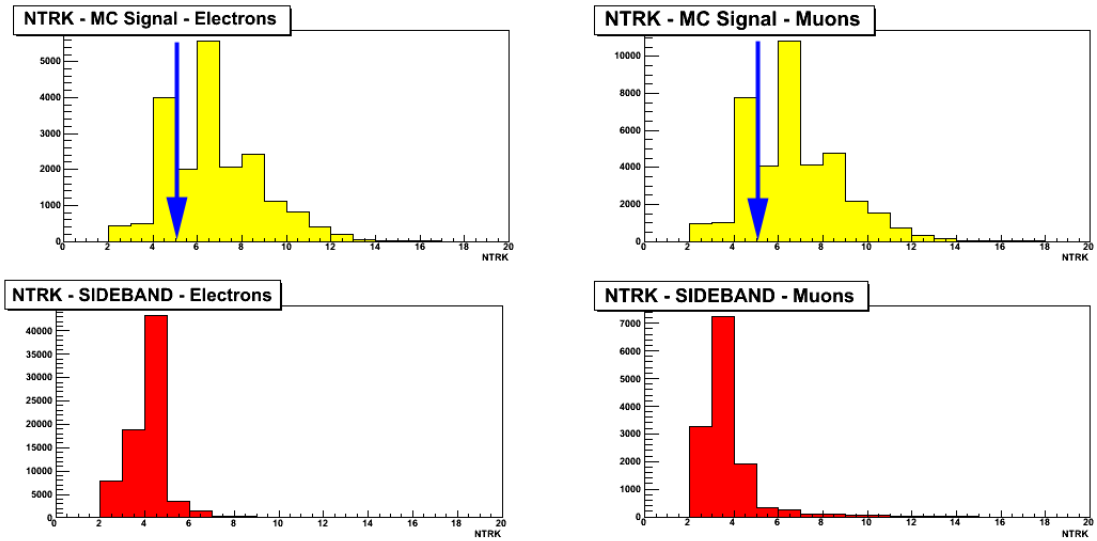

Figure 4.4: *$e^+e^- \to J/\psi c\bar{c} \to \ell^+\ell^- c\bar{c}$: NTRK distribution after all the other selection criteria in the signal MC (yellow) and in the J/ψ sidebands (red), for electrons and muons. The MC events are truth matched.*

4.3.4 Momentum of the J/ψ in the CM frame

We also studied the J/ψ momentum in the CM frame named $p^*_{J/\psi}$, whose distribution are shown in Fig. 4.5.

The events populating the low momentum region $p^* < 3$ GeV/c, equivalent to a recoil mass against the $J/\psi > 5.5$ GeV/c^2, are dominated by B decays (See Fig. 4.6 (a)).

The events populating the high momentum region $p^* > 4.5$ GeV/c that is equivalent to < 2.5 GeV/c^2 of recoil mass are due to the initial state radiation interaction (i.e. $e^+e^- \to \gamma J/\psi$) (See Fig. 4.6 (b)).

In order to remove B decays and ISR events we require:

$$3 \text{ GeV/c} < p^*_{J/\psi} < 4.5 \text{ GeV/c}$$

for both electronic and muonic decay channels.

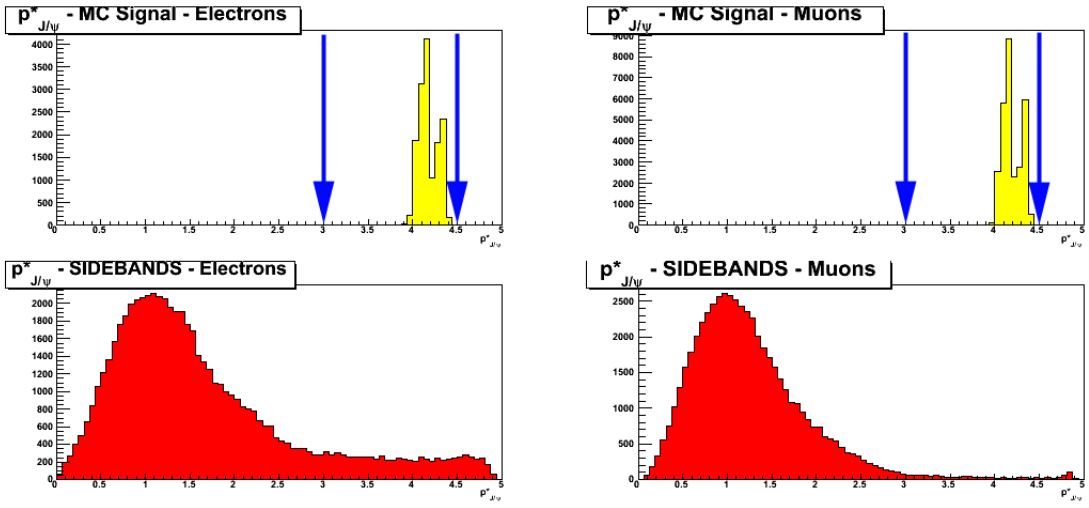

Figure 4.5: $e^+e^- \to J/\psi c\bar{c} \to \ell^+\ell^- c\bar{c}$: $p^*_{J/\psi}$ *distribution after all the other selection criteria in the signal MC (yellow) and in the* J/ψ *sidebands (red), for electrons and muons. The MC events are truth matched.*

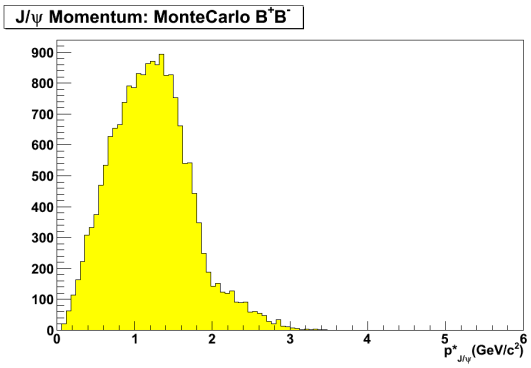

(a) Distribution of $p^*_{J/\psi}$ for Monte Carlo B^+B^-

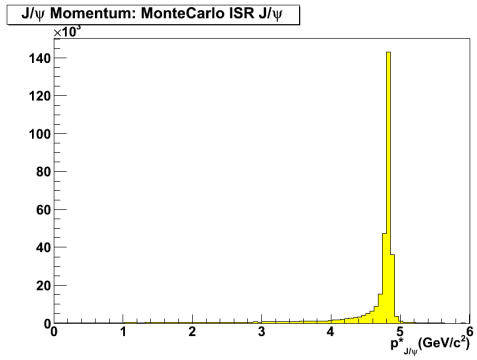

(b) ISR J/ψ Monte Carlo distribution for $p^*_{J/\psi}$

Figure 4.6: $e^+e^- \to J/\psi c\bar{c} \to \ell^+\ell^- c\bar{c}$: $p^*_{J/\psi}$ *distribution for different background contribution: B meson background and ISR* J/ψ *background*

4.3.5 J/ψ helicity angle

In order to further suppress the background due to radiative QED processes, we studied the J/ψ helicity angle. The helicity angle of the J/ψ decay is the angle between the lepton momentum direction in the J/ψ rest frame and the J/ψ momentum direction in the center of mass frame.
Fig 4.7 shows the distribution of the cosine of the J/ψ helicity in the signal MC and in the J/ψ sidebands, for both electronic and muonic decays of the J/ψ, whereas in Fig. 4.8 we show the J/ψ helicity distribution evaluated from Monte Carlo for various background sources. From the optimization we obtain:

$$-0.8 < cosH_{J/\psi} < 0.8$$

for both electronic and muonic decay channels.

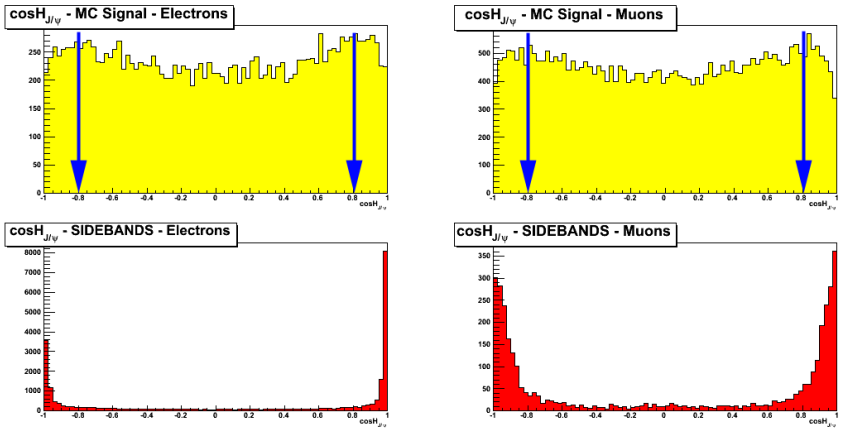

Figure 4.7: $e^+e^- \to J/\psi c\bar{c} \to \ell^+\ell^- c\bar{c}$: *Cosine of the J/ψ helicity distribution after all the other cuts in the signal MC (yellow) and in the J/ψ sidebands (red) for electrons and muons. The MC events are truth matched.*

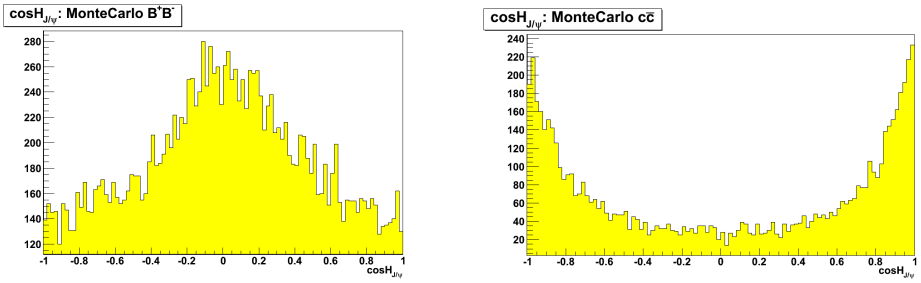

(a) Background contribution in the J/ψ helicity distribution from Monte Carlo B^+B^-

(b) Background contribution in the J/ψ helicity distribution from Monte Carlo $c\bar{c}$

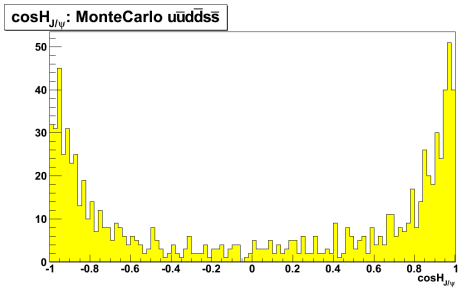

(c) Background contribution in the J/ψ helicity distribution from Monte Carlo $u\bar{u}d\bar{d}s\bar{s}$

Figure 4.8: $e^+e^- \to J/\psi c\bar{c} \to \ell^+\ell^- c\bar{c}$: *Monte Carlo distribution of J/ψ helicity angle for different background contributions (B decays, $c\bar{c}$ events, $u\bar{u}d\bar{d}s\bar{s}$ events).*

4.3.6 Maximum photon energy in the CM system

Most QED events from radiative Bhabha, radiative di-muon or ISR J/ψ have an energetic photon in the final state. In order to suppress these background contributions, we studied the variable E^*_γ, the maximum photon energy in the CM system. In Fig. 4.9 we show the distribution of E^*_γ in the signal MC and in the J/ψ sidebands, for both electronic and muonic decays of the J/ψ.
We select events with:

$$E^*_\gamma < 3.5 \text{ GeV}$$

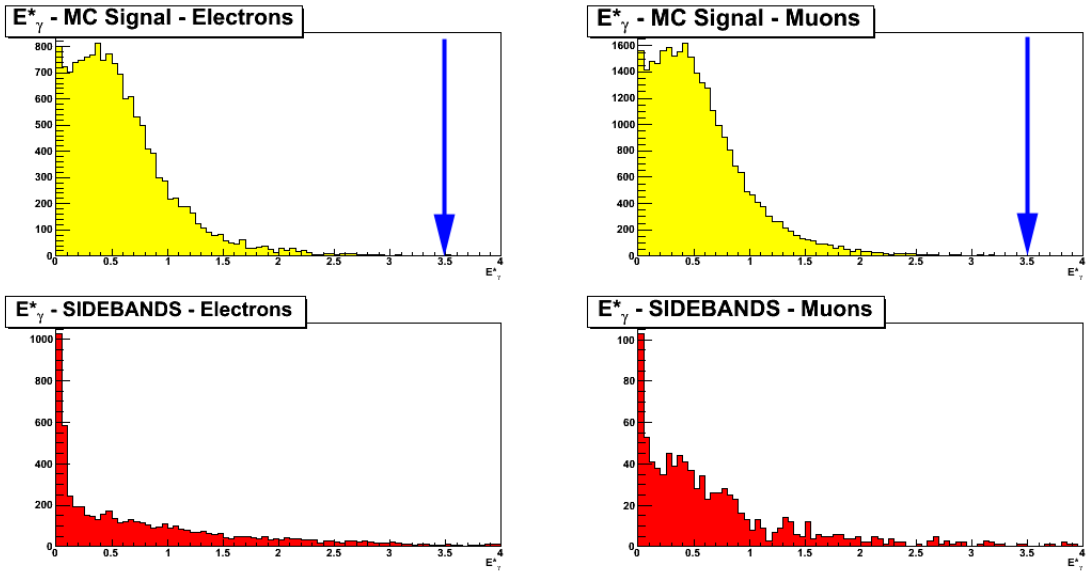

Figure 4.9: $e^+e^- \to J/\psi c\bar{c} \to \ell^+\ell^- c\bar{c}$: *$E^*_\gamma$ distribution after all the other selection criteria in the signal MC (yellow) and in the J/ψ sidebands (red) for electrons and muons. The MC events are truth matched.*

4.3.7 $cos\theta_{J/\psi}$ in the CM system

In order to suppress the ISR background we studied the $cos\theta_{J/\psi}$ in the CM system. This variable is the cosine of the angle between the J/ψ momentum and the z coordinate (beam direction) in the center of mass frame.
Fig. 4.10 shows the distribution of the $cos\theta_{J/\psi}$ in the CM frame in the signal MC and in the J/ψ sidebands, for both electronic and muonic decays of the J/ψ.
From the optimization performed on this variable we obtain the following cut:

$$\text{-0.8}< cos\theta^*_{J/\psi} < 0.8 \text{ for } J/\psi \to e^+e^-$$
$$\text{-0.9}< cos\theta^*_{J/\psi} < 0.9 \text{ for } J/\psi \to \mu^+\mu^-$$

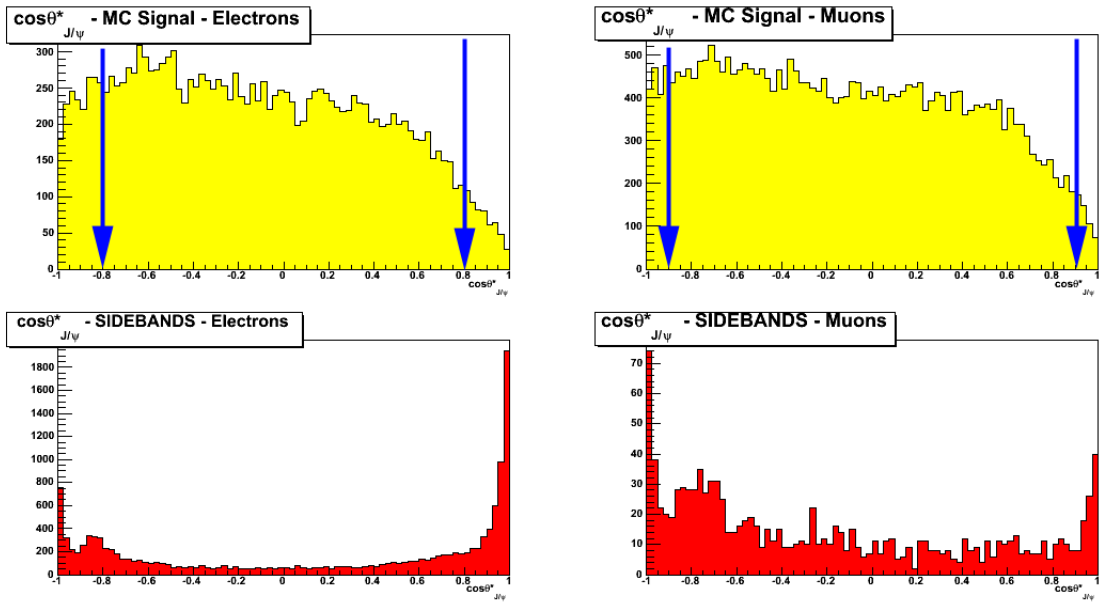

Figure 4.10: $e^+e^- \to J/\psi c\bar{c} \to \ell^+\ell^- c\bar{c}$: $cos\theta^*_{J/\psi}$ *distribution after all the other selection criteria in the signal MC (yellow) and in the* J/ψ *sidebands (red) for electrons and muons. The MC events are truth matched.*

4.3.8 Summary of the selection criteria

The final selection criteria are summarized in Table 4.6. The MC efficiency and

	$J/\psi \to e^+e^-$	$J/\psi \to \mu^+\mu^-$
Lepton PID	both are eLHBremLH	both are muBDTVeryLoose
J/ψ Candidate	[-50, +30] MeV/c^2	[-30, +30] MeV/c^2
Number of charged Tracks	> 4	
$p^*_{J/\psi}$	[3, 4.5] GeV/c^2	
$cosH_{J/\psi}$	$[-0.8, 0.8]$	
E^*_γ	< 3.5 GeV	
$cos\theta^*_{J/\psi}$	$[-0.8, 0.8]$	$[-0.9, 0.9]$
$\psi(2S)$ veto	$\lvert m(\ell^+\ell^-\pi^+\pi^-) - M_{\psi(2S)}\rvert < 15$ MeV/c^2	

Table 4.6: *The final selection criteria for* $e^+e^- \to J/\psi c\bar{c} \to \ell^+\ell^- c\bar{c}$.

the survival rate in the full data sample after each cut, for e^+e^- and $\mu^+\mu^-$ are listed in Tab. 4.7 and Tab. 4.8. The values for MC signal are referred to the channel $e^+e^- \to J/\psi\eta_c, \chi_{c0}, \eta_c(2S)$.

The MC efficiencies for the recoil resonances X(3940) are reported in Tab. 4.9.

The distributions of the variables studied during the selection optimization are reported, for the full data sample, in Fig. 4.11 and Fig. 4.12 for the electronic and the muonic channels respectively. All the variables are plotted after all the selection criteria have been applied.

Fig. 4.13 shows the J/ψ mass distribution in the signal MC (yellow) and in the full data sample (green), before the selection criteria for e^+e^- and $\mu^+\mu^-$ samples; in Fig. 4.14 the same distributions after all the selection criteria.

A comparison between Fig. 4.13 and Fig. 4.14 shows the much improved signal-to-noise ratio in the data after all selection cuts have been applied.

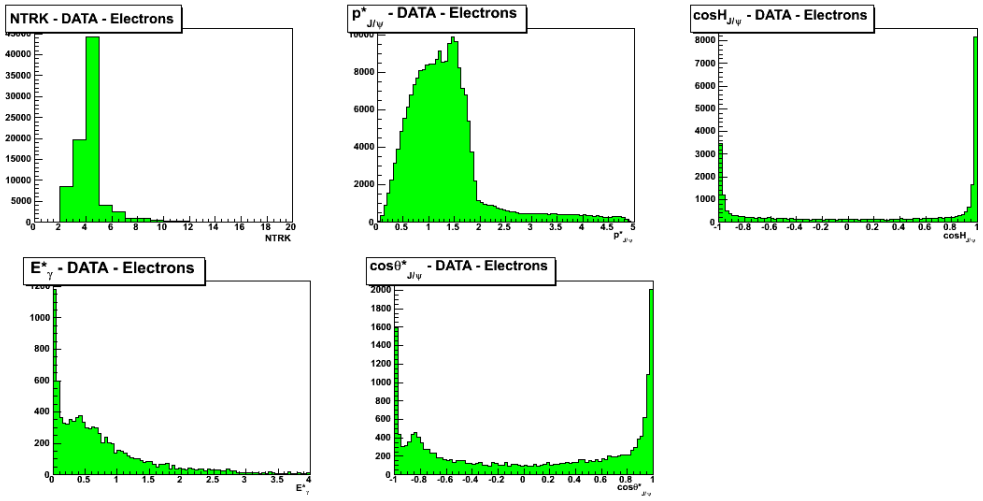

Figure 4.11: $e^+e^- \to J/\psi c\bar{c} \to \ell^+\ell^- c\bar{c}$: *Distribution for NTRK, the* J/ψ *momentum* ($p^*_{J/\psi}$), *the* J/ψ *helicity angle, the maximum photon energy* (E^*_γ) *and* $cos\theta_{J/\psi}$ *for the full data sample, for* $J/\psi \to e^+e^-$. *All the selection criteria have been applied.*

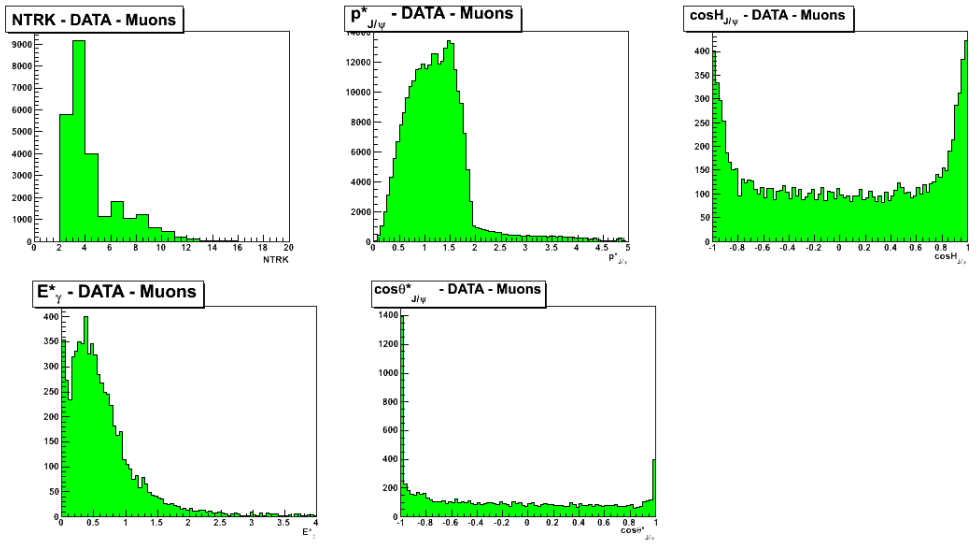

Figure 4.12: $e^+e^- \to J/\psi c\bar{c} \to \ell^+\ell^- c\bar{c}$: *Distribution for NTRK, the* J/ψ *momentum* ($p^*_{J/\psi}$), *the* J/ψ *helicity angle, the maximum photon energy* (E^*_γ) *and* $cos\theta_{J/\psi}$ *for the full data sample, for* $J/\psi \to \mu^+\mu^-$. *All the selection criteria have been applied.*

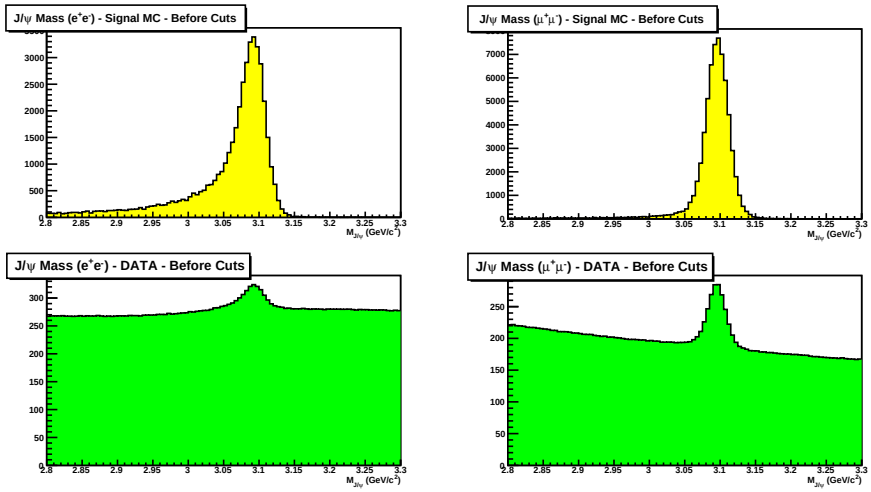

Figure 4.13: $e^+e^- \to J/\psi c\bar{c} \to \ell^+\ell^- c\bar{c}$: *Distribution of the* J/ψ *mass before the selection criteria in the signal MC (yellow) and in the full data sample (green): in* e^+e^- *decay on the left and* $\mu^+\mu^-$ *decay on the right. The MC events are truth matched.*

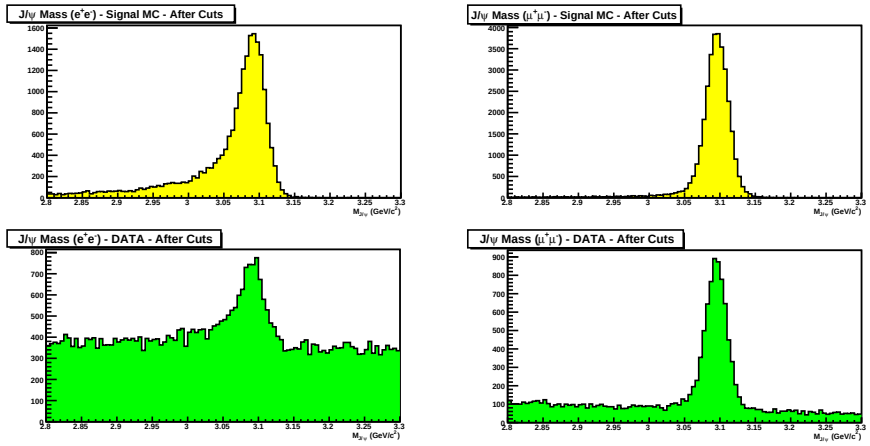

Figure 4.14: $e^+e^- \to J/\psi c\bar{c} \to \ell^+\ell^- c\bar{c}$: *Distribution of the* J/ψ *mass after the selection criteria in the signal MC (yellow) and in the full data sample (green): in* e^+e^- *decay on the left and* $\mu^+\mu^-$ *decay on the right. The MC events are truth matched.*

	$J/\psi \to e^+e^-$			
Cut	Signal MC	Efficiency ϵ_{sig}	Data	Survival rate ϵ_{data}
Generated	108000	100%	249788188	-
Preselection	60989	56.47%	27877860	100%
J/ψ candidate	42887	39.71%	4224486	15.15%
NTRK	31612	29.27%	545113	1.96%
$p^*_{J/\psi}$	31600	29.26%	64915	0.23%
$cosH_{J/\psi}$	25202	23.34%	22437	0.08%
E^*_γ	25159	23.33%	21622	0.07%
$cos\theta^*_{J/\psi}$	21288	19.71%	10547	0.04%
$\lvert m(\ell^+\ell^-\pi^+\pi^-) - M_{\psi(2S)}\rvert$	20027	18.54%	9406	0.03%

Table 4.7: *$e^+e^- \to J/\psi c\bar{c} \to \ell^+\ell^- c\bar{c}$: Surviving events after each selection criteria in both signal MC and full data sample for the process $e^+e^- \to J/\psi\eta_c, \chi_{c0}, \eta_c(2S)$. The MC efficiencies and the data survival rates are listed for electronic J/ψ decay.*

	$J/\psi \to \mu^+\mu^-$			
Cut	Signal MC	Efficiency ϵ_{sig}	Data	Survival rate ϵ_{data}
Generated	108000	100%	249788188	-
Preselection	66313	61.40%	19818660	100%
J/ψ candidate	56760	52.56%	2855333	14.41%
NTRK	41735	38.64%	440311	2.22%
$p^*_{J/\psi}$	41658	38.57%	17294	0.09%
$cosH_{J/\psi}$	33072	30.62%	12265	0.06%
E^*_γ	33048	30.60%	11702	0.06%
$cos\theta^*_{J/\psi}$	30644	28.37%	7857	0.04%
$\lvert m(\ell^+\ell^-\pi^+\pi^-) - M_{\psi(2S)}\rvert$	28803	26.67%	6658	0.03%

Table 4.8: *$e^+e^- \to J/\psi c\bar{c} \to \ell^+\ell^- c\bar{c}$: Surviving events after each selection criteria in both signal MC and full data sample for the process $e^+e^- \to J/\psi\eta_c, \chi_{c0}, \eta_c(2S)$. The MC efficiencies and the data survival rates are listed for muonic J/ψ decay.*

	$J/\psi \to e^+e^-$		$J/\psi \to \mu^+\mu^-$	
Cut	Signal MC	Efficiency ϵ_{sig}	Signal MC	Efficiency ϵ_{sig}
Generated	108000	100%	108000	100%
Preselection	61425	56.88%	66411	61.49%
J/ψ candidate	43553	40.33%	56968	52.75%
NTRK	38559	35.70%	50618	46.87%
$p^*_{J/\psi}$	38538	35.68%	50507	46.77%
$cosH_{J/\psi}$	31938	29.57%	42144	39.02%
E^*_γ	31916	29.55%	42124	39.00%
$cos\theta^*_{J/\psi}$	27716	25.66%	39432	36.51%
$\lvert m(\ell^+\ell^-\pi^+\pi^-) - M_{\psi(2S)}\rvert$	26223	24.28%	37294	34.53%

Table 4.9: $e^+e^- \to J/\psi c\bar{c} \to \ell^+\ell^- c\bar{c}$*: Surviving events number each selection criteria in signal MC for the process* $e^+e^- \to J/\psi X(3940)$*. The MC efficiencies are listed for both electronic and muonic* J/ψ *decays.*

4.4 Event selection for $e^+e^- \to \psi(2S)c\bar{c} \to \ell^+\ell^- c\bar{c}$

4.4.1 Calculation of $N_{S_{exp}}$ and $N_{B_{exp}}$

The selection strategy is aimed to maximized the figure of merit $N_S/\sqrt{N_S + N_B}$ where N_S and N_B are the number of signal and background events, respectively. In the next paragraph we will explain how $N_{S_{exp}}$ and $N_{B_{exp}}$ have been computed.
$N_{S_{exp}}$ is the number of events that contains a true $\psi(2S)$: events where a $\psi(2S)$ is actually well reconstructed and corresponding to the system against which another charmonium state recoils. $N_{B_{exp}}$ is the number of events with a fake $\psi(2S)$ (i.e QED events).
The optimization process is performed evaluating the number of signal events in the mass distribution curve of the state recoiling against $\psi(2S)$. We perform this calculation for $\psi(2S) \to e^+e^-$ and for $\psi(2S) \to \mu^+\mu^-$ and for each recoil charmonium resonances (η_c, $\eta_c(2S)$, χ_{c0} and $X(3940)$).

$\mathbf{N}_{S_{exp}}$:

The expected number of signal events includes those events that are below the peak of the $c\bar{c}$ state recoiling against $\psi(2S)$, in the range of the the signal window, that identifies a $\psi(2S)$ candidate:

- -0.050 GeV/c$^2 < m(e^+e^-) - M_{\psi(2S)} < 0.030$ GeV/c^2
- -0.030 GeV/c$^2 < m(\mu^+\mu^-) - M_{\psi(2S)} < 0.030$ GeV/c^2

It is calculated using the following formula:

$$N_{S_{exp}} = \sigma(e^+e^- \to \psi(2S)c\bar{c}) \cdot B(c\bar{c} \to \geq 1 charged) \cdot L \cdot \epsilon_{sel} \cdot B(\psi(2S) \to \ell^+\ell^-)$$

where

- $\sigma(e^+e^- \to \psi(2S)c\bar{c}) \cdot B(c\bar{c} \to \geq 1 charged)$ is the product of the Belle double charmonium production cross section times the branching fraction for final states with more than zero charged tracks [38]; for the X(3940), we do not have any measurement, so we assume the $\sigma \cdot B(c\bar{c} \to 2ch)$ of the J/ψ analysis.
- L=476 fb^{-1} is the integrated luminosity;
- ϵ_{sel} is the selection efficiency calculated on the signal MC in this analysis;
- $B(\psi(2S) \to \ell^+\ell^-)$ is the branching ratio for the $\psi(2S)$ going to e^+e^- or $\mu^+\mu^-$ from PDG [4], whose value is:

$$B(\psi(2S) \to \ell^+\ell^-) = \begin{cases} (7.72 \pm 0.17) \cdot 10^{-3} & for \quad \psi(2S) \to e^+e^- \\ (7.7 \pm 0.8) \cdot 10^{-3} & for \quad \psi(2S) \to \mu^+\mu^- \end{cases}$$

In Tab. 4.15 are reported all the values of above parameters for each resonance in the recoil system.
We evaluate $N_{S_{exp}}$ using the efficiency reconstructed in this analysis.

$\mathbf{N}_{B_{exp}}$:
The number of expected background events is the number of events in the $\psi(2S)$ sidebands mass distribution, defined in Eq. 4.4, Eq. 4.5.

4.4.2 J/ψ veto

Lepton pairs with masses within ranges -0.050 GeV/c^2 $< M_{e^+e^-} - M_{\psi(2S)} <$ 0.030 GeV/c^2 for e^+e^- and -0.030 GeV/c^2 $< M_{e^+e^-} - M_{\psi(2S)} <$ 0.030 GeV/c^2 for $\mu^+\mu^-$ are referred as $\psi(2S)$ candidates on the signal MC in the following sections.
Since we obtain very similar values for η_c, χ_{c0}, $\eta_c(2S)$ and X(3940), we decide to choose one single cut for electrons and muons for all the recoil resonances.
In order to suppress the QED background due to the initial state radiation process of the J/ψ, we require that no J/ψ candidate satisfy:

$$|m(\ell^+\ell^-) - M_{J/\psi}| < 20 \text{ MeV/c}^2$$

$\psi(2S) \to e^+e^-$			
Recoil system	$\sigma \cdot B(c\bar{c} \to 0ch)(fb)$	$\epsilon_{sel}(e^+e^-)$	$N_{S_{exp}}(e^+e^-)$
$\eta(1S)$	$16.3 \pm 4.6 \pm 3.9$	(12.16±0.19)%	7 ± 2
χ_{c0}	$12.5 \pm 3.8 \pm 3.1$	(16.32±0.24)%	7 ± 2
$\eta_c(2S)$	$16.0 \pm 5.1 \pm 3.8$	(11.32±0.21)%	7 ± 2
X(3940)	$10.6 \pm 2.5 \pm 2.4$	(20.83±0.14)%	8 ± 2
$\psi(2S) \to \mu^+\mu^-$			
Recoil system	$\sigma \cdot B(c\bar{c} \to 0ch)(fb)$	$\epsilon_{sel}(\mu^+\mu^-)$	$N_{S_{exp}}(\mu^+\mu^-)$
$\eta(1S)$	$16.3 \pm 4.6 \pm 3.9$	(20.06±0.24)%	12 ± 3
χ_{c0}	$12.5 \pm 3.8 \pm 3.1$	(25.19±0.28)%	12 ± 4
$\eta_c(2S)$	$16.0 \pm 5.1 \pm 3.8$	(18.52±0.26)%	11 ± 4
X(3940)	$10.6 \pm 2.5 \pm 2.4$	(30.99±0.16)%	12 ± 3

Table 4.10: $e^+e^- \to \psi(2S)c\bar{c} \to \ell^+\ell^- c\bar{c}$: *Summary of the double charmonium production cross section, the selection efficiency and the expected signal events for each recoil resonance, both in electronic and muonic channel. Note that, for X(3940), the cross section value is from $J/\psi \to \ell^+\ell^-$ because there are no previous measurement of the cross section.*

4.4.3 Number of charged tracks

The plot in Fig. 4.15 shows the distribution of the number of charged tracks (NTRK) in the signal MC and in the $\psi(2S)$ sidebands, for both electronic and muonic decays of the $\psi(2S)$.
To remove background events, in the electronic and muonic decay channels, we select events with at least 5 charged tracks. Some signal events have NTRK=3 and NTRK=4 but the $\psi(2S)$ mass peak for NTRK=3 and NTRK=4 have a signal-background ratio too poor to be included in the final signal sample, so the final decision is $NTRK > 4$.

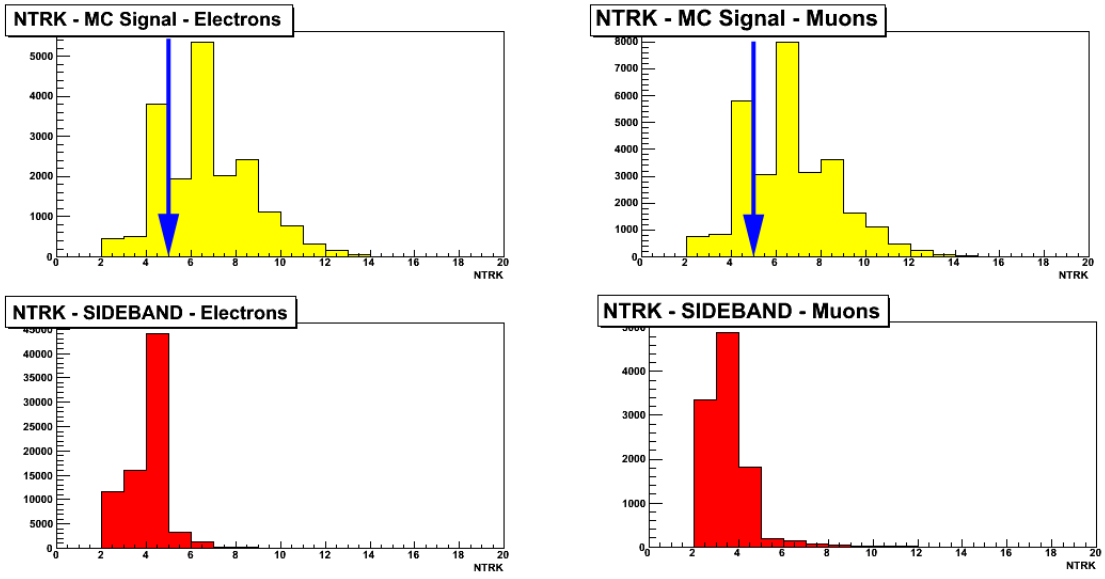

Figure 4.15: $e^+e^- \rightarrow \psi(2S)c\bar{c} \rightarrow \ell^+\ell^- c\bar{c}$: *NTRK distribution after all the other selection criteria in the signal MC (yellow) and in the $\psi(2S)$ sidebands (red), for electrons and muons. The MC events are truth matched.*

4.4.4 Momentum of the $\psi(2S)$ in the CM frame

We also studied the $\psi(2S)$ momentum in the CM frame named $p^*_{\psi(2S)}$, whose distribution are shown in Fig. 4.16.
The events populating the low momentum region $p^* < 3$ GeV/c, equivalent to a recoil mass against the $\psi(2S) > 5.5$ GeV/c^2, are dominated by B decays (see Fig. 4.17 (a)).
The events populating the high momentum region $p^* > 4.5$ GeV/c that is equivalent to < 2.5 GeV/c^2 of recoil mass are due to the initial state radiation interaction (i.e. $e^+e^- \to \gamma\psi(2S)$). (see Fig. 4.17 (b))
In order to remove these contributions we select events in the range:

$$3 \text{ GeV/c} < p^*_{\psi(2S)} < 4.5 \text{ GeV/c}$$

for both electronic and muonic decay channels.

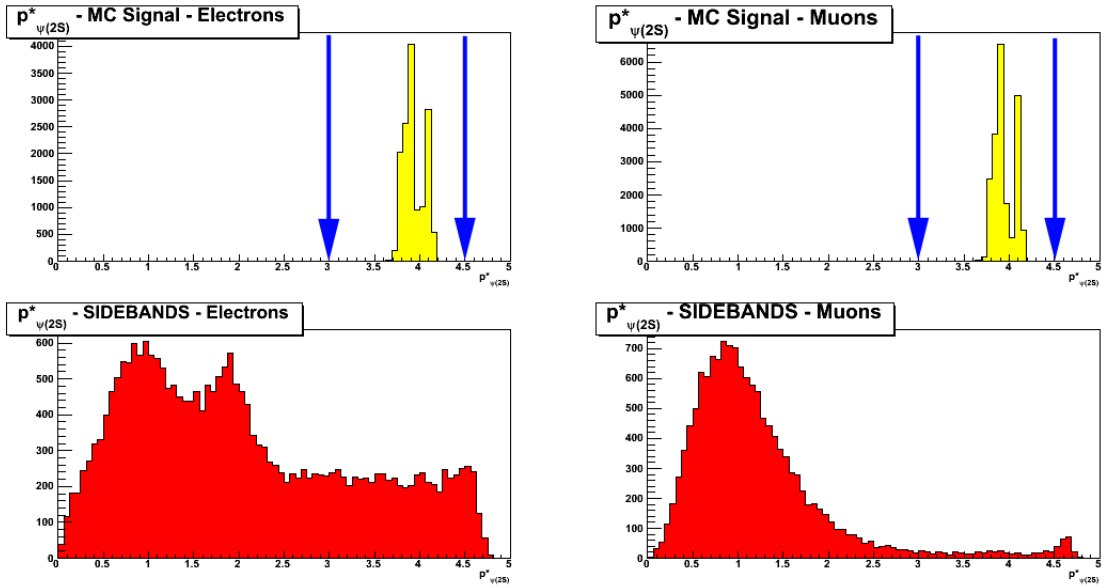

Figure 4.16: $e^+e^- \to \psi(2S)c\bar{c} \to \ell^+\ell^- c\bar{c}$: $p^*_{\psi(2S)}$ *distribution after all the other selection criteria in the signal MC (yellow) and in the* $\psi(2S)$ *sidebands (red), for electrons and muons. The MC events are truth matched.*

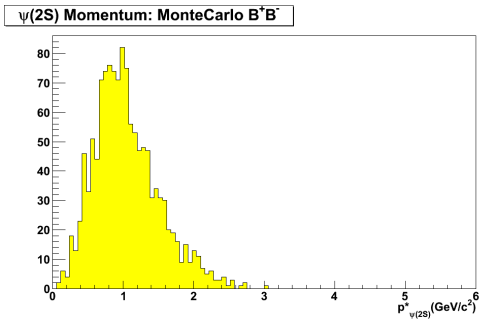

(a) Distribution of $p^*_{\psi(2S)}$ for Monte Carlo B^+B^-

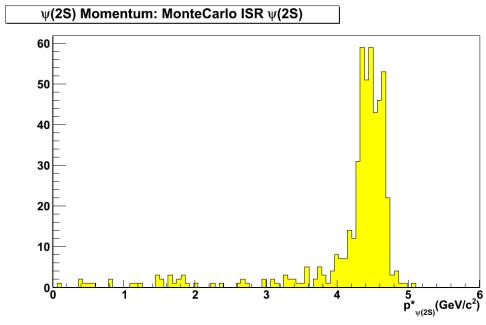

(b) ISR $\psi(2S)$ Monte Carlo distribution for $p^*_{\psi(2S)}$

Figure 4.17: $e^+e^- \to \psi(2S)c\bar{c} \to \ell^+\ell^- c\bar{c} : p^*_{\psi(2S)}$ *distribution for different background contribution: B meson background and ISR* J/ψ *background.*

4.4.5 $\psi(2S)$ helicity angle

In order to further suppress the background due to radiative QED processes, we also studied the $\psi(2S)$ helicity angle. The helicity angle of the $\psi(2S)$ decay is the angle between the lepton momentum direction in the $\psi(2S)$ rest frame and the $\psi(2S)$ momentum direction in the center of mass frame.
Fig 4.18 shows the distribution of the cosine of the $\psi(2S)$ helicity in the signal MC and in the $\psi(2S)$ sidebands, for both electronic and muonic decays of the $\psi(2S)$, whereas in Fig. 4.19 we show the $\psi(2S)$ helicity distribution evaluated from Monte Carlo for various background sources.
From the optimization we obtain:

$$-0.8 < cosH_{\psi(2S)} < 0.8$$

for both electronic and muonic decay channels.

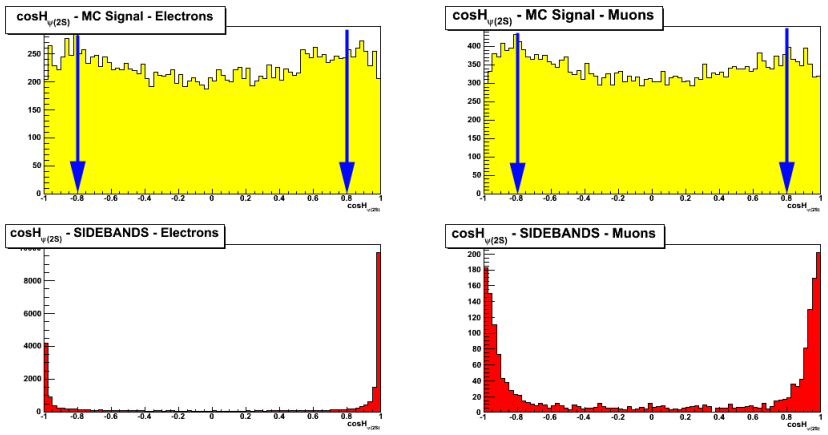

Figure 4.18: $e^+e^- \to \psi(2S)c\bar{c} \to \ell^+\ell^- c\bar{c}$: *$\psi(2S)$ helicity angle distribution after all the other selection criteria in the signal MC (yellow) and in the $\psi(2S)$ sidebands (red) for electrons and muons. The MC events are truth matched.*

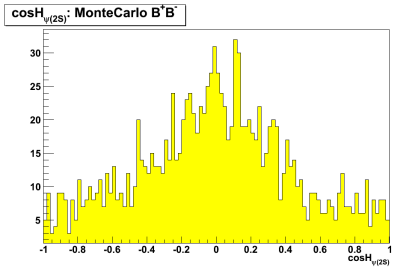

(a) Background contribution in the $\psi(2S)$ helicity distribution from Monte Carlo B^+B^-

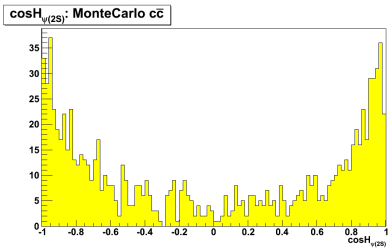

(b) Background contribution in the $\psi(2S)$ helicity distribution from Monte Carlo $c\bar{c}$

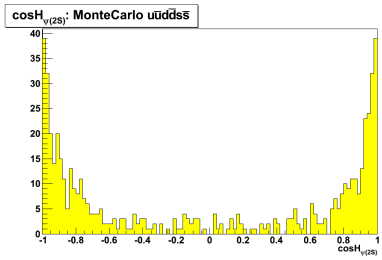

(c) Background contribution in the $\psi(2S)$ helicity distribution from Monte Carlo $u\bar{u}d\bar{d}s\bar{s}$

Figure 4.19: $e^+e^- \to \psi(2S)c\bar{c} \to \ell^+\ell^- c\bar{c}$: *Monte Carlo distribution of $\psi(2S)$ helicity angle for different background contributions (B decays, $c\bar{c}$ events, $u\bar{u}d\bar{d}s\bar{s}$ events).*

4.4.6 Maximum photon energy in the CM system

Most QED events from radiative Bhabha, radiative di-muon or ISR $\psi(2S)$ have an energetic photon in the final state. In order to suppress these background contributions, we studied the variable E^*_γ, the maximum photon energy in the CM system. In Fig. 4.20 we show the distribution of E^*_γ in the signal MC and in the $\psi(2S)$ sidebands, for both electronic and muonic decays of the $\psi(2S)$.
We select events with:

$$E^*_\gamma < 3.5 \text{ GeV}$$

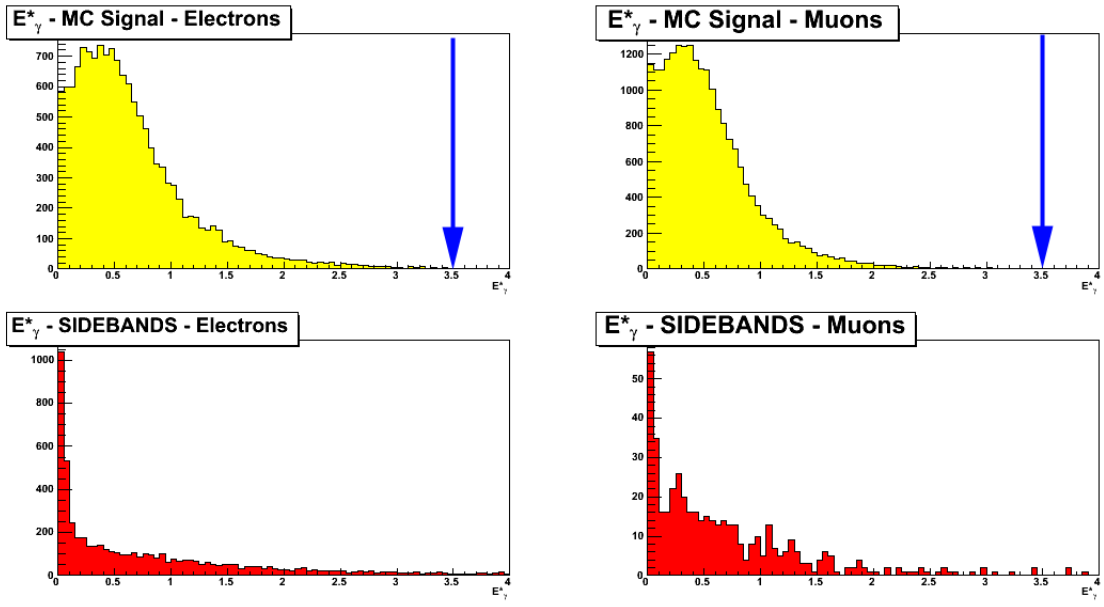

Figure 4.20: $e^+e^- \to \psi(2S)c\bar{c} \to \ell^+\ell^- c\bar{c}$: E^*_γ *distribution after all the selection criteria in the signal MC (yellow) and in the sidebands (red) for electrons and muons. The MC events are truth matched.*

4.4.7 $cos\theta_{\psi(2S)}$ in the CM system

In order to suppress the ISR background we studied the $cos\theta_{\psi(2S)}$ in the CM system. This variable is the cosine of the angle between the $\psi(2S)$ momentum and the z coordinate (beam direction) in the center of mass frame.
Fig. 4.21 shows the distribution of the $cos\theta_{\psi(2S)}$ in the CM frame in the signal MC and in the $\psi(2S)$ sidebands, for both electronic and muonic decays of the $\psi(2S)$. The optimization performed on this variable gives the following results:

$$\text{-0.8}< cos\theta^*_{\psi(2S)} < 0.8 \text{ for } \psi(2S) \to e^+e^-$$
$$\text{-0.9}< cos\theta^*_{\psi(2S)} < 0.9 \text{ for } \psi(2S) \to \mu^+\mu^-$$

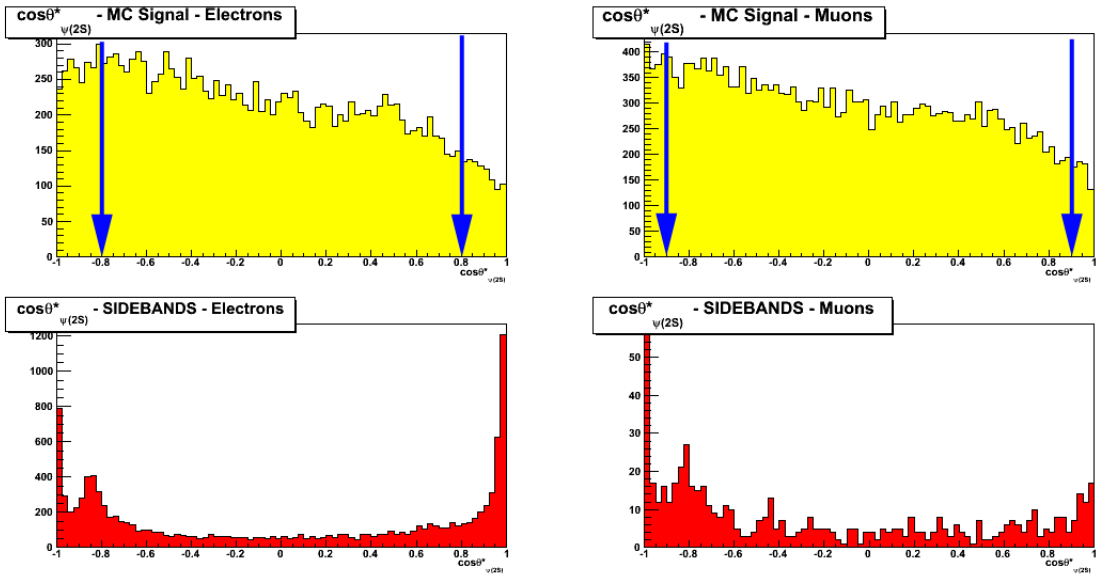

Figure 4.21: $e^+e^- \to \psi(2S)c\bar{c} \to \ell^+\ell^- c\bar{c}$: $cos\theta^*_{\psi(2S)}$ *distribution after all the other selection criteria in the signal MC (yellow) and in the* $\psi(2S)$ *sidebands (red) for electrons and muons. The MC events are truth matched.*

4.4.8 Summary of the selection criteria

The final selection criteria are summarized in Table 4.11.

	$\psi(2S) \to e^+e^-$	$\psi(2S) \to \mu^+\mu^-$
Lepton PID	both are eLHBremLH	both are muBDTVeryLoose
$\psi(2S)$ Candidate	[-50, +30] MeV/c^2	[-30, +30] MeV/c^2
Number of charged Tracks	> 4	
$p^*_{\psi(2S)}$	[3, 4.5] GeV/c^2	
$cosH_{\psi(2S)}$	$[-0.8, 0.8]$	
E^*_γ	< 3.5 GeV	
$cos\theta^*_{\psi(2S)}$	$[-0.8, 0.8]$	$[-0.9, 0.9]$
J/ψ veto	$\lvert m(\ell^+\ell^-) - M_{J/\psi}\rvert < 20$ MeV/c^2	

Table 4.11: *The final selection criteria for* $e^+e^- \to \psi(2S)c\bar{c} \to \ell^+\ell^- c\bar{c}$.

The MC efficiency and the survival rate in the full data sample after each cut, for e^+e^- and $\mu^+\mu^-$ are listed in Tab. 4.12 and Tab. 4.13. The values for MC signal are referred to the channel $e^+e^- \to \psi(2S)\eta_c, \chi_{c0}, \eta_c(2S)$.
The MC efficiencies for the recoil resonances X(3940) are reported in Tab. 4.14.
The distributions of the variables studied during the selection optimization are reported, for the full data sample, in Fig. 4.22 and Fig. 4.23 for the electronic and the muonic channel respectively. All the variables are plotted after all the other selection criteria have been applied.
Fig. 4.24 shows the $\psi(2S)$ mass distribution in the signal MC (yellow) and in the full data (green), before the selection procedure for e^+e^- and $\mu^+\mu^-$ samples; in Fig. 4.25 the same distributions after all the selection criteria.
The bottom left plot of Fig. 4.25 shows that the background for $\psi(2S) \to e^+e^-$ is huge and it is not removed after we applied the selection criteria. For $\psi(2S) \to \mu^+\mu^-$ (bottom right plot of Fig. 4.25) the background level is smaller than the $\psi(2S) \to e^+e^-$ but still pretty significant, compared to the J/ψ analysis.

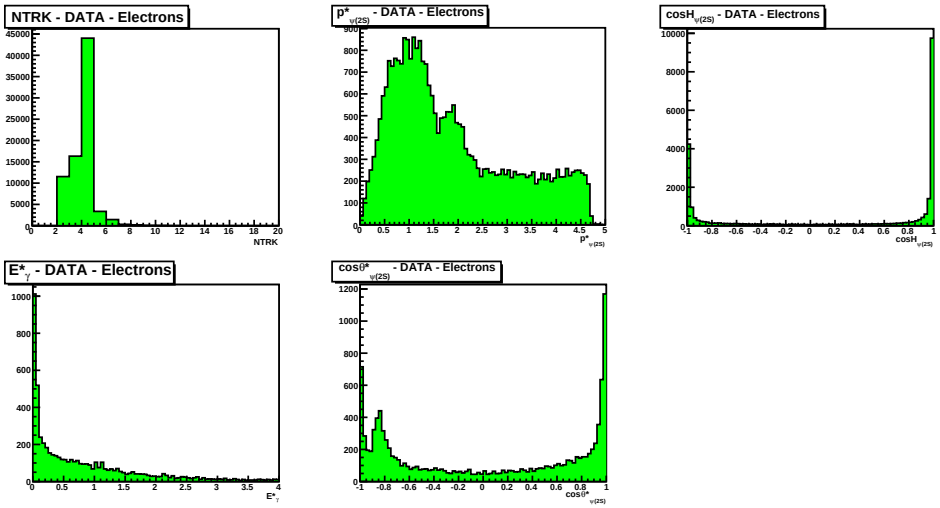

Figure 4.22: $e^+e^- \to \psi(2S)c\bar{c} \to \ell^+\ell^- c\bar{c}$: *Distribution for NTRK, the* $\psi(2S)$ *momentum* ($p^*_{\psi(2S)}$), *the* $\psi(2S)$ *helicity angle, the maximum photon energy* (E^*_γ) *and* $cos\theta_{\psi(2S)}$ *for the full data sample, for* $\psi(2S) \to e^+e^-$. *All the selection criteria have been applied.*

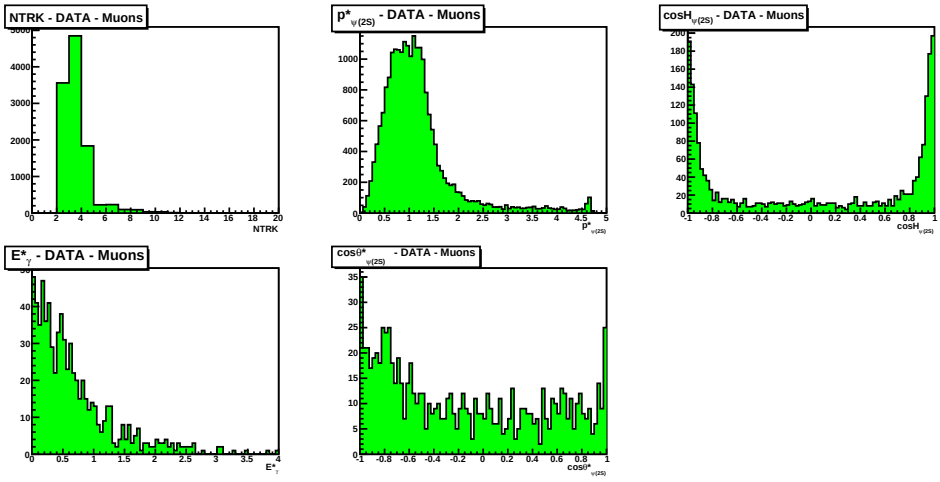

Figure 4.23: $e^+e^- \to \psi(2S)c\bar{c} \to \ell^+\ell^- c\bar{c}$: *Distribution for NTRK, the* $\psi(2S)$ *momentum* ($p^*_{\psi(2S)}$), *the* $\psi(2S)$ *helicity angle, the maximum photon energy* (E^*_γ) *and* $cos\theta_{\psi(2S)}$ *for the full data sample, for* $\psi(2S) \to \mu^+\mu^-$. *All the selection criteria have been applied.*

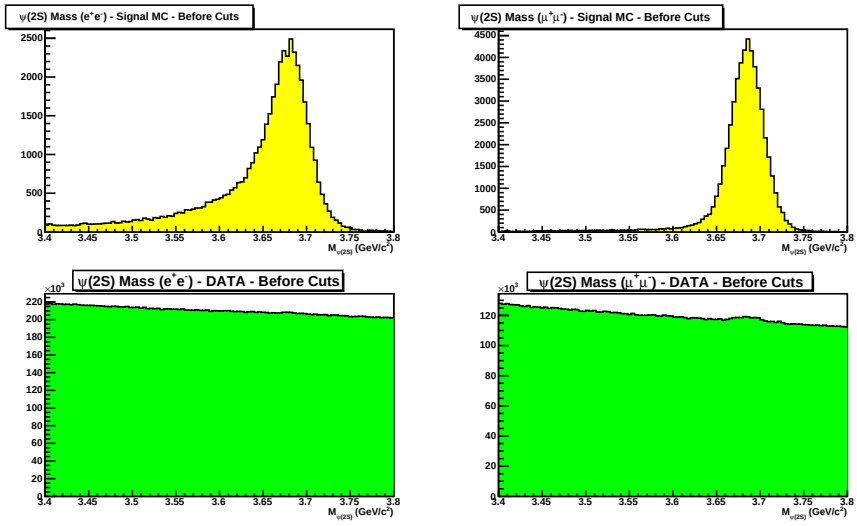

Figure 4.24: $e^+e^- \to \psi(2S)c\bar{c} \to \ell^+\ell^- c\bar{c}$: *Distribution of the* $\psi(2S)$ *mass before the selection criteria in the signal MC (yellow) and in the full data sample (green): in* e^+e^- *decay on the left and* $\mu^+\mu^-$ *decay on the right. The MC events are truth matched.*

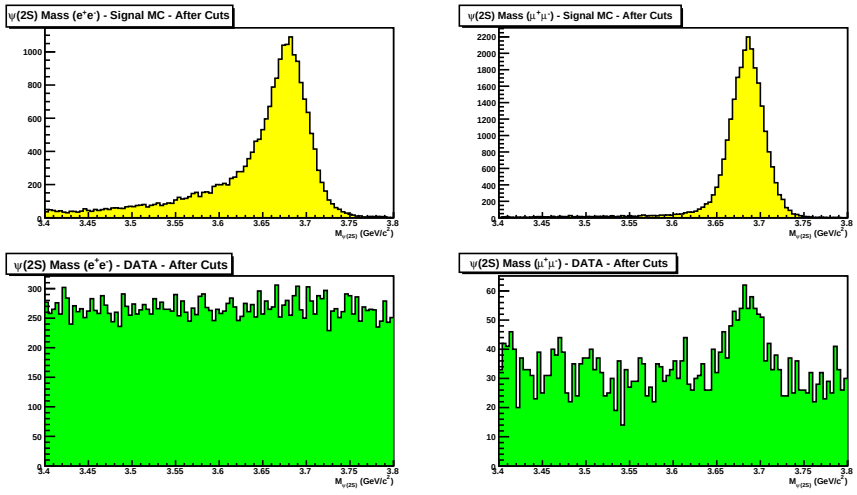

Figure 4.25: $e^+e^- \to \psi(2S)c\bar{c} \to \ell^+\ell^- c\bar{c}$: *Distribution of the* $\psi(2S)$ *mass after the selection criteria in the signal MC (yellow) and in the full data sample (green): in* e^+e^- *decay on the left and* $\mu^+\mu^-$ *decay on the right. The MC events are truth matched.*

	$\psi(2S) \to e^+e^-$			
Cut	Signal MC	Efficiency ϵ_{sig}	Data	Survival rate ϵ_{data}
Generated	108000	100%	249788188	-
Preselection	49238	45.59%	26015490	100%
$\psi(2S)$ candidate	32556	30.14%	4150215	15.95%
NTRK	24017	22.24%	223864	0.86%
$p^*_{\psi(2S)}$	24008	22.23%	64362	0.25%
$cosH_{\psi(2S)}$	19020	17.61%	13171	0.05%
E^*_γ	18999	17.59%	12705	0.05%
$cos\theta^*_{\psi(2S)}$	15578	14.42%	6082	0.02%
$\lvert m(\ell^+\ell^-) - M_{J/\psi}\rvert$	14311	13.25%	5488	0.02%

Table 4.12: $e^+e^- \to \psi(2S)c\bar{c} \to \ell^+\ell^- c\bar{c}$: *Surviving events after each selection criteria in both signal MC and full data sample for the process* $e^+e^- \to \psi(2S)\eta_c, \chi_{c0}, \eta_c(2S)$. *The MC efficiencies and the data survival rates are listed for electronic* $\psi(2S)$ *decay.*

	$\psi(2S) \to \mu^+\mu^-$			
Cut	Signal MC	Efficiency ϵ_{sig}	Data	Survival rate ϵ_{data}
Generated	108000	100%	249788188	-
Preselection	54015	50.01%	14735660	100%
$\psi(2S)$ candidate	44132	40.86%	1767022	11.99%
NTRK	32486	30.08%	41247	0.28%
$p^*_{\psi(2S)}$	32447	30.04%	2625	0.02%
$cosH_{\psi(2S)}$	25736	23.83%	982	0.007%
E^*_γ	25723	23.82%	969	0.007%
$cos\theta^*_{\psi(2S)}$	23331	21.60%	803	0.005%
$\lvert m(\ell^+\ell^-) - M_{J/\psi}\rvert$	21415	19.83%	730	0.005%

Table 4.13: $e^+e^- \to \psi(2S)c\bar{c} \to \ell^+\ell^- c\bar{c}$: *Surviving events after each selection criteria in both signal MC and full data sample for the process* $e^+e^- \to \psi(2S)\eta_c, \chi_{c0}, \eta_c(2S)$. *The MC efficiencies and the data survival rates are listed for muonic* $\psi(2S)$ *decay.*

	$\psi(2S) \to e^+e^-$		$\psi(2S) \to \mu^+\mu^-$	
Cut	Signal MC	Efficiency ϵ_{sig}	Signal MC	Efficiency ϵ_{sig}
Generated	108000	100%	108000	100%
Preselection	59774	55.35%	65894	61.01%
$\psi(2S)$ candidate	40059	37.09%	54031	50.03%
NTRK	35465	32.84%	47907	44.36%
$p^*_{\psi(2S)}$	35462	32.84%	47873	44.33%
$cosH_{\psi(2S)}$	29377	27.20%	39720	36.78%
E^*_γ	29360	27.19%	39712	36.77%
$cos\theta^*_{\psi(2S)}$	24622	22.80%	36551	33.84%
$\lvert m(\ell^+\ell^-) - M_{J/\psi}\rvert$	22572	20.90%	33476	31.00%

Table 4.14: $e^+e^- \to \psi(2S)c\bar{c} \to \ell^+\ell^- c\bar{c}$: *Surviving events after each selection criteria in both signal MC for the process* $e^+e^- \to \psi(2S)X(3940)$. *The MC efficiencies are listed for both electronic and muonic* $\psi(2S)$ *decays.*

4.5 Event selection for $e^+e^- \to \psi(2S)c\bar{c} \to J/\psi\pi^+\pi^- c\bar{c}$

4.5.1 Calculation of $N_{S_{exp}}$ and $N_{B_{exp}}$

The selection strategy is aimed at maximizing the figure of merit $N_S/\sqrt{N_S + N_B}$ where N_S and N_B are the signal and the background samples, respectively. In the next paragraph we will explain how $N_{S_{exp}}$ and $N_{B_{exp}}$ have been computed.
$N_{S_{exp}}$ is the number of events that contain a true $\psi(2S)$: events where a $\psi(2S)$ is actually well reconstructed and corresponding to the system against which another charmonium state recoils. $N_{B_{exp}}$ is the number of events with a fake $\psi(2S)$ (i.e QED events).
The optimization process is performed evaluating the number of signal events in the mass distribution of the state recoiling against $\psi(2S)$. We perform this calculation for $J/\psi \to e^+e^-$ and for $J/\psi \to \mu^+\mu^-$ and for each recoil charmonium resonances (η_c, $\eta_c(2S)$, χ_{c0} and $X(3940)$).

$\mathbf{N}_{S_{exp}}$:

The expected number of signal events includes those events that are below the peak of the $c\bar{c}$ state recoiling against $\psi(2S)$, in the range of the the signal window, that identifies a $\psi(2S)$ candidate:

$$-0.010 \text{ GeV/c}^2 < m(\ell^+\ell^-\pi^+\pi^-) - M_{\psi(2S)} < 0.010 \text{ GeV/c}^2$$

It is calculated using the following formula:

$$N_{S_{exp}} = \sigma(e^+e^- \to \psi(2S)c\bar{c}) \cdot B(c\bar{c} \to \geq 1charged) \cdot L \cdot \epsilon_{sel} \cdot B(\psi(2S) \to J/\psi\pi^+\pi^-) \cdot B(J/\psi \to \ell^+\ell^-)$$

where

- $\sigma(e^+e^- \to \psi(2S)c\bar{c}) \cdot B(c\bar{c} \to \geq 1charged)$ is the product of the Belle double charmonium production cross section times the branching fraction for final

states with more than zero charged tracks [38]; for the X(3940) one, we do not have any measurement, so we assume the $\sigma \cdot B(c\bar{c} \to 2ch)$ of the J/ψ analysis.

- L=476 fb^{-1} is the integrated luminosity;
- ϵ_{sel} is the selection efficiency calculated on the signal MC in this analysis;
- $B(\psi(2S) \to J/\psi\pi^+\pi^-)$ is the branching ratio for the $\psi(2S)$ going to $J/\psi\pi^+\pi^-$ from PDG [4], whose value is:

$$B(\psi(2S) \to J/\psi\pi^+\pi^-) = (31.8 \pm 0.6)\%$$

- $B(J/\psi \to \ell^+\ell^-)$ is the branching ratio for the J/ψ going to e^+e^- or $\mu^+\mu^-$ from PDG [4], whose value is:

$$B(J/\psi \to \ell^+\ell^-) = \begin{cases} (5.94 \pm 0.06)\% & for \quad J/\psi \to e^+e^- \\ (5.93 \pm 0.06)\% & for \quad J/\psi \to \mu^+\mu^- \end{cases}$$

In Tab. 4.15 are reported all the values of the above parameters for each resonance in the recoil system.
We evaluate $N_{S_{exp}}$ using the efficiency reconstructed by this analysis.

$\mathbf{N}_{B_{exp}}$:

The number of expected background events is the number of events in the $\psi(2S)$ sidebands mass distribution, defined in Eq. 4.6.

4.5.2 $\psi(2S)$ candidate selection

Lepton pairs with masses within ranges -0.010 GeV/c^2 $< M_{\ell^+\ell^-\pi^+\pi^-} - M_{\psi(2S)} <$ 0.010 GeV/c^2 are referred to as $\psi(2S)$ candidates.
Since we obtain very similar values for η_c, χ_{c0}, $\eta_c(2S)$ and X(3940), we decide to choose one single cut for electrons and muons for all the recoil resonances.

$J/\psi \to e^+e^-$			
Recoil system	$\sigma \cdot B(c\bar{c} \to 0ch)(fb)$	$\epsilon_{sel}(e^+e^-)$	$N_{S_{exp}}(e^+e^-)$
$\eta(1S)$	$16.3 \pm 4.6 \pm 3.9$	(22.21±0.27)%	34 ± 10
χ_{c0}	$12.5 \pm 3.8 \pm 3.1$	(25.44±0.34)%	30 ± 9
$\eta_c(2S)$	$16.0 \pm 5.1 \pm 3.8$	(25.21±0.32)%	38 ± 12
X(3940)	$10.6 \pm 2.5 \pm 2.4$	(23.36±0.16)%	24 ± 8
$J/\psi \to \mu^+\mu^-$			
Recoil system	$\sigma \cdot B(c\bar{c} \to 0ch)(fb)$	$\epsilon_{sel}(\mu^+\mu^-)$	$N_{S_{exp}}(\mu^+\mu^-)$
$\eta(1S)$	$16.3 \pm 4.6 \pm 3.9$	(26.11±0.28)%	40 ± 11
χ_{c0}	$12.5 \pm 3.8 \pm 3.1$	(28.57±0.31)%	34 ± 10
$\eta_c(2S)$	$16.0 \pm 5.1 \pm 3.8$	(26.80±0.32)%	41 ± 13
X(3940)	$10.6 \pm 2.5 \pm 2.4$	(25.83±0.16)%	26 ± 6

Table 4.15: $e^+e^- \to \psi(2S)c\bar{c} \to J/\psi\pi^+\pi^- c\bar{c}$*: Summary of the double charmonium production cross section, the selection efficiency and the expected signal events for each recoil resonance, both in electronic and muonic channel. Note that, for X(3940), the cross section value is from* $J/\psi \to \ell^+\ell^-$ *because there are no previous measurement of the cross section.*

4.5.3 Number of charged tracks

The plot in Fig. 4.26 shows the distribution of the number of charged tracks (NTRK) in the signal MC and in the $\psi(2S)$ sidebands, for both electronic and muonic decays of the $\psi(2S)$.
It is possible to remove background, in the electronic and muonic decay channels, selecting events with at least 5 charged tracks. A part of signal events have NTRK=3 and NTRK=4 but the $\psi(2S)$ mass peak for NTRK=3 and NTRK=4 have a signal-background ratio too poor to be included in the final signal sample, so the final decision is $NTRK > 4$.

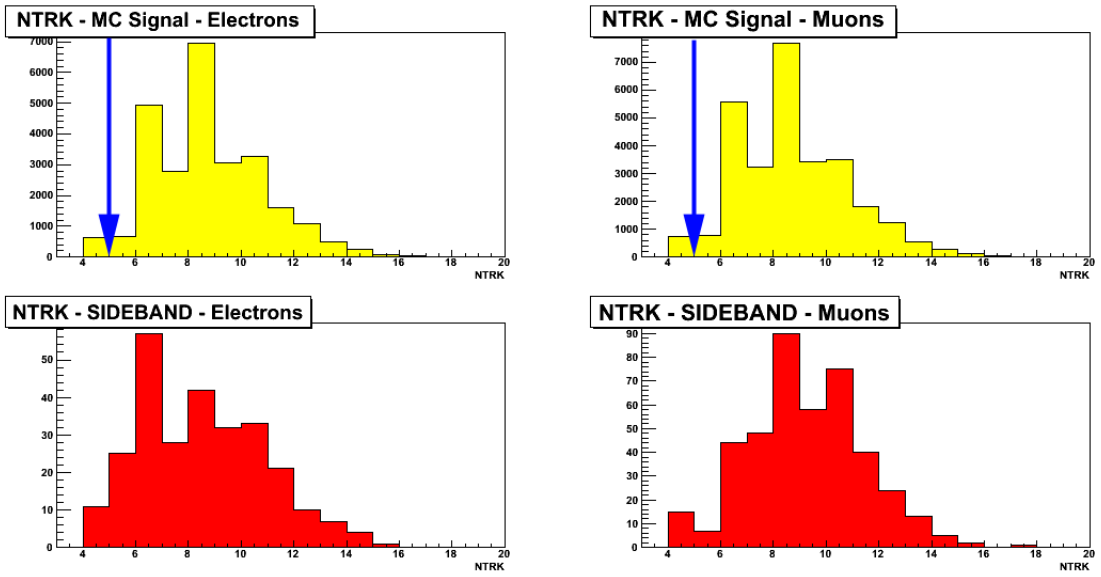

Figure 4.26: *$e^+e^- \to \psi(2S)c\bar{c} \to J/\psi\pi^+\pi^-c\bar{c}$: NTRK distribution after all the other selection criteria in the signal MC (yellow) and in the $\psi(2S)$ sidebands (red), for electrons and muons. The MC events are truth matched.*

4.5.4 Momentum of the $\psi(2S)$ in the CM frame

We also studied the $\psi(2S)$ momentum in the CM frame named $p^*_{\psi(2S)}$, whose distribution are shown in Fig. 4.27.
The events populating the low momentum region $p^* < 3$ GeV/c, equivalent to > 5.5 GeV/c^2 of recoil mass against $\psi(2S)$ are dominated by B decays (see Fig. 4.28 a).
The events populating the high momentum region $p^* > 4.5$ GeV/c that is equivalent to < 2.5 GeV/c^2 of recoil mass are due to the initial state radation interaction (i.e. $e^+e^- \to \gamma\psi(2S)$) (see Fig. 4.28 b).
In order to remove contributions from B decays and ISR processed we select events in the range:

$$3 \text{ GeV/c} < p^*_{\psi(2S)} < 4.5 \text{ GeV/c}$$

for both electronic and muonic decay channels.

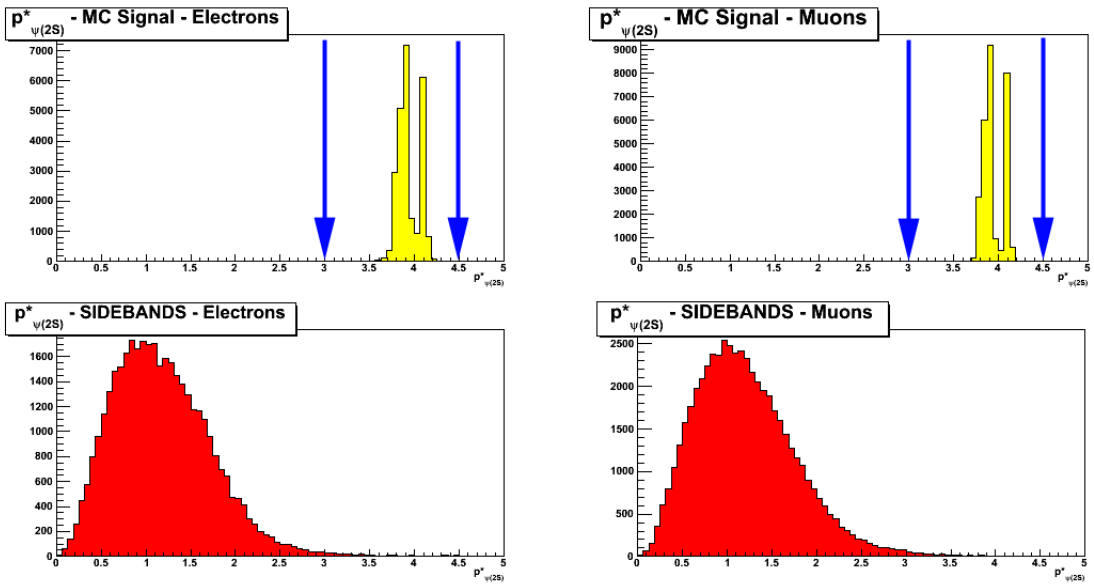

Figure 4.27: $e^+e^- \to \psi(2S)c\bar{c} \to J/\psi\pi^+\pi^- c\bar{c}$: $p^*_{\psi(2S)}$ *distribution after all the other selection criteria in the signal MC (yellow) and in the* $\psi(2S)$ *sidebands (red), for electrons and muons. The MC events are truth matched.*

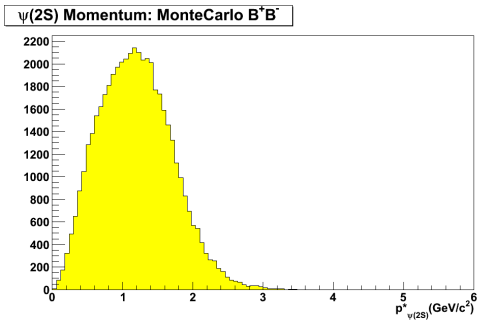

(a) Distribution of $p^*_{\psi(2S)}$ for Monte Carlo B^+B^-

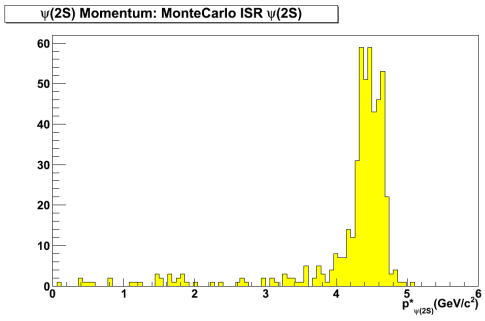

(b) ISR $\psi(2S)$ Monte Carlo distribution for ISR $p^*_{\psi(2S)}$

Figure 4.28: $e^+e^- \to \psi(2S)c\bar{c} \to J/\psi\pi^+\pi^- c\bar{c}$: $p^*_{\psi(2S)}$ *distribution for different background contribution: B meson background and ISR* $\psi(2S)$ *background.*

4.5.5 J/ψ helicity angle

In order to further suppress the background due to radiative QED processes, we studied the J/ψ helicity angle. The helicity angle of the J/ψ decay is the angle between the lepton momentum direction in the J/ψ rest frame and the J/ψ momentum direction in the center of mass frame.
Fig 4.29 shows the distribution of the cosine of the J/ψ helicity angle in the signal MC and in the $\psi(2S)$ sidebands, for both electronic and muonic decays of the J/ψ, whereas in Fig. 4.30 we show the J/ψ helicity distribution evaluated from Monte Carlo for various background sources. From the optimization we obtain:

$$-0.85 < cosH_{J/\psi} < 0.85$$

for both electronic and muonic decay channels.

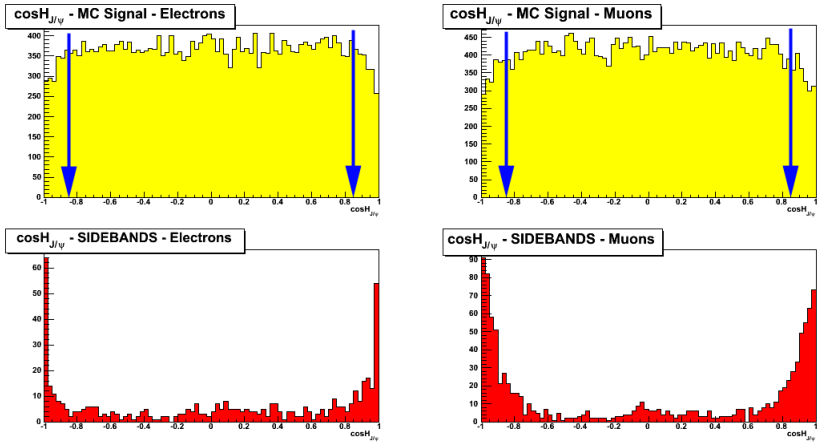

Figure 4.29: $e^+e^- \to \psi(2S)c\bar{c} \to J/\psi\pi^+\pi^- c\bar{c}$: *$J/\psi$ helicity distribution after all the other selection criteria in the signal MC (yellow) and in the $\psi(2S)$ sidebands (red) for electrons and muons. The MC events are truth matched.*

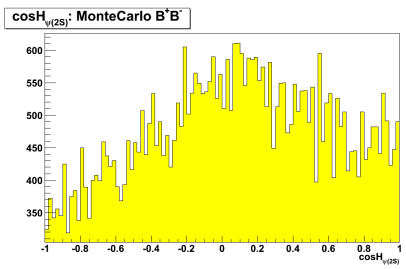

(a) Background contribution in the $\psi(2S)$ helicity distribution from Monte Carlo B^+B^-

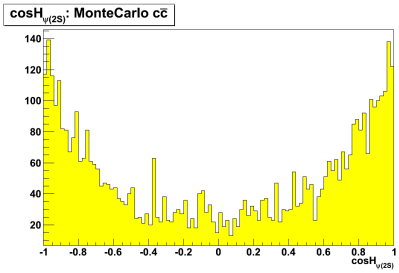

(b) Background contribution in the $\psi(2S)$ helicity distribution from Monte Carlo $c\bar{c}$

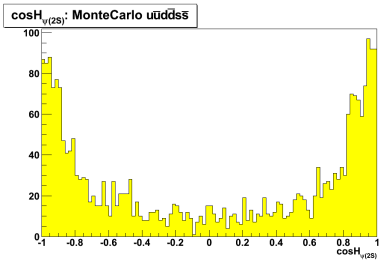

(c) Background contribution in the $\psi(2S)$ helicity distribution from Monte Carlo $u\bar{u}d\bar{d}s\bar{s}$

Figure 4.30: $e^+e^- \to \psi(2S)c\bar{c} \to J/\psi\pi^+\pi^- c\bar{c}$: *Monte Carlo distribution of $\psi(2S)$ helicity angle for different background contributions (B decays, $c\bar{c}$ events, $u\bar{c}d\bar{d}s\bar{s}$ events).*

4.5.6 Maximum photon energy in the CM system

Most QED events from radiative Bhabha, radiative di-muon or ISR $\psi(2S)$ have an energetic photon in the final state. In order to suppress these background contributions, we studied the variable E^*_γ, the maximum photon energy in the CM system. In Fig. 4.31 we show the distribution of E^*_γ in the signal MC and in the $\psi(2S)$ sidebands, for both electronic and muonic decays of the J/ψ.
In both electronic and muonic decay channel we select events with:

$$E^*_\gamma < 3.5 \text{ GeV}$$

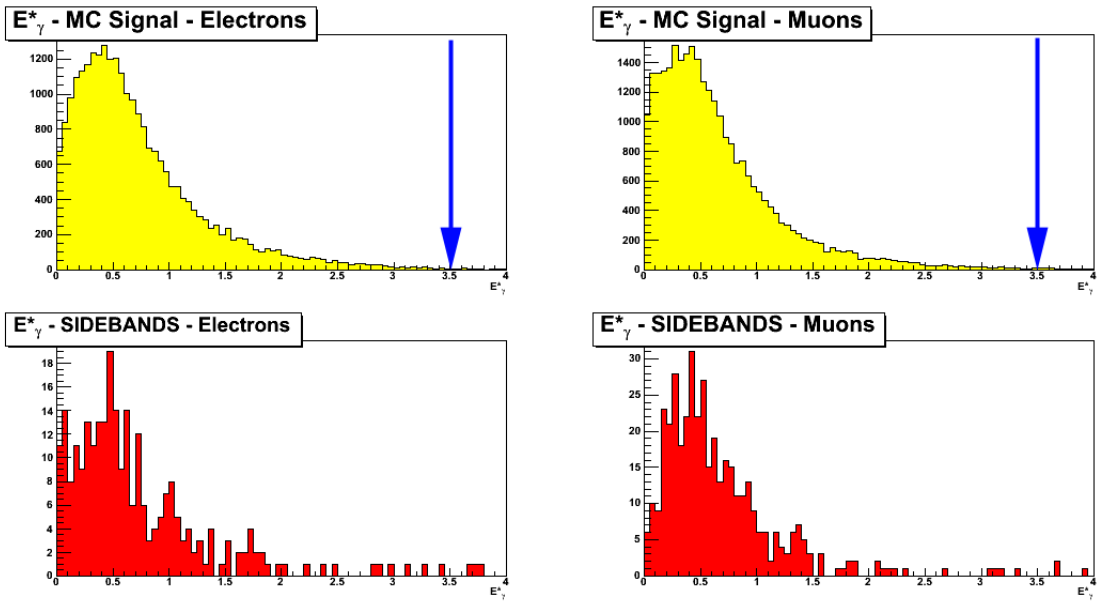

Figure 4.31: $e^+e^- \to \psi(2S)c\bar{c} \to J/\psi\pi^+\pi^- c\bar{c}$: *$E^*_\gamma$ distribution after all the other selection criteria in the signal MC (yellow) and in the $\psi(2S)$ sidebands (red) for electrons and muons. The MC events are truth matched.*

4.5.7 $cos\theta_{\psi(2S)}$ in the CM system

In order to suppress the ISR background we studied the $cos\theta_{\psi(2S)}$ in the CM system. This variable is the cosine of the angle between the $\psi(2S)$ momentum and the z coordinate (beam direction) in the center of mass frame.
Fig. 4.32 shows the distribution of the $cos\theta_{\psi(2S)}$ in the CM frame in the signal MC and in the $\psi(2S)$ sidebands, for both electronic and muonic decays of the J/ψ.
The optimization performed on this variable gives as result the following cut:

$$\text{-}0.85 < cos\theta^*_{\psi(2S)} < 0.85$$

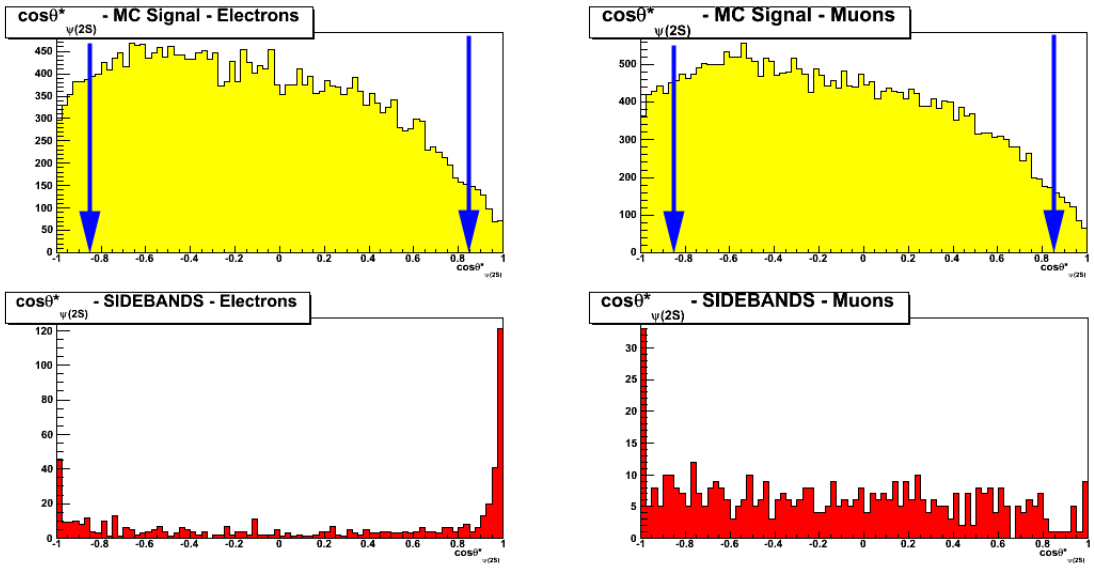

Figure 4.32: *$e^+e^- \to \psi(2S)c\bar{c} \to J/\psi\pi^+\pi^- c\bar{c}$: $cos\theta^*_{\psi(2S)}$ distribution after all the other selection criteria in the signal MC (yellow) and in the $\psi(2S)$ sidebands (red) for electrons and muons. The MC events are truth matched.*

4.5.8 Summary of the selection criteria

The final selection criteria are summarized in Table 4.16.

	$J/\psi \to e^+e^-$	$J/\psi \to \mu^+\mu^-$
Lepton PID	both are eLHBremLH	both are muBDTVeryLoose
Pion PID	both are PionLHVeryLoose	
$\psi(2S)$ Candidate	[-10, +10] MeV/c^2	
Number of charged Tracks	> 4	
$p^*_{\psi(2S)}$	[3, 4.5] GeV/c^2	
$cosH_{J/\psi}$	$[-0.85, 0.85]$	
E^*_γ	< 3.5 GeV	
$cos\theta^*_{\psi(2S)}$	$[-0.85, 0.85]$	

Table 4.16: *The final selection criteria for* $e^+e^- \to \psi(2S)c\bar{c} \to J/\psi\pi^+\pi^- c\bar{c}$.

The MC efficiency and the survival rate in the full data sample after each selection criteria, for $J/\psi \to e^+e^-$ and $J/\psi \to \mu^+\mu^-$ are listed in Tab. 4.17 and Tab. 4.18. The values for MC signal are referred to the channel $e^+e^- \to \psi(2S)\eta_c, \chi_{c0}, \eta_c(2S)$; the MC efficiencies for the recoil resonances X(3940) are reported in Tab. 4.19.
The distributions of the variables studied during the selection optimization are reported, for the full data sample, in Fig. 4.33 and Fig. 4.34 for the electronic and the muonic channel respectively. All the variables are plotted after all the selection criteria have been applied.
Fig. 4.35 shows the $\psi(2S)$ mass distribution in the signal MC (yellow) and in the full data sample (green), before the selection procedure for $J/\psi \to e^+e^-$ and $J/\psi \to \mu^+\mu^-$ samples; in Fig. 4.36 the same distributions after all the selection criteria.
A comparison between Fig. 4.35 and Fig. 4.36 shows the much improved signal-to-noise ratio in the data after all selection cuts have been applied.

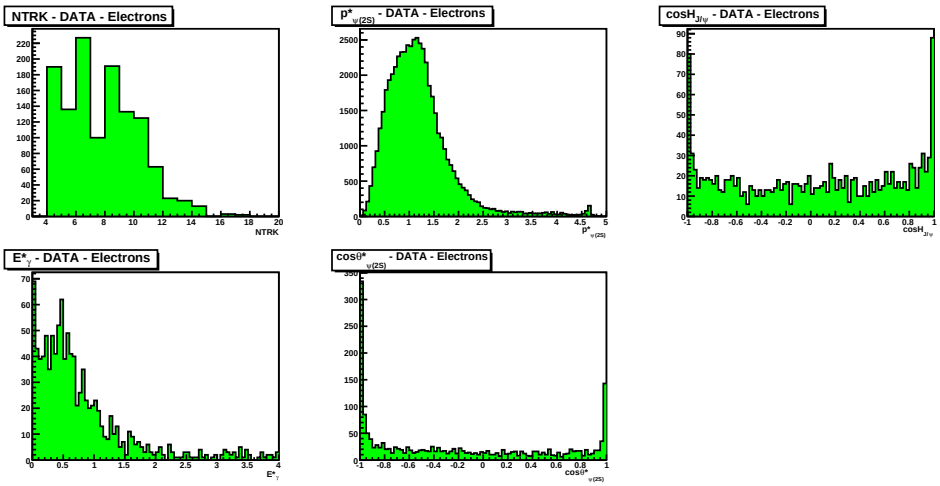

Figure 4.33: $e^+e^- \to \psi(2S)c\bar{c} \to J/\psi\pi^+\pi^-c\bar{c}$: *Distribution for NTRK, the* $\psi(2S)$ *momentum* ($p^*_{\psi(2S)}$), *the* J/ψ *helicity angle, the maximum photon energy* (E^*_γ) *and* $cos\theta_{\psi(2S)}$ *for the full data sample, for* $J/\psi \to e^+e^-$. *All the selection criteria have been applied.*

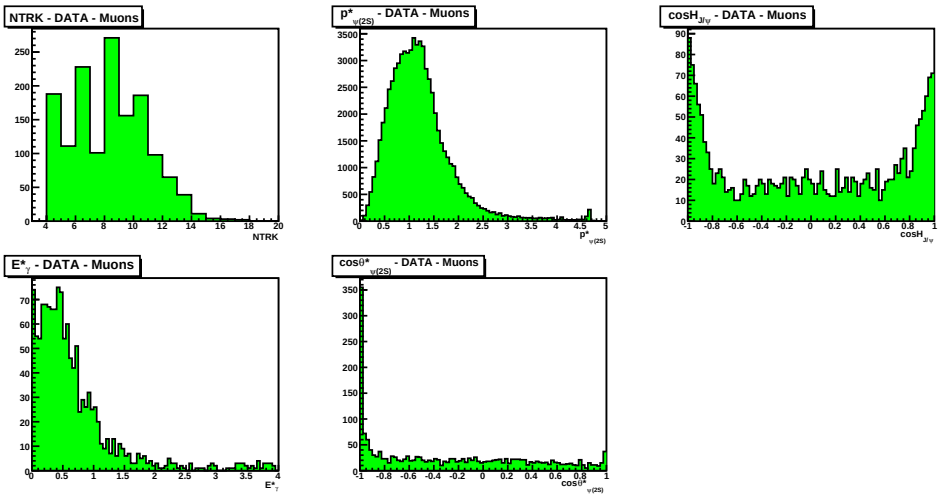

Figure 4.34: $e^+e^- \to \psi(2S)c\bar{c} \to J/\psi\pi^+\pi^-c\bar{c}$: *Distribution for NTRK, the* $\psi(2S)$ *momentum* ($p^*_{\psi(2S)}$), *the* J/ψ *helicity angle, the maximum photon energy* (E^*_γ) *and* $cos\theta_{\psi(2S)}$ *for the full data sample, for* $J/\psi \to \mu^+\mu^-$. *All the selection criteria have been applied.*

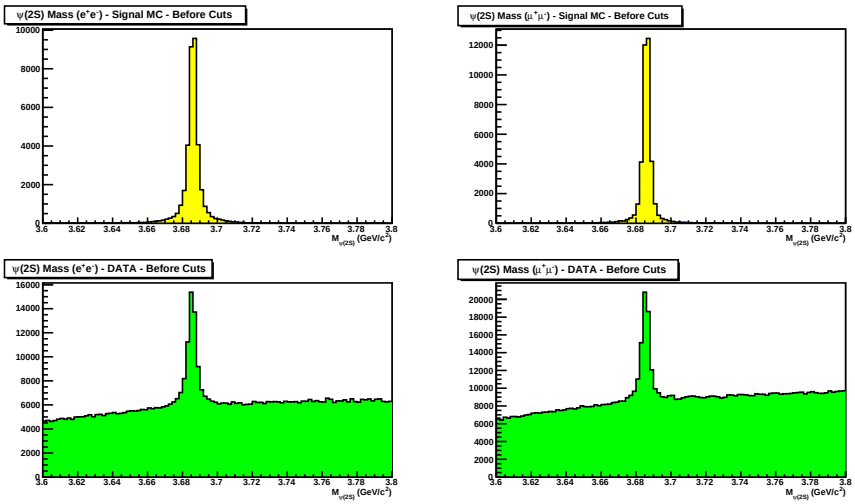

Figure 4.35: $e^+e^- \to \psi(2S)c\bar{c} \to J/\psi\pi^+\pi^- c\bar{c}$: *Distribution of the* $\psi(2S)$ *mass before the selection criteria in the signal MC (yellow) and in the full data sample (green): in* e^+e^- *decay on the left and* $\mu^+\mu^-$ *decay on the right. The MC events are truth matched.*

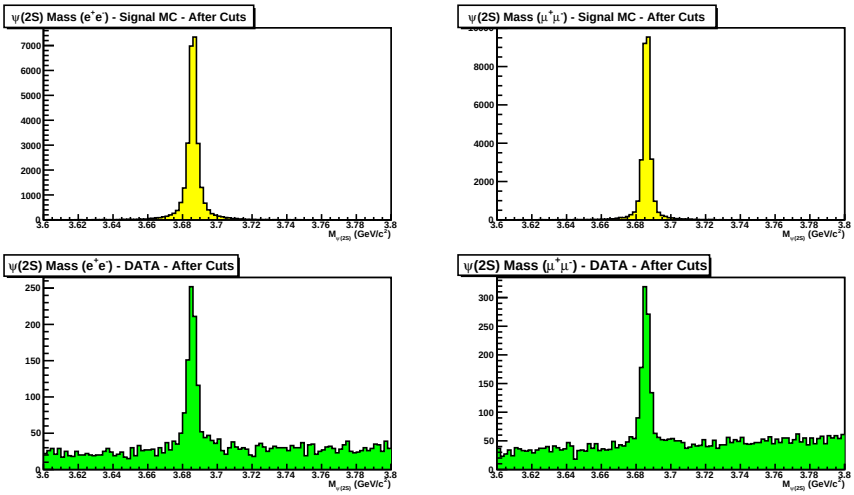

Figure 4.36: $e^+e^- \to \psi(2S)c\bar{c} \to J/\psi\pi^+\pi^- c\bar{c}$: *Distribution of the* $\psi(2S)$ *mass after the selection cuts in the signal MC (yellow) and in the full data sample (green): in* e^+e^- *decay on the left and* $\mu^+\mu^-$ *decay on the right. The MC events are truth matched.*

	$J/\psi \to e^+e^-$			
Cut	Signal MC	Efficiency ϵ_{sig}	Data	Survival rate ϵ_{data}
Generated	108000	100%	249788188	-
Preselection	65778	60.91%	1177162	100%
$\psi(2S)$ candidate	35339	32.72%	91722	7.79%
NTRK	34474	31.92%	77396	6.57%
$p^*_{\psi(2S)}$	34395	31.85%	2480	0.21%
$cosH_{J/\psi}$	29871	27.66%	1921	0.16%
E^*_γ	29809	27.60%	1831	0.15%
$cos\theta^*_{\psi(2S)}$	26809	24.82%	1036	0.09%

Table 4.17: *$e^+e^- \to \psi(2S)c\bar{c} \to J/\psi\pi^+\pi^- c\bar{c}$: Surviving events after each selection criteria in both signal MC and full data sample for the process $e^+e^- \to \psi(2S)\eta_c, \chi_{c0}, \eta_c(2S)$. The MC efficiencies and the data survival rates are listed for electronic J/ψ decay.*

	$J/\psi \to \mu^+\mu^-$			
Cut	Signal MC	Efficiency ϵ_{sig}	Data	Survival rate ϵ_{data}
Generated	108000	100%	249788188	-
Preselection	70994	65.74%	1691132	100%
$\psi(2S)$ candidate	39018	36.13%	124941	7.39%
NTRK	38048	35.23%	107262	6.34%
$p^*_{\psi(2S)}$	37885	35.08%	2887	0.17%
$cosH_{J/\psi}$	33040	30.59%	2028	0.12%
E^*_γ	32975	30.53%	1957	0.12%
$cos\theta^*_{\psi(2S)}$	29586	27.39%	1275	0.08%

Table 4.18: *$e^+e^- \to \psi(2S)c\bar{c} \to J/\psi\pi^+\pi^- c\bar{c}$: Surviving events after each selection criteria in both signal MC and full data sample for the process $e^+e^- \to \psi(2S)\eta_c, \chi_{c0}, \eta_c(2S)$. The MC efficiencies and the data survival rates are listed for muonic J/ψ decay.*

	$J/\psi \to e^+e^-$		$J/\psi \to \mu^+\mu^-$	
Cut	Signal MC	Efficiency ϵ_{sig}	Signal MC	Efficiency ϵ_{sig}
Generated	108000	100%	108000	100%
Preselection	92939	86.05%	100687	93.23%
$\psi(2S)$ candidate	34507	31.95%	37787	34.99%
NTRK	34290	31.75%	37551	34.77%
$p^*_{\psi(2S)}$	33678	31.18%	36799	34.07%
$cosH_{J/\psi}$	29322	27.15%	32063	29.69%
E^*_γ	29291	27.12%	32027	29.65%
$cos\theta^*_{\psi(2S)}$	26890	24.90%	29378	27.20%

Table 4.19: $e^+e^- \to \psi(2S)c\bar{c} \to J/\psi\pi^+\pi^-c\bar{c}$*: Surviving events after each selection criteria in both signal MC for the process* $e^+e^- \to J/\psi X(3940)$*. The MC efficiencies are listed for both electronic and muonic* J/ψ *decays.*

4.6 Efficiency studies

In order to estimate the reconstruction efficiencies for the recoil resonances, we perform an extended maximum likelihood fit to the recoil mass spectrum on signal MC using a Voigtian function, for the resonance states, plus a 2^{nd} order polynomial for the background. The Voigtian function is a Breit-Wigner function convoluted with a single Gaussian to account for the experimental resolution.

4.6.1 $e^+e^- \to J/\psi c\bar{c} \to \ell^+\ell^- c\bar{c}$

In Fig 4.37 we show the fit to the Monte Carlo sample to the recoil mass spectrum for η_c, χ_{c0} and $\eta_c(2S)$ in the electronic and muonic channels.
Fig. 4.38 shows the fit to the recoil mass spectrum for X(3940) in the electronic and muonic decay channels.
The results of the reconstruction efficiency study are reported in Tab. 4.20 and they are consistent with the previous analysis [21].

Recoil	Generated	$J/\psi \to e^+e^-$		$J/\psi \to \mu^+\mu^-$	
Resonance	Events	N	Efficiency ϵ	N	Efficiency ϵ
η_c	36000	5884±80	(16.34±0.22)%	9183±98	(25.51±0.27)%
χ_{c0}	36000	8453±102	(23.48±0.28)%	11593±112	(32.20±0.31)%
$\eta_c(2S)$	36000	5678±85	(15.77±0.24)%	7979±94	(22.16±0.27)%
X(3940)	108000	26181±162	(24.24±0.15)%	37116±200	(34.37±0.18)%

Table 4.20: *$e^+e^- \to J/\psi c\bar{c} \to \ell^+\ell^- c\bar{c}$: Reconstruction efficiency for the recoil mass system in the signal MC with corresponding errors. We require the J/ψ candidate.*

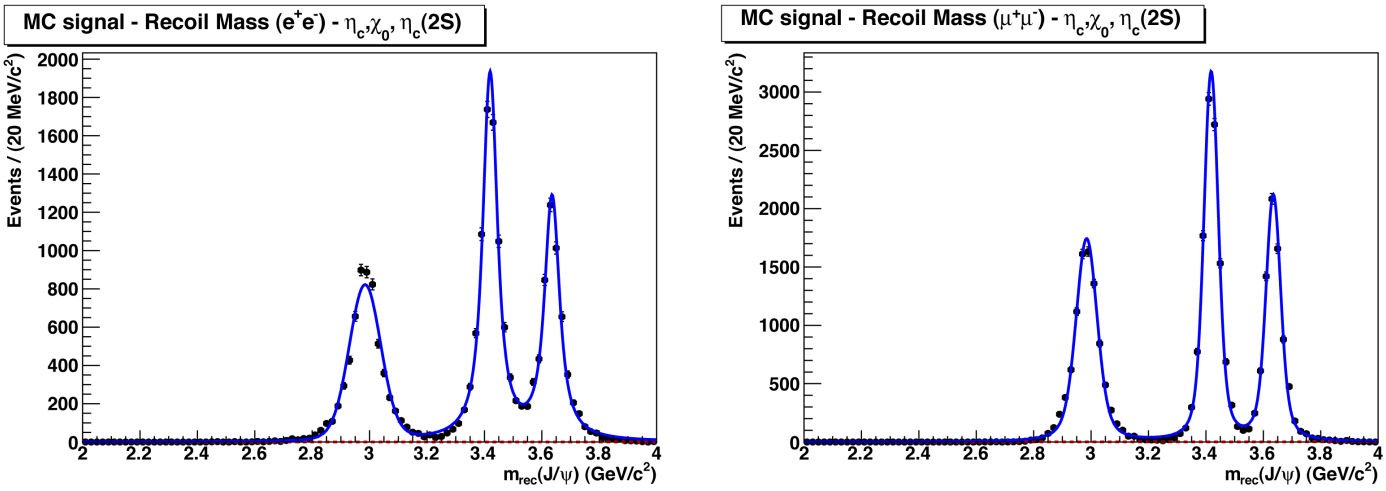

Figure 4.37: $e^+e^- \to J/\psi c\bar{c} \to \ell^+\ell^- c\bar{c}$: *Fit to the recoil mass against the* J/ψ *in the signal MC for the states* η_c, χ_{c0} *and* $\eta_c(2S)$. *For* $J/\psi \to e^+e^-$ *on the left and for* $J/\psi \to \mu^+\mu^-$ *on the right.*

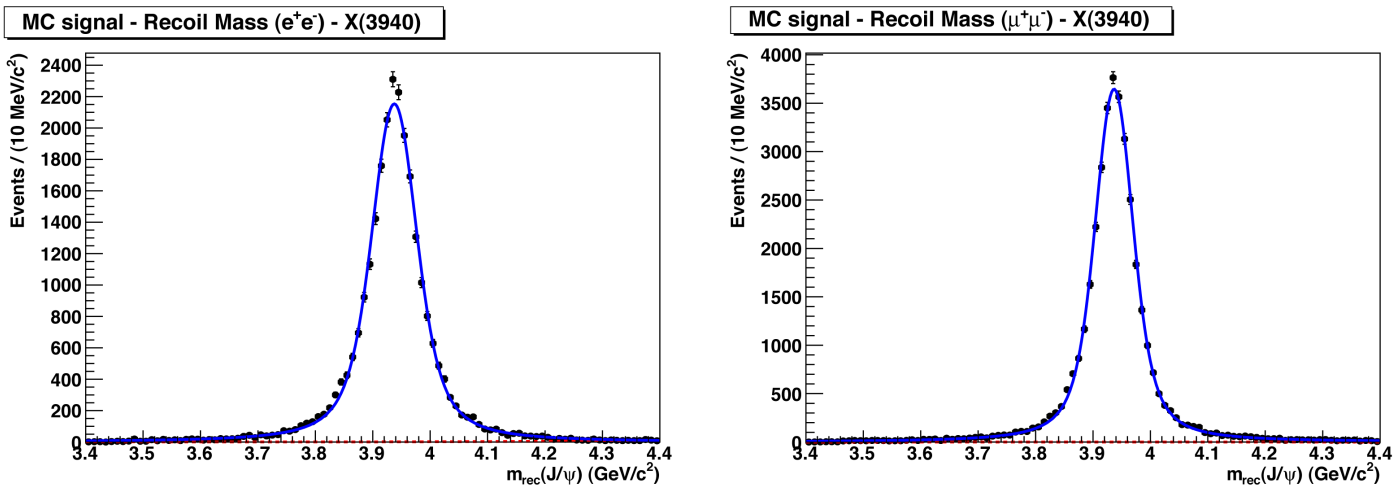

Figure 4.38: $e^+e^- \to J/\psi c\bar{c} \to \ell^+\ell^- c\bar{c}$: *Fit to the recoil mass against the* J/ψ *in the signal MC for the states X(3940). For* $J/\psi \to e^+e^-$ *on the left and for* $J/\psi \to \mu^+\mu^-$ *on the right.*

4.6.2 $e^+e^- \to \psi(2S)c\bar{c} \to \ell^+\ell^- c\bar{c}$

In Fig.4.39 we show the fit to the Monte Carlo sample to the recoil mass spectrum for η_c, χ_{c0} and $\eta_c(2S)$ in the electronic and muonic channels.
Fig. 4.40 shows the fit to the recoil mass spectrum for X(3940) in the electronic and muonic decay channels.
The results of the reconstruction efficiency study are reported in Tab. 4.21.

Recoil	Generated	$\psi(2S) \to e^+e^-$		$\psi(2S) \to \mu^+\mu^-$	
Resonance	Events	N	Efficiency ϵ	N	Efficiency ϵ
η_c	36000	4376±69	(12.16±0.19)%	7220±87	(20.06±0.24)%
χ_{c0}	36000	5876±88	(16.32±0.24)%	9069±100	(25.19±0.28)%
$\eta_c(2S)$	36000	4074±74	(11.32±0.21)%	6667±93	(18.52±0.26)%
X(3940)	108000	22500±150	(20.83±0.14)%	33470±170	(30.99±0.16)%

Table 4.21: *$e^+e^- \to \psi(2S)c\bar{c} \to \ell^+\ell^- c\bar{c}$: Reconstruction efficiency for the recoil mass system in the signal MC with corresponding errors. We require the $\psi(2S)$ candidate.*

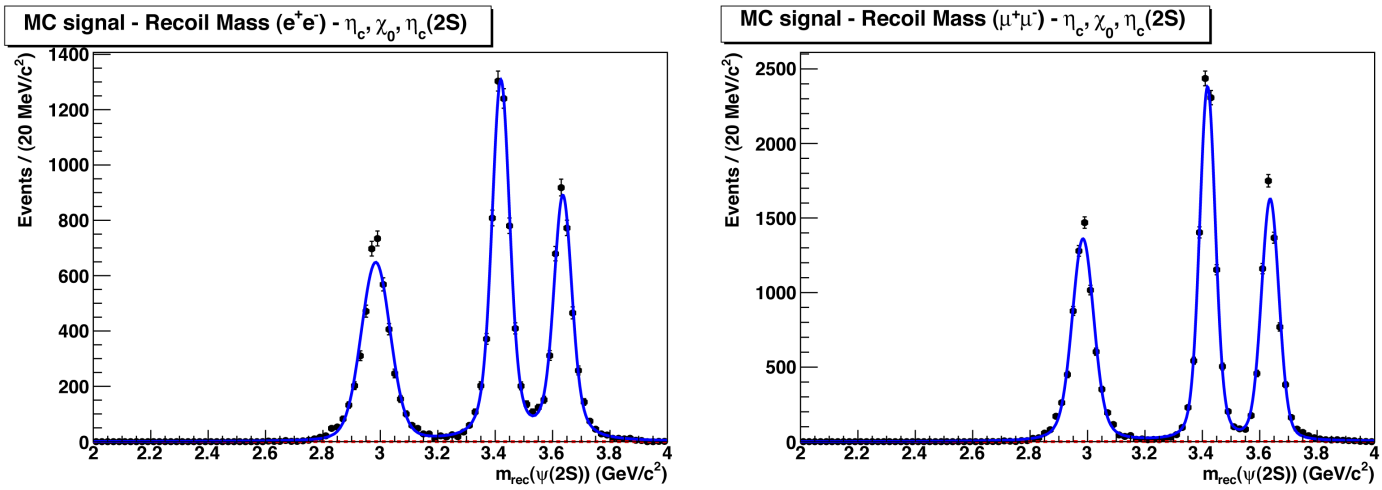

Figure 4.39: $e^+e^- \to \psi(2S)c\bar{c} \to \ell^+\ell^- c\bar{c}$: *Fit to the recoil mass against the* $\psi(2S)$ *in the signal MC for the states* η_c, χ_{c0} *and* $\eta_c(2S)$. *For* $\psi(2S) \to e^+e^-$ *on the left and for* $\psi(2S) \to \mu^+\mu^-$ *on the right.*

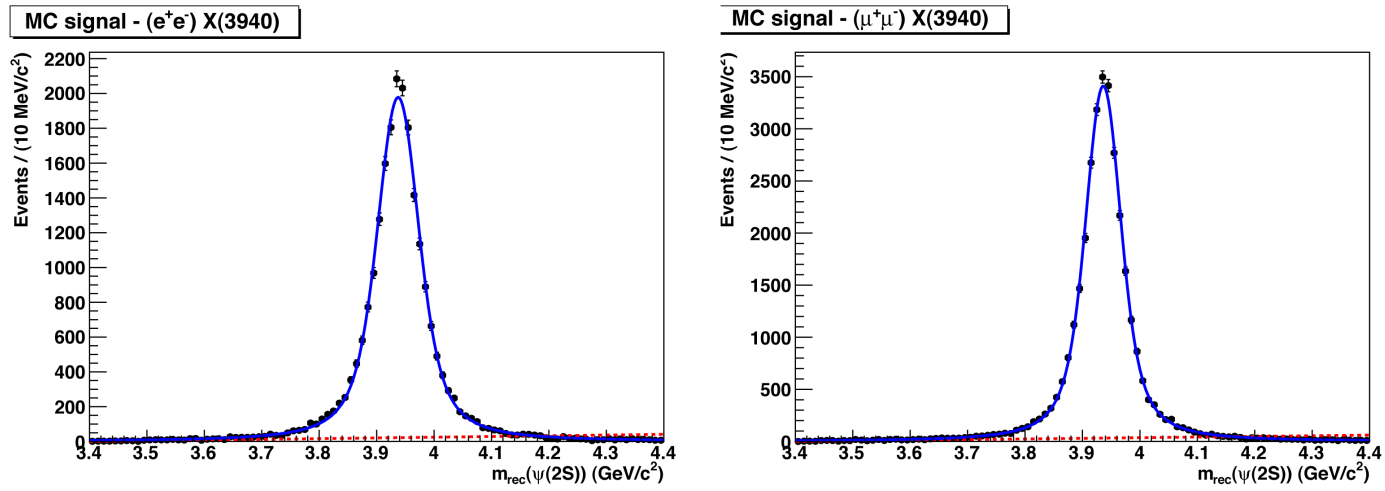

Figure 4.40: $e^+e^- \to \psi(2S)c\bar{c} \to \ell^+\ell^- c\bar{c}$: *Fit to the recoil mass against the* $\psi(2S)$ *in the signal MC for the states X(3940). For* $\psi(2S) \to e^+e^-$ *on the left and for* $\psi(2S) \to \mu^+\mu^-$ *on the right.*

4.6.3 $e^+e^- \to \psi(2S)c\bar{c} \to J/\psi\pi^+\pi^- c\bar{c}$

In Fig.4.41 we show the fit to the Monte Carlo sample to the recoil mass spectrum for η_c, χ_{c0} and $\eta_c(2S)$ in the electronic and muonic channels.
Fig. 4.42 shows the fit to the recoil mass spectrum for X(3940) in the electronic and muonic decay channels.
The results of the reconstruction efficiency study are reported in Tab. 4.22.

Recoil	Generated	$J/\psi \to e^+e^-$		$J/\psi \to \mu^+\mu^-$	
Resonance	Events	N	Efficiency ϵ	N	Efficiency ϵ
η_c	36000	7994±96	(22.21±0.27)%	9398±102	(26.11±0.28)%
χ_{c0}	36000	9157±123	(25.44±0.34)%	10285±112	(28.57±0.31)%
$\eta_c(2S)$	36000	9075±115	(25.21±0.32)%	9647±114	(26.80±0.32)%
X(3940)	108000	25224±170	(23.36±0.16)%	27900±172	(25.83±0.16)%

Table 4.22: $e^+e^- \to \psi(2S)c\bar{c} \to J/\psi\pi^+\pi^- c\bar{c}$*: Reconstruction efficiency for the recoil mass system in the signal MC with corresponding errors. We require the* $\psi(2S)$ *candidate.*

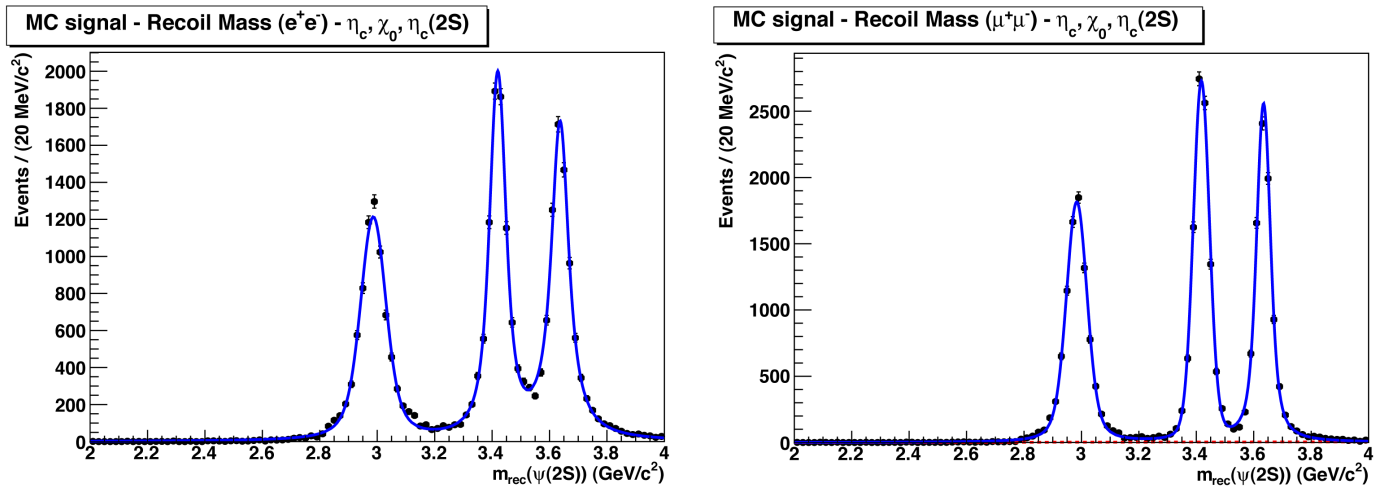

Figure 4.41: $e^+e^- \to \psi(2S)c\bar{c} \to J/\psi\pi^+\pi^- c\bar{c}$: *Fit to the recoil mass against the* $\psi(2S)$ *in the signal MC for the states* η_c, χ_{c0} *and* $\eta_c(2S)$. *For* $J/\psi \to e^+e^-$ *on the left and for* $J/\psi \to \mu^+\mu^-$ *on the right.*

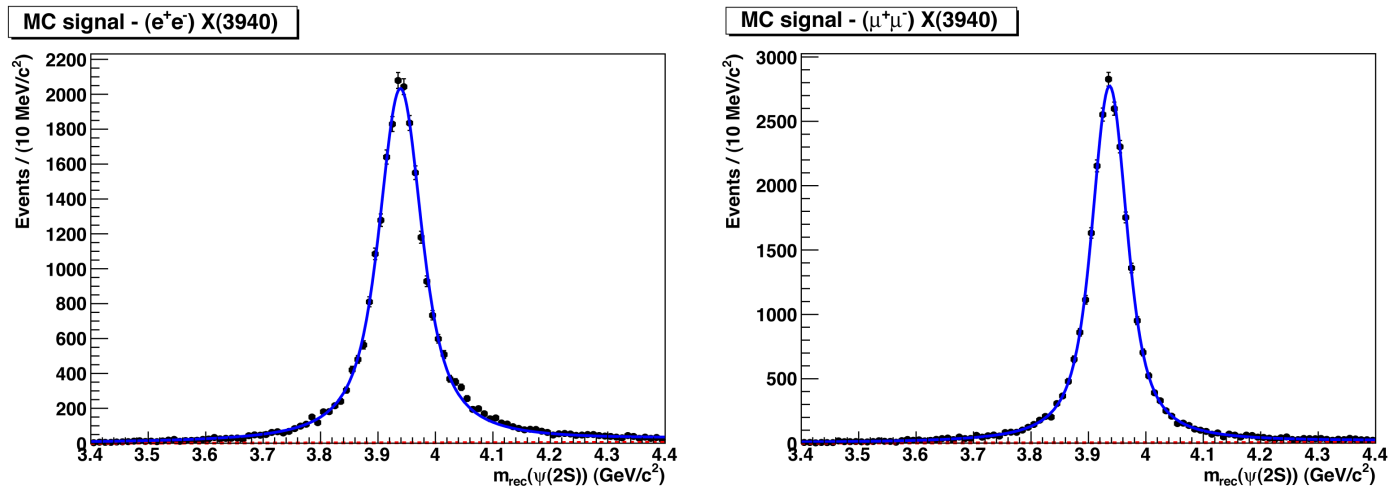

Figure 4.42: $e^+e^- \to \psi(2S)c\bar{c} \to J/\psi\pi^+\pi^- c\bar{c}$: *Fit to the recoil mass against the* $\psi(2S)$ *in the signal MC for the states X(3940). For* $J/\psi \to e^+e^-$ *on the left and for* $J/\psi \to \mu^+\mu^-$ *on the right.*

4.7 Resolution studies

We study the detector resolution for each recoil resonance: η_c, χ_{c0}, $\eta_c(2S)$ and X(3940). In order to do that, we generated a signal MC with *zero width* for the charmonium recoil resonances.
After that, each recoil resonance distribution is fitted with the following function:

$$f = N\left[(1-\alpha)\cdot G_1(m,\mu_1,\sigma_1) + \alpha\cdot G_2(m,\mu_2,\sigma_2)\right] \tag{4.7}$$

where:

$$G_1(m,\mu_1,\sigma_1) = \frac{1}{\sqrt{2\pi}\sigma_1} e^{-\frac{-(m-\mu_1)^2}{2\sigma_1^2}} \tag{4.8}$$

$$G_2(m,\mu_2,\sigma_2) = \frac{1}{\sqrt{2\pi}\sigma_2} e^{-\frac{-(m-\mu_2)^2}{2\sigma_2^2}} \tag{4.9}$$

and where μ_1 (μ_2) is the mean of the gaussian G_1 (G_2); the widths of the two gaussians are given by the parameters σ_1 and σ_2. The overall normalization is given by N, and the fraction of events described by the first (second) gaussian are given by $1-\alpha$ (α).
Since it is not obvious how one can assign the width that is the resolution value, associated with the function *f*, it is necessary to explain how we extracted it from each fit.
The resolution value is given by:

$$\sigma = \frac{|m_1 - m_0| + |m_2 - m_0|}{2} \tag{4.10}$$

where
- m_0 is the mass where the fitting function peaks;
- m_1 is the mass where the fitting function is half maximum to the right of the peak;
- m_2 is the mass where the fitting function is half maximum to the left of the peak

and the uncertainty associated with the resolution value is given by:

$$\delta\sigma = ||m_1 - m_0| - |m_2 - m_0|| \tag{4.11}$$

The results obtained, for each analysis, from the fit are reported in Tab. 4.23.
The fits are shown in Fig. 4.43 for $e^+e^- \to J/\psi c\bar{c} \to \ell^+\ell^- c\bar{c}$, Fig. 4.44 for $e^+e^- \to$

$\psi(2S)c\bar{c} \to \ell^+\ell^- c\bar{c}$ and Fig. 4.45 for $e^+e^- \to \psi(2S)c\bar{c} \to J/\psi\pi^+\pi^- c\bar{c}$.
In Fig. 4.46 we report the dependence of the resolution on the recoil mass for each decay mode. It can be seen that the resolution depends very weakly on the recoil mass.

Particle	$J/\psi \to \ell^+\ell^-$ σ (MeV/c^2)	$\psi(2S) \to J/\psi\pi^+\pi^-$ σ (MeV/c^2)	$\psi(2S) \to \ell^+\ell^-$ σ (MeV/c^2)
η_c	41.23 ± 1.08	38.61 ± 0.44	36.92 ± 0.97
χ_{c0}	32.26 ± 0.98	30.47 ± 0.42	31.14 ± 0.28
$\eta_c(2S)$	31.54 ± 1.36	29.84 ± 0.75	29.40 ± 0.17
X(3940)	27.29 ± 0.21	25.33 ± 0.17	26.39 ± 0.53

Table 4.23: *Resolution obtained from the fit for each analysis.*

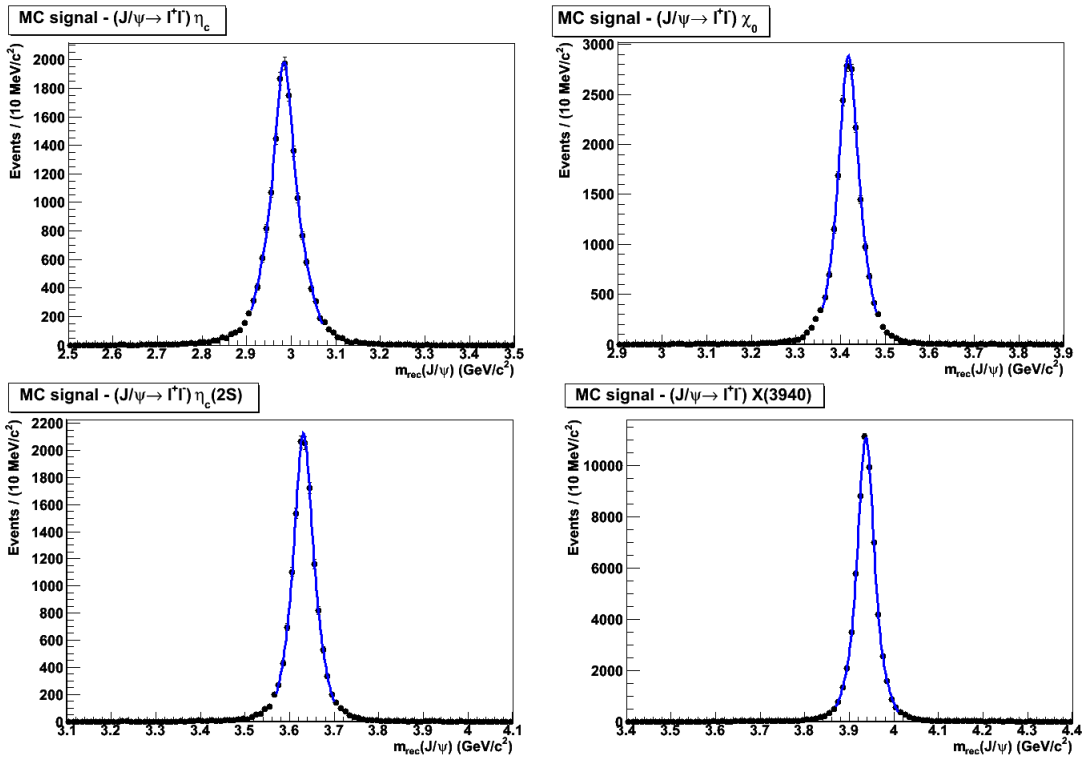

Figure 4.43: $e^+e^- \to J/\psi c\bar{c} \to \ell^+\ell^- c\bar{c}$: *Fit to the recoil mass against the* J/ψ *in the signal MC for the states* η_c, χ_{c0}, $\eta_c(2S)$ *and X(3940) for* $J/\psi \to \ell^+\ell^-$. *The recoil resonances are generated with zero width.*

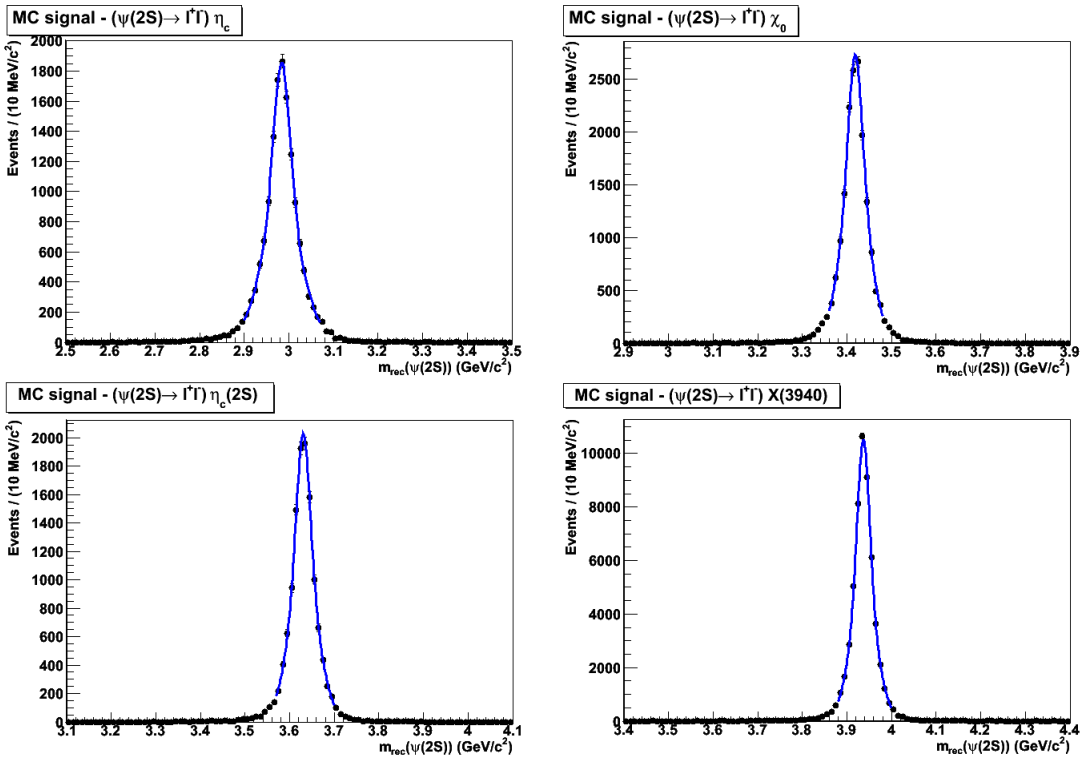

Figure 4.44: $e^+e^- \to \psi(2S)c\bar{c} \to \ell^+\ell^- c\bar{c}$: *Fit to the recoil mass against the* $\psi(2S)$ *in the signal MC for the states* η_c, χ_{c0}, $\eta_c(2S)$ *and X(3940) for* $\psi(2S) \to \ell^+\ell^-$. *The recoil resonances are generated with zero width.*

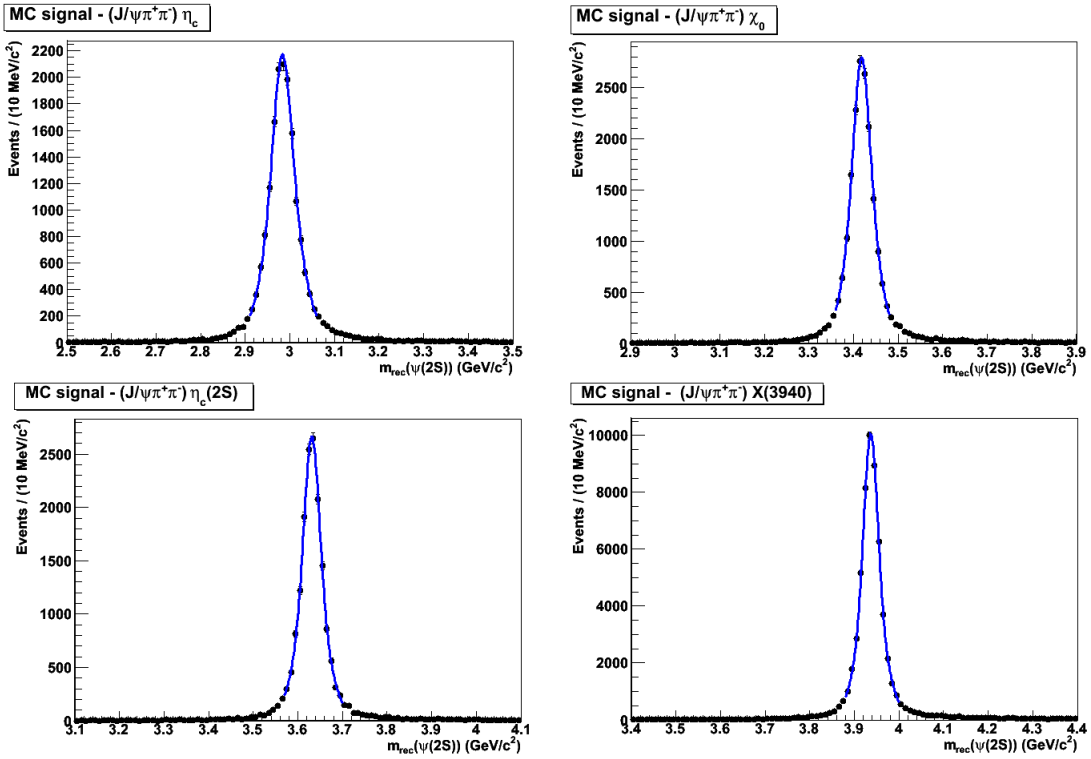

Figure 4.45: $e^+e^- \to \psi(2S)c\bar{c} \to J/\psi\pi^+\pi^- c\bar{c}$: *Fit to the recoil mass against the* $\psi(2S)$ *in the signal MC for the states* η_c, χ_{c0}, $\eta_c(2S)$ *and X(3940) for* $J/\psi \to \ell^+\ell^-$. *The recoil resonances are generated with zero width.*

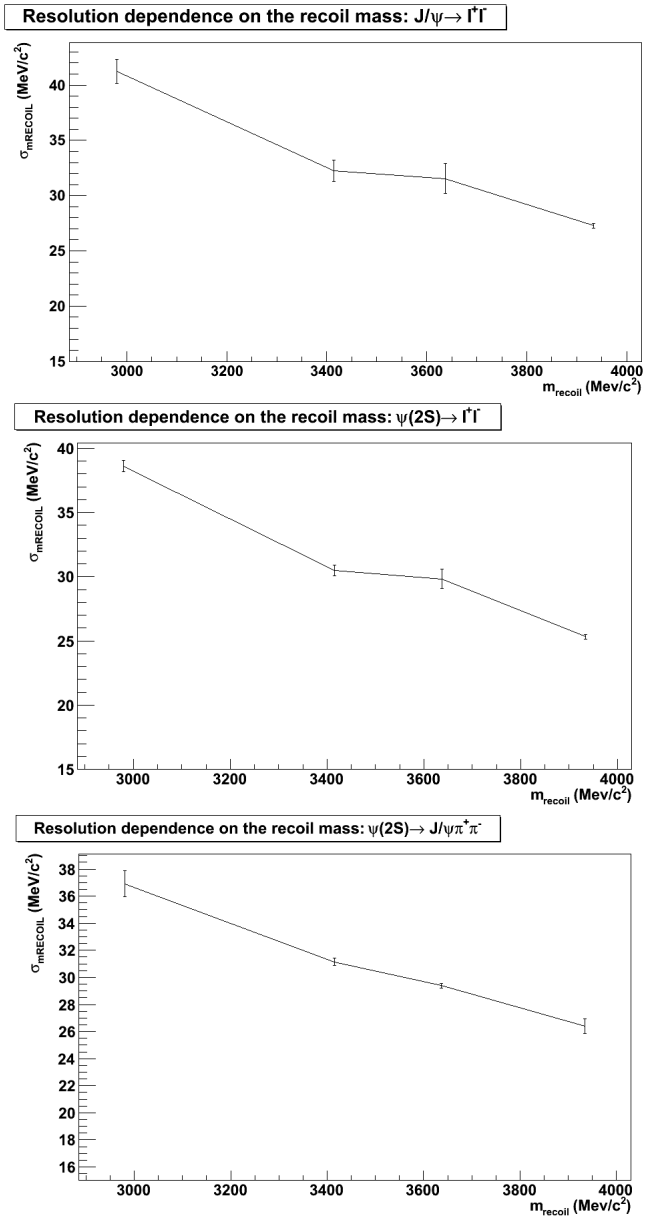

Figure 4.46: *Resolution dependence on the recoil mass. The point are the resolutions of the recoil mass against the J/ψ at the nominal masses of η_c, χ_{c0}, $\eta_c(2S)$ and X(3940).*

4.8 Background evaluation

4.8.1 $e^+e^- \to J/\psi c\bar{c} \to \ell^+\ell^- c\bar{c}$

There are two main background sources in this analysis: events with genuine J/ψ mesons and combinatorial background.
To estimate the combinatorial background due to random tracks we used the J/ψ mass sidebands, defined in Eq. 4.2, Eq. 4.3.
The mass recoiling against the J/ψ from the J/ψ mass sidebands is shown in Fig. 4.47.

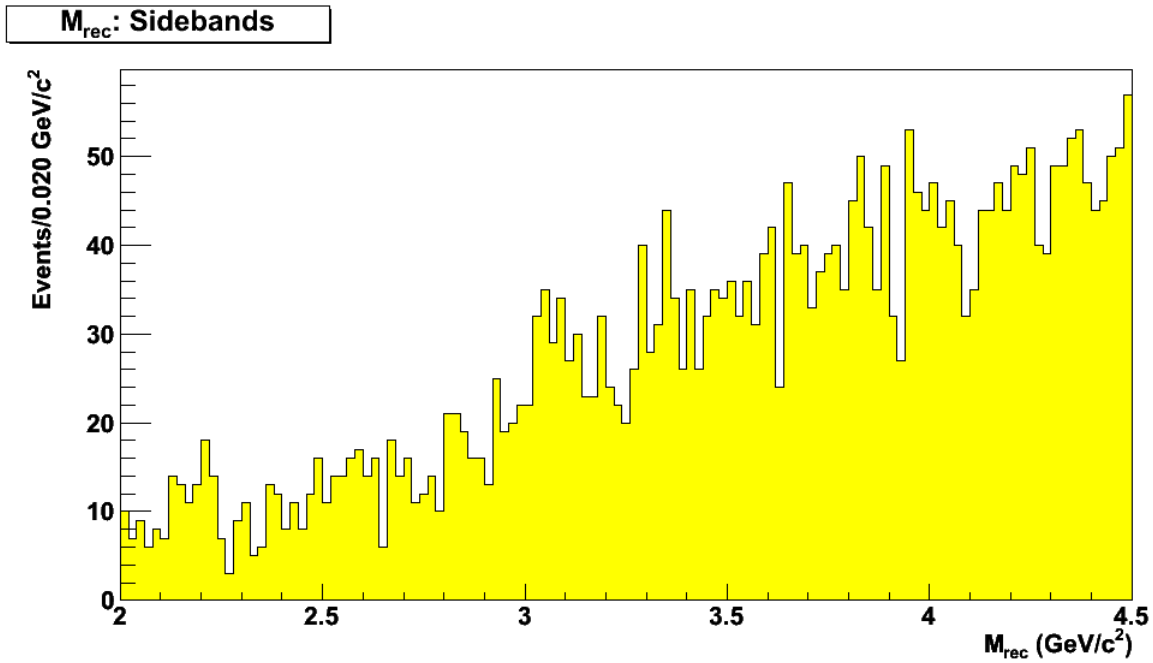

Figure 4.47: $e^+e^- \to J/\psi c\bar{c} \to \ell^+\ell^- c\bar{c}$: *Distribution of the mass recoling against the* J/ψ *from the* J/ψ *mass sidebands in the data.*

The largest backgrounds are due to real J/ψ mesons from QED processes:

- The $B\bar{B}$ events contain J/ψ which are of mostly low CM momenta. They are rejected by the minimum momentum requirement $p^*(J/\psi) < 3$ GeV/c and hence do not contribute to the observed recoiling charmonia below 5.5 GeV/c^2.
- Contributions from ISR $\psi(2S)$ have been evaluated with Monte Carlo samples of $e^+e^- \to \gamma_{ISR}\psi(2S)$ where $\psi(2S) \to X$. Most of them are rejected by the $\psi(2S)$ veto, but still some pass the cuts. The recoil mass of the leftover events is estimated with the ISR $\psi(2S)$ MC sample: the distribution is scaled to the data and is shown in Fig. 4.48.

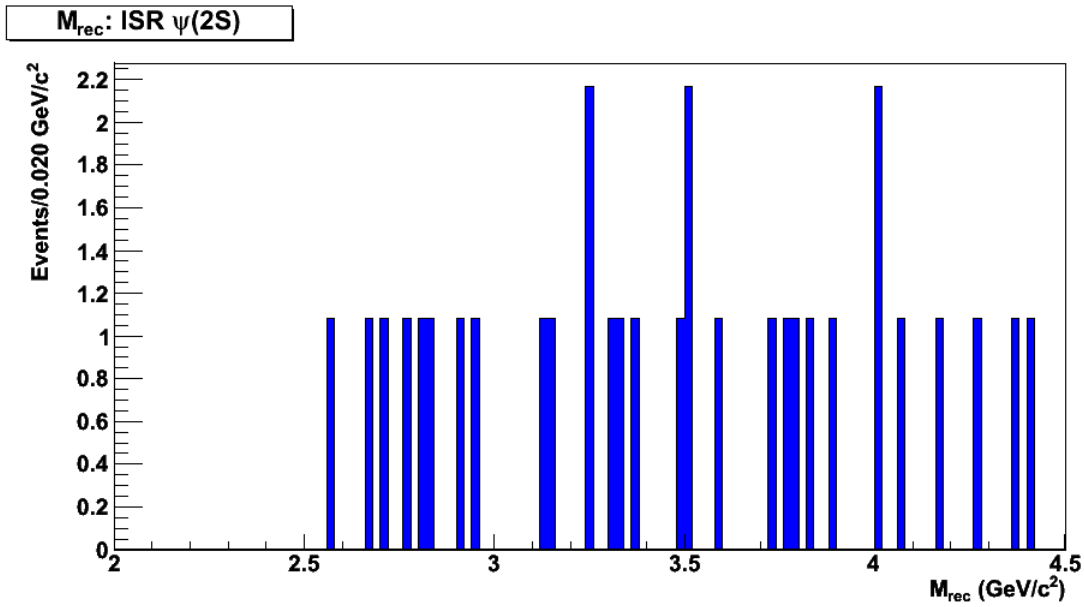

Figure 4.48: $e^+e^- \to J/\psi c\bar{c} \to \ell^+\ell^- c\bar{c}$: *Scaled distribution of the mass recoiling against the J/ψ in the ISR $\psi(2S)$ MC sample.*

- The possible $\psi(2S)$ feed down background is estimated using $\psi(2S)$ events selected in the data. The distribution mass recoiling against the J/ψ from this feed down is shown in Fig. 4.49.

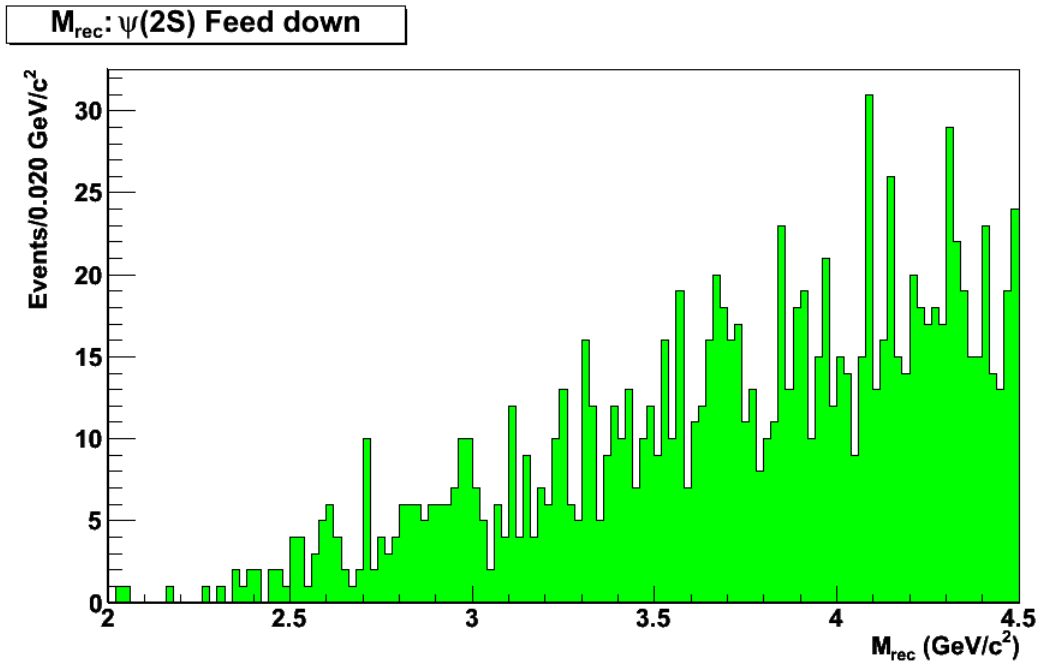

Figure 4.49: $e^+e^- \to J/\psi c\bar{c} \to \ell^+\ell^- c\bar{c}$: *Distribution of the mass recoiling against the* J/ψ *from the* $\psi(2S)$ *feed down in the data.*

Fig. 4.50 shows the distribution of the mass recoiling against the J/ψ from all the main background sources.

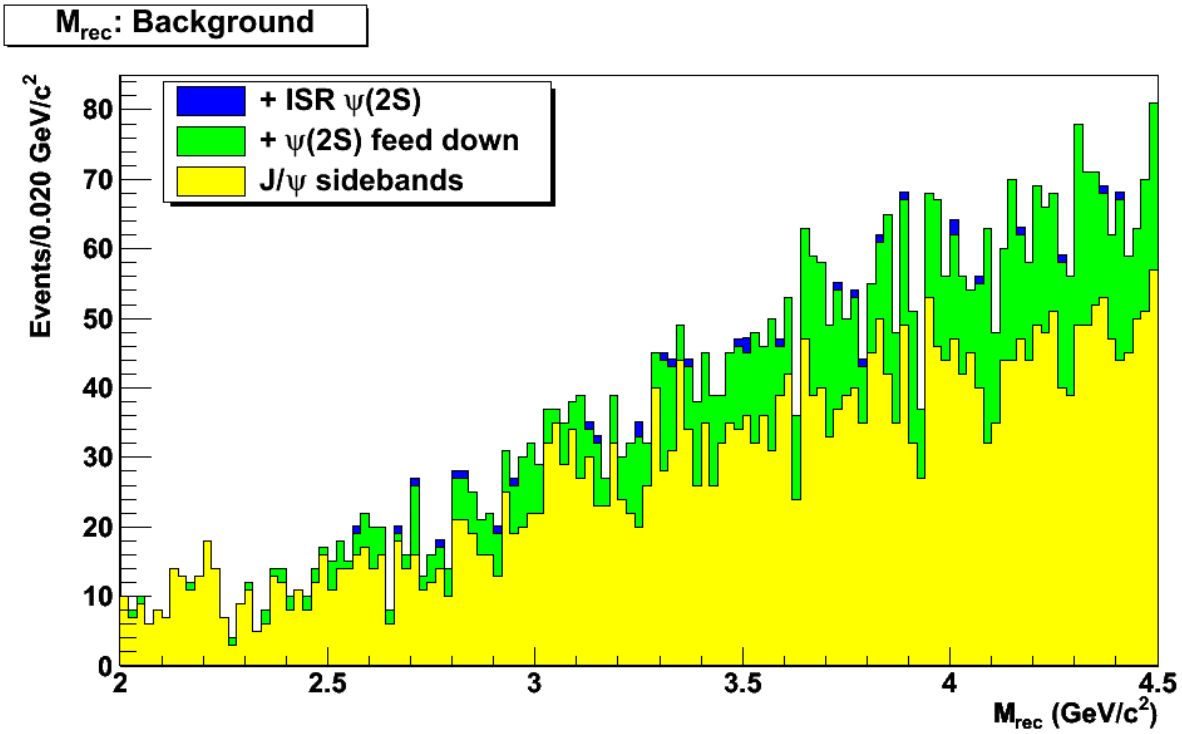

Figure 4.50: $e^+e^- \to J/\psi c\bar{c} \to \ell^+\ell^- c\bar{c}$: *Distribution of the mass recoiling against the J/ψ from the J/ψ mass sidebands (yellow), ISR $\psi(2S)$ (blue) and $\psi(2S)$ feed down (green) in the data.*

4.8.2 $e^+e^- \to \psi(2S)c\bar{c} \to \ell^+\ell^- c\bar{c}$

To estimate the combinatorial background due to random tracks we used the $\psi(2S)$ mass sidebands, defined in Eq. 4.4 and Eq. 4.5.
The mass recoiling against the $\psi(2S)$ from the $\psi(2S)$ mass sidebands is shown in Fig. 4.51.

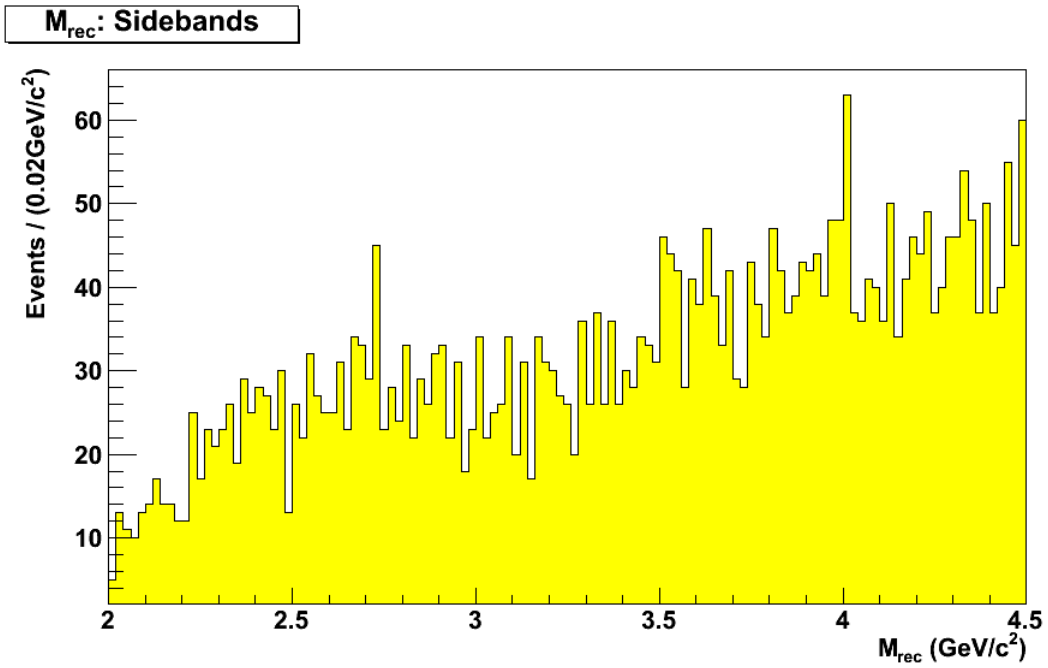

Figure 4.51: $e^+e^- \to \psi(2S)c\bar{c} \to \ell^+\ell^- c\bar{c}$: *Distribution of the mass recoiling against the* $\psi(2S)$ *from the* $\psi(2S)$ *mass sidebands in the data.*

Since the background is huge and we expect to see few events in the mass recoiling against the $\psi(2S)$ (See section 4.1.1), we didn't considered any other background sources.
For this reasons this analysis will not be carried any further.

4.8.3 $e^+e^- \to \psi(2S)c\bar{c} \to J/\psi\pi^+\pi^- c\bar{c}$

There are two main background sources in this analysis: events with genuine $\psi(2S)$ mesons and combinatorial background.
To estimate the combinatorial background due to random tracks we used the $\psi(2S)$ mass sidebands, defined in Eq. 4.6. The mass recoiling against the $\psi(2S)$ from the $\psi(2S)$ mass sidebands is shown in Fig. 4.52.

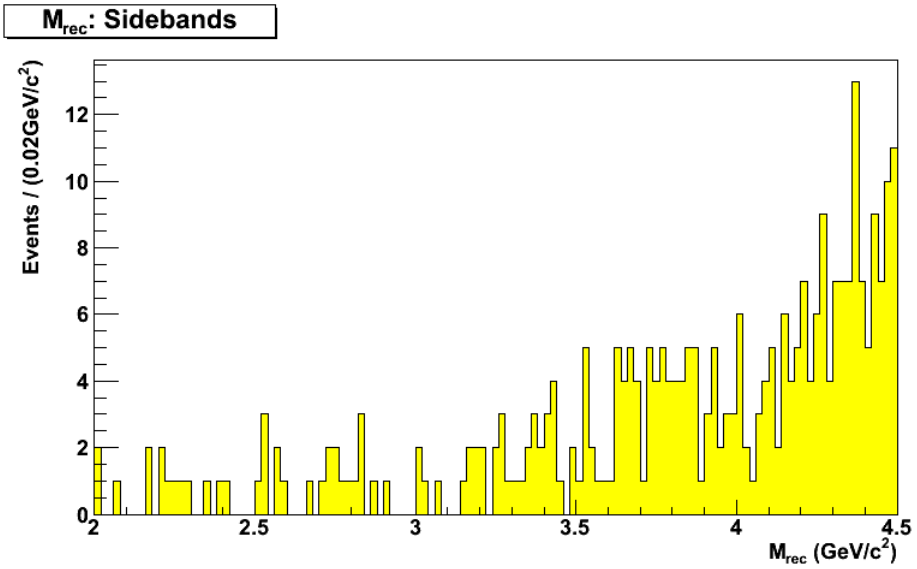

Figure 4.52: $e^+e^- \to \psi(2S)c\bar{c} \to J/\psi\pi^+\pi^- c\bar{c}$*: Distribution of the mass recoling against the* $\psi(2S)$ *from the* $\psi(2S)$ *mass sidebands in the data.*

The other backgrounds are due to real $\psi(2S)$ mesons from QED processes:

- The $B\bar{B}$ events contain $\psi(2S)$ which are of mostly low CM momenta. They are rejected by the minimum momentum requirement $p^*(\psi(2S)) < 3$ GeV/c and hence do not contribute to the observed recoiling charmonia below 5.5 GeV/c^2.
- Contributions from ISR $\psi(2S)$ have been evaluated with MonteCarlo samples of $e^+e^- \to \gamma_{ISR}\psi(2S)$ where $\psi(2S) \to X$. The contribution is negligible.

4.9 Simultaneous fit

After all the selection criteria we perform as a fit validation a simultaneous fit to our signal MC rescaled to the expected signal in the data and to our background contribution.

4.9.1 $e^+e^- \to J/\psi c\bar{c} \to \ell^+\ell^- c\bar{c}$

For this decay mode, we consider as signal the Monte Carlo data scaled to our expected number of events and as background the J/ψ sidebands, the ISR $\psi(2S)$ and the feed down contribution; in this way it is possible to reproduce the expected distribution of the recoil mass distribution, once the data is unblinded.
Fig. 4.53 shows the simultaneous fit for the channel $J/\psi \to \ell^+\ell^-$ and table 4.24 summarizes the fitted parameters obtained from this fit.

Particle	Mean (GeV/c^2)	N_{events} (e^+e^-)	N_{events} $(\mu^+\mu^-)$
η_c	2.995 ± 0.007	250 ± 30	129 ± 14
χ_{c0}	3.411 ± 0.009	189 ± 30	92 ± 16
$\eta_c(2S)$	3.640 ± 0.006	253 ± 53	160 ± 21
X(3940)	3.937 ± 0.003	100 ± 32	132 ± 25
Background	-	2609 ± 93	751 ± 47

Table 4.24: $e^+e^- \to J/\psi c\bar{c} \to \ell^+\ell^- c\bar{c}$*: Results of the simultaneous fit of the recoil mass against the* J/ψ*.*

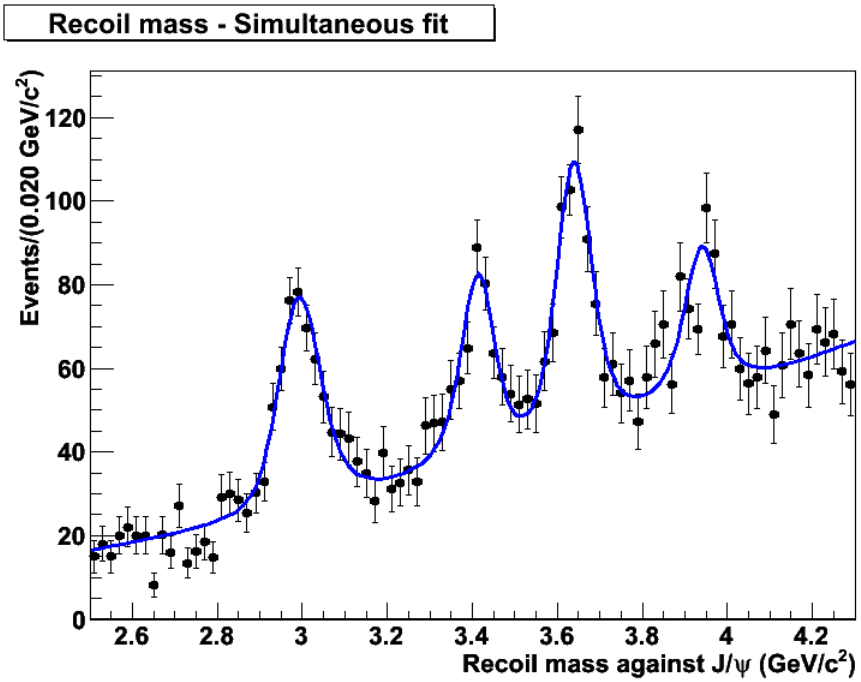

Figure 4.53: *Simultaneous fit on the recoil mass distribution (GeV/c^2) for the channel $e^+e^- \to J/\psi c\bar{c} \to \ell^+\ell^- c\bar{c}$ for $J/\psi \to \ell^+\ell^-$. The signal is fitted by Voigtian functions, and the background is fitted by a 2^{nd} order polynomial. χ^2/NDF=0.96*

4.10 Summary

In this chapter, we described the analysis strategy and the selection criteria, in addition we obtained the reconstruction efficiency and the resolution for all the decay mode studied.
We also defined the fit procedure to the recoil mass against the J/ψ and the $\psi(2S)$, that we will use in the next chapter for our final fit.

Chapter 5

Results

5.1 $e^+e^- \to J/\psi c\bar{c} \to \ell^+\ell^- c\bar{c}$

5.1.1 Unblinding the data up to 3.8 GeV

After the fit validation performed in section 4.9.1 of the previous chapter, we are ready to unblind the data on the region of interest. Anyway we first unblind the region of the mass recoiling against the J/ψ, for the Run1-Run6 data-taking periods, in the *BABAR* data in order to validate this analysis in the same region of the old one [21], with an increased statistics.
In Fig. 5.1 (a) and 5.1 (b) are shown the distributions of the recoil mass against the J/ψ for the electron and muon channels respectively.
Fig. 5.2 shows the global fit to the recoil mass against the J/ψ. J/ψ sidebands, ISR $\psi(2S)$ and feed down contributions to the background are presented in this plot; the fit results are presented in Tab. 5.1.

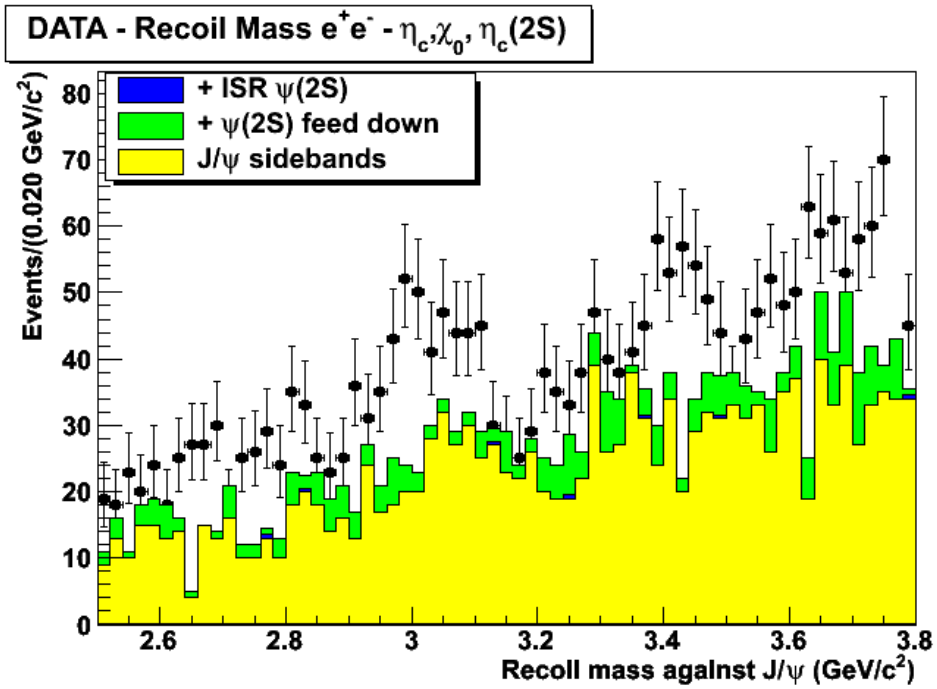

(a) Distribution of M_{rec}, for the sample with $J/\psi \to e^+e^-$ using the total dataset available from *BABAR*

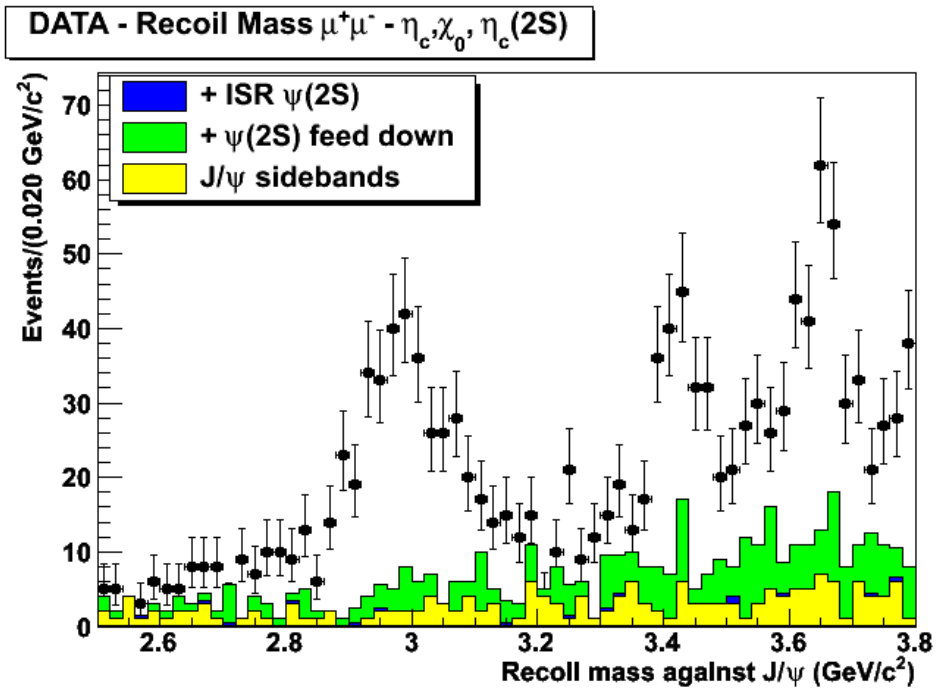

(b) Distribution of M_{rec}, for the sample with $J/\psi \to \mu^+\mu^-$ using the total dataset available from *BABAR*

Figure 5.1: *$e^+e^- \to J/\psi c\bar{c} \to \ell^+\ell^- c\bar{c}$: Distribution of M_{rec} (GeV/c^2), for the samples with $J/\psi \to e^+e^-$ and $J/\psi \to \mu^+\mu^-$, respectively, using the total dataset available from BABAR*

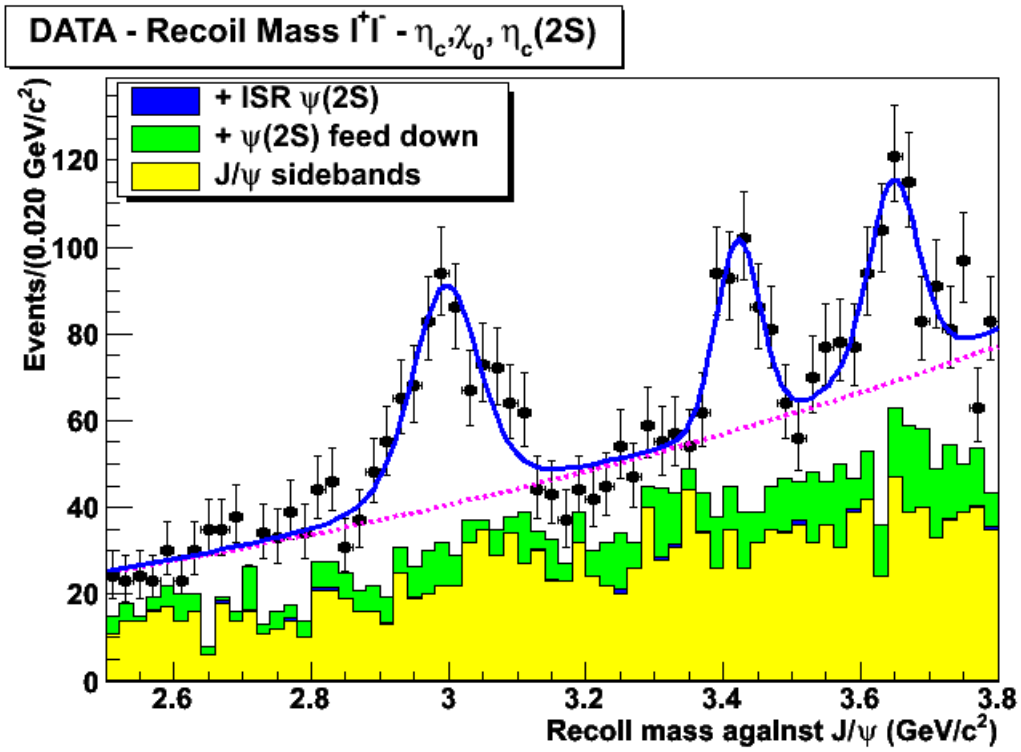

Figure 5.2: *Fit to the distribution of M_{rec} (GeV/c^2) using the full dataset available in BABAR for the channel $e^+e^- \to J/\psi c\bar{c} \to \ell^+\ell^- c\bar{c}$ for $J/\psi \to \ell^+\ell^-$. The signal is fitted by Voigtian functions, and the background is fitted by a 2^{nd} order polynomial (magenta line). χ^2/NDF=0.71*

Particle	Mean (GeV/c^2)	N_{events}
η_c	2.996 $\pm$ 0.006	354 $\pm$ 33
χ_{c0}	3.422 $\pm$ 0.006	171 $\pm$ 27
$\eta_c(2S)$	3.648 $\pm$ 0.007	231 $\pm$ 36

Table 5.1: *$e^+e^- \to J/\psi c\bar{c} \to \ell^+\ell^- c\bar{c}$: Fit results of the recoil mass against the J/ψ, in the full BABAR dataset, for $J/\psi \to \ell^+\ell^-$.*

5.1.2 Unblinding the data up to 4.3 GeV

One of the aims of this analysis is to confirm the new state X(3940), claimed by Belle collaboration [35], but not yet confirmed by *BABAR* . In this section the results of the fit to M_{rec} up to 4.3 GeV are shown.
In Fig. 5.3 (a) and in Fig. 5.3 (b) are shown the distributions of the recoiling against the J/ψ for $J/\psi \to e^+e^-$ and for $J/\psi \to \mu^+\mu^-$ respectively.
Fig. 5.4 shows the distribution of the mass recoiling against the J/ψ with the data collected by *BABAR* in the data-taking periods Run1-Run6.
A structure in the high region of the distribution is visible, and it has been fitted as a resonance centered at 3.940 GeV/c^2.

5.1.3 Final results

In summary, in the mass spectrum of the system recoiling against the fully reconstructed J/ψ, three enhancements at 2.995, 3.420 and 3.646 GeV/c^2, consistent with η_c, χ_{c0} and $\eta_c(2S)$, respectively, are observed: this is a confirmation of the results obtained in the previous *BABAR* analysis [21].
With the unblinding up to 4.3 GeV/c^2, a structure is observed, with mass centered around 3.940 GeV/c^2 and width compatible with the Belle measurement: this is a confirmation of the X(3940) state, seen by Belle [35]. The significance of the X(3940) signal is higher than 4 σ.
In table 5.2 a summary of the results of this analysis is shown. In addition a comparison with the cross section measured by Belle [38] and by the previous analysis done by *BABAR* [21] is summarized in table 5.3.

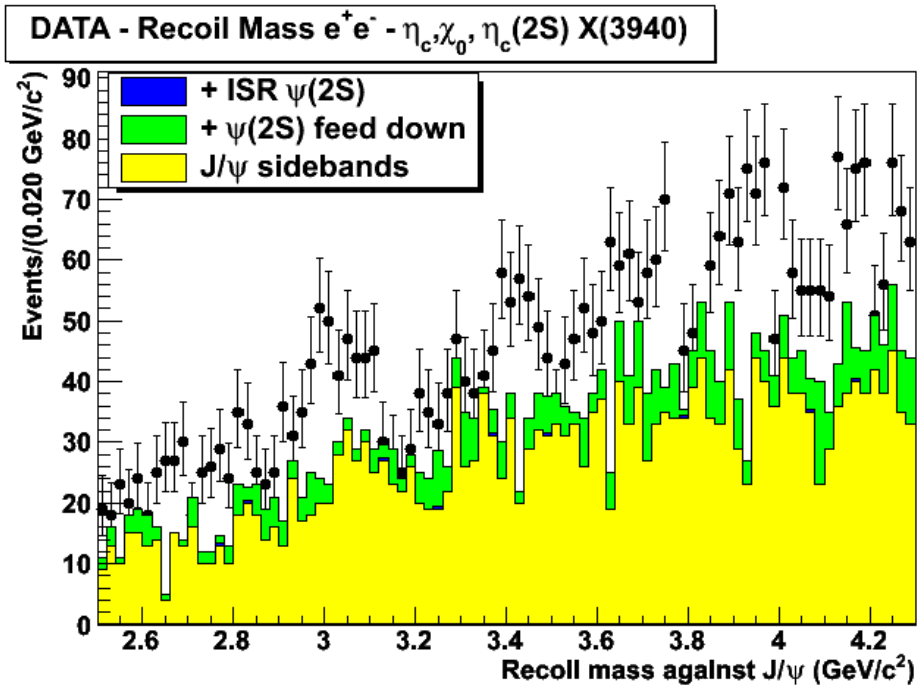

(a) Distribution of M_{rec}, for the sample with $J/\psi \to e^+e^-$ using the total dataset available from *BABAR*

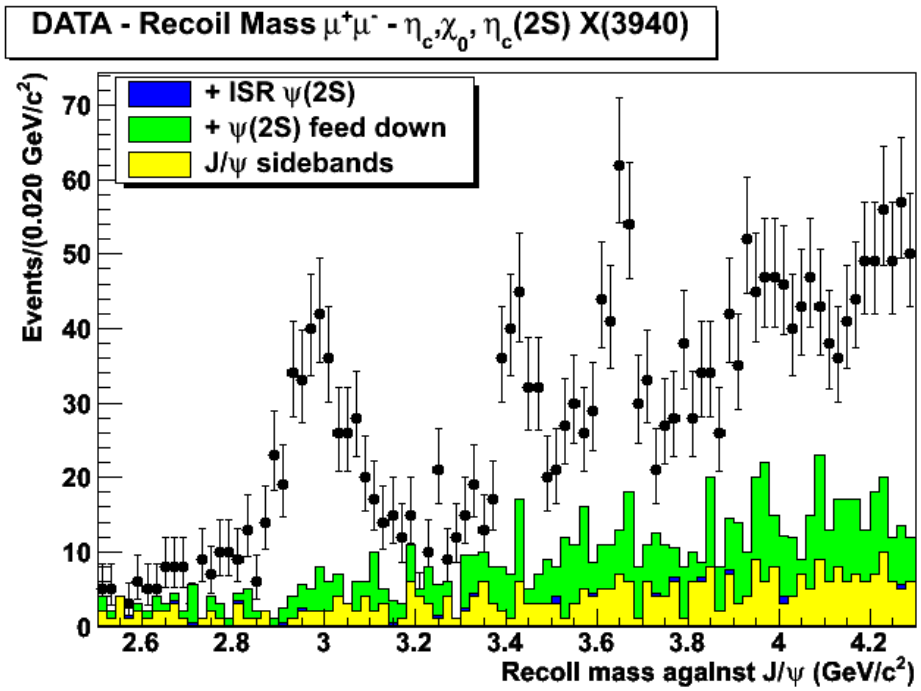

(b) Distribution of M_{rec}, for the sample with $J/\psi \to \mu^+\mu^-$ using the total dataset available from *BABAR*

Figure 5.3: $e^+e^- \to J/\psi c\bar{c} \to \ell^+\ell^- c\bar{c}$: *Distribution of* M_{rec} (GeV/c^2), *for the samples with* $J/\psi \to e^+e^-$ *and* $J/\psi \to \mu^+\mu^-$, *respectively, using the total dataset available from BABAR*

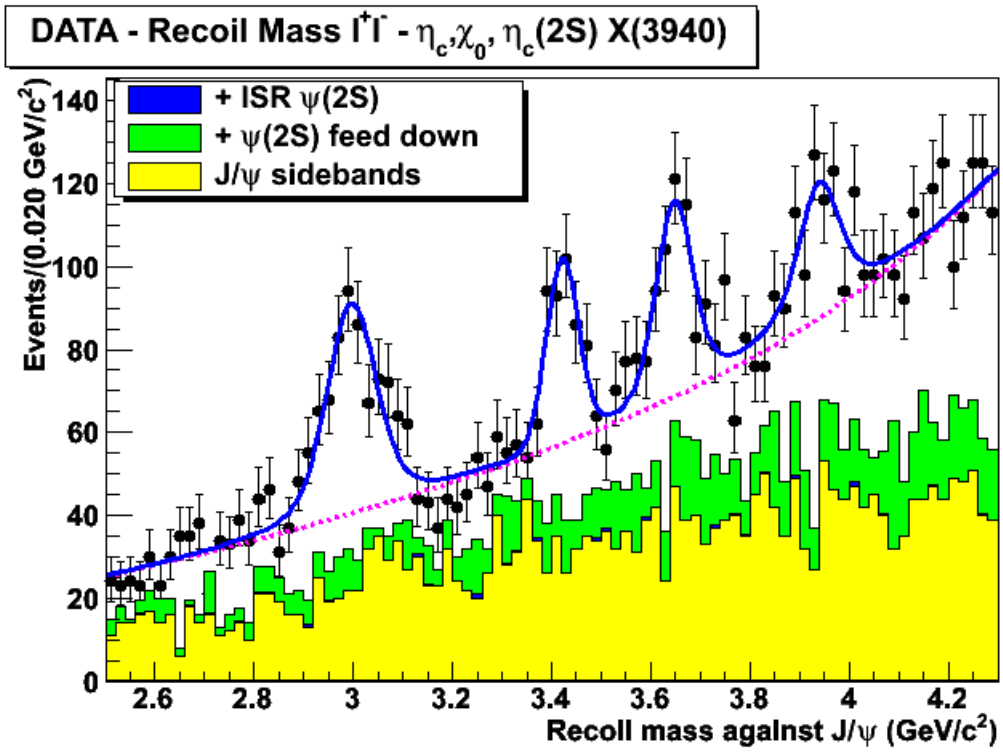

Figure 5.4: *Fit to the distribution of M_{rec} (GeV/c^2) using the full dataset available in BABAR for the channel $e^+e^- \to J/\psi c\bar{c} \to \ell^+\ell^- c\bar{c}$ for $J/\psi \to \ell^+\ell^-$. The signal is fitted by Voigtian functions, and the background is fitted by a 2^{nd} order polynomial (magenta line). χ^2/NDF=0.70*

Particle	Mean (GeV/c^2)	Efficiency (%)	N_{events}	Born cross-section (fb)
η_c	2.995 ± 0.006	20.73 ± 0.18	354 ± 29	29.90 ± 3.31
χ_{c0}	3.420 ± 0.005	28.06 ± 0.21	165 ± 23	10.29 ± 1.64
$\eta_c(2S)$	3.646 ± 0.006	18.98 ± 0.18	213 ± 31	19.65 ± 3.44
X(3940)	3.940 ± 0.009	30.13 ± 0.10	174 ± 39	10.11 ± 2.50

Table 5.2: $e^+e^- \to J/\psi c\bar{c} \to \ell^+\ell^- c\bar{c}$*: Summary of the final results*

Particle	*BABAR* [21]	Belle [38]	This analysis
η_c	17.6 ± 2.8 ± 2.1	25.6 ± 2.8 ± 3.4	29.90 ± 3.31
χ_{c0}	10.3 ± 2.8 ± 2.1	6.4 ± 1.7 ± 1.0	10.29 ± 1.64
$\eta_c(2S)$	16.4 ± 2.8 ± 2.1	16.5 ± 3.0 ± 2.4	19.65 ± 3.44
X(3940)	-	10.6 ± 2.5 ± 2.4	10.11 ± 2.50

Table 5.3: $e^+e^- \to J/\psi c\bar{c} \to \ell^+\ell^- c\bar{c}$*: Comparison of cross sections (in fb) with the results measured by* BABAR *and Belle*

5.2 $e^+e^- \to \psi(2S)c\bar{c} \to J/\psi\pi^+\pi^- c\bar{c}$

5.2.1 Unblinding the data up to 3.8 GeV

We first unblind the region of the mass recoiling against the $\psi(2S)$, for the Run1-Run6 data-taking periods, in the *BABAR* data in order to validate this analysis in the same region of the Belle analysis [38], with an increased statistics.
In Fig. 5.5 (a) and 5.5 (b) are shown the distributions of the recoil mass against the $\psi(2S)$ for the electron and muon channel respectively.
Fig. 5.6 shows the global fit to the recoil mass against the $\psi(2S)$. $\psi(2S)$ sidebands contribution to the background are presented in this plot; the fit results are presented in Tab. 5.4.

Particle	Mean (GeV/c^2)	N_{events}
η_c	2.999 $\pm$ 0.011	88 $\pm$ 15
χ_{c0}	3.431 $\pm$ 0.008	58 $\pm$ 13
$\eta_c(2S)$	3.648 $\pm$ 0.013	55 $\pm$ 17

Table 5.4: *Fit results of the recoil mass against the* $\psi(2S)$ *for the channel* $e^+e^- \to \psi(2S)c\bar{c} \to J/\psi\pi^+\pi^- c\bar{c}$, *in the full BABAR dataset, for* $J/\psi \to \ell^+\ell^-$.

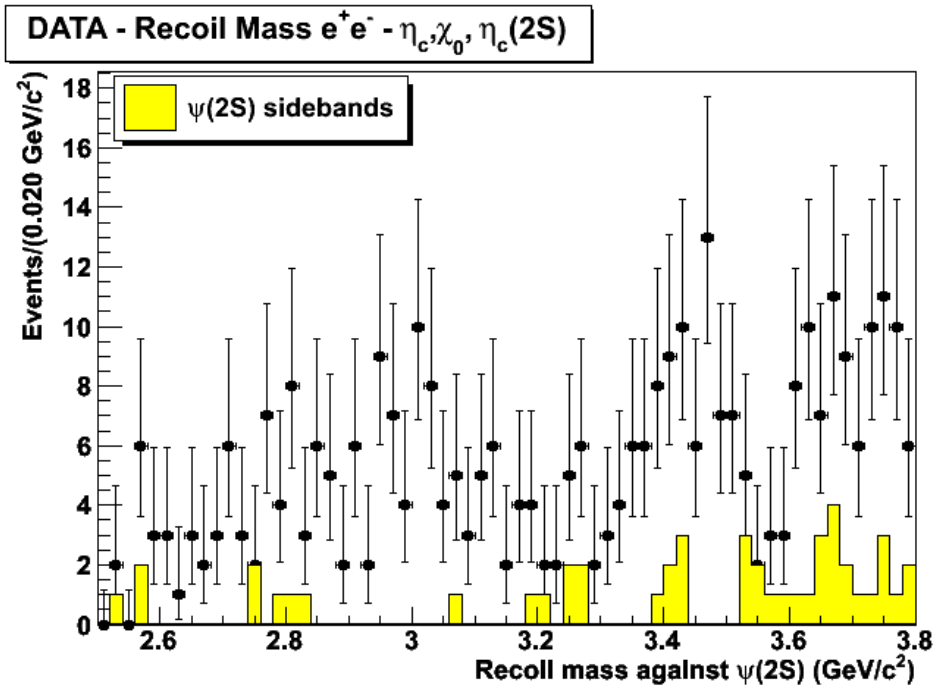

(a) Distribution of M_{rec}, for the channel $e^+e^- \to \psi(2S)c\bar{c} \to J/\psi\pi^+\pi^-c\bar{c}$ for $J/\psi \to e^+e^-$ using the total dataset available from *BABAR*

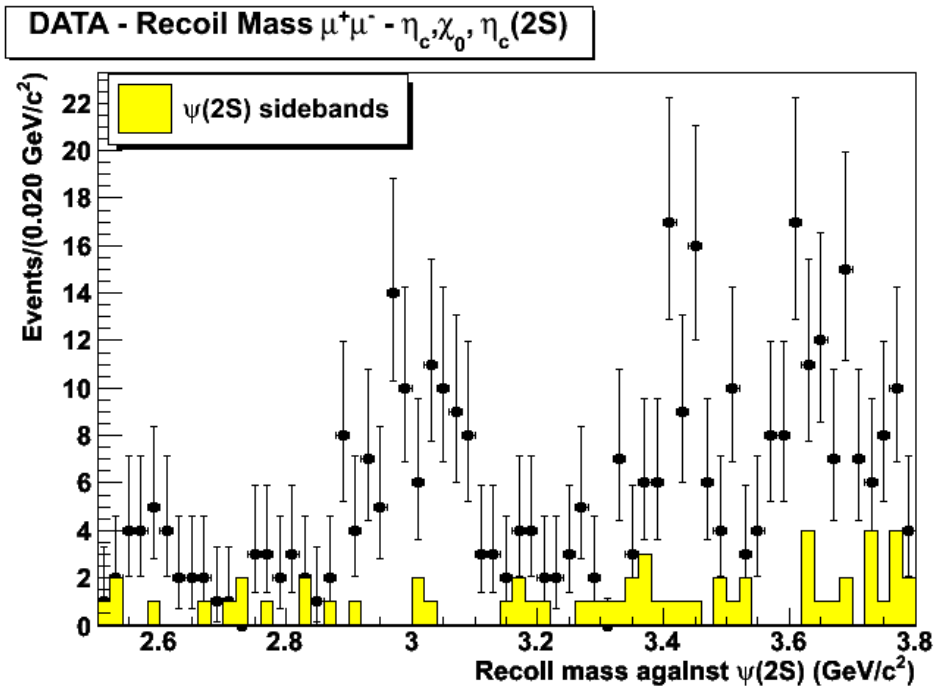

(b) Distribution of M_{rec}, for the channel $e^+e^- \to \psi(2S)c\bar{c} \to J/\psi\pi^+\pi^-c\bar{c}$ for $J/\psi \to \mu^+\mu^-$ using the total dataset available from *BABAR*

Figure 5.5: *Distribution of M_{rec} (GeV/c^2), for the channel $e^+e^- \to \psi(2S)c\bar{c} \to J/\psi\pi^+\pi^-c\bar{c}$ for $J/\psi \to e^+e^-$ and $J/\psi \to \mu^+\mu^-$, respectively, using the total dataset available from BABAR*

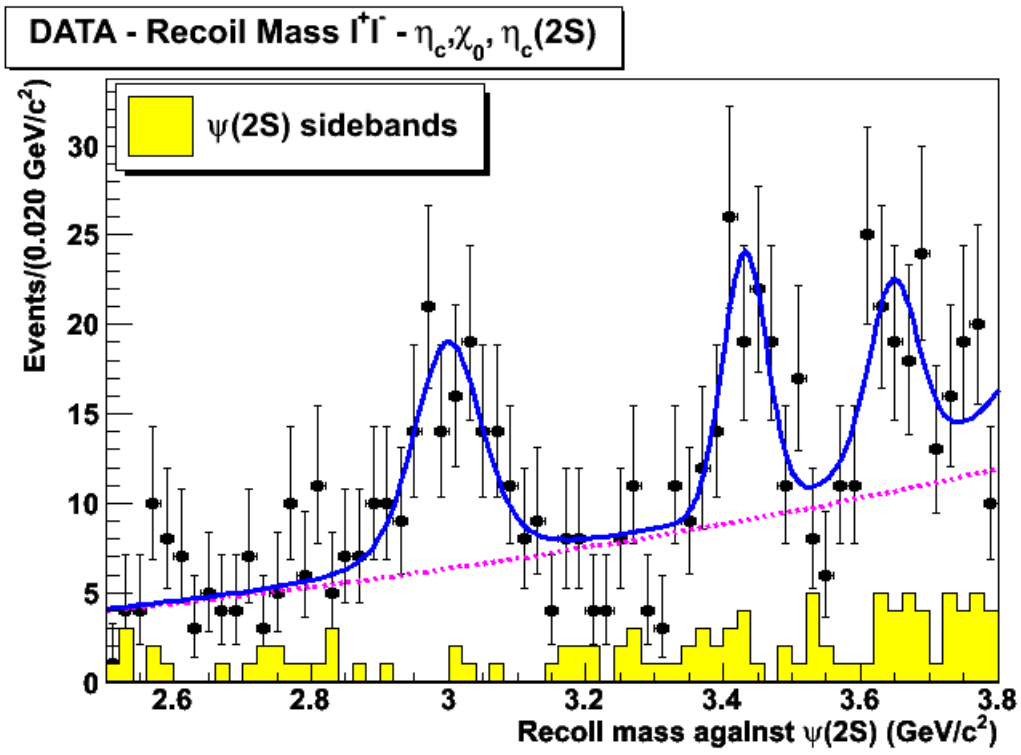

Figure 5.6: *Distribution of M_{rec} (GeV/c^2) using the full dataset available in* BABAR *for the channel $e^+e^- \to \psi(2S)c\bar{c} \to J/\psi\pi^+\pi^- c\bar{c}$ for $J/\psi \to \ell^+\ell^-$. The signal is fitted by Voigtian functions, and the background is fitted by a 2^{nd} order polynomial (magenta line). χ^2/NDF=0.72*

5.2.2 Unblinding the data up to 4.3 GeV

One of the aims of this analysis is to confirm the new state X(3940), never studied in this decay mode. In this section the results of the fit to M_{rec} up to 4.3 GeV are shown.
In Fig. 5.7 (a) and in Fig. 5.7 (b) are shown the distributions of the recoiling against the $\psi(2S)$ for $J/\psi \to e^+e^-$ and for $J/\psi \to \mu^+\mu^-$ respectively.
Fig. 5.8 shows the distribution of the mass recoiling against the $\psi(2S)$ with the data collected by *BABAR* in the data-taking periods Run1-Run6.
In this decay mode we can see that the X(3940) resonance is not significant for this reason we will not include its contribution in the final result.

5.2.3 Final results

In summary, in the mass spectrum of the system recoiling against the fully reconstructed $\psi(2S)$, three enhancements at 2.999, 3.431 and 3.648 GeV/c^2, consistent with η_c, χ_{c0} and $\eta_c(2S)$, respectively, are observed: this is a confirmation of the results obtained in the previous Belle analysis [38].
With the unblinding up to 4.3 GeV/c^2, the X(3940) is not visible.
In table 5.5 a summary of the results of this analysis is shown. In addition a comparison with the cross section measured by Belle [38] is summarized in table 5.6.

Particle	Mean (GeV/c^2)	Efficiency (%)	N_{events}	Born cross-section (fb)
η_c	2.999 $\pm$ 0.011	24.03 $\pm$ 0.19	88 $\pm$ 15	19.08 $\pm$ 3.26
χ_{c0}	3.431 $\pm$ 0.008	26.96 $\pm$ 0.23	58 $\pm$ 13	11.21 $\pm$ 2.52
$\eta_c(2S)$	3.648 $\pm$ 0.013	25.75 $\pm$ 0.22	55 $\pm$ 17	11.13 $\pm$ 3.44

Table 5.5: $e^+e^- \to \psi(2S)c\bar{c} \to J/\psi\pi^+\pi^- c\bar{c}$*: Summary of the final results*

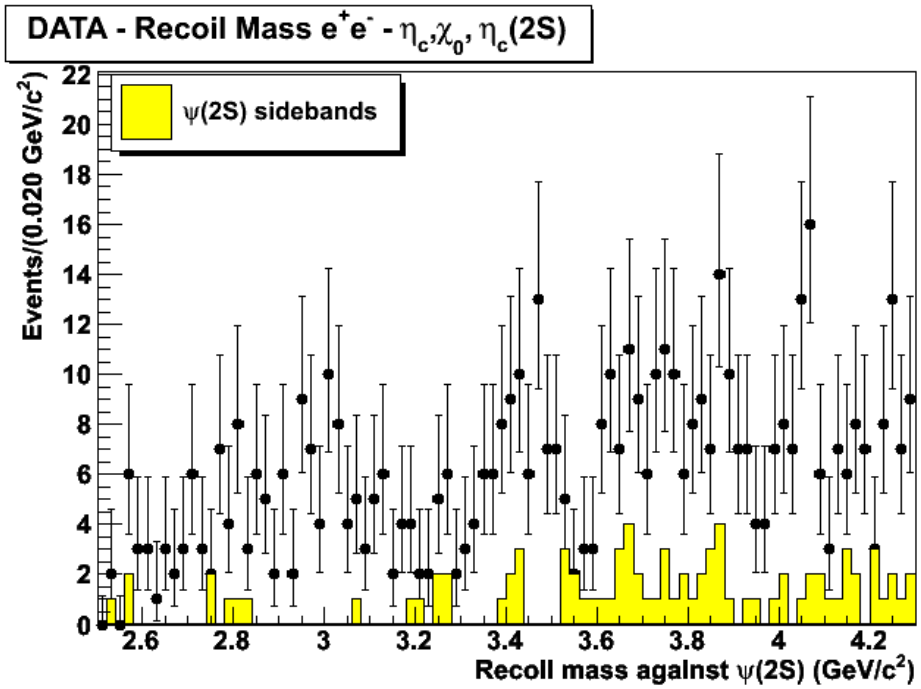

(a) Distribution of M_{rec}, for the channel $e^+e^- \to \psi(2S)c\bar{c} \to J/\psi\pi^+\pi^-c\bar{c}$ for $J/\psi \to e^+e^-$ using the total dataset available from *BABAR*

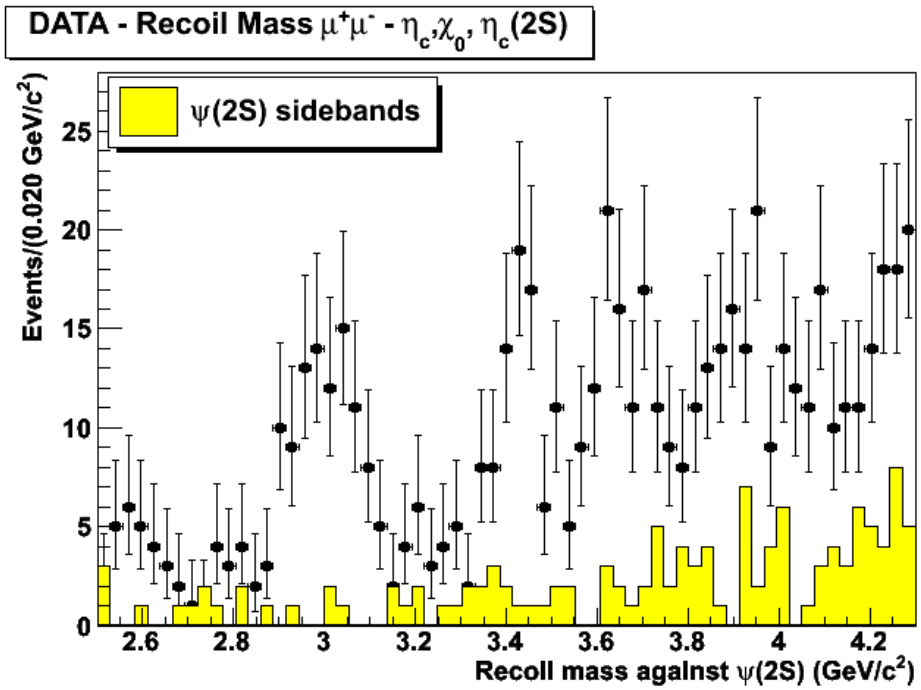

(b) Distribution of M_{rec}, or the channel $e^+e^- \to \psi(2S)c\bar{c} \to J/\psi\pi^+\pi^-c\bar{c}$ for $J/\psi \to \mu^+\mu^-$ using the total dataset available from *BABAR*

Figure 5.7: *Distribution of M_{rec} (GeV/c^2), for the channel $e^+e^- \to \psi(2S)c\bar{c} \to J/\psi\pi^+\pi^-c\bar{c}$ for $J/\psi \to e^+e^-$ and $J/\psi \to \mu^+\mu^-$, respectively, using the total dataset available from BABAR*

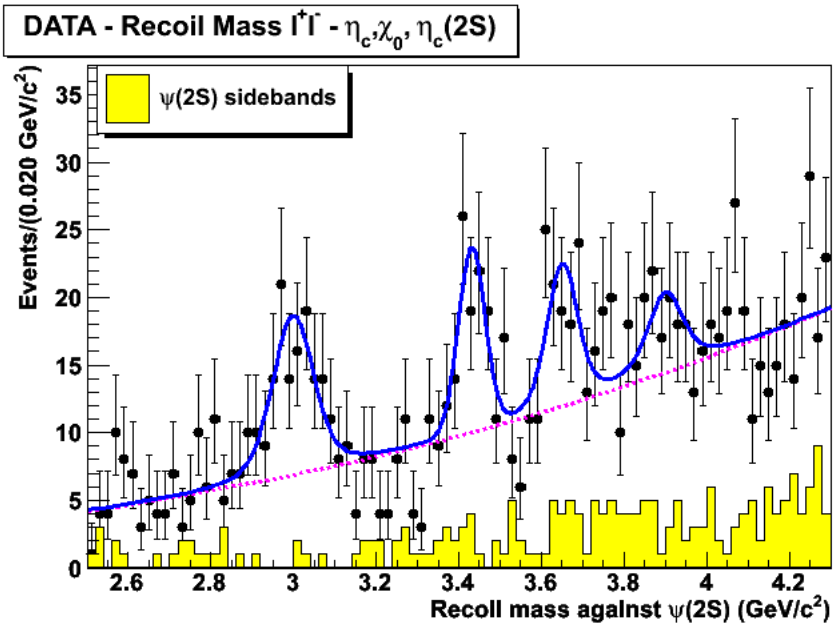

(a) Distribution of M_{rec}, for the channel $e^+e^- \to \psi(2S)c\bar{c} \to J/\psi\pi^+\pi^- c\bar{c}$ for $J/\psi \to e^+e^-$ using the total dataset available from *BABAR* . The fit to X(3940) is shown. χ^2/NDF=0.72

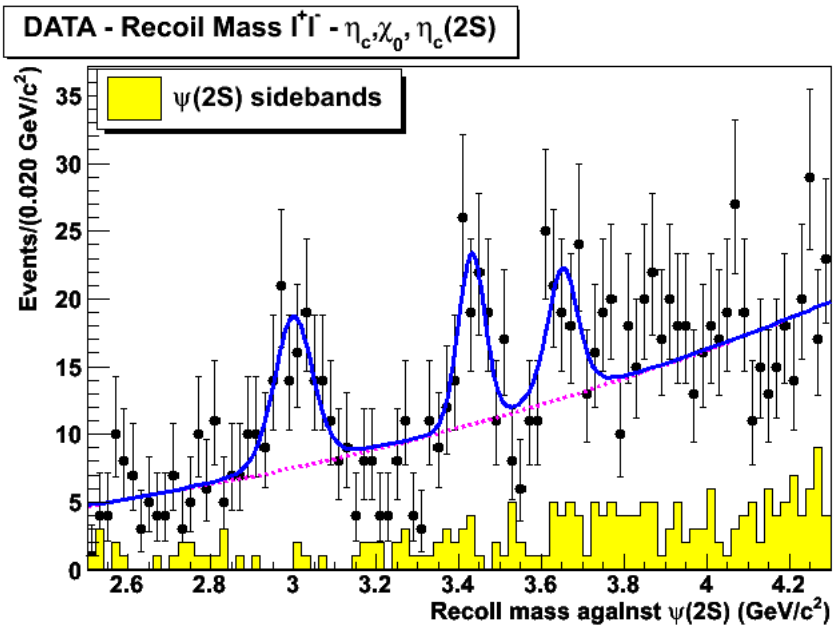

(b) Distribution of M_{rec}, or the channel $e^+e^- \to \psi(2S)c\bar{c} \to J/\psi\pi^+\pi^- c\bar{c}$ for $J/\psi \to \mu^+\mu^-$ using the total dataset available from *BABAR* . The fit is without the X(3940) resonance. χ^2/NDF=0.72

Figure 5.8: *Distribution of M_{rec} (GeV/c^2), for the channel $e^+e^- \to \psi(2S)c\bar{c} \to J/\psi\pi^+\pi^- c\bar{c}$ for $J/\psi \to e^+e^-$ and $J/\psi \to \mu^+\mu^-$, respectively, using the total dataset available from BABAR . The signal is fitted by Voigtian functions, and the background is fitted by a 2^{nd} order polynomial (magenta line).*

Particle	Belle [38]	This analysis
η_c	$16.3 \pm 4.6 \pm 3.9$	19.08 ± 3.26
χ_{c0}	$12.5 \pm 3.8 \pm 3.1$	11.21 ± 2.52
$\eta_c(2S)$	$16.0 \pm 5.1 \pm 3.8$	11.13 ± 3.44

Table 5.6: $e^+e^- \to \psi(2S)c\bar{c} \to J/\psi\pi^+\pi^- c\bar{c}$: *Comparison of cross sections (in fb) with the results measured by Belle*

5.3 $e^+e^- \to \psi(2S)c\bar{c} \to \ell^+\ell^- c\bar{c}$

We have estimated in section 4.4.1 that we expect very few signal events for each resonance and in addition the background level for this channel is very high. Fig. 5.9 shows that our expectations were right and there is no signal presence.

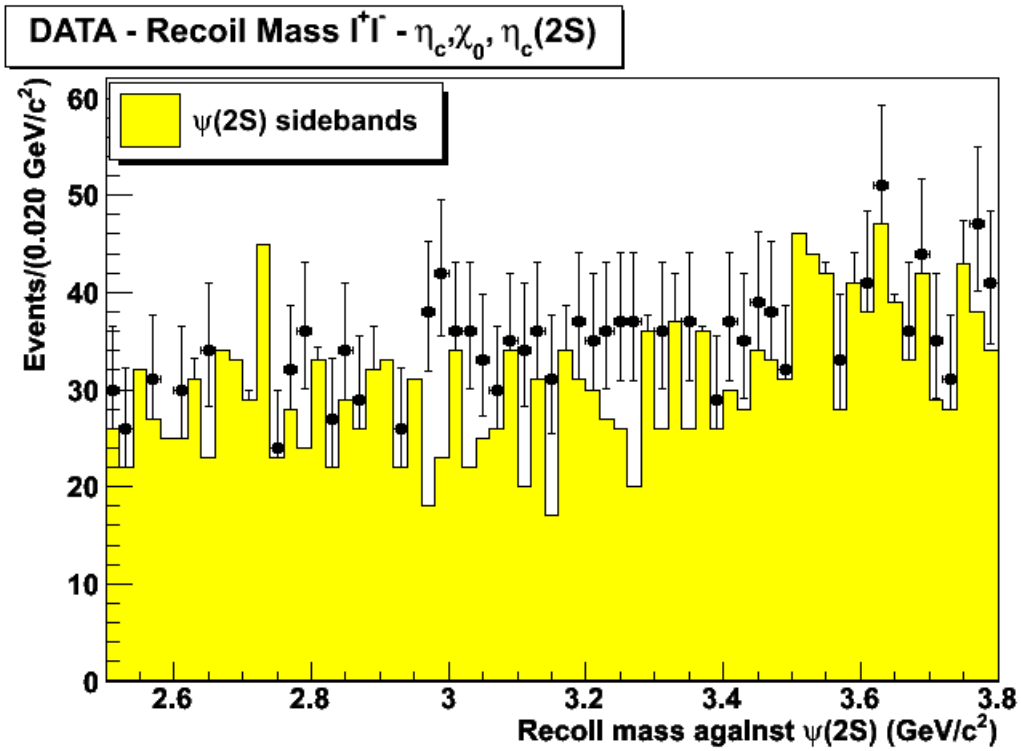

Figure 5.9: *Distribution of M_{rec} ($GeV(c^2)$) using the full dataset available in BABAR for the channel $e^+e^- \to \psi(2S)c\bar{c} \to \ell^+\ell^- c\bar{c}$.*

Summary and conclusion

We have studied the double charmonium production with the *BABAR* detector at $\sqrt{s}$=10.58 GeV. In particular we have studied three decay modes:

- $e^+e^- \to J/\psi c\bar{c} \to \ell^+\ell^- c\bar{c}$
- $e^+e^- \to \psi(2S) c\bar{c} \to J/\psi\pi^+\pi^- c\bar{c}$
- $e^+e^- \to \psi(2S) c\bar{c} \to \ell^+\ell^- c\bar{c}$

1. $\mathbf{e^+e^- \to J/\psi c\bar{c} \to \ell^+\ell^- c\bar{c}}$

   The double charmonium analysis $e^+e^- \to J/\psi c\bar{c} \to \ell^+\ell^- c\bar{c}$ was already done by the *BABAR* collaboration [21] and by the Belle collaboration [38] which reported the observation of η_c, χ_{c0} and $\eta_c(2S)$ in the mass distribution of the system recoiling against the J/ψ. In addition Belle also reported in the recoil spectrum the resonance X(3940) [35] that is probably a candidate of $\eta_c(3S)$.
   The work presented in this thesis is an update of a previous *BABAR* study with more statistic: from 124 fb^{-1} (Run1-Run3) to 478 fb^{-1} (Run1-Run6).
   In the mass spectrum of the system recoiling against the fully reconstructed J/ψ, three enhancements at 2.995, 3.420 and 3.646 GeV/c^2, consistent with η_c, χ_{c0} and $\eta_c(2S)$, respectively, are observed: this is a confirmation of the results obtained in the previous *BABAR* analysis [21].
   With the unblinding up to 4.3 GeV/c^2, a structure is observed, with mass centered around 3.940 GeV/c^2 and width compatible with the Belle measurement: this is a confirmation of the X(3940) state, seen by Belle [35]. The significance of the X(3940) signal is higher than 4 σ.

A comparison with the cross section measured by Belle [38] and by the previous analysis done by *BABAR* [21] is summarized in table 5.7.

Particle	*BABAR* [21]	Belle [38]	This analysis
η_c	17.6 ± 2.8 ± 2.1	25.6 ± 2.8 ± 3.4	29.90 ± 3.31
χ_{c0}	10.3 ± 2.8 ± 2.1	6.4 ± 1.7 ± 1.0	10.29 ± 1.64
$\eta_c(2S)$	16.4 ± 2.8 ± 2.1	16.5 ± 3.0 ± 2.4	19.65 ± 3.44
X(3940)	-	10.6 ± 2.5 ± 2.4	10.11 ± 2.50

Table 5.7: *$e^+e^- \to J/\psi c\bar{c} \to \ell^+\ell^- c\bar{c}$: Comparison of cross sections (in fb) with the results measured by BABAR and Belle*

2. **$e^+e^- \to \psi(2S)c\bar{c} \to J/\psi\pi^+\pi^- c\bar{c}$**

   The double charmonium analysis $e^+e^- \to \psi(2S)c\bar{c} \to J/\psi\pi^+\pi^- c\bar{c}$ was already done by the Belle collaboration [38] which reported the observation of η_c, χ_{c0} and $\eta_c(2S)$ in the mass distribution of the system recoiling against the $\psi(2S)$. The confirmation by *BABAR* of this observation is important. One improvement on this analysis consists in more statistics: 155 fb^{-1} to 478 fb^{-1}.

   In the mass spectrum of the system recoiling against the fully reconstructed $\psi(2S)$, three enhancements at 2.999, 3.431 and 3.648 GeV/c^2, consistent with η_c, χ_{c0} and $\eta_c(2S)$, respectively, are observed: this is a confirmation of the results obtained in the previous Belle analysis [38]. With the unblinding up to 4.3 GeV/c^2, the X(3940) is not visible, probably the reason is that we have not enough statistics to see it.

   A comparison with the cross section measured by Belle [38] is summarized in table 5.8.

3. **$e^+e^- \to \psi(2S)c\bar{c} \to \ell^+\ell^- c\bar{c}$**

   For the double charmonium analysis $e^+e^- \to \psi(2S)c\bar{c} \to \ell^+\ell^- c\bar{c}$ there are no experimental reference available. We have estimate in the section 4.4.1 that we expect very few signal events for each resonance and in addition the background level for this channel is very high. The unblinding on the data shows that our expectation were right and there is no signal presents.

Particle	Belle [38]	This analysis
η_c	$16.3 \pm 4.6 \pm 3.9$	19.08 ± 3.26
χ_{c0}	$12.5 \pm 3.8 \pm 3.1$	11.21 ± 2.52
$\eta_c(2S)$	$16.0 \pm 5.1 \pm 3.8$	11.13 ± 3.44

Table 5.8: $e^+e^- \to \psi(2S)c\bar{c} \to J/\psi\pi^+\pi^- c\bar{c}$*: Comparison of cross sections (in fb) with the results measured by Belle*

The future plans is to submit this work to the collaboration for a pubblication.

Appendix A

BABAR Particle Identification

BABAR Track List:

- **TaggingList**: Candidates with non-zero charge. Mass hypothesis, is assigned by the tagging algorithm.
- **ChargedTracks:** Same as TaggingList, but with pion mass hypothesis assigned.
- **CalorNeutral:** Candidates which are single EMC bumps not matched with any tracks. Photon mass hypothesis assigned. All single-bump neutral clusters show up both in the CalorNeutral and in the CalorClusterNeutral lists.
- **CalorClusterNeutral:** Candidates that are multi-bump neutral clusters or single bumps which are not part of a cluster which is matched with a tracks. These candidates may be embedded in charged candidates. All single-bump neutral clusters show up in both the CalorNeutral and CalorClusterNeutral lists.
- **NeutralHad:** Candidates with charge zero and no EMC information. (i.e. a neutral candidate with IFR info which has not been merged with a track or an EMC bump/cluster.)
- **SingleBumpNeutralClusters:** Single Bump Neutral Clusters in the EMC.

- **GoodTracksVeryLoose:** Charged Tracks with Min Transverse Momentum: 0.0 GeV, Max Momentum: 10 GeV, Min number of Dch Hits: 0, Min Fit Chi-Square Prob.: 0, Max DOCA (Distance of closest approach) in XY plane: 1.5 cm, Min Z Doca: -10 cm, Max Z Doca: 10 cm.
- **GoodTracksLoose:** Same cuts as GoodTracksVeryLoose with Min Transverse Momentum: 0.1 GeV and Min number of Dch Hits: 12.
- **GoodPhotonLoose:** Candidates from CalorNeutral satisfying: Min Raw Energy: 0.030 GeV, Min Num of Crystal: 0, Max Lateral Momentum: 0.8

BABAR Particle Identification (PID) selectors:

The *BABAR* PID group provides several different types of PID selector:

- Cut-based selectors impose simple cuts on the PID variables. Different levels of selector- VeryLoose (most efficiency, least pure), Loose, Tight, VeryTight (most pure, least efficient) correspond to looser or tighter sets of cuts. The level of selector required is determined by studying the efficiencies and purities of those selectors for a specific analysis.
- Likelihood selectors use the PID variables to compute Likelihood functions for different particle ID hypothesis. Different levels of selector correspond to tighter or looser cuts on the Likelihood functions. For example, the kaon likelihood selector requires that the likelihood for kaons be higher than the likelihood for pions.
- Neural network selectors use the PID variables as inputs to a neural network algorithm. Neural networks predict outcomes based on a large sample of previous examples. For PID, this means that they are given examples of how PID variables behave for different particles and optimize the selection based on this training.
- Boost Decision Tree is a binary tree structured classifier where repeated yes/no decisions are taken on one single variable at a time until a stop criterion is fulfilled.

Electrons

For electrons there are several Cut-based ("Micro") selector (eMicroNoCal, eMicroVeryLoose, eMicroLoose, eMicroTight, eMicroVeryTight) and a Likelihood ("LH") selector, PidLHElectrons. These selectors use the following PID variables:

- E/p where E is the measured energy of a shower in the calorimeter and p is the measured momentum of the corresponding charged tracks. When an electron enters the calorimeter, it produces an electromagnetic shower consisting of photons, electrons and positrons, which together deposit the energy of the original electron. In an ideal calorimeter therefore, electrons should have an E/p ratio close to unity. Muons on the other hand deposit energy only as a single ionizing particle. Charged hadrons sometimes pass through the calorimeter without interacting, appearing like muons, and sometimes interact leaving a larger fraction of their energy in the calorimeter. Muons and charged hadrons therefore generally have values of E/p less than unity.

- N_{cry} Number of EMC crystals hit.

- LAT Lateral energy distribution of showers in the EMC.

$$LAT = \frac{\sum_{i=3}^{N} E_i r_i^2}{\sum_{i=3}^{N} E_i r_i^2 + E_1 r_0^2 + E_2 r_0^2}$$

  where
  - N is the number of crystals associated with the shower;
  - E_i is the energy deposited in the i-th crystal of the EMC numbering them such that $E_1 > E_2 > ... > E_N$;
  - r_1, ϕ_i are the polar coordinates in the plane perpendicular to the line pointing from the interaction point to the shower center;
  - r_0 is the average distance between two crystals, which is about 5 cm for the *BABAR* EMC.

  This variable is constructed to discriminate between electromagnetic and hadronic showers based on their average properties. The summation in the numerator

omits the two crystals containing the highest amount of energy. Electrons deposit most of their energy in two or three crystals, so that the valur of LAT is small for electromagnetic showers.

- $A42$ Zernike Moment in the EMC. Another approach is to expand the LAT into various moments which contain information about the azimuthal distribution with respect to the particle's initial direction.

$$A_{nm} = \sum_{r_i<R_0}^{n} \frac{E_i}{E} f_{nm}\left(\frac{r_i}{R_0}\right) e^{-im\phi_i}$$

where $R_0 = 15$ cm and

$$f_{nm}\left(\rho_i = \frac{r_i}{R_0}\right) = \sum_{s=0}^{(n-m)/2} \frac{(-1)^s (n-s)! \phi_i^{n-2s}}{s!(n+m)(2-s)!(n-m)(2-s)!}$$

with n,m integer and positive; n-m even number; r_i is the distance between the crystal and the shower axis.
The only Zernike moment used is A_{42} which take into account that the electromagnetic showers are more regular than the hadronic ones.

- dE/dx Energy loss in the DCH
- θ_c Cherenkov angle in the DIRC
- N_γ Number of photons in the DIRC
- $N_{\gamma exp}$ Number of photons expected
- Δ_ϕ Track-bump separation. It is the difference between the azimuthal angle ϕ_{EMC} of the intersection of the charged tracks with the detector model of the EMC and the angle $\phi_{cluster}$ which is the azimuth of the cluster associated to the track:

$$\Delta\phi = q(\phi_{EMC} - \phi_{cluster})$$

where q is the charge of the particle. (A cluster is a set of adjacent crystals with the sum of their energies above some threshold.) While the electrons shower shortly after entering the EMC, the interacting hadrons usually shower later and thus show a larger $\Delta\phi$.

Muons

For muons there are several Cut-based ("Micro") selectors (muMicroMinimumIonizing, muMicroVeryLoose, muMicroLoose, muMicroTight, muMicroVeryTight), a Likelihood ("LH") selector (muLikeTight), several neural network selectors (muNNVeryLoose, muNNLoose, muNNTight, muNNVeryTight) and several Boost Decision Tree selectors (muBDTVeryLoose, muBDTLoose, muBDTTight, muBDTVeryTight). These selectors use the following PID variables:

- E_{cand}: the energy released in the EMC;
- N_L: the number of IFR hit layer in the 3-D cluster;
- Λ_{meas}: Measured number of interaction lengths traversed by the track in the *BABAR* detector. It is estimated from the last layer hit by the extrapolated track in the IFR;
- $\Delta\Lambda = \Lambda_{exp} - \Lambda_{meas}$: where Λ_{exp} is the number of interaction lenghts expected to be traversed by the track in the muon hypothesis;
- $\chi^2_{fit} : \chi^2/dof$ of the IFR hit strips in a polynomial fit of the cluster;
- $\chi^2_{mat} : \chi^2/dof$ of the IFR hit strips in the cluster with respect to the IFR Kalman track extrapolation;
- T_c: the continuity of the track in the IFR;
- m and σ_m: Average multiplicity of hit strips per layer and its standard deviation.

Pions

For pions there are several Likelihood ("LH") selectors (piLHVeryLoose, piLHLoose, piLHTight, piLHVeryTight). These selectors use the following PID variables:

- dE/dx Energy loss in the SVT and DCH;

- θ_c Cherenkov angle in the DIRC;
- N_γ: Number of photons in the DIRC;
- Track quality in the DIRC;
- iselectron: Whether the track passes the LH electron selector;
- ismuon: Whether the track passes the MicroVeryTight muon selector.

In the following we give a brief description of the PID lists used for this analysis.

eLHBremLH

This is a list of electron candidates, done by the merging of eBremRecoPid (bremsstrahlung corrected electrons) and PidLHElectrons.

eBremRecoPid

This is a cut-based merged list of PidLHElectrons and GoodPhotonLoose, satisfying the following criteria:

- photon energy is between 0.030 and 10.58 GeV;
- photon LAT (Lateral energy distribution) is between 0.0001 and 0.8 GeV;
- photon A42 (Zernike moment) is 0.25;
- electron and photon point in the same direction (based on ϕ and θ cuts).

PidLHElectrons

This list contains electrons survived to a Likelihood selector with the following requests:

- center of mass momentum $p* > 4$ GeV/c;

- ratio between energy deposited in EMC to momentum 0.5 < E/p <1.5;
- number of crystals hit in EMC $N_{cry} \geq 4$;
- number of photons revealed $N_{\gamma} \geq 6$.

muNNVeryLoose

This list contains muons that passed a neural network selector with these cuts:

- energy deposited in EMC $E_{cal} < 0.5$ GeV;
- number of hit layers in IFR $N_L > 2$;
- number of interaction lengths traversed $\Lambda_{meas} > 2$ and $\Delta_{\Lambda} < 2.5$;
- track continuity $T_c > 0.1$;
- average multiplicity of hit strips $m < 10$ and $\sigma_m < 6$.

muBDTVeryLoose

This is a cut based list with the same selection criteria of the muNNVeryLoose list; the difference between these two lists is that muBDTVeryLoose identifies muons using the Boost Decision Tree algorithm.

List of Tables

List of Figures

Bibliography

[1] J. J. Aubert et al. [E598 Collaboration], "*Experimental Observation of a Heavy Particle J*", Phys. Rev. Lett. 33 (1974) 1404.

[2] J. E. Augustin et al. [SLAC Collaboration], "*Discovery of a Narrow Resonance in e+e- Annihilation*", Phys. Rev. Lett. 33 (1974) 1406.

[3] G. S. Abrams et al. [SLAC Collaboration], "*Discovery of a Second Narrow Resonance in e^+e^- Annihilation*", Phys. Rev, Lett. 33, 1453 (1974).

[4] K. Nakamura et al. (Particle Data Group), J. Phys. G 37, 075021 (2010).

[5] S. L. Glashow, J. Ilioupoulos, L. Maiani, "*Weak Interactions with Lepton-Hadron Symmetry*", Phys. rev. D 2, 1285 (1970).

[6] E. Segrè, Nuclei e Particelle (Zanichelli, 1982).

[7] E. Eichten, K. Gottfried, T. Kinoshita, K. D. Lane and T. M. Yan, "*Charmonium: The model*", Phys. Rev. D 17 (1978) 3090 [Erratum-ibid. D 21 (1980) 313].

[8] W. Kwong, J. L. Rosner and C. Quigg, "*Heavy-Quark System*", Annual Review of Nuclear and Particle Science Vol. 37 (1987) 325-382.

[9] R. Gupta, "*Introduction to Lattice QCD*", arXiv:hep-lat/9807028.

[10] D. J. Gross and F. Wilczek, "*Ultraviolet Behavior of Non-Abelian Gauge Theories*", Phys. Rev. Lett. 30 (1973) 1343.

[11] H. D. Politzer, "*Reliable Perturbative Results for Strong Interactions?*", Phys. Rev. Lett. 30 (1973) 1346.

[12] E. E. Salpeter, "*Bethe-Salpeter Equation - The Origins*", arXiv:0811.1050 [physycs.hist-ph].

[13] H. Sonoda, "*Wilson's Renormalization Group and Its Applications in Perturbation Theory*", arXiv:hep-th/0603151.

[14] N. Isrgur and M. B. Wise, "*Weak transition form factors between heavy mesons*", Phys. Lett. B 237 (1990) p. 527.

[15] M. Neubert, "*Heavy Quark Symmetry*", Phys. Rept. 245 (1994) 259 [arXiv:hep-ex/9306320].

[16] G. T. Bodwin, E. Braaten and G. P. Lepage, "*Rigorous QCD Analysis of Inclusive Annihilation and Production of Heavy Quarkonium*", Phys. Rev. D 51 (1995) 1125 [Erratum-ibid. D 55 (1997) 5853] [arXiv:hep-ex/9407339].

[17] W. E. Caswell and G. P. Lepage, "*Effective lagrangians for bound state problems in QED, QCD and other field theories*", Phys. Lett. B 167 (1986) 437.

[18] R. McClary and N. Byers, "*Relativistic effects in heavy-quarkonium spectroscopy*", Phys. Rev D 28, 1692 (1983).

[19] K. Abe et al., [BELLE Collaboration], "*Observation of Double $c\bar{c}$ Production in e^+e^- Annihilation at $\sqrt{s}$ ~10.6 GeV*", Phys. Rev. Lett. 89, 142001 (2002).

[20] R. Partridge et al., "*Observation of an η_c Candidate State with Mass 2978±9 MeV*", Phys. Rev. Lett. 45, 1150 (1980).

[21] B. Aubert et al., [*BABAR* Collaboration], "*Measurement of double charmonium production in e^+e^- annihilations at $\sqrt{s}$=10.6 GeV*", Phys. Rev. D 72, 031101 (2005).

[22] P. Dalpiaz In: H. Poth, Editor, Proceedings of the first LEAR Workshop Karlsruhe, Germany (1979).

[23] S. C. Choi et al., [BELLE Collaboration], "*Observation of the $\eta_c(2S)$ in exclusive $B \to KK_S K^- \pi^+$ decays*", Phys. Rev. Lett. 89, 102001 (2002).

[24] M. Andreotti et al., "*Measurement of the resonance parameters of the charmonium ground state, η_c (1^1S_0)*", Phys. Lett. B566 (2003) 45.

[25] B. Aubert et al., [*BABAR* Collaboration], "*Measurements of the Mass and Width of the η_c Meson and of an $\eta_c(2S)$ Candidate*", Phys. Rev. Lett. 92 (2004) 142002.

[26] T.A. Armstrong et al., [E760 Collaboration], "*Measurement of the J/ψ and ψ' resonance parameters in $p\bar{p}$ annihilation*", Phys. Rev. D47, (1993) 772.

[27] S. Bagnasco et al., "*New measurements of the resonance parameters of the χ_{c0} of the 1^3P_0 state of charmonium*", Phys. Lett. B 533, 237 (2002).

[28] M. Andreotti et al., "*Measurement of the resonance parameters of the χ_{c1} (1^3P_1) and χ_{c2} (1^3P_2) states of charmonium formed in antiproton-proton annihilations.*" Nucl. Phys. B 717, 34 (2005).

[29] T. Armstrong et al., [E760 Collaboration], "*Observation of the P wave singlet state of charmonium*", Phys. Rev. Lett. 69, 2337-2340 (1992).

[30] J. L. Rosner et al., [CLEO Collaboration], "*Observation of the h_c (1^1P_1) State of Charmonium*", Phys. Rev. Lett. 95, 102003 (2005).

[31] P.A. Rapidis et al., "*Observation of a Resonance in e^+e^- Annihilation Just above Charm Threshold*", Phys. Rev. Lett. 39, 526 (1977).

[32] S.C. Choi et al., [BELLE Collaboration], "*Observation of a Narrow Charmoniumlike State in Exclusive $B^\pm \to K^\pm \pi^+ \pi^- J/\psi$ Decays*", Phys. Rev. Lett 91, 262001 (2003).

[33] F. Close and S. Godfrey, "*Charmonium hybrid production in exclusive B-meson decays*", Phys. Lett. B 574, 210 (2003).

[34] K. Abe et. al., [BELLE Collaboration], "*Evidence for $X(3872) \to \gamma J/\psi$ and the sub-threshold decay $X(3872) \to \omega J/\psi$*", arXiv:hep-ex/0505037.

[35] K. Abe et al., [BELLE Collaboration], "*Observation of a new charmonium state in double charmonium production in e^+e^- annihilation at $\sqrt{s} \sim 10.6$*", Phys. Rev. Lett. 98, 082001 (2007) [arXiv:hep-ex/0507019].

[36] B. Aubert et al., [*BABAR* Collaboration], "*Observation of a Broad Structure in the $\pi^+\pi^- J/\psi$ Mass Spectrum around 4.26 GeV/c^2*", Phys. Rev. Lett. 95, 142001 (2005).

[37] E. Kou and O. Pène, "*Suppressed decay into open charm for the Y(4260) being an hybrid*", Phys. Lett. B 631, 164 (2005).

[38] K. Abe et al., [BELLE Collaboration], "*Study of double charmonium production in e^+e^- annihilation at $\sqrt{s} = 10.6$ GeV*", Phys. Rev. D70 (2004) 071102 [arXiv:hep-ex/0407009].

[39] E. Braaten and J. Lee, "*Exclusive Double-Charmonium Production from e^+e^- Annihilation into a Virtual Photon*", Phys. Rev. D 67 (2003) 054007. [Erratum-ibid. D 72 (2005) 099901] [arXiv:hep-ex/0211085].

[40] J. P. Ma and Z. G. Si, "*Predictions for $e^+e^- \to J/\psi\eta_c$ with light-cone wave functions*", Phys. Rev. D 70 (2004) 074007 [arXiv:hep-ph/0405111].

[41] V. V. Braguta, "*Double charmonium production at B-factories within light cone formalism*", Phys. Rev. D 79 074018 [arXiv:hep-ex/0811.2640].

[42] Y. J. Zhang, Y. J. Gao and K. T. Chao, "*Next-to-Leading Order QCD Correction to $e^+e^- \to J/\psi + \eta_c$ at $\sqrt{s} = 10.6$ GeV*", Phys. Rev. Lett. 96 (2006) 092001 [arXiv:hep-ex/0506076].

[43] D. Ebert and A. P. Martynenko, "*Relativistic effects in the production of pseudoscalar and vector doubly heavy mesons from e^+e^- annihilation*", Phys. Rev. D 74 (2006) 054008 [arXiv:hep-ex/0605230].

[44] D. Ebert, R. N. Faustov, V. O. Galkin and A. P. Martynenko, "*Semileptonic decays of doubly heavy baryons in the relativistic quark model*", Phys. Rev. D70 (2004) 014018 [Erratum-ibid D 77 (2008) 079903] [arXiv:hep-ph/0404280].

[45] A. P. Martynenko, "*Relativistic effects in the processes of heavy quark fragmentation*", Phys. Rev. D 72 (2005) 074022 [arXiv:hep-ph/0506324].

[46] R. Ammar et al., [CLEO Collaboration], "*Measurement of the total cross section for e^+e^- $\rightarrow$hadrons at $\sqrt{s}$ $\sim$10.52 GeV*", Phys. Rev. D 57 (1998) 1350 [arXiv:hep-ex/9707018].

[47] G. T. Bodwin, J. Lee and E. Braaten, "*e^+e^- Annihilation into $J/\psi + J/\psi$*", Phys. Rev. Lett. 90 (2003) 162001 [arXiv:hep-ph/0212182].

[48] G. T. Bodwin, J. Lee and E. Braaten, "*Exclusive double-charmonium production from e^+e^- annihilation into two virtual photons*", Phys. Rev. D 67 (2003) 054023 [erratum-ibid D72 (2005) 099904] [arXiv:hep-ph/0212352].

[49] M. Gremm and A. Kapusting, "*Annihilation of S-wave quarkonia and the measurement of α_s*", Phys. Lett. B 407 (1997) 323.

[50] V. V. Braguta, A. K. Likhoded and A. V. Luchinsky, "*Excited charmonium mesons production in e^+e^- annihilation at $\sqrt{s} = 10.6$ GeV*", Phys. Rev. D72 (2005) 074019 [arXiv:hep-ph/0507275].

[51] G. P. Lepage and S. J. Brodsky, "*Exclusive Processes in Quantum Chromodynamics: The Form Factors of Baryons at Large Momentum Transfer*", Phys. Rev. Lett 43 (1979) 545 [Erratum-ibid. 43 (1979) 1625]

[52] G. P. Lepage and S.J. Brodsky, "*Exclusive processes in perturbative quantum chromodynamics*", Phys. Rev. D 22 (1980) 2157.

[53] Z. G. He, Y. Fan and K. T. Chao, "*Relativistic corrections to J/ψ exclusive and inclusive double charm production at B factories*", Phys. Rev. D 75 (2007) 074011 [arXiv:hep-ph/0702239].

[54] G. T. Bodwin, J. Lee and C. Yu, "*Resummation of relativistic corrections to $e^+e^- \rightarrow J/\psi + \eta_c$*". Phys. Rev. D 77 (2008) 094018 [arXiv:0710.0995 [hep-ph]].

[55] R. McClary and N. Byers, "*Relativistic effects in heavy-quarkonium spectroscopy*", Phys. Rev D 28, 1692 (1983).

[56] B. Aubert et al., [*BABAR* Collaboration], "*Measurement of the B^+B^0 Production Ratio from the $\Upsilon(4S)$ Meson using $B^+ \to J/\psi K^+$ and $B^0 \to J/\psi K^0_S$ Decays*", Phys. Rev. D 69, 071101 (2004). [aXiv:hep-ex/0401028v1]

[57] P. F. Harrison and H. R. Quinn [*BABAR* Collaboration], "*The BaBar Physics Book: Physics at an asymmetric B factory*".

[58] A. Sessler and E. Wilson, *Engines of Discovery - A century of Particle Accelerators* (World Scientific Publishing, 2007).

[59] PEP-II Conceptual Design Report, SLAC-R-418 (1993).

[60] W. Kozanecki et al., "Trickle-charge: A new operational mode for PEP-II".

[61] I. Adam et al. [*BABAR* Collaboration], "*The DIRC particle identification system for the BABAR experiment*", Nuclear Instruments and Methods in Physics Research A 538 (2005) 281.

[62] D. Boutigny et al. [*BABAR* Collaboration], "*BABAR* technical design report", chapter 7.

[63] T. Barnes, S. Godfrey and E. S. Swanson, "*Higher charmonia*", Phys. Rev. D 72, 054026 (2005)

[64] T. Barnes, "*The XYZs of charmonium at BES*", Int. J. Mod. Phys. A 21, 5583 (2006)

[65] K. Y. Liu, Z. G. He and K. T. Chao, "*Search for excited charmonium states in e^+e^- Annihilation at $\sqrt{s} = 10.6$ GeV*", Phys. Rev. D77 (2008) 014002 [arXiv:hep-ph/0408141]

Ringraziamenti

It was not an easy period but at the end of it I would like to thank people who contribute to make my work more interesting and formative.
First of all, I thank Prof. Diego Bettoni for his support during these years, he was fundamental for me and for my work.
Thanks also to the other collegues of the *BABAR* group in Ferrara.
I gratefully acknowledge Valentina Santoro for her continuous presence during these years: without her care I couldn't arrive at this point of my studies.
Thanks to Irma because she is my "American mom", you teach me every day a lot of things! You are really a beautiful person, and I cannot forget your and your friendship!

Sono giunta al termine di questo percorso, tra alti e bassi, devo ammettere che non è stato un percorso facile, ma sono state tante le persone che mi hanno aiutato e che mi sento in dovere di ringraziare.
La prima persona a cui va il mio pensiero è il Prof. Diego Bettoni, una collarazione iniziata già durante la tesi di laurea, e continuata durante il dottorato. Devo ringraziarlo per la sua continuità disponibilità e comprensione dimostratami puntualmente ogni volta.
Di certo non dimentico di ringraziare Valentina Santoro, il suo aiuto è stato davvero fondamentale in ogni occasione. Senza di lei non sarei sicuramente arrivata a questo punto. Il sua disponibilità ma anche la sua comprensione sono stati davvero un punto fermo durante questi anni di dottorato per me. Grazie anche per gli sfoghi e l'amicizia!

Un ringraziamento particolare va a Matteo Negrini, per le utilissime discussioni di fisica fatte insieme!
Ci sono poi persone che mi sono state vicine, con le quali ho condiviso le gioie e i dolori di questa esperienza.
Grazie di cuore a Susanna Bertelli, un'amicizia coltivata da diversi anni, che tra alti e bassi ho sempre custodito gelosamente nel mio cuore. Sei una persona speciale, che sa dare nell'amicizia qualcosa di veramente speciale che non ho riscontrato in nessuno.
Un ringraziamento a Elisabetta Prencipe, la stima che ho di te è grande e lo sai, e il tuo aiuto morale e non solo è stato fondamentale per me in tanti momenti. Non mi scorderò mai le nostre chiacchierate e le nostre risate, e non mi scorderò mai tutti i tuoi insegnamenti. Sei una persona molto umile e sempre disponibile e gentile. Grazie! Un grazie particolare va a Mauro Munerato, collega di ufficio per tre anni, con lui ho condiviso tutti i momenti no e tutte le gioie; grazie per le mille consulenze tecniche che mi ha sempre dato, ma un grazie soprattutto per l'amicizia che è nata tra di noi e per aver reso questo periodo molto divertente!
Grazie ad Annalisa Cecchi, mentre eri all'Università ci siamo proprio divertite un sacco e poi sei stata un appoggio molto valido per me! Grazie mille!
Un ringraziamento a Gaia, nonchè la mia socia preferita, per tutto quello che mi ha dato e che continua a darmi tutti i giorni.... di certo c'è che mi manchi davvero tanto ma che ho tantissimi ricordi di te e di noi!!
Non posso dimenticare la mia amica Elena, fondamentale per me in diversi momenti in questi anni, la nostra amicizia è cresciuta pian piano e ora sei davvero una persona che stimo moltissimo. Ti voglio bene amica!
Grazie alla mia mitica sorella Elisa, perchè ci sei e ci sei sempre stata! Ti voglio davvero un sacco di bene!
Grazie a Fabiano, allo zio che non ho mai avuto, e anche se per colpa del mio carattere non ci sentiamo per lunghi periodi di tempo, sai sempre essere comprensivo con me! Grazie!
Grazie ai miei nonni Walter e Caterina, perchè mi fate morire dalle risate!! E un pensiero anche ai nonni Maria, Lidia e Cosemino e alla zia Vivetta, i miei angeli custodi... avete visto che ho ottenuto anche questo risultato..?

Infine ringrazio la mia famiglia, mamma e papà, le persone più importanti della mia vita, che sono state sempre in penombra per farsì che io potessi risplendere e camminare sotto il sole a testa alta. Grazie per avermi protetto in mille occasioni, e per avermi sempre asciugato le lacrime... Siete due persone fantastiche, non potevo desiderare dei genitori migliori! Grazie per avermi sempre lasciata libera di scegliere e anche di sbagliare. Tutto ciò è impagabile e voi lo sapete bene...!
Grazie a mio fratello David, perchè da buon saggio dissi "forse non è che per essere amici bisogna seguire delle regole scritte dalla società ma è sufficente la disponibilità ad ascoltare ed aiutarsi anche moralmente", ed è proprio vero, i sentimenti vengono dal cuore, e io per te provo un bene immenso fratello! E ricordati sempre "Sognando California..." perchè mai una canzone fu così profetica...!

Infine ringrazio Matteo, a cui è dedicata questa tesi, sei la persona più bella che io abbia mai incontrato nella mia vita, le mie giornate trascorse al tuo fianco sono semplicemente stupende, sei la mia stella di riferimento, senza di te ora non saprei cosa fare. Ti sei innamorato subito di me, ma hai saputo aspettare che il mio cuore ritornasse felice, grazie perchè pensavo di non essere più in grado di amare, ma tu hai saputo farmi innamorare della tua splendida persona. Grazie che mi hai aspettato, grazie di tutto, grazie che ci sei, grazie che mi ami.